Study on the effect of very cohesive ultra-fine particles in mixtures on compression, consolidation, permeation, and fluidization

Dissertation
zur Erlangung des akademischen Grades

Doktoringenieur
(Dr.-Ing.)

von M.Sc. **Abbas Kamranian Marnani**
geb. am 18. August 1978 in Esfahan, Iran

genehmigt durch die Fakultät für Verfahrens- und Systemtechnik der Otto-von-Guericke-Universität Magdeburg

Promotionskommission: Prof. Dr.-Ing. Berend van Wachem (Vorsitz)
Prof. Dr.-Ing. Dominique Thévenin (Gutachter)
Prof. Dr.-Ing. Sergiy Antonyuk (Gutachter)
Prof. Dr.-Ing. Andreas Bück (Gutachter)

Eingereicht am: 27.03.2020
Promotionskolloquium am: 23.11.2020

This dissertation is dedicated

To: My lovely wife, *Maryam,* for her understanding, sacrifice, strength, and unceasing love that supports me to complete this dissertation.

To: My daughter, *Ayeh*, whose love has redefined my world.

To: My parents, *Mohammad and Firouzeh*, and **My Siblings**, *Maryam, Zahra, and Alireza,* for their endless love, support, and encouragement since I was born.

Declaration

I hereby declare that I prepared the work submitted without inadmissible assistance and without the use of any aids other than those indicated. Facts or ideas taken from other sources, either directly or indirectly have been marked as such.

In particular, I did not use the services of a commercial graduation consultation. Further, I have not made payments to third parties either directly or indirectly for any work connected with the contents of the submitted dissertation.

The work has not been submitted as a dissertation either in Germany or abroad in the same or similar form and has also not been published as a whole.

Magdeburg,
March 27, 2020 Abbas Kamranian Marnani

Schriftliche Erklärung

Ich erkläre hiermit, dass ich die vorliegende Arbeit ohne unzulässige Hilfe Dritter und ohne Benutzung anderer als der angegebenen Hilfsmittel angefertigt habe. Die aus fremden Quellen direkt oder indirekt übernommenen Gedanken sind als solche kenntlich gemacht.

Insbesondere habe ich nicht die Hilfe einer kommerziellen Promotionsberatung in Anspruch genommen. Dritte haben von mir weder unmittelbar noch mittelbar geldwerte Leistungen für Arbeiten erhalten, die im Zusammenhang mit dem Inhalt der vorgelegten Dissertation stehen.

Die Arbeit wurde bisher weder im Inland noch im Ausland in gleicher oder ähnlicher Form als Dissertation eingereicht und ist als Ganzes auch noch nicht veröffentlicht.

Magdeburg,
März 27, 2020 Abbas Kamranian Marnani

Certification of Non-Conviction

I hereby declare that I have not been convicted of any offense with a connection to scholarship.

Magdeburg,
March 27, 2020 Abbas Kamranian Marnani

Erklärung zur strafrechtlichen Verurteilung

Ich erkläre hiermit, nicht wegen einer Straftat verurteilt worden zu sein, die Wissenschaftsbezug hat.

Magdeburg,
März 27, 2020 Abbas Kamranian Marnani

Abstract

Typical flow problems of ultra-fine cohesive powders are caused by undesirable particle cohesion, poor flowability, and large compressibility and are increased by poor permeability. Unfortunately, the knowledge about the behavior and properties of fine and ultra-fine particles is very limited. So it can be said that a study on fluidization, compression, and permeation of these particles is certainly beneficial for understanding their properties. This work focuses on the behavior of fine and ultra-fine particulate material in three main processes of fluidization, compression, permeation and also the effect of compression, as well as combined effect of compression and permeation on re-fluidization of compressed and/or permeated beds. The most important part of this study will be related to the effect of the presence of ultra-fine powders in different mixtures with fine materials during all of the above-mentioned processes. Two mixtures with a dominant mass fraction of either fine or ultra-fine particles and a mixture of these two materials in the same weight fraction will be considered. Practically, a mixture of fine and ultra-fine particles can happen due to breakage or surface abrasion of the fine particles in some processes which totally changes the size distribution and also its behavior during a fluid-particle interaction process like fluidization. The materials used in this study are both ground calcium carbonate (GCC); fine is CALCIT MVT 100 (Geldart's group A) and ultra-fine is CALCIT MX 10 (group C). Fine particles need a pre-classification for removing almost all of ultra-fine powders from the original material of CALCIT FW 270. However, the classification of ultra-fine adhesive particles shows insufficient classification characteristics due to the inter-particle cohesive forces. Different methods, considering their limitations and efficiencies, were used. Finally, the most effective method (wet sieving) and the controlling process parameters are thoroughly discussed. The experimental results of fluidization for different binary mixtures of these materials show that the physical properties of the mixtures are close to those of pure ultra-fine powders. The fluidization behavior of the mixtures is non-reproducible and includes cracking, channeling and agglomeration (like for pure ultra-fine powders). Increasing the portion of ultra-fine materials in the mixture causes a delay in starting partial fluidization, an increase in the bed pressure drop as well as a delay in reaching the peak point. During compression tests, different mixtures of fine and ultra-fine particles are compressed at three pressure levels. The results show that by increasing the applied pressure, the compressibility decreases due to a change in the compaction regime. Subsequently, for the higher pressure, the slope of packing density versus applied stress curves is noticeably different. However, this slope does not depend on the size distribution of mixtures, but on the type of material. Comparing fluidization and re-fluidization curves (bed pressure drop vs. gas velocity) shows an increase in the maximum bed pressure drop (ΔP_{peak}) for re-fluidization. By increasing the portion of ultra-fine particles in the binary mixture,

ΔP_{peak} increases in a non-linear manner. Furthermore, the incipient fluidization point moves to a higher gas velocity. After compression, the peak of the bed pressure drop in the re-fluidization test happens at a lower gas velocity than in the initial fluidization test. Thus, the slope of the loading curve is much larger for re-fluidization. The opposite is observed for the unloading curves. During permeation, the rearrangement of fine and ultrafine particles in porous media causes a reduction in permeability and the formation of preferential flow paths. The observations show a permanent decrease in permeability which was attributed to structural changes in the pore network, such as sealing of pore channels or expansion and reorientation of particles within the pores. The results show that by adding the ultra-fine powders in the particle bed, even only 30% of ultra-fines in the mixture, the slope of fitted linear curves indicates a sharp change (about 50 times smaller) in the permeability of the mixture material. The results also reveal that the trend of decreasing the permeability for all three levels of applied pressures are almost the same. However, the rate of decreasing the permeability in the first stages of applying pressures is far more than in the last stages for all three pressure levels. Increasing the pressure to the maximum pressure of each level reduces the rate of permeability change. Analyzing the re-fluidization test results shows that for re-fluidization after compression and permeation, the peak of the bed pressure drops increases, while the superficial gas velocity corresponding to the peak point is smaller; consequently, the slope of the loading curve is much larger for re-fluidization. The opposite is observed for the unloading curves. Finally, this study is closed with the simulation of fine particle bed fluidization. For this simulation, a coupled CFD-DEM is required to simulate the interaction of gas and solid phases beside each other. For the DEM (Discrete Element Method), EDEM software, a product of DEM Solution Company and for CFD, ANSYS-FLUENT are used. The results show that by enlarging the scaled-down geometry as representative geometry of the real experimental setup, the agreement of the simulation results with the experimental data improves. The consideration of the particle size distribution (PSD) in the simulation could considerably impact the simulation results. Therefore, a combination of these two steps could result in a better agreement. However, an increase in the number of particles or a decrease in the simulation time-step due to decreasing the minimum size of particles in the simulation domain result in a notable increase in computational costs.

Keywords: Fine and ultra-fine particles, fluidization, compression, permeation, simulation, CFD, DEM

Zusammenfassung

Typische Fließprobleme von ultrafeinen kohäsiven Pulvern werden durch unerwünschte Partikelkohäsion, schlechte Fließfähigkeit, große Kompressibilität und geringe Permeabilität verursacht. Leider sind die Kenntnisse über das Verhalten und die Eigenschaften von feinen und ultrafeinen Partikeln sehr begrenzt. So kann man sagen, dass eine Untersuchung der Fluidisierung, Komprimierung und Permeation dieser Partikel sicherlich zum Verständnis ihrer Eigenschaften beiträgt. Diese Arbeit konzentriert sich auf das Verhalten von feinem und ultrafeinem teilchenförmigem Material in drei Hauptprozessen der Fluidisierung, Kompression, Permeation und auch der Auswirkung der Kompression sowie der kombinierten Auswirkung der Komprimierung und Permeation auf die erneute Fluidisierung verschiedener Partikelbetten. Der wichtigste Teil dieser Studie befasst sich mit der Auswirkung des Vorhandenseins von ultrafeinen Pulvern in verschiedenen Mischungen mit feinen Materialien bei allen oben genannten Prozessen. Es werden zwei Gemische mit einem dominanten Massenanteil von entweder feinen oder ultrafeinen Partikeln und ein Gemisch dieser beiden Materialien in der gleichen Gewichtsfraktion betrachtet. In der Praxis kann eine Mischung aus feinen und ultrafeinen Partikeln aufgrund von Bruch oder Oberflächenabrieb der feinen Partikel in einigen Prozessen auftreten, was die Größenverteilung und auch deren Verhalten während eines Fluid-Partikel-Wechselwirkungsprozesses wie der Fluidisierung vollständig verändert. Die Materialien, die in dieser Studie verwendet werden, bestehen aus gemahlene Calciumcarbonat (GCC); Fein ist CALCIT MVT 100 (Geldarts Gruppe A) und Fein ist CALCIT MX 10 (Gruppe C). Feine Partikel benötigen eine Vorklassifizierung, um fast alle ultrafeinen Pulver aus dem Originalmaterial von CALCIT FW 270 zu entfernen. Die Klassifizierung von ultrafeinen Partikeln zeigt jedoch unzureichende Klassifikationseigenschaften aufgrund der Kohäsionskräfte zwischen den Partikeln. Verschiedene Methoden, unter Berücksichtigung ihrer Grenzen und Effizienz, wurden verwendet. Schließlich werden die effektivste Methode (Nasssiebung), und die entsprechenden Prozessparameter gründlich diskutiert. Die experimentellen Ergebnisse der Fluidisierung für verschiedene binäre Gemische dieser Materialien zeigen, dass die physikalischen Eigenschaften der Mischungen nahe an denen von reinem ultra-feinem Pulver sind. Das Fluidisierungsverhalten der Gemische ist nicht reproduzierbar und umfasst Cracken, Kanalisieren und Agglomerieren (wie für reines ultrafeine Pulver). Das Erhöhen des Anteils ultrafeiner Materialien in der Mischung verursacht eine Verzögerung beim Starten der partiellen Fluidisierung, eine Erhöhung des Bettdruckabfalls sowie eine Verzögerung beim Erreichen des Spitzenpunktes. Bei Kompressionstests werden verschiedene Gemische aus feinen und ultrafeinen Partikeln auf drei Druckstufen zusammengepresst. Die Ergebnisse zeigen, dass durch Erhöhen des angelegten Drucks

die Kompressibilität aufgrund einer Änderung des Verdichtungsregimes abnimmt. Anschließend ist für den höheren Druck die Steigung der Packungsdichte gegenüber dem angelegten Stresskurven merklich unterschiedlich. Diese Steigung hängt jedoch nicht von der Größenverteilung der Gemische ab, sondern von der Art des Materials. Vergleicht man der Kurven für die Fluidisierung und die erneute Fluidisierung (Bettdruckabfall gegen Gasgeschwindigkeit) zeigt einen Anstieg des maximalen Bettdruckabfalls (ΔP_{peak}) bei der erneuten Fluidisierung. Durch Erhöhen des Anteils ultrafeiner Partikel in der binären Mischung steigt ΔP_{peak} nichtlinear an. Darüber hinaus bewegt sich der beginnende Fluidisierungspunkt zu einer höheren Gasgeschwindigkeit. Nach der Kompression passiert die Spitze des Bettdruckabfalls im erneuten Fluidisierungstest bei einer niedrigeren Gasgeschwindigkeit als in der anfänglichen Fluidisierung. Somit ist die Steigung der Belastungskurve viel größer für die erneute Fluidisierung. Das Gegenteil wird für die Entladung beobachtet. Während der Permeation bewirkt die Umlagerung von feinen und ultrafeinen Partikeln in porösen Medien eine Verringerung der Permeabilität und die Bildung bevorzugter Strömungswege. Die Beobachtungen zeigen eine permanente Abnahme der Permeabilität, die auf strukturelle Veränderungen im Porennetzwerk zurückzuführen ist, wie das Verschließen von Porenkanälen oder die Expansion und Neuausrichtung von Partikeln innerhalb der Poren. Die Ergebnisse zeigen, dass durch die Zugabe der ultrafeinen Pulver in das Partikelbett, auch für nur 30% der ultra-Feinteile in der Mischung, die Steigung der angepassten linearen Kurven eine scharfe Änderung (etwa 50-mal kleiner) in der Permeabilität des Mischungsmaterials aufweist. Die Ergebnisse zeigen auch, dass die Tendenz zur Verringerung der Permeabilität für alle drei Niveaus des angewendeten Drucks nahezu gleich ist. Die Rate der Verringerung der Permeabilität in den ersten Stufen des Aufbringens der Drücke ist jedoch weitaus höher als in den letzten Stufen, für alle drei Druckniveaus. Tatsächlich wird durch Erhöhen des Drucks auf den Maximaldruck jedes Niveaus die Änderungsrate der Permeabilität verringert. Eine Analyse der erneuten Fluidisierung zeigt, dass für die erneute Fluidisierung nach der Kompression und Permeation der Peak des Bettdruckabfalls zunimmt, während die Oberflächengasgeschwindigkeit am Spitzenpunkt kleiner ist; folglich ist die Steigung der Belastungskurve viel größer für die erneute Fluidisierung. Das Gegenteil wird für die Entladung beobachtet. Schließlich wird diese Studie mit der Simulation der Feinpartikelbettfluidisierung abgeschlossen. Für diese Simulation wird ein gekoppeltes CFD-DEM benötigt, um die Wechselwirkung von Gas- und Festphasen zu simulieren. Für die DEM (Diskrete Elemente Methode), wird die EDEM-Software, ein Produkt der DEM Solution Ltd Gesellschaft, und für CFD, ANSYS-FLUENT verwendet. Die Ergebnisse zeigen, dass durch eine Vergrößerung repräsentativen Geometrie des realen Versuchsaufbaus, die Übereinstimmung der Simulationsergebnisse mit den experimentellen Daten zunimmt. Die Berücksichtigung der Partikelgrößenverteilung (PSD) in der Simulation könnte die Simulationsergebnisse erheblich verbessern. Daher könnte eine Kombination dieser beiden Aspekte zu einer

besseren Übereinstimmung führen. Eine Zunahme der Partikelanzahl oder eine Abnahme des Simulationszeitschritts (aufgrund einer Abnahme der Mindestgröße von Partikeln in der Simulationsdomäne) führen jedoch zu einer merklichen Zunahme der Rechenkosten.

Keywords: Feine und ultrafeine Partikel, Fluidisierung, Kompression, Permeation, Simulation, CFD, DEM

Table of Contents

Nomenclature

Roman symbols

a	Contact radius (m)
A	Bed cross-section area (m^2)
a_c	Critical contact radius based on the JKR model (m)
Ae	Particle agglomeration number (-)
a_{JKR}	Contact radius based on the JKR model (m)
A_p	Surface area of the particle (m^2)
Ar	Archimedes number (-)
Bo_g	Granular Bond number (-)
c	Intensity of cohesiveness ($kg/m{\cdot}s^2$)
C_D	Drag coefficient (-)
C_H	Hamaker constant ($kg.m^2/s^2$)
C_M	Intensity of cohesive stress of binary mixtures ($kg/m.s^2$)
D	Bed column diameter (m)
d, d_p	Particle diameter (m)
D_0	Diffusion coefficient; given by the Stokes-Einstein relation for a single spherical particle in a liquid with low Reynolds number (-)
$d_{50,3}$	Mass-mean particle diameter (m)
d_{a1} , d_{a2}	Diameters of two colliding agglomerates (m)
d_{ag}	Size of new agglomerates (m)
d_{crit}	Critical particle size wherein the elutriation rate is maximum (does not increase for smaller sizes) (m)
D_e	Equivalent diameter of the tube/pipe (m)
D_f	Fractal dimension of formed agglomerates (-)
D_h	Hydraulic diameter (m)
d_m	Average of the bed particle size (m)
d_p	Particle diameter (m)
d_s	Surface equivalent diameter of the particles (m)
D_s	Separation distance (m)

D_{s_0}	Minimum separation between two particles in contact (m)
$D_{s_{max}}$	Rupture distance between two particles (m)
d_{ST}, d_{32}	Sauter mean diameter of particles (m)
d_v	Volume equivalent diameter of the particles (m)
e	Coefficient of restitution (-)
E^*	Equivalent Young's modulus (kg/m.s^2)
E_c	Cohesive effect on minimum fluidization velocity (-)
E_G	Gravitational effect on minimum fluidization velocity (-)
E_i, E_j	Young's modulus of two particles i and j (kg/m.s^2)
E_{vdW}	van der Waals interaction free energy per unit area (kg/s^2)
f	Friction factor; a function of particle Reynolds number and particle roughness (-)
f_1, f_2	A representative of a function (Eq. 5-26)
$\boldsymbol{F_b}$	External body forces (kg.m/s^2)
F_c	Cohesive force between agglomerates and their peripheral adhered powders (kg·m/s^2)
F_{CG}	Centrifugal force (kg.m/s^2)
F_D	Drag force (particle-fluid interaction) (kg.m/s^2)
F_{el}	Electrostatic force (kg.m/s^2)
ff_c	Bulk solid flowability (-)
F_g	Gravity of the peripheral adhered spherical powders (kg·m/s^2)
F_{g-b}	Gravity-buoyancy force (kg.m/s^2)
F_{JKR}	JKR normal force (kg.m/s^2)
f_{K-C}	Carman-Kozeny function (Eq. 5-21)
F_{ld}	Dynamic exhibit of the liquid bridge force (kg.m/s^2)
F_{ls}	Static exhibit of the liquid bridge force (kg.m/s^2)
$F_{ls,max}$	Maximum static liquid bridge force at contact (kg.m/s^2)
F_n	Normal forces related to the contact including cohesive and collision forces (kg.m/s^2)
F_n^d	Dissipative forces related to the contact including cohesive and collision forces (kg.m/s^2)
Fr	Froude number (-)
F_t	Tangential force (kg.m/s^2)
$\boldsymbol{F^t}$	Total volumetric particle-fluid interaction forces
F_{vdW}	Van der Waals force (kg.m/s^2)
g	Gravity acceleration (m/s^2)
G^*	Equivalent shear modulus (kg/m.s^2)
h_1,h_2	Manometer heads at the top and the bottom of the column (m)
h_b	Height of the bed (m)
HG	Hydraulic gradient (-)

H_{mb}	Height of the bed at minimum bubbling condition (m)
H_{mf}	Height of the bed at minimum fluidization condition (m)
Δh_w	Pressure difference (drop) across the bed (m)
$\boldsymbol{I}$	Unit tensor
I_i	Moment of inertia for particle i (kg.m^2)
K	Ratio of size enlargement (-)
k	Permeability (m^2)
k_0	Factor depending upon the shape of the cross-section of the channel
k_1, k_2, k_3	Coefficients of the resistance to the flow of a fluid through a pipe/particle bed (Eqs. 5-13, 5-14, and 5-15)
K_2	Variable as a function of porosity (Eq. 5-12)
k_b	Boltzmann's constant
K_c	Hydraulic conductivity (m/s)
k_K	Kozeny constant
k_n	Normal stiffness (kg/s^2)
k_s	Spring stiffness (kg/s^2)
k_t	Tangential stiffness (kg/s^2)
L_0	Settled initial bed height (m)
L_e	Tortuous passage length (m)
m	Mass (kg)
$\dot{m}$	Mass flow rate of fluid flow through the bed (kg/s.m^2)
m^*	Equivalent mass of particles (kg)
m_i	Mass of particle i (kg)
m_p	Mass of the particle (kg)
m_s	Total mass of particle bed (kg)
n	Compressibility index (-)
n_c	Number of sample points contained within the mesh cell of particle p
N_f	Number of cell faces (-)
P	Total pressure (Pa)
p_1, p_2	Static pressures at the top and the bottom of the column (Pa)
P_a	Gage pressure within the apparatus (Pa)
Pe	Peclet number (-)
p_i , p_j	Positions of particles i and j (m)
P_{JKR}	Value of maximum cohesion force, called pull-off force (Pa)
ΔP_{lb}	Pressure reduction within the bridge concerning the pressure of its surroundings (Pa)
P_{pull}	Pull of force (kg.m/s^2)
P_{wb}	Total weight per cross-section area of the particle bed (kg/m.s^2)
Δp	Pressure drop (Pa)
ΔP_b	Bed pressure drop (Pa)

ΔP_D	Pressure drop of the gas distributor (Pa)
q_1 , q_2	Charges on the particles (C or A.s)
R	Frictional force per unit area (kg/m.s^2)
r_1	Curvature radius of the liquid bridge between two particles (m)
r_2	Minimum thickness of the liquid bridge between two particles (m)
R_1, R_2	Spherical particle radius (m)
R_{ci}	Distance of the center of mass to the contact point (m)
Re	Reynolds number (-)
$\mathrm{Re_{mf}}$	Reynolds number at minimum fluidization velocity (-)
$\mathrm{Re_p}$	Particle Reynolds number (-)
$\mathrm{Re_t}$	Reynolds number at entrainment (-)
Re_{fc}	Reynolds numbers for complete fluidization (-)
Re_{fi}	Reynolds numbers for incipient fluidization (-)
r_h	Mean hydraulic radius (m)
RH	Relative humidity
$\mathrm{RH_c}$	Critical value of relative humidity
R_i	Elutriation rate constant (-)
R_{lt}	Ratio of "laminar to turbulent"
R_{min}	Minimum particle radius (m)
R_n	Equivalent radius of two spherical particles in contact (m)
S	Surface of packed bed per unit volume of bed (1/m)
S_0	Surface to volume ratio of the particles (1/m)
S_m	Mass source in the continuity equation due to the existence of solid-phase beside the fluid phase
$S_{\varphi_{sc}}$	Source of scalar φ_{sc} per unit of volume V_c
T	Temperature (K)
T_i	Total torque acting on particle i (kg·m^2/s^2)
T_R	Rayleigh time step (s)
Δt_c	Critical time-step for DEM model (s)
u	Mean velocity of the fluid / The apparent velocity (m/s)
U_{ad}	Velocity of after disruption point (Peak point) (m/s)
U_{fc}	Complete fluidization velocity (m/s)
U_{mb}	Minimum bubbling velocity (m/s)
U_{mf}	Minimum fluidization velocity (m/s)
u_r	Radial velocity of particles (m/s)
U_{sg}	Superficial gas velocity (m/s)
V_c	Volume of a control volume (m^3)
V	Volume of fluid flowing in the moment of t (m^3)
$\dot{V}$	Volumetric flow rate of the fluid passing through a porous medium (m^3/s)
v_1, v_2	Fluid flow velocities at the top and bottom of the column (m/s)

v_i	Velocity of particle i (m/s)
V_{lb}	Volume of the liquid bridge (m^3)
V_n^{rel}	Normal component of the relative velocity (m/s)
V_p	Pore volume in the particle bed (m^3)
V_p	Volume of the particle (m^3)
v_{p-p}	Particle-particle relative velocity (m/s)
v_r	Radial velocity of gas (m/s)
V_s	Solid particle volume in the particle bed (m^3)
V_t	Total volume of the particle bed (m^3)
v_t^{rel}	Tangential component of the relative velocity (m/s)
V_θ	Tangential velocity (m/s)
W	Total weight of the bed (kg)
w	Weight fraction of a sample particle in a mixture (-)
x_i	Mass fraction of particles having the average diameter of d_i (-)

Greek symbols

β	Bridge half-filling angle (∘)
β_{p-f}	Coefficient of particle-fluid interaction ($kg/m^3.s$)
γ	Liquid-vapor surface energy (kg/s^2)
γ_1, γ_2	Surface energy of two particles 1 and 2 ($kg.m^2/s^2$)
$\Delta\gamma_{JKR}$	Net surface energy of the contact in the JKR model ($kg.m^2/s^2$)
$\Gamma_{\varphi_{sc}}$	Coefficient of diffusion for scalar φ_{sc}
δ_c	Maximum gap between particles with non-zero force (m)
δ_{JKR}	Overlap caused by the additional surface force based on the JKR model (m)
δ_n	Normal overlap between two particles (m)
δ_t	Tangential overlap between two particles (m)
ε	Void fraction of particle bed / Porosity (-)
ε_0	Permittivity of a vacuum ($A^2s^4/kg.m^3$)
ε_{mf}	Void fraction at minimum fluidization condition (-)
ε_r	Relative permittivity of the medium with respect to vacuum (-)
λ_L	Leva particle shape factor (-)
μ_g, μ_f	Dynamic viscosity of fluid (gas) (kg/m·s)
μ_s	Coefficient of static friction (-)
ϑ	Slope of particle volume fraction versus the dimensionless applied stress
ϑ_g	Kinematic viscosity of the fluid (gas) (m^2/s)
ν_i, ν_j	Poisson's ratios of two particles i and j (-)
ρ_a	Air density (kg/m^3)
ρ_{ag}	Density of agglomerate (kg/m^3)
ρ_b	Bulk density of particulate material (kg/m^3)

ρ_f, ρ_g	Density of the fluid or gas (kg/m^3)
ρ_p	Density of particle (kg/m^3)
σ	Normal stress (kg/m·s^2)
σ_0	Isostatic tensile strength (kg/m.s^2)
σ_1	Major principal normal stress (kg/m.s^2)
σ_2	Minor principal normal stress (kg/m.s^2)
σ_{c0}	Critical pressure (Empirical parameter) (kg/m.s^2)
σ_{ca}	Applied compression stress (kg/m.s^2)
$\hat{\sigma}_c$	The dimensionless applied pressure (σ_c/σ_{c0}) (-)
$\sigma_{M,st}$	Average pressure (($\sigma_1 + \sigma_2$)/2)
σ_c	Uniaxial compressive strength (kg/m.s^2)
τ	Shear stress (kg/m·s^2)
$\boldsymbol{\tau}$	Stress tensor
τ_{ri}	Applying torque due to the rolling friction (kg·m^2/s^2)
φ	Particle (solid) volume fraction (-)
φ_j	Jammed particle volume fraction (-)
φ_i	Angle of internal friction (-)
φ_{st}	Stationary angle of internal friction (-)
Φ	A representative of a function (Eq. 5-25)
φ_s	Particle sphericity (-)
φ_{sc}	A scalar quantity
$\nabla\varphi_{sc}$	Gradient of the scalar φ_{sc}
$\nabla\varphi_{sc_n}$	Quantity of the gradient of the scalar φ_{sc} normal to face
ω_i	Angular velocity for particle i (1/s)

Abbreviations

AMG	Algebraic multigrid method
API	Application Programming Interface
CALCIT	Calcite (CaCO3)
CGS	Centimeter, Gram, Second unit system
CPU	Central Processing Unit
DEM	Discrete Element Method
DPM	Discrete Particle Method
EMP	Eulerian Multi-Phase method
FCPR	Fluidization, Compression, Permeation, and Re-fluidization tests
FCR	Fluidization, Compression, and Re-fluidization tests
FVM	Finite Volume Method
GCC	Ground Calcium Carbonate
JKR	Johnson-Kendall-Roberts model

MP-PIC	Multi-Phase Particle-In-Cell method
PDE	Partial Differential Equation
PISO	Pressure-Implicit with Splitting of Operators
PM10	A particulate matter with a mean aerodynamic diameter of 10 μm
PM2.5	A particulate matter with a mean aerodynamic diameter of 2.5 μm
PSD	Particle Size Distribution
RAM	Random Access Memory
SI	Système international d'unités
SIMPLE	Semi-Implicit Method for Pressure-Linked Equations
SMD	Sauter Mean Diameter
STP	Standard Temperature and Pressure (273 K and 1 atm).
TFM	Two-Fluid Model

CHAPTER 1

General Introduction

In this chapter, a general introduction will be provided, consisting of an overview of the study, problems and motivation, main contributions, and an outlook of the dissertation contents.

1.1 Overview

Typical flow problems of ultra-fine cohesive powders are caused by particle cohesion, poor flowability, and large compressibility, and are escalated by poor permeability [1]. Unfortunately, the knowledge about the behavior and properties of fine and ultra-fine particles is very limited. So it can be said that a study on fluidization, compression, and permeation of these particles is certainly beneficial for understanding their properties. In addition, for the appropriate manufacturing of a chemical product and to improve the process efficiency in particle-based industries, the study of micromechanics of this kind of particles in the flowing process, interaction and transportation, and also permeability of the powder bed is necessary [1].

This work focuses on the behavior of fine and ultra-fine particulate material in three main processes of fluidization, compression, and permeation. In addition, the effect of compression on the re-fluidization of compressed beds as well as the combined effect of compression and permeation on the re-fluidization of compressed and permeated beds will be discussed. The most important part of this study will be related to the effect of the presence of ultra-fine powders in different mixtures with fine materials during all of the above-mentioned processes. In the following, according to the previous studies, the importance of these three processes in different industries and also natural phenomena as well as the general behavior of fine and ultra-fine particles in each process will be briefly discussed. This study will be closed with a simulation of the fluidization process for fine particle bed. The size of ultra-fine particles and the related time-step for DEM simulation of processes associated with such small sizes make the simulation of this kind of powders computationally impossible.

1.1.1 Fluidization behavior of fine and ultra-fine particles

Increasing the heat and mass transfer in a fluidization process of particulate materials by increasing the surface-to-volume ratio is the main reason for the growing use of fluidization in chemical and industrial processes (e.g., granulation, mixing, combustion, coating, and chemical reaction processes). Suspended particles have a larger effective surface area (meaning the surface of the particles exposed to the surrounding fluid) than a packed bed. On the other hand, this higher ratio (surface-to-volume) along with the short distance between the small particles lead to strong interactions between them. These interactions affect the flow properties of the particulate material.

Based on previous studies [2–6], the fluidization of ultra-fine, and even sometimes of fine, particles is challenging. The cohesive inter-particle forces (van der Waals, electrostatic, liquid bridge forces) are the main reasons for the poor fluidization of such powders. Generally speaking, the flow or handling of these powders in practical industrial processes is difficult. According to Valverde [7], a gas-fluidized bed of particulate materials can only be stabilized if inter-particle attraction forces have the same order of magnitude as particle weight. However, for fine and ultra-fine particles, the ratio of inter-particle forces to the weight of particles is in the range of hundreds to thousands.

Fine (d <100 μm) and ultra-fine (d <10 μm) particles have broad applications in many processes (e.g., medicines, paints, catalysts). Nevertheless, the fluidization of these two groups of particles is entirely different. According to Geldart [8], the fluidization of particles by a fluid is classified into four different groups according to the Sauter mean diameter of particles and to the relative density of fluid and particles. Following this classification, the used material in this study, i.e., CALCIT MVT 100 (fine) and CALCIT MX 10 (ultra-fine), are classified in the easy to fluidize-free flowing-Geldart's Group A, and laborious to fluidize-cohesive-Geldart's Group C, respectively. The preparation process of these materials, their properties and specifications will be discussed in the next chapter.

The fluidization behavior of particles is affected by both particles and gas properties; i.e., density, relative humidity, and viscosity of the gas as well as particle parameters such as density, size distribution, surface roughness and hardness, shape, adhesive surface energy, and porosity. In addition, the temperature and total pressure of the fluidization column can have significant effects on the fluidization process. Because most of the catalysts used in fluidized bed reactors are classified in Group A, extensive studies have been dedicated to this group of particles. Previous studies [2,9–11] have shown that the fluidization behavior of Group A of solid particles in a gas is characterized by easy, particulate or aggregative (bubbling) fluidization with proper mixing, slow dearation rate, and high aeratability.

Considering the measured value of minimum fluidization velocity and the calculated Froude number $Fr = {U_{mf}}^2/gd_p$ [12], the fluidization of the fine particles used in this study (introduced later in chapter 2) is classified in the aggregative fluidization behavior. For fine particles, the adhesion-to-weight ratio (inter-particle forces to hydrodynamics forces) is in the range of 1 to 100, leading to slightly adhesive particles [13]. However, this range of inter-particle forces might be beneficial since they are responsible for an expanded dense phase, which limits the growth of bubbles in the first stage of fluidization [2].

In contrast to this behavior, for ultra-fine powders, the inter-particle forces are the dominant forces. Practically, for ultra-fine powders that are categorized in the Group C of Geldart's classification, the adhesion-to-weight ratio is in the range of 100 to 10^4, leading to a cohesive or very cohesive material [13]. Therefore, the gas stream cannot easily separate particles; then, cracking or channeling happens, resulting in poor fluidization. Due to the complex behavior of this kind of powders, the investigations about the fluidization of ultra-fine powders have attracted less attention. However, such powders are interesting for a variety of industrial processes, even if their fluidization behavior is still poorly understood [2,3,14]. Corresponding powders are characterized by poor flowability, considerable compressibility, and poor permeability.

Experimental results and previous studies indicate that the fluidization of ultra-fine particles usually involves cracking, channeling, plugging (slugging), agglomeration, and combinations of those [3,7]. Once cracking (horizontal or sloping cracks) happens, the gas phase flows through the resulting narrow openings. Then, when the gas velocity further increases, channeling (vertical channel) occurs, and the contact of gas with solid is limited to the channeling zone.

At higher gas velocities, another kind of fluidization may occur. In fact, due to high cohesive forces between particles, some agglomerates are formed with different sizes during fluidization [15,16]; the largest ones are found at the bottom of the bed (some of them are even de-fluidized), and the smallest at the top of it [3]. For improving the fluidization quality of ultra-fine powders, two main methods are available. The first one relies on external forces such as vibrations, either mechanical [17–20], acoustic [21,22], or magnetic [7,23]. Resulting forces help to overcome poor contacting by breaking up the particle agglomerates, destroying most of the formed channels, and increasing the bed pressure drop. Therefore, the contact between powders and gas increases and a better suspension of powders arises.

The second method involves changing the inherent properties of the particles, either by modifying their surface, like coating the particle surface with nanoparticles [24] or mixing them with other particles that are different in size, density or shape [9,25–27]. The latter method does not need any change in the fluidization column or any extra equipment [9] and is thus particularly attractive. When coating with nanoparticles, the van der Waals force, the dominant interparticle force for dry and neutral powders, decreases dramatically with increasing particle surface distance. When mixing with coarser particles, the resulting bubble motion helps to break the formed agglomerates at the lower half of the fluidization column.

According to Ajbar et al. [9], the mixing of particles belonging to different Geldart's classification groups could introduce some interesting behavior that is not found for single-group fluidization. For example, by adding a small proportion of Group B-particles to a Group D-particle bed, the famous character of coarse particle fluidization (slugging) can be significantly suppressed [28].

Considering the importance of fluidization processes in the industry and the open questions associated to mixed materials fluidization, the first goal of this study is to investigate the effect of the presence of different portions of Group C powders on fluidization of fine (Group A) particle beds, varying the mass fraction between the fine and ultra-fine materials. Two mixtures with a dominant mass fraction of either fine or ultra-fine particles and a mixture of these two materials in the same weight fraction will be considered. In many industrial processes, parts of the material are fragmented and converted to ultra-fine material due to breakage or surface abrasion of the fine particles as a result of mechanical stresses during particle-particle or particle-wall collisions. This modification of the particle size distribution can change the fluidization of the new mixture. Knowledge about the modified fluidization behavior of a fine particle bed in the presence of ultra-fine powders with the same particle density and origin is important for designing and troubleshooting of these processes.

One example of changes in particle size distribution during a process is the comminution of limestone during batch fluidized bed calcination and sulfation. Here, different comminution processes can occur, "namely primary fragmentation due to release of carbon dioxide during calcination or suddenly heat up of the particles; percolative fragmentation due to loss of connections in the porous structure of the particles; secondary fragmentation yielding relatively coarse non-elutriable fragments; and attrition by surface abrasion due to collisions and surface wear of sorbent particles with bed solids and reactor walls and internals yielding elutriable particles" [29].

In this study, the process of increasing the gas velocity for fluidizing the particles will be called the fluidization loading process. On the other hand, the process of decreasing the gas velocity for a fluidized bed to reach the rest condition will be called the fluidization unloading process.

1.1.2 Compression of fine and cohesive particulate material

The importance of forced compaction as one of the essential steps for the manufacturing of tablets in the pharmaceutical industries is obvious. In addition, the natural compaction or densification due to gravitation happens during the storage of particulate materials and is one of the main issues in bulk material handling, impacting flowability and particle flow rates in many applications of chemical, pharmaceutical, food, and petrochemical industries. The fine particles' packing is one of the remarkable processes in numerous industries in which the control of bulk material densities is important. In the sintering and ceramic industry, the most important process is achieving a compact structure by a compression process. In this process, an initial low-density packing changes to a higher density under an outwardly applied force. On the other hand, powder behavior at small consolidations has been the focus of many industrial applications. This could influence powder flow conditions.

During compaction, two main processes occur, i.e., compression and consolidation. The compressibility is the ability of a particle bed to reduce its volume due to rearrangement, deformation, and breakage under pressure [30,31]. The consolidation is characterized by the formation of interparticle interactions; it describes the ability of a powder bed to form mechanically durable bonds with sufficient strength [30,32].

Compaction of a particle bed depends not only on the physical properties of the particles but also on the apparatus setting [33] like the filling method. In this process, the rate of increase and also the absolute magnitude of the applied pressure force play significant roles [30]. Additionally, the pre-conditioning of the particle bed before applying the compression force has a critical effect on the final results [33]. The pre-conditioning is more significant for processes using fine and ultra-fine particles. In fact, the history of the applied forces and the previous deformations of particles before a new process might completely change the outcome.

In practical applications, compaction is affected by many parameters, such as the applied force and inter-particle forces when the range of particle sizes is less than 50 μm [34,35]. Increasing the role of inter-particle cohesion forces between particles is the starting point of lasting arch formation in the arrangement of particles adjacent to each other in the bed [36]. Due to the creation of these arches between adjacent particles, the number and the volume of voids between them increase, which results in a decrease in the bulk density of

the bed and a looser structure of the particulate material for finer particle beds. The reduced bulk density of fine and ultra-fine particulate material has an essential effect on the behavior of the bed after applying stress (pressure); they show increased compressibility.

1.1.3 Permeation of a fluid through a particle bed

In many technical processes, liquids or gases flow through beds of solid particles. They could be a single fluid flow through a bed of granular solid or a two-phase countercurrent flow of liquid and gas through packed columns. The first one, which is mostly considered in this study, involves in different applications such as filtration, fixed bed reactors or packed beds, adsorption, seepage of underground water or petroleum, etc. Fluid flow through porous media extensively happens in nature and manufactured materials [37], and its theory has been used in all types of knowledge-based and technological areas, such as petroleum engineering, geothermal engineering, soil mechanics, chemical industry, mineral engineering, environmental engineering, water supply engineering, and so on.

The theory of the laminar flow of fluid through a homogeneous porous packed bed is based on Darcy law proposed originally in 1856. According to this law, the total volumetric rate of the fluid passing through the fixed bed can be represented regarding the height and cross-section area of the powder bed. Therefore, one of the outcomes of this law is that the mean velocity of the fluid through the porous media is a function of a constant depending on the physical properties of the bed and fluid (permeability) and also the bed pressure drop. Many attempts have been made to obtain general expressions for pressure drop and mean velocity of flow through packing regarding porosity and specific surface. One of the famous expressions is the Carman-Kozeny equation. The permeability process is a complex process. However, its complexities increase when it relates to the fine or especially ultra-fine particles. Table 1.1 shows the reference values of permeability and flow behavior (flow function ff_c) of different particle beds.

Table 1.1 Permeability and flow function of soil material [38]

k_f in m/s	Permeability	Soil behavior	$ff_c = \sigma_1/\sigma_c$	Flowability	d_{ST} in μm
0 - 10^{-9}	Practically impermeable (- 3.15 cm/a)	Very binding	0 - 2	Very cohesive	0 - 0.5
10^{-9} - 10^{-7}	Very low (- 26 cm/month)				0.5 - 5
10^{-7} - 10^{-5}	Low (- 86 cm/d)	Binding	2 - 4	Cohesive	5 - 50
10^{-5} - 10^{-3}	Medium (- 3.6 m/h)	Non-binding	> 4	Easy to free flowing	50 - 500
10^{-3} - 1	High				500 - 15000

Therefore, the study on the permeation process for these kinds of materials and also their mixtures especially after different levels of compression could be so important. One of the goals of this study is related to such an important investigation.

1.2 Problem and Motivation

Fine particles, ranging in size from about one micrometer to hundred microns, are abundant in nature and many human-made products. Using particulate materials and especially fine particles has become of serious interest in recent decades. Many products in the food, pharmaceutical, chemicals, agriculture, and ceramics industries are made from such particles. In reaction engineering and catalyst production, fine particles intensify reaction rates like what happen in fluid catalytic cracking (FCC) process widely used to convert the high-boiling, high-molecular-weight hydrocarbon fractions of petroleum crude oils into more valuable gasoline, olefinic gases, and other products.

In earth's subsurface, fine particles affect the quality of soil, groundwater, and also oil or natural gas. They can totally change the permeation properties of the underground soils. Some of the soil properties affecting plant growth include soil texture (coarse of fine), aggregate size, porosity, aeration (permeability), and water holding capacity. All of these factors can be easily changed by the proportion of fine and ultra-fine particles in the combination of underground soil.

In the atmosphere, fine particles impact both climate warming and cooling. In addition, one of the challenging issues in the industries is how to capture or control the produced dust during the manufacturing of the products. In the vital systems of living organisms, fine particles have an important effect on organism health and viability. In fact, only micron or sub-micron particles could pass through the cell membranes of living organisms. All of these applications reveal the importance of fine and ultra-fine particles in nature and also in the manufactured products. However, insufficient knowledge about the effect of the presence of this kind of materials (fine particles) in the properties and the behavior of different industrial or natural processes limit the capability to predict, troubleshoot, control and evaluate the performance of particle-based systems.

Due to the importance of cohesive inter-particle forces in fine particles, they display totally different behavior relevant to the other particulate materials. This challenging behavior makes research on these kinds of materials very difficult. It is well known that fines and ultra-fines can cause severe problems in mineral processing. In general, most of the ores contain valuable minerals in finely distributed form. However, working with such fine mineral particles is exceedingly difficult [39]. Considerable interest is demonstrated in developing suitable process technology for recovering metal values from

fine size ranges which are classified as below, as suggested by Sivamohan and Forssberg [40–42] which is well accepted:

- Fines: particles below 100 micron size
- Very fines particles below 20 micron size
- Ultra-fines particles less than 5 microns size
- Colloids particles less than 1 micron size
- Super colloids particles less than 0.2 micron size

The focus of this study is on fine and ultra-fine particulate materials. Using these kinds of materials is very complicated and unpredictable. Ultra-fines have poor flowability, high compressibility and low permeability under pressure.

In the previous studies in the chair of Mechanical Process Engineering (OvGU), using the self-developed microscopic particle contact force-displacement models [35,43], new macroscopic normal stress-strain relations of powder compression including elastic and elastic-plastic loading, unloading and reloading have been developed. That includes the physically plausible modeling of permeation behavior of particle packing [1] at compression and de-aeration, yielding, expansion as well as ingress of fluid (aeration).

However, the micro-macro transition of compression, permeation and flow behavior of ultrafine, cohesive and compressible powders remains unsolved. These materials are property-distributed particle populations ($d < 10\ \mu m$) which have poor permeability as well. Although the knowledge about powder behavior and its properties is inadequate, in the last decades, several scientific works have been done to figure out these behaviors. Understanding the behavior of fine and ultra-fine particles in flow (fluidization), compression, and permeation could deliver crucial information about their properties.

On the other hand, whereas the knowledge about behaviors of fine and ultra-fine particles in the above-mentioned processes is important, in most of the particle-based applications, the size distribution of the material is a mixture of different size distributions (poly-disperse) of particles. If the mixture is a combination of different size distributions of a material that are in the same Geldart classification, the behavior of the mixture in the fluidization or other processes is almost predictable. However, when they belong to different groups of Geldart classification, it can lead to fascinating and undiscovered results. Therefore, investigating about the effect of the presence of very cohesive Geldart C ultra-fine particles on fluidization, compression, and permeation of a fine particle bed and also on the re-fluidization of a consolidated bed (history effect after compression or combined effects of compression and permeation) could give very crucial information about the behavior of industrial mixtures of fine and ultra-fine particles in different processes.

Consequently, the focus of this study will be on investigating the properties of fine and ultra-fine as well as different mixtures of these two materials during fluidization, compression, and permeation. The experimental work will continue by considering the compression and permeation process effects (history effects) on the re-fluidization of different mixtures of materials. This investigation will be completed by the simulation of fine particle bed fluidization.

1.3 Novelty

This study is a comprehensive study about the effect of the presence of ultra-fine powders in a fine particle bed during fluidization, compression and consolidation, and permeation processes and also in the re-fluidization of the compressed and consolidated and/or permeated bed of a binary mixture. The effect of adding fine particles to improve the fluidization of ultra-fine cohesive beds have been investigated by other researchers. In previous publications considering the addition of coarser particles (e.g., [9,25–27]), the added materials were different, leading in particular to a different density, size, and surface properties. In contrast, the present study considers only mixtures of the same material; both particulate materials used in this study are constituted of ground calcium carbonate (GCC) with a rhombohedral crystalline structure. The difference between these materials is only the particle size distribution.

In this study, in the first series of tests, the behavior of different mixtures of fine and ultra-fine particles is investigated in a fluidization process. During this process, the effect of changing in the combination of mixtures during the fluidization process is checked by comparison of the fluidization curve (bed pressure drops by increasing or decreasing superficial gas velocity). In this comparison, the linear behavior of bed pressure drop in the packed bed condition (before fluidization), the behavior of the bed pressure drop after starting fluidization (even partially) including the peak point of the bed pressure drop and its corresponding gas velocity, as well as the behavior during the unloading stage (decreasing the gas velocity) are studied.

In addition to the fluidization process, in the second phase, the effect of the presence of ultra-fine powder and fine particles besides each other in a binary mixture is investigated during the compression process in different test conditions and applied pressures. To complete the second part, the effect of the compression phase on the re-fluidization of the compressed bed is investigated (history effect). The compression and re-fluidization of compressed bed processes are very important in the storage and flow of bulk materials. Discharging the consolidated material by fluidization aid is not similar to the fluidization of a loosed packed bed and the behavior of the bulk material is entirely different. These kinds of processes often happen in chemical, pharmaceutical, and food industries where the fine and ultra-fine particulate materials are used for producing different products.

The third phase of this study is related to the effect of the presence of ultra-fine powder in mixtures with fine materials in the compression and subsequently permeation and also on the history effect of compressed and permeated bed during re-fluidization. Finally, the fluidization of fine materials is simulated by a coupled CFD-DEM method and compared with the experimental results.

Therefore, the new works of this study can be summarized as:

a. Investigation of fluidization behavior of mixtures of two different classes of Geldart classification (Group A and C) as happens in many industrial applications due to abrasion or mechanical breakage between fine particles in contact and the effect of increasing the ultra-fine powders in the mixture.
b. Contrary to all available studies, this study is done with the same material. The difference between the two constituents of the mixtures is only in the particle size distribution.
c. Investigating the effect of applying different levels of compression force on a mixture of two class of materials considering different combinations of fine and ultra-fine particles in the mixture.
d. Investigation of the effect of compression (history effect) on re-fluidization of a consolidated bed (due to compression) for different mixtures of materials.
e. Study and comparison of the resistance of different particle beds to pass the airflow (permeation) considering the ratio of ultra-fine powders in the mixture, previous forces applied to the bed, and classification of different mixtures based on their permeation behavior.
f. Investigation of the effect of permeation (history effect) of the gas flow in a compressed bed on re-fluidization of a consolidated bed (due to combined effect of compression and permeation) for different mixtures of materials.

All of these processes have their own applications in the industry. Therefore, a study on these items is useful to better understand the behavior of real particulate materials in different industrial processes and also to better troubleshoot the problems.

1.4 Outline of contents

The descriptive outline of contents for the next chapters of this dissertation is as follows:

Chapter 2 presents the powder bed raw materials used in the experimental parts of this study as well as the method of preparing the final test materials. In this chapter, the results of several common classification methods used for preparing the fine material are compared. Finally, the in-house method of wet sieving along with a drying process will be introduced using the optimized parameters. In the following, the experimental apparatus with all of the components and instruments and the method of measuring

different parameters will be illustrated. As a complementary part of this chapter, the methodology of performing experiments for all three sets of processes will thoroughly be described.

Chapter 3 starts with an introduction to fluidization. It includes fluidization regimes, the different classification of particulate materials based on fluidization behavior, different adhesion forces between fine particles, agglomerate formation mechanisms and states, de-fluidization, elutriation, the effect of particle size on fluidization, and finally, the effect of adding different particle size particles on fluidization of cohesive powders. In the following, the experimental results of this study will be reported and discussed. To have a comprehensive study of the fluidization process, some concepts related to this part of the study such as agglomeration number, agglomeration states, etc. will be introduced and used to evaluate and interpret the behavior of different mixtures of materials in fluidization.

Chapter 4 thoroughly describe the effect of adding ultra-fine powders in a fine material on the behavior of the mixture during compression test with different levels of applied pressure as well as the effect of different compression test of each mixture on the re-fluidization of compressed bed. This chapter starts with an introduction to the importance of a compression test for discovering the behavior of particulate materials in real industrial applications, the compression regimes and the relation of mechanical properties of the material with its compressibility index. This chapter will continue with the experimental methodology used in these sets of experiments. Each experiment starts with initial fluidization to decrease the effect of pre-consolidation in the bed. Then, the compression tests are performed in three pressure levels to evaluate the effect of increasing applied pressure on compression. The last part of each test is the re-fluidization of the compressed bed. In this manner, the effect of the compression test is evaluated by comparing the behavior of particle bed in the initial fluidization and re-fluidization process. In this part, the history effect is completely evaluated and the changes in the behaviors are interpreted at macro- and micro-scale.

Chapter 5 focuses on the effect of ultra-fine powders in mixtures on the permeation behavior of particle bed. This chapter starts with an introduction to the permeation of a fluid through a porous media constructed by particles. Then, the experimental methodology is discussed. In these sets of experiments again, the tests start with initial fluidization before compression. Thereafter, the compression is done similar to chapter 4. The next part will be the permeation tests for similar pressures as used in compression tests. In fact, the permeation of air will be investigated through a compressed bed under different levels of pressure. The final part of this work is the evaluation of fluidization

behavior of compressed and permeated bed by comparing the initial fluidization results and re-fluidization after permeation.

Chapter 6 starts with an introduction of the methods for simulating particulate material behavior in interaction with fluids. In this part, the Eulerian-Eulerian and Eulerian-Lagrangian methods are introduced and compared. Then, the selected method for simulating the fluidization of fine particle bed fluidization (CFD-DEM coupled method) is thoroughly discussed in three subsections (Discrete Element Method, Computational Fluid Dynamics, and DEM-CFD coupling method). In each subsection, the modeling, governing equations, numerical schemes, etc. are illustrated in brief. Thereafter, the simulation results, considering different geometry sizes, different size distribution assumptions, different friction coefficients in particle-particle and particle-wall contacts, different wall boundary conditions, and different geometry structures, are reported and compared.

CHAPTER 2

Powder bed materials / Experimental apparatus and methodology

In this chapter, the raw materials used as the powder bed in the experimental parts of this study, as well as the method of preparing the final test materials, will be introduced and discussed. The results and discussion of the material preparation section in this chapter were published in the conference paper of "Classification of ultra-fine adhesive particles at fine cohesive powders", 12th International Conference on Bulk Materials Storage, Handling and Transportation (ICBMH 2016), Darwin, Australia, 2016, pages 393-402, ISBN: 9781922107886. In the following, the experimental apparatus and methodology for all three sets of experiments will thoroughly be described.

2.1 Powder bed materials

The present study considers only mixtures of the same material; both particle groups are constituted of ground calcium carbonate with a rhombohedral crystalline structure (according to the technical datasheets of the materials, see Table 2.1). Calcium Carbonate (also called CALCIT in this study) is a versatile and inexpensive mineral. It has a wide variety of uses in constructional, industrial, and environmental applications. Ground calcium carbonate is widely used as the main ingredient of fillers, ceramic tile adhesive, and sealant material. Ground Calcium Carbonate (GCC) is a natural source of alkalinity used for de-acidification of rivers, desulphurization of flue gas in power plants, and treatment of drinking water. In food industries, GCC is used as a dietary calcium supplement or as a chemical binder. Because of this wide range of applications, GCC has been selected as the test material in this study.

According to the datasheet and particle size distribution measurement of the raw materials, the ultrafine CALCIT MX 10 could directly be considered as ultrafine material ($d \leq 10\ \mu m$). However, for fine particles, a pre-process of preparation is required. The fine (Geldart Group A) material, named in this study as CALCIT MVT 100, was prepared by classification of CALCIT FW 270. For the classification of ultra-fine powders from CALCIT FW 270, several devices and methods were tested in this study. The results of each method and the final acceptable solution will be reported in the next section [44].

Table 2.1 Chemical and physical properties of the used materials based on their Technical Data Sheet (Sh minerals GmbH company).

Mineralogical Analysis		CALCIT MX 10	CALCIT FW 270
Origin:		Plant Heidenheim (Germany)	
Characteristics:		Fine crystalline GCC with a rhombohedral crystalline structure.	
Chemical Analysis:	• $CaCO_3$	99.3 %	98.6 %
	• $MgCO_3$	0.3 %	0.5 %
	• Fe_2O_3	0.05 %	0.1 %
	• HCI-insoluble	0.3 %	0.7 %
Physical Properties:	• Density (ISO 787/10)	2.7 g/cm³	2.7 g/cm³
	• Hardness (Mohs)	3	3
	• pH-value (ISO 787/9)	9	9
	• Refractive index	1.59	1.59
Product Characteristics:	• Particle size distribution (Laser granulometer CILAS 920)	0 - 6 μm	0 - 210 μm
	• Mean particle diameter (d50) (Laser granulometer CILAS 920)	1.8 μm	70 μm

2.2 Classification of ultra-fine adhesive particles at fine cohesive powders

Ultra-fine particle classification is a pivotal phase in powder preparation. Essential physical product properties that depend on particle size distributions are one of the reasons that some products do not meet the application requirements. Ultra-fine particle fractions often have unsuitable effects in the processing or make the final product undesirable for specified applications. Such products require additional processing efforts to meet the desired product size distributions. However, due to the inherent physical and chemical properties of ultrafine particles, their classification is highly challenging.

Classification of solid particles by fluids (air or liquids) is based on differences of density, shape, hydrodynamic surface, electrical and magnetic properties of the materials in the mixture [45]. Several criteria have been used to categorize separation methods. One consists of classifying them according to the phases involved, i.e., solid-liquid (e.g., sedimentation), solid-solid (e.g., screening, and air classification), liquid-liquid (e.g., distillation), solid-gas (e.g., cyclone). In food processing, there are important applications for separation of ultrafine particles, such as the removal of particles from dust-laden air in milling operations, and the cleaning of grains prior to processing [46]. In addition, wet classifiers such as elutriators, wet sieving and classifying hydro-cyclones use settling or flow in water or a liquid to separate or classify powdered materials based on particle size or shape. However, the classification of ultra-fine adhesive particles shows totally

different features. The performance is negatively impacted by insufficient separation characteristics and enormous product impurities. The inter-particle forces, i.e., van der Waals or electrostatic adhesion, make the process very difficult.

From an environmental point of view, preventing the emission of fine particles into the atmosphere and trapping them during a separation process are the major challenges [47]. Fine particles, especially PM10 (PM10 is a particulate matter with a mean aerodynamic diameter of 10 μm) and PM2.5 (PM2.5 is correctly defined as a particulate matter with a mean aerodynamic diameter of 2.5 μm [48]) are the main materials that usually cause industrial smog as well as problems for human health [49]. PM10 materials can penetrate in the human nasal cavity while PM2.5 after passing the breathing system can deposit into the bronchi and alveoli. Normally, using only one single method can separate particles with coarser size. For the case of ultrafine particles such as PM10 or PM2.5, using conventional techniques seems inefficient. A high-efficiency classification method would facilitate the manufacturing of special products and reduce environmental pollution by particles.

In the present study, different laboratory methods for the classification of particles will be used and compared. The goal of this work is the classification of ultra-fine particles with a diameter below 10 μm from the raw material, i.e. CALCIT FW 270. As observations show, CALCIT FW 270 is supplied initially as a mix of fine and coarse fractions. Therefore, to meet the study prerequisite, a laboratory-scale separation process is required to remove all (if possible) or limit the fine particle fractions to an acceptable range (defined here as 5%). According to the size distribution measurements, the Q_3(10 μm) in the raw material is about 19.9%. The final objective of this study will be using the final material, called CALCIT MVT 100, as a Geldart classification group A particles in a series of fluidization, compression, or permeation tests. So, the less ultra-fine particles we obtain, the less is the effect of inter-particle adhesive force between particles in the bed, and the better the fluidization will be. In the next sections, the material preparation techniques: (1) Mechanical sieving method (2) Air classification method (3) Air jet sieving method, and (4) Initiated water-jet sieving method are presented and compared. The best technique finally used for preparing the coarse particle material is based on the effectiveness of removing the ultrafine particle from the raw sample.

For the preparation of the fine material (CALCIT MVT 100), CALCIT FW 270 is used as the raw solid material. CALCIT FW 270 consists of a fine, crystalline, ground calcium carbonate with a rhombohedral crystalline structure. It is manufactured in state of the art by dry grinding and air sifting processes. This material comes from a quarry of bright Jura calcite and it has an outstandingly high level of chemical purity. The frequency and cumulative size distribution function of this material according to our measurements by

Mastersizer 2000 of Malvern Instruments Ltd (based on a dry laser diffraction measurement method) is shown in Fig. 2.1.

For this measurement, the dispersing of the agglomerates is important. In the present work, a dry sample dispersion method is used. The dry dispersion process normally needs a higher energy process than wet dispersion. Three different dispersion mechanisms act simultaneously on the sample during a dry method. These mechanisms of increasing energy input are velocity gradients due to shear stress, particle-particle, and also particle-wall collisions, respectively. The shear stress is induced by controlling the pressure drop of the disperser. The significance of each mechanism depends on the material type, airflow rate or its induced pressure drop, and also the geometry of disperser. By employing these mechanisms, all agglomerates are disintegrated into primary particles. To reduce attrition, high flow rates of air are used. To check reproducibility, all measurements have been repeated several times [50].

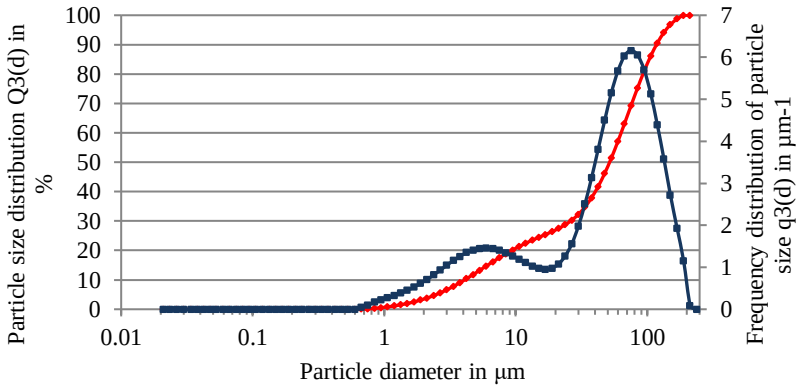

Fig. 2.1 Frequency and cumulative size distribution function of CALCIT FW 270

In this study, air and water are employed as a continuous phase (fluid) in classification methods.

2.3 Classification methods (description, results, and discussion)

2.3.1 Mechanical sieving method

Sieving is the most traditional approach to classify solid particles into specified particle size fractions. Sieving can be used to fractionate a heterogeneous sample into size fractions or to analyze the particle size distribution in view of particle characterization. Many different procedures and standards are still based on using the sieving method. Besides, it is often referred to as the reference method for other particle characterization techniques. In the sieving method, the sieves are mounted on an electromagnetic agitator. This provides the necessary process conditions with various agitating amplitude and sieving duration.

In this study, a sample of 200g of CALCIT FW-270 was fed to the top sieve of the sieves arrangement (Sieve A-200 μm, B-110 μm, and C-32 μm) which are placed on electromagnetic agitator (Fig. 2.2). A sieving machine (MLW Labortechnik, Ilmenau, G.D.R.) is used as the source of vibration. This test is performed for 34 different process conditions (different agitator intensity and duration of sieving). Table 2.2 shows two sets of them for discussion (samples A and B).

Fig. 2.2 Sieving Machine Arrangement

Table 2.2 Different sieving condition for representative samples

Sample	Duration (Min)	Vibration Intensity
A	180	8/10
B	90	10/10

After finishing the classification process, the samples collected on sieve C used for a confirmatory test of the particle size distribution (PSD) using the Mastersizer 2000 dry method. The results are shown and compared in Table 2.3 and Fig. 2.3.

Table 2.3 Comparing sieving results and process goal for ultrafine (d<10 μm) particles in mass %

Initial Condition	Goal of Study	Sieved Sample A	Sieved Sample B
19.9 %	< 5 %	22.16 %	10.39 %

The results show that the sieving technique is not suitable enough to separate effectively the ultrafine particles. Main observations are: (1) the electro-mechanical agitation subjected the particles into surface abrasion and attrition, thereby producing more ultrafine particles as noted in sample A (ultrafine particle fractions increased to 22.16%), (2) due to the effect of abrasion and attrition, some of the desired bigger particle sizes were lost, and (3) decreasing sieving time while increasing agitating intensity shows better results. However, considering 34 different process conditions, no test could meet the objective of this classification.

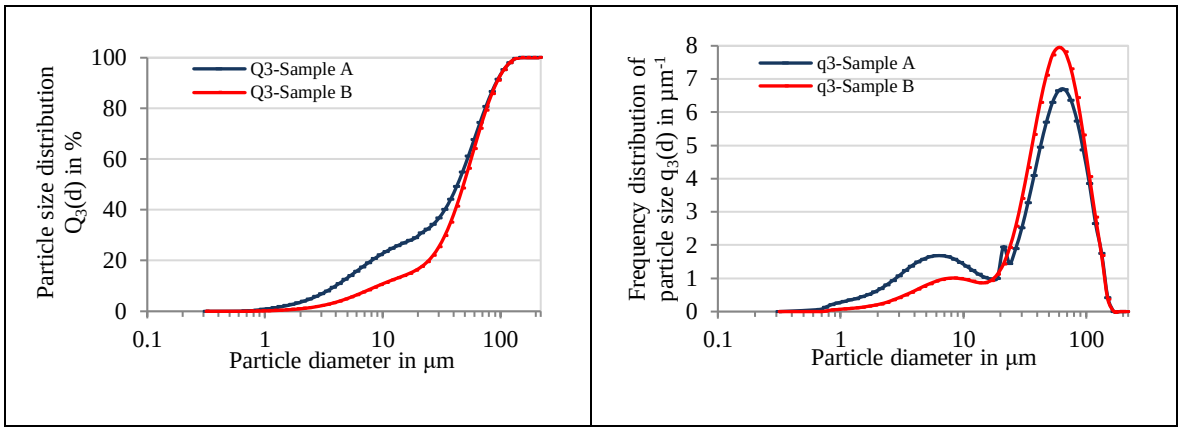

Fig. 2.3 Cumulative (left) and frequency (right) size distribution function after sieving

2.3.2 Air classification system

An air classifier is a machine used for the classification of materials into two classes (fine and coarse particles). In this system, the material is stored in a hopper and after moving on a tray agitated by a mechanical vibrating machine (AEG Vibrationstechnik type KF 0.5-1-CR/R2) enters to the material entrance section of the preliminary cyclone. The suction of material into the cyclone is produced by a centrifugal blower. Then, the particle-laden flow enters this cyclone.

In the centrifugal counter-flow zone of the cyclone, a flat air vortex is produced inside a cylindrical chamber. The airflow is delivered into the chamber by a tangential inlet and goes out of the blower in the center. This means that the airflow in the vortex rotates and flows radially towards the central exit. The separation is controlled by the radial flow. The particles will rotate with the radial flow and are affected by centrifugal (inertial) force. Separation is the result of balancing between the centrifugal force and the drag force.

Due to the centrifugal force, coarse particles will float outwards from the outlet and downwards due to gravity. The fine particles will follow the airflow towards the outlet in the center of the cyclone. The centrifugal force depends on the radial position of the particle. This means that the cut size may vary due to the radial position [51]. In this step, the coarse particles are stored in a cylindrical container connected to the underneath of the preliminary cyclone (See Fig. 2.4).

In the next step, the output flow is delivered by the centrifugal blower to the secondary cyclone. The flow of fine particles ejected from the first cyclone enters tangentially into the secondary cyclone. The separation process of the fine particles in this cyclone is the same as the previous one. The central flow of ultrafine particles outflow is vacuumed by a vacuum cleaner from the central outlet. Similar to the previous cyclone, the fine particles are stored in a container connected to the lower part of the secondary cyclone (See Fig. 2.4).

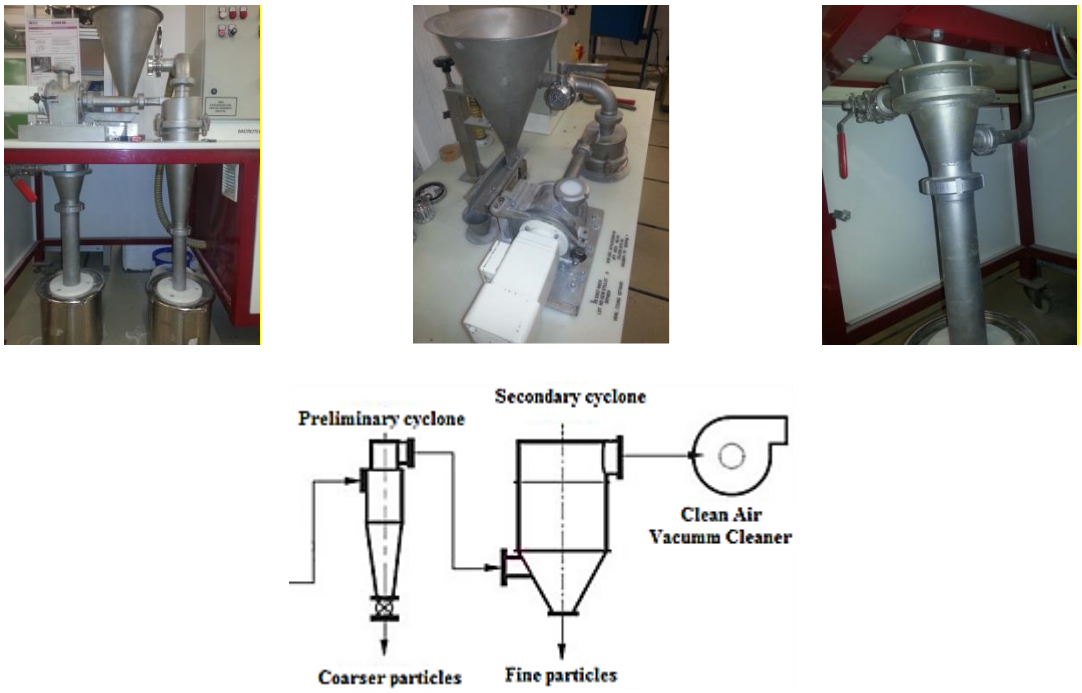

Fig. 2.4 Images and flow diagram of air classifier

The classification results obtained by air classifiers for fine materials are controlled by the physical properties of the material to be classified, such as PSD and cut-point, particle behavior in a gas flow, moisture content, gas viscosity, electrostatic force between charged particles, flow properties, the surface area of particles, and particle hardness.

For a separation zone of a cyclone, the cut size is based on balancing the centrifugal force and the drag force that the particles experience in the airflow, as follows:

$$F_{CG} = m\frac{V_\theta^2}{r} \tag{2-1}$$

$$F_D = \frac{1}{2}AC_D\rho_a(v_r - u_r)^2 \tag{2-2}$$

The cut size of a centrifugal air classifier is where the centrifugal and the drag forces are balanced and the radial velocity of the particle is zero. It is given by [52]:

$$d_{cut} = \frac{3rC_D\rho_a{v_r}^2}{4\rho_p V_\theta^2} \tag{2-3}$$

A practical air classifier deals with a large number of particles with different sizes. Within it, the airflow is turbulent. Turbulence and particle-particle interactions influence classification and, thus, the cut size will depend on more parameters than just the air velocity.

In this study, 300g of CALCITFW-270 was charged into the air classifier at different angular velocity (RPM) of the blower and different stages of classification (e.g., 2-stages mean that the coarse particles collected in the lower container of the preliminary cyclone are charged again into the storage hopper and the classification process is repeated) to optimize the classification quality. The angular velocity of the centrifugal blower and the number of stages are set according to Table 2.4 for samples C to G. These samples have been chosen from 31 different settings of RPM and stages (up to six) for discussion. After finishing the classification process, the material collected in the cylindrical container connected to the underneath of the preliminary cyclone (the coarser particles fraction) is used for a confirmatory test of the particle size distribution (PSD). The results are compared in Fig. 2.5 and Table 2.5.

Table 2.4 Different process condition for air classifier samples

Sample	RPM	Stage
C-300g	2000	2-stages classification
D-300g	1500	2-stages classification
E-300g	1000	2-stages classification
F-300g	600	1-stage classification
G-300g	600	2-stages classification

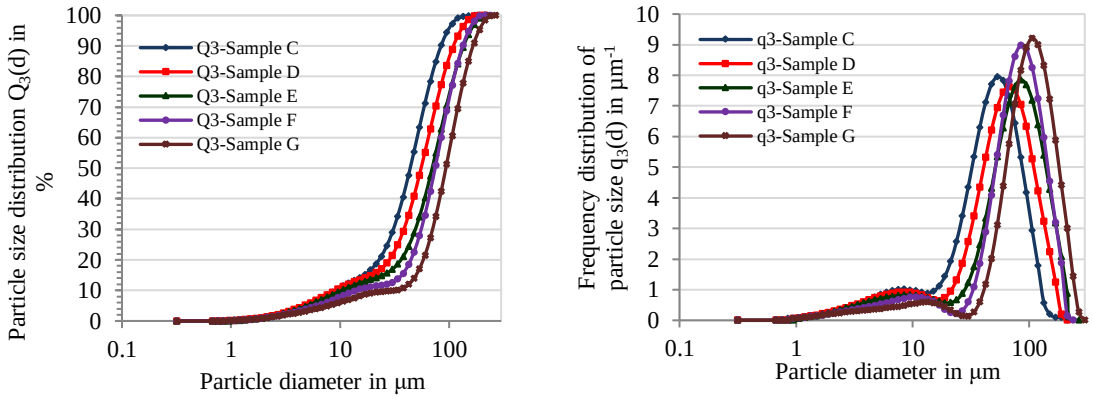

Fig. 2.5 Cumulative (left) and frequency (right) size distribution function after air classification

Table 2.5 Comparing air-classifier results and process goal for ultrafine particles in mass%

Initial Condition	Goal of Study	Sample C	Sample D	Sample E	Sample F	Sample G
19.9	< 5	10.39	10.32	9.36	7.52	5.77

Using air-classification with different process conditions and classification stages was not satisfactory to reduce the fraction of the ultrafine particles to less than 5%. As expected,

reducing the centrifugal force by reducing the angular velocity leads to better results. In addition, the comparison between samples G and F shows that increasing the stages of classification has a positive effect on the final results. However, when increasing the number of stages, a large amount of raw powder is lost. When considering six stages, about 80% of the material is lost; still, the results did not satisfy the objective of the test.

2.3.3 Air jet sieving system

In this method, the air jet sieving device model 200 LS of Hosokawa Alpine company is employed for the classification of particles (Fig. 2.6(a)). In this sieving method and according to its operation manual, a strong jet of air exiting the slotted nozzle results in a continuous cleaning of the sieve mesh (Fig. 2.6(b)). The airflow is the only source of material movement. The mechanical effect of the rotating nozzle ensures an excellent dispersion of the particles.

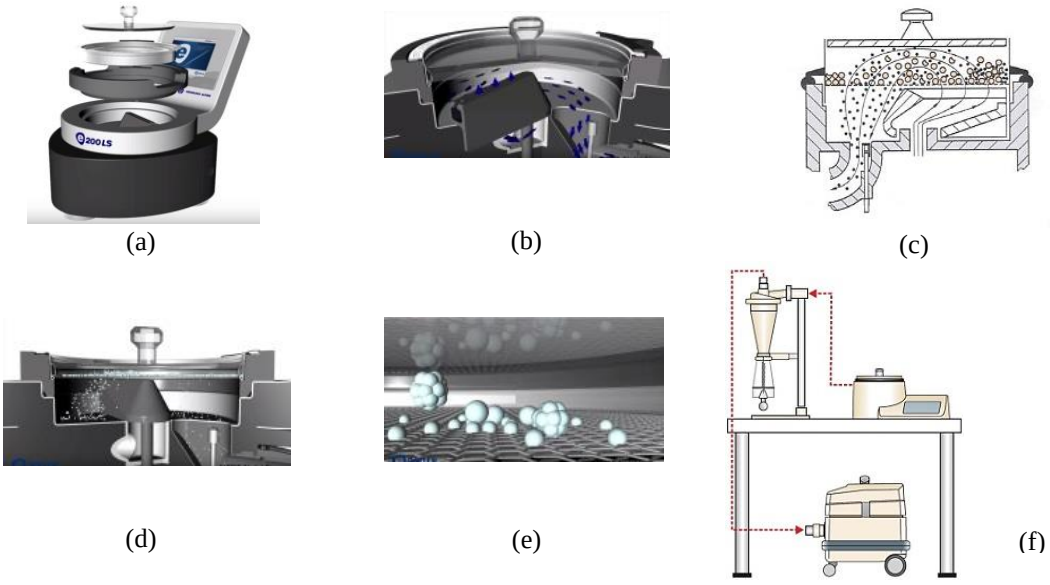

Fig. 2.6 (a) Snapshot, (b-e) Operation principle, and (f) Accessories combination of air jet sieving method

The material that is smaller than the mesh size of the sieve is transported by the backflow of the air to the cyclone or to the vacuum cleaner (Figures 2.6(c) and 2.6(d)). The air jet helps to de-agglomerate the particles and constantly purges the sieve mesh (Fig. 2.6(e)). In this device, the classification is performed for any type of dry material. The sample masses considering the cut-size diameter could be from 0.3 to 100 g (in the case that the cut size is equal to 10 μm, the mass of sample should be less than 15 g). The plastic transparent cover permits the sieving process to be monitored during the process. As is shown in Fig. 2.6(f), in addition to the air jet sieving machine, the device includes a high-

performance industrial vacuum cleaner to generate the operating air as well as a high-efficiency cyclone and glass bottle to collect the fine particles.

In this study, the mesh size of the sieve is 32 micrometers. The specific weight of raw material (CALCIT FW-270) was charged into the air-jet sieve chamber at a specified pressure and duration of classification. Table 2.6 reveals the different mass, pressure and classification duration for samples H to K. These selected samples have been chosen among 20 different process conditions for further discussion. After finishing the classification process, the samples collected in the sieve (i.e., the coarser particles fraction) is collected for a confirmatory test of PSD. The results are compared in Table 2.7 and Fig. 2.7.

Table 2.6 Different Process Conditions for Air Jet Sieving Samples

Sample	Mass in (g)	Time in (min)	Set Pressure in (kPa)
H	15	3.0	3000
I	15	5.0	3000
J	15	3.0	2000
K	5	3.0	3000

Table 2.7 Comparison of Air Jet Sieving Results and Process Goal for Ultrafine Particles in Mass%

Initial Condition	Goal of Study	Sample H	Sample I	Sample J	Sample K
19.9	< 5	8.78	9.34	10.09	9.08

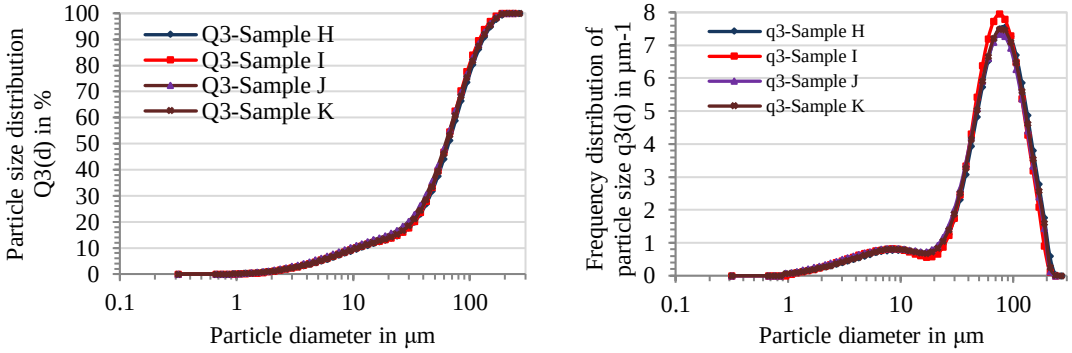

Fig. 2.7 Cumulative (left) and frequency (right) size distribution function after air-jet sieving

Though different process conditions have been considered for the operation of the air jet sieving machine, this method was also unable to attain the targeted process goal of classifying the ultrafine particles to less than 5%. According to the results, the optimum

classification condition is for a sample with 15g mass, 3000 kPa pressure, and 3 min process duration time.

2.3.4 Initiated water-jet sieving

The results of all previous methods show that the separation of ultrafine particles ($d < 10\ \mu m$) from this kind of material (CALCIT FW 270), in order to reach the goal of this study (less than 5% in mass), appears impossible. The combinations of these different methods have been also checked. However, the results were still not satisfactory. According to the qualitative observations of the final materials (obtained from previous methods) by a KEYENCE digital microscope system (VH-Z250R, Dual-light High-magnification Zoom Lens (250-2500X)), it was found that the most important factor explaining the failed classification of ultrafine particles is sticking of these particles to the coarser particles. For a dry powder, the main adhesive inter-particle forces would be van der Waals and electrostatic forces. Therefore, to have a high-efficiency classification method, it is necessary to decrease these forces between particles. Hence, investigating further the theory of these two forces and the important parameters affecting them is necessary.

An electrodynamic effect is the origin of the van der Waals force. This effect proceeds from the interactions between atoms or molecules when the electrical dipoles oscillate or rotate within the interacting media. Three types of interactions contribute to the van der Waals force: (1) Keesom force defined as the interaction between two permanent dipoles, (2) Debye force defined as the interaction between one permanent dipole and one induced dipole, and (3) London force defined as the interaction between two induced dipoles. Hamaker [53] calculated the free energy of macroscopic bodies as a function of the distance. He showed that the van der Waals interaction free energy per unit area between two semi-infinite parallel plates is given by:

$$E_{vdW} = -\frac{C_H}{12\pi D_s^2} \tag{2-4}$$

where C_H is Hamaker constant and D_s is the separation distance. In addition, the van der Waals interaction energy of a particle approaching a surface is given by [54]:

$$E_{vdW}(D) = -\frac{C_H R_n}{6D_s} \tag{2-5}$$

In the case of spherical particle - flat plate contact, $R_n = R_1$, and for spherical particle - spherical particle contact, $R_n = R_1 R_2/(R_1 + R_2)$. The van der Waals force can be obtained by differentiating the energy with respect to distance as:

$$F_{vdW} = -\frac{dE_{vdW}}{dD_s} = \frac{C_H R_n}{6D_s^2} \tag{2-6}$$

The Hamaker constant is a constant of the materials that depends on the material properties of the two sides of interaction and also on the separating media. The van der Waals energy depends on the geometry of the two interacting bodies. In fact, it is proportional to ${D_s}^{-2}$ for parallel plates and to ${D_s}^{-1}$ for two spherical particles at short separation distances. Following Hamaker [53] calculations, Lifshitz [55] offered a more accurate method where each body is considered as a continuum with certain dielectric properties [56]. This method includes the effect of multi objects on each other, which is ignored in the Hamaker calculations. The Hamaker constant C_H is equal to $0.2 - 40 \times 10^{-20}$ J for solid–liquid–solid interaction [35] and according to the continuum theory of Lifshitz [55] is related to the interstitial media and depends on their permittivities (dielectric constants) and refractive indices; for details see [56].

Since the size, the dielectric constant, the reflective indices and the distance between the bodies are not controllable in the process, the only modifiable parameter in order to reduce van der Waals force between particles is changing the interstitial fluid between the particles. According to the measurements reported in [56], for Calcium carbonate ($CaCO_3$), changing the intervening media from air to water could decrease the Hamaker constant from 10.1 to 1.44. In other words, water as an intervening media reduces the van der Waals force by seven times.

On the other hand, for non-conducting particles, the distribution of charge on the surface of the particle is also likely to be non-uniform. As a result, it is generally not easy to estimate the magnitude of the electrostatic force acting between pairs of particles or particles and surfaces [57]. For two charged particles, the following equation may be used to estimate the electrostatic force experienced by each particle:

$$F_{el} = -\frac{q_1 q_2}{4\pi\varepsilon_0\varepsilon_r {D_s}^2} \tag{2-7}$$

Again, since there is not any control on the charges (q_1 and q_2) and distances between the particles (D), ε_r is the only parameter for decreasing the electrostatic force and detaching the ultrafine particles from the coarser ones. ε_r is a function of the interstitial fluid and temperature. In the STP condition, ε_r for air and water are 1.00058986 and 80.1, respectively. Therefore, replacing air by water as the interstitial fluid can reduce the electrostatic force up to 80 times.

Considering the effect of electrostatic and van der Waals forces on the classification quality, the initiated water jet sieving method is designed and employed for the classification of this material. In this process, water is used as the interstitial fluid for

reducing the effects of the cohesive forces and separating the ultrafine particles from the coarser ones. This method starts with mixing the raw material (CALCIT-FW270) with water in a container. Then the prepared slurry decants stepwise on a 32 μm sieve for each batch washing. The water is sprayed with a flat jet nozzle at a regulated jet flow on the batch mixture continuously until all the opaque sewage disappears in the collected waste stream. The washing process for each batch takes about 90 min. Figure 2.8 shows the setup prepared for this method.

Fig. 2.8 Initiated Water Jet Sieving Setup

Table 2.8 Different Drying Conditions for Initiated Water Jet Sieving Method

Sample	Oven Temperature (°C)	Drying Time (hour)	Cooling Condition
L	250	2	Room temperature cooling
M	250	2	Oven Cooling
N	175	3	Room temperature cooling
O	175	3	Oven Cooling
P	250	3	Room temperature cooling
Q	175	5	Room temperature cooling

The washed sample left in the sieve should be dried in a drying chamber. For this purpose, there are some affecting parameters such as set drying temperature, time, and cooling conditions. According to the first tests, these parameters have notable effects on the results. Table 2.8 shows six different drying conditions for samples L to Q. These samples have been extracted from 40 different process conditions for discussion. After finishing the classification process, the samples collected in the sieve (the coarser particles fraction) are gathered and dried according to the designed conditions and used for a confirmatory test of the particle size distribution (PSD). The results are compared in Table 2.9 and Fig. 2.9.

Table 2.9 Comparison of Water Jet Sieving Results and Process Goal for Ultrafine Particles in Mass%

Initial Condition	Goal of Study	Sample L	Sample M	Sample N	Sample O	Sample P	Sample Q
19.9	< 5	3.33	4.61	4.45	4.93	3.81	5.02

Comparing the quality of the washed samples with different drying conditions shows that all the samples now meet the process goal (less than 5% residual ultrafine particle in the produced material, i.e., CALCIT MVT-100). Since it is important to maximize product quality, process conditions corresponding to sample L are favored for all further tests.

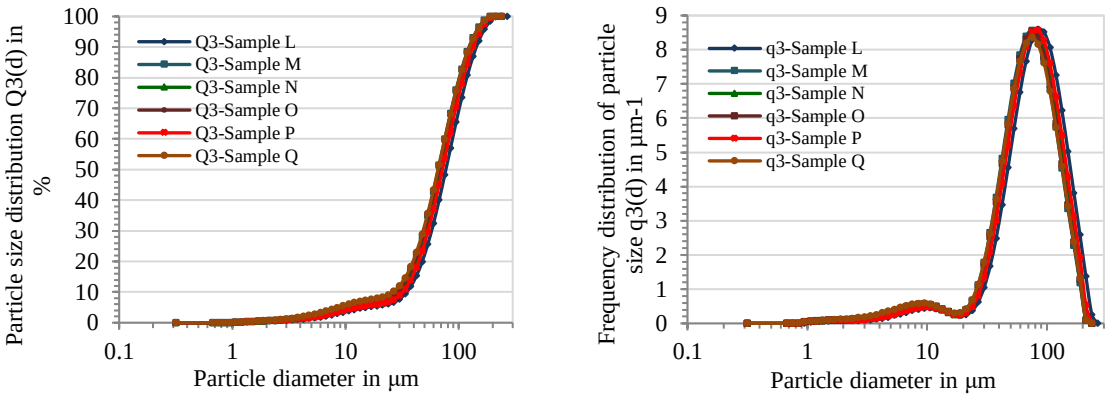

Fig. 2.9 Cumulative (left) and frequency (right) size distribution function after initiated water jet sieving

Finally, according to the set parameters of the sample L, the classification of ultra-fine powders was done and the final material was used as the fine material in this study. Figure 2.10 shows the cumulative size distribution functions of the used materials. The measurement of particle size distribution is done by a laser diffraction method (Malvern Mastersizer 2000).

The principle of this method is based on measuring the angular variation in the intensity of light scattered as a laser beam passes through a dispersed particle. Large particles scatter light at small angles and small particles scatter light at large angles relative to the laser beam. In both wet and dry methods, it is important to distinguish the agglomerates from dispersed particles. In the present work, a dry measurement is used.

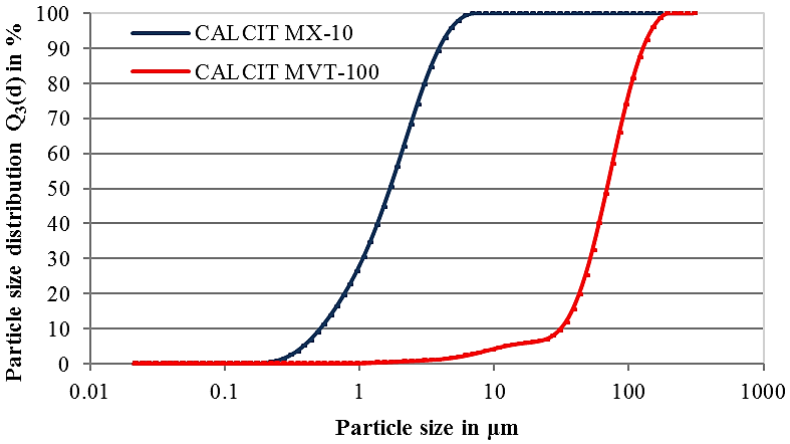

Figure 2.10 Cumulative size distribution functions of both used materials (Malvern Mastersizer 2000).

The properties of the particles used in this study are summarized in Table 2.10. This table compares the mass-mean particle diameter (d_{50}), Sauter mean diameter (d_{ST}), bulk density (ρ_b), particle density (ρ_p), the intensity of cohesiveness (c), and also flow function (ff_c) of these two materials. The two latter properties of the materials, as well as bulk density, have been extracted from experimental results using a ring shear cell (Dr. Dietmar Schulze-RST-XS.S) shown in Fig. 2.11(a). According to the shear test theory for the yield locus line (the yield locus represents the shear stress that is required to initiate flow (failure) as a function of normal stress), the intensity of cohesiveness (c) is related to the shear stress (τ) and normal stress (σ) by

$$\tau = \sigma \tan\varphi_i + c \tag{2-8}$$

where φ_i is the angle of internal friction. For clarification, Fig. 2.11(b) shows a general graph describing the Yield Locus line. The second parameter, the flow function of the bulk solid is calculated as the ratio between its consolidation stress, σ_1, and the unconfined yield strength, σ_c, in a determined storage period, t. It is written as $ff_c = \sigma_1/\sigma_c$. A smaller ff_c represents a worse bulk solid flowability. According to Table 2.10, the fine material is a free-flowing material ($ff_c > 10$), while the ultra-fine material is classified as a very cohesive material ($1 < ff_c < 2$) [58].

Table 2.10 Properties of powders used in this study.

Particulate Material	$d_{50} \times 10^6$ (m)	$d_{ST} \times 10^6$ (m)	ρ_b (kg/m^3)	ρ_p (kg/m^3)	c (N/m^2)	ff_c
CALCIT MVT 100	73	38	1241	2700	84	11
CALCIT MX 10	1.8	1.23	756	2700	915	1.33

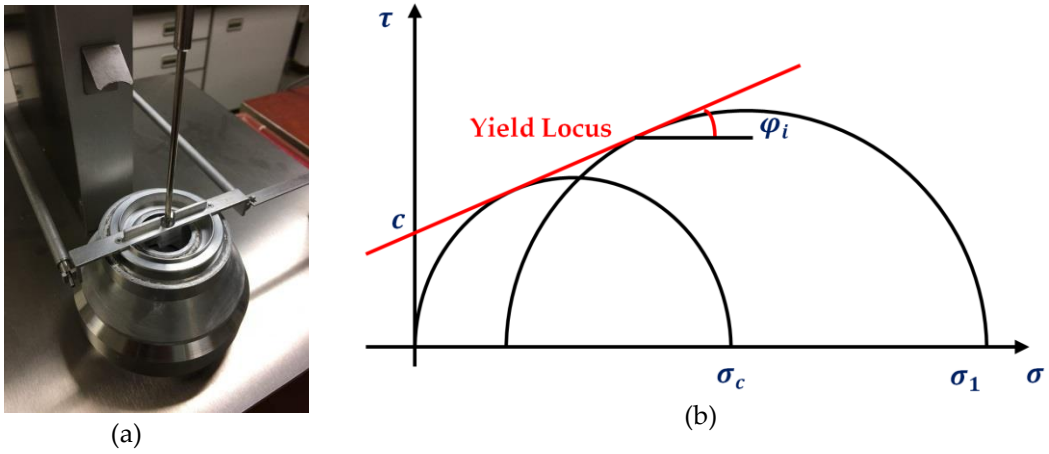

Fig. 2.11 (a) Ring shear cell, (b) Yield locus line.

Given that the fluidization process occurs in a fixed-geometry column (same cross-section area), to have the same conditions for comparing the results of all experimental tests, the total weight of materials (pure or mixed) in all particle beds used in this study is the same. Since all of the material in the different experiments have the same weight, comparing directly the bed pressure drop to investigate fluidization behavior is reasonable. Also, since both base materials have the same origin, the particle densities of both fine and ultra-fine materials are the same (Table 2.10).

2.4 Experimental apparatus and methodology

Figure 2.12(a) shows the test rig designed for this study. The principal component of the experimental test rig is a transparent glass column with 760 mm height, 100 mm inner diameter and 10 mm wall thickness. To ensure a uniform gas distribution in the fluidization process, an aluminum gas distributor plate with staggered rows (60°) arrangement of numerous identical holes with a diameter of 1.5 mm and a pitch of 2.35 mm is placed at the bottom of the column. This perforated plate is covered with a set of two Sartorius FT-3-202-125 Filter Papers-Grade 289 to prevent particles from passing through the distribution plate during fluidization unloading or permeation process.

Dried compressed air at ambient temperature is used as the fluidizing gas, and its flow rate is controlled by a calibrated Burkert flow controller. The humidity and temperature of air are measured during all fluidization tests with a Testo-480 device to ensure negligible changes concerning moisture content. Three Kalinsky pressure transmitters are used to monitor the pressure drop of the gas distributor (ΔP_D), the bed pressure drop (ΔP_b) and the gauge pressure within the apparatus (P_a). They operate in the range of 0-2000 mbar. The height of the bed (h_b) is measured by the ultrasonic method, based on sending an ultrasonic wave and measuring the reflection time. In this study, the bed height in each measurement is obtained by averaging the measured heights at eight different locations.

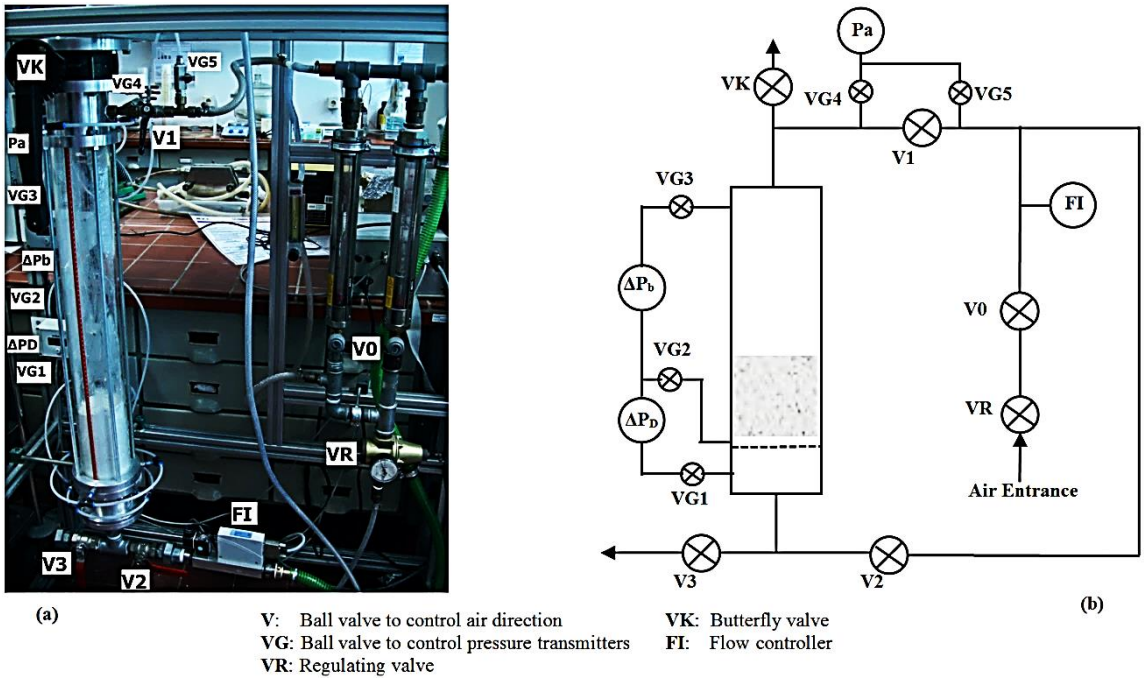

Fig. 2.12 (a) Snapshot, and (b) scheme of the test rig.

An exhaust air filter at the top of the test rig is used to prevent elutriation loss. Before transferring the particulate materials to the fluidization column, an anti-static spray is used to limit the effect of electric charges on the column wall. Each mixture is prepared carefully using an Eirich mixer (EL01). Then, four samples are prepared from four different positions of the mixed material, and the particle size distribution is checked to ensure the homogeneity of the mixture. Some segregation and compaction could happen during the transfer of materials to the column. This effect is small, due to the gradual transfer and to the low height from the free surface of the bed and new charged material. In this manner, similar conditions are obtained for all tests, reducing possible history effects as much as possible.

Figure 2.12(b) shows the scheme of the experimental apparatus. In this study, three classes of tests are designed and performed to understand the effect of the presence of very cohesive Geldart C ultra-fine particles during fluidization, compression, permeation, and re-fluidization processes of a fine particle bed. These classes of tests include a) Fluidization test, b) Fluidization, compression, and re-fluidization of the compressed and consolidated bed, and finally, c) Fluidization, compression, permeation of air through a compressed and consolidated bed, and re-fluidization after combined effect of compression and permeation. The working principle for each experiment is depicted in Fig. 2.13. Chapters 3, 4, and 5 will report the results of these three classes of tests, respectively.

For the fluidization and re-fluidization tests, the dried air used as fluidization gas, after passing through the V2 valve (V1 valve is closed), enters the system from the bottom of the bed. Then, after passing through the particle bed, exits from the top of the bed, from the VK valve (see Figure 2.12(b)). Conversely, for the compression and permeation tests, the dried compressed air, after passing through the V1 valve (V2 valve is closed), comes to the system from the top side. For compression, there is not any exit. However, for permeation, the V3 valve is open and the airflow can exit from the bottom of the column after passing the consolidated bed. In this condition, the V2 valve is closed.

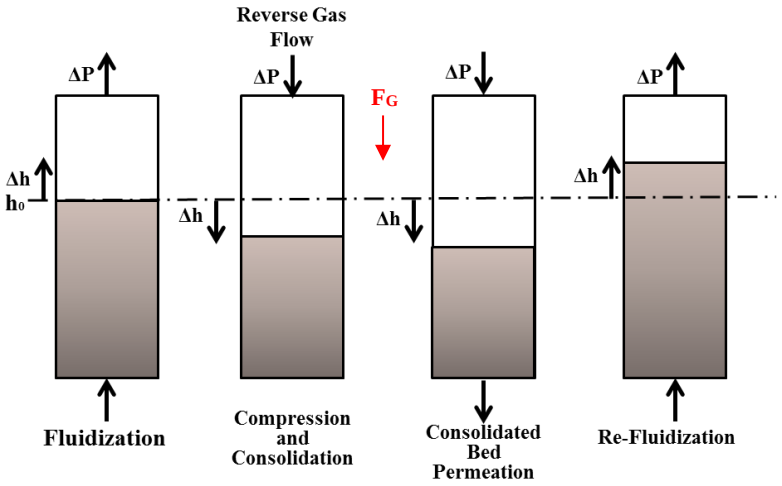

Fig. 2.13 Working principle for different experiments, involving four steps of fluidization, compression, permeation, and re-fluidization.

In this study, two mixtures with a dominant mass fraction of either fine or ultra-fine particles and a mixture of these two materials in the same weight fraction will be considered; i.e., the portions of ultra-fine powders in the mixtures are 30%, 68%, and 50%, respectively. The method of selecting the percentage of ultra-fine material will be discussed in chapter 3.

CHAPTER 3

Fluidization Test

In this chapter, the results of the first class of the tests performed in this study will be reported and discussed. To better understand the concepts and interpretation of the results, in the first part of this chapter, a targeted review on the fluidization process and its involved phenomena will be presented. The results and discussion of this chapter were partly published in the article "The Effect of the Presence of Very Cohesive Geldart C Ultra-Fine Particles on the Fluidization of Geldart A Fine Particle Beds", Processes, 2019, 7,35; DOI:10.3390/pr7010035.

3.1 Introduction

Fluidization is a process in which solids behave like a fluid by blowing gas or liquid upwards through the particle bed. Fluidization is widely used in industrial operations. It is used in two categories. The first concerns physical operations, such as heating, mixing, transportation, and absorption of fine powders, and the second one is associated with chemical operations, like reactions of solids with gases. Since the particles are well mixed, there are low temperature gradients in the process [10].

Increasing the heat and mass transfer in a fluidization process of particulate materials due to increasing the surface-to-volume ratio is the main reason for the growing use of fluidization in chemical and industrial processes (e.g., granulation, mixing, combustion, coating, and chemical reaction processes). Suspended particles have a larger effective surface area than a packed bed. On the other hand, this higher ratio (surface-to-volume) along with the short distance between the small particles leads to strong interactions between them. These interactions affect the flow properties of the particulate material. Accordingly, in recent years, lots of scientific projects have been done to improve the performance of fluidization for different particulate materials.

3.1.1 Fluidization regimes

The superficial gas velocity and the properties of gas and solid change the behavior of a fluidized bed. There are a number of fluidization regimes, as shown in Fig. 3.1. When the

flow rate of the fluidizing gas increases, at the first steps, the height is constant as the bed stays at rest. This regime is called a fixed bed (Fig. 3.1A). With increasing gas velocity, a point is reached where the drag force applied on the particles by the upward fluidizing gas equals the total particles' weight. In this condition, the voidage of the bed increases slightly. This condition is the onset of fluidization and is called minimum fluidization (Fig. 3.1B) with a corresponding minimum fluidization velocity, U_{mf}.

Further increase in the gas flow causes the formation of bubbles in the fluidization. At this point, a bubbling fluidized bed occurs as shown in Fig. 3.1C. As the gas velocity is further increased, the bubbles in a bubbling fluidized bed will coalesce and grow as they rise. If the ratio of the height to the diameter of the bed is high enough, the size of bubbles may become almost the same as the diameter of the bed. This is called slugging (Fig. 3.1D). If the particles are fluidized at a high enough gas flow rate, the velocity exceeds the terminal velocity of the particles. Then the upper surface of the bed disappears. In this condition, instead of bubbles, one observes a turbulent motion of solid clusters and voids of gas of various sizes and shapes. Beds under these conditions are called turbulent beds as shown in Fig. 3.1E. With a further increase in gas velocity, finally, the fluidized bed becomes an entrained bed in which the behavior changes to disperse, dilute or lean phase fluidized bed, which changes to pneumatic transport of solids [10].

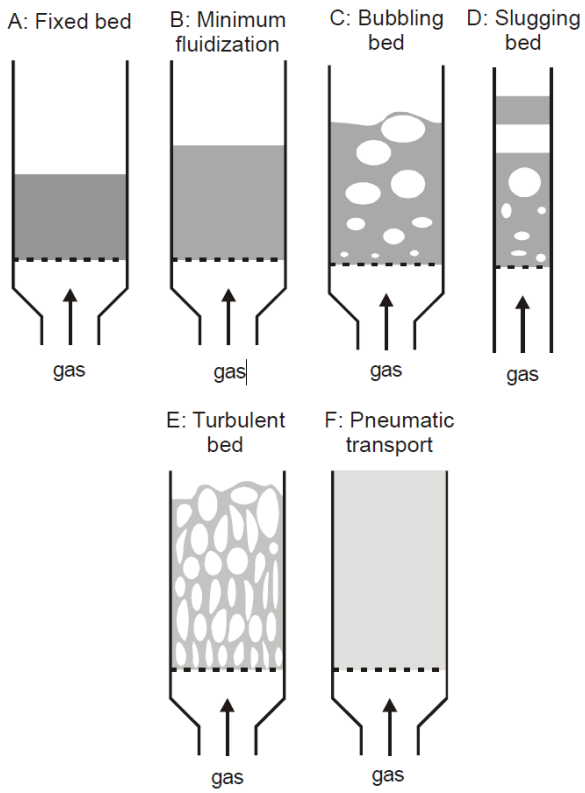

Fig. 3.1 Schematic representations of fluidized beds in different regimes [59].

Yerushalmi and Cankurt [60] also worked on fluidization regimes. They found that when the gas velocity through a bubbling fluidized bed is slowly increased, the heterogeneous, two-phase structure of the bed first peaks, then gradually changes to a condition of increasing uniformity culminating in the turbulent state in which large discrete bubbles or voids are absent. In the turbulent fluidized bed, the upper bed surface is considerably more diffuse than in a bubbling fluidized bed because it has a greater freeboard activity due to operation at higher gas velocities.

The turbulent regime extends to the so-called transport velocity. Near transport velocity, there is a sharp increase in the rate of particle carryover, and in the absence of solid recycling, the bed would empty in a short time. Beyond the transport velocity, if solid is fed to the bottom of the column, it transverses in fully entrained transport flow, and the concentration or density of the resulting suspension depends not only on the velocity of the gas but also on the solid flow rate. If the solid rate is low, dilute-phase flow results; if the solid rate is sufficiently high, then it is possible to maintain a high solid concentration in the vessel; this is typical of the fast fluidized bed.

Yerushalmi and Cankurt [60] presented data obtained with several particulate materials that were used to define the fluidization regimes noted above and their boundaries. These results provide a clear map of fluidization regimes. Fig 3.2 shows the qualitative fluidization map for fine particles.

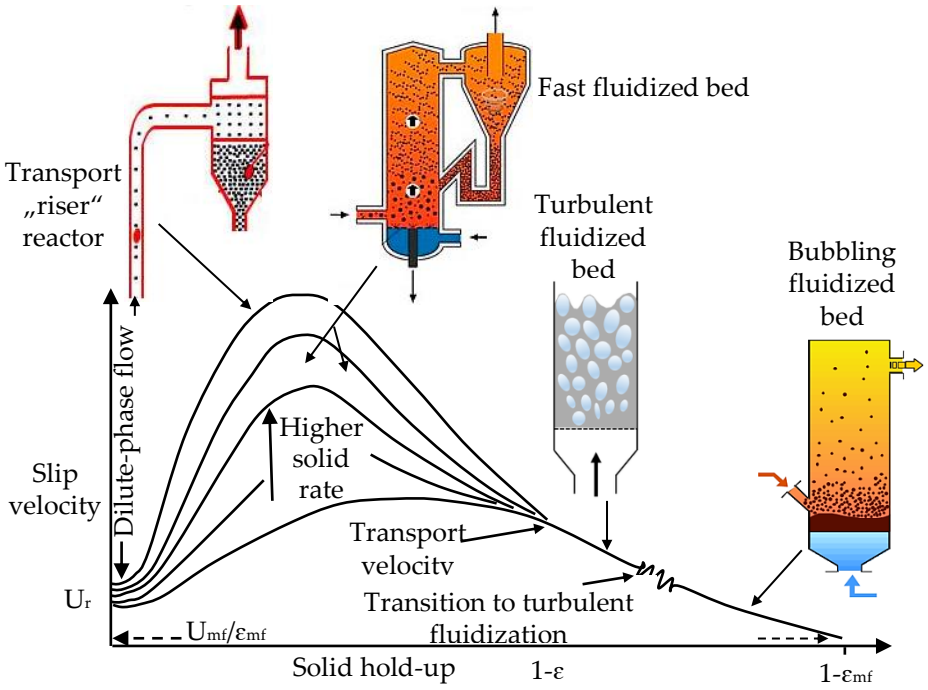

Fig. 3.2 The qualitative fluidization map for fine particles [60].

3.1.2 Classification of particles based on fluidization behavior

Geldart classified the fluidization of particulate material into four distinct groups [8]: A, aeratable; B, sand-like; C, cohesive; and D, spoutable. The behavior of each of them is described as following [10]:

- Group A is identified as aeratable particles. These materials usually have a small mean particle size (d_p< 100 μm) or low particle density (ρ_p<1.4 g/cm^3). Fluid cracking catalysts (FCC) typically are in this category. These solids fluidize easily, with smooth fluidization at low gas velocities without the formation of bubbles. At higher gas velocity, a point is eventually reached when bubbles start to form and the minimum bubbling velocity, U_{mb} is always greater than the minimum fluidization velocity U_{mf}.

- Group B is labeled as sand-like or bubbly particles. The range of particle size of this group is between 150 to 500 μm and the particle density from 1.4 to 4 g/cm^3. For these particles, once the minimum fluidization velocity is exceeded, the excess gas appears in the form of bubbles. Bubbles can grow to a large size. Glass beads and coarse sand are typically classified as group B materials.

- Group C materials are cohesive and ultra-fine powders. Their sizes are usually less than 30 μm, and they are extremely difficult to fluidize because of inter-particle cohesive forces. For these materials, cohesive forces are relatively large, compared to hydrodynamics force. Fluidization of group C particles easily gives rise to channeling. Talc, flour, and starch are classified as group C materials.

- Group D is recognized as spoutable particles. They are either very large or very dense materials. They are difficult to fluidize in deep beds. Unlike group B particles, as the superficial gas velocity increases, a jet can be formed in the bed and material may then be blown out in a spouting motion. If the gas distribution is not smooth, spouting behavior and severe channeling can be expected. Examples of group D materials are roasting coffee beans, lead shot, and some roasting metal ores.

The Geldart classification is based on the density difference between the particulate material and the fluidizing fluid as well as the Sauter diameter of the particulate material. The Sauter mean diameter (SMD or d_{32}) is an average of particle size. It is defined as the diameter of a sphere that has the same volume to surface area ratio as the examined particulate material. SMD is typically defined in terms of the surface diameter d_s and volume diameter d_v as:

$$d_{32} = d_v^3/d_s^2 \tag{3-1}$$

where $d_s = \sqrt{A_p/\pi}$ and $d_v = \left(6V_p/\pi\right)^{1/3}$. On the other side, if the volume of the particle, V_p, is divided by the surface area of the particle, A_p, then:

$$\frac{V_p}{A_p} = \frac{\frac{4}{3}\pi(d_v/2)^3}{4\pi(d_s/2)^2} = \frac{(d_v/2)^3}{3(d_s/2)^2} = \frac{d_{32}}{6} \tag{3-2}$$

Therefore, the equation could be rewritten for d_{32} as:

$$d_{32} = 6\,V_p/A_p \tag{3-3}$$

Figure 3.3 shows the Geldart classification graph. The focus of this research is on the particles classified in the Geldart groups A and C and also different mixtures of these two classes of particulate materials.

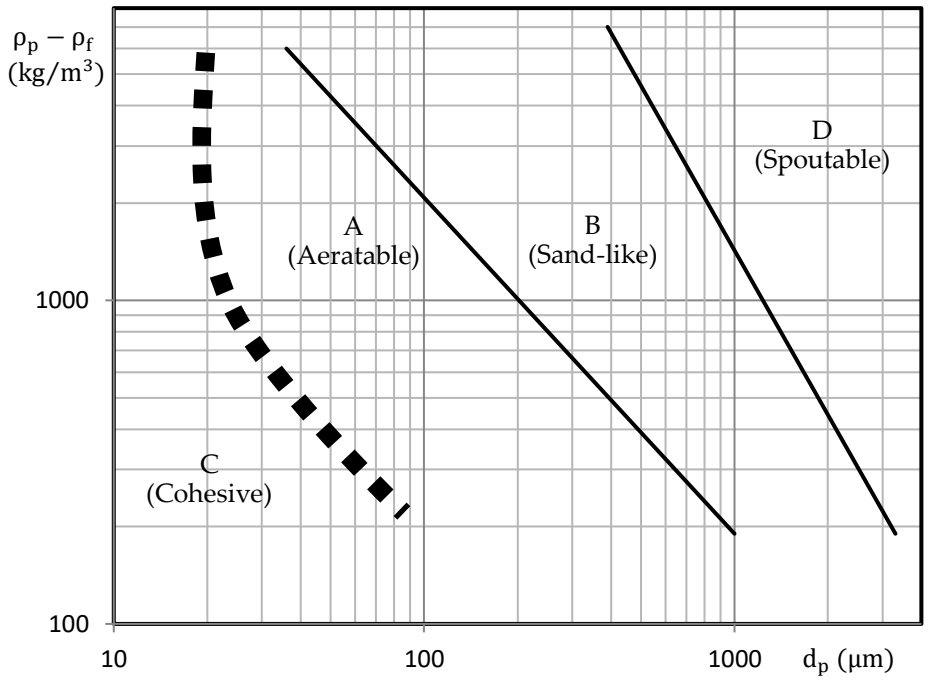

Fig. 3.3 Simplified diagram for classifying powders according to their fluidization behavior in the air at ambient conditions (Geldart, [8])

Dry et al. [5] have re-examined the validity of the assumptions built into the two-phase theory for a range of fine powders. These assumptions are that, in the dense phase of a bubbling fluidized bed, the voidage and velocity correspond to these two parameters at the incipient fluidization. In their study, eleven different powders were used; the average particle size and density varied from 12 to 67 μm and between 1300 and 5200 kg/m^3, respectively. Using the bed collapse technique, velocity and voidage were measured for the dense phase. It has been shown that at high fines proportions, the minimum fluidization point loses its meaning.

In this condition; a transitional class on the Geldart classification diagram [8], called class A/C was proposed. This class was characterized by the absence of a meaningful incipient fluidization point and the absence of shrinkage of the bed when bubbles first begin to pass through. The voidage of the dense phase increased more strongly than expected. It correlated strongly with the portion of finer particles. Particle density, in the range used in their study, had an insignificant effect on the voidage of the dense phase. Furthermore, the velocity of the gas in the dense phase was also increased and correlated strongly with the portion of finer particles. In their study, the existence of a class AC between Geldart group A and C has been demonstrated. They indicated that the two-phase assumptions are not suitable for the transition class of AC.

Geldart [8] suggested his diagram for the classification of fluidized particles in the ambient air, based on bubbling fluidization behavior. In the following, Molerus [61] offered his particle classification diagram for gas-fluidized systems by considering the first fundamentals of flow in disperse systems. In the study of Goossens [62], the relative importance of the effects of laminar and turbulent flow, when a fluidizing fluid interacts with the particles, was considered as the dominant factor for classifying the behavior of fluidized particles. The relative importance of laminar and turbulent phenomena is mathematically described by the ratio "laminar to turbulent", R_{lt} defined as:

$$R_{lt} = \frac{Lam}{Turb} = \frac{18\mathrm{Re_t}}{1/3\,\mathrm{Re_t^2}} = \frac{54}{\mathrm{Re_t}} \tag{3-4}$$

or

$$R_{lt} = \frac{1638\mathrm{Re_{mf}}}{\frac{91}{3}\mathrm{Re_{mf}^2}} = \frac{54}{\mathrm{Re_{mf}}} \tag{3-5}$$

where Re_t is the Reynolds number at entrainment and Re_{mf} is the Reynolds number at incipient fluidization. The critical value for the ratio between the effects of laminar and turbulent flow at entrainment or at minimum fluidization is Archimedes number (Ar). Therefore, Ar was proposed for the classification of fluidized particles. In this case, the classification was generally accepted for liquid fluidization as well as for gas fluidization (any fluidizing fluid) at any pressure and temperature.

In viscous fluid dynamics, the Archimedes number is used to determine the motion of fluids due to density differences. It is a dimensionless number defined as the ratio of external forces to internal viscous forces.

$$\mathrm{Ar} = \frac{g d_p^3 \rho_f (\rho_p - \rho_f)}{\mu_f^2} \tag{3-6}$$

where g is the gravitational acceleration, ρ_f is the fluid density, ρ_p is the particle density, μ_f is the dynamic viscosity of the fluid, and d_p is the particle size.

This procedure of classification of fluidized particles was used by Ergun [63]. In this method, the laminar and turbulent effects are added together to show the simultaneous occurrence of laminar and turbulent phenomena in the real hydrodynamics. The assumption of the relative importance of both phenomena is also valid for the fluidization process. This theory was well approved at entrainment. In Stokes' law state, the laminar phenomenon is noticeable, i.e., the friction force (2/3 of shear stress and 1/3 of normal stress) is dominant [61]. In Newton's law state, the turbulent hydrodynamics is the most important, i.e., the effects of inertia are dominant in the fluid flow; the friction force is insignificant in comparison to the drag force [61]. In the transition regime, both phenomena are present.

Ar = 0.97 boundary criterion was applied to the recognition between free-flowing particles and cohesive solids. This criterion indicated that the effects of laminar flow during the fluidization, even at entrainment were dominant. This was the upper limit of the Archimedes number for the group C particles, according to Geldart's classification.

The second criterion was characterized by the minimum fluidization status. Considering the laminar-to-turbulent ratio at minimum fluidization as an identical critical value of 1000, similar to the entrainment situation, the Archimedes number was calculated as Ar =88.5. This number referred to the boundary between Geldart's group A and B. For group A particles, at minimum fluidization, the effects of turbulent flow are negligible, while for group B particles, the turbulent effects start to be comparable with the laminar effects.

The third criterion was related to the situation in which the hydrodynamic effects of laminar and turbulent are balanced at the beginning of fluidization. In this condition Ar=176900. Similar to the previous case, this critical Archimedes number referred to the boundary between two other Geldart's groups; i.e., groups B and D. For group B particles, at minimum fluidization, the effects of turbulent flow are at maximum equal to the effects of laminar flow; for group D of particles, from the beginning of the entrainment, the effects of turbulence are dominate.

To complete this kind of classification of particles base on the fluidization behavior, a fourth criterion was defined here considering the effect of cohesive forces in the fine powders. For the definition of this criterion, the focus was on a condition that the local

inter-particle cohesive force between adjacent particles has been broken by the inertia forces of the fluid. Inherently, the laminar flow phenomena could not able to do this work. Furthermore, the ordinary cohesive forces between adjacent particles can be broken by fluid inertia force only when the effects of turbulent hydrodynamic at entrainment start to be discernible.

In their study [62], this condition was defined as the laminar-to-turbulent ratio as the value of 100. The corresponding critical Archimedes number was Ar = 9.8. This number referred to the boundary between Geldart's group A and A/C. The fluidization of particles belonging to group A is considered to be smooth. In fact, at entrainment, some significant effects of turbulent are present and could increase the possibility of breaking of the temporarily formed clusters (formed by inter-particle forces even at the beginning of fluidization). Therefore, particles were moved as individual bodies in the fluidized bed.

For the particles belonging to the border A/C (Ar < 9.8), the effects of turbulent flow are limited but sufficiently powerful (Ar > 0.97) to make a loose structure of particles with partial contact within the fluidized bed [64] (Note: these criteria refer to hard particles. Cohesive interparticle forces can be greater than this for soft finer particles, irregular particles, and particles with specific adsorption properties). Based on the four criteria introduced here, five classes of fluidized particles were detectable. They can be revealed on a logarithmic scale of Ar vs. Re (Reynolds number) in Fig. 3.4.

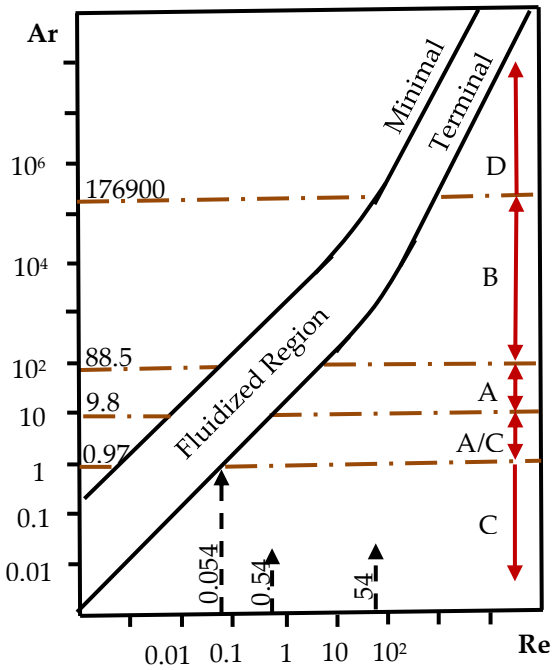

Fig. 3.4 General classification diagram for fluidized particles [62].

Goossens [62] also compared the new classification based on the Archimedes number with the classifications of Geldart [8] and the classification of Molerus [61]. The dash lines

in Fig. 3.5 reveal the Geldart's classification boundaries based on bubbling behavior. Comparing these boundaries with the new method lines, it appears that for the frequently used particles with a particle density of about 2000 kg/m^3 qualitatively good correspondence is obtained. Furthermore, the trends of PQ and ZZ dash lines are analogous to the lines regarding Ar=0.97 and Ar= 176900, respectively.

However, the XX dash line, the boundary between classes A and B, gives a different trend. The main difference in the trend of the XX dash line and the new classification is probably related to the difficulties to measure a reliable minimum bubbling velocity. The measurement of the minimum bubbling velocity needs a slow and very careful increase of the gas velocity along with attentive monitoring of the first bubbles in the expanding fluidized bed. Geldart [8] has reported the influence of fine particles on the bubble development. In addition, the main question is how large the void-volume should be considered as a first bubble.

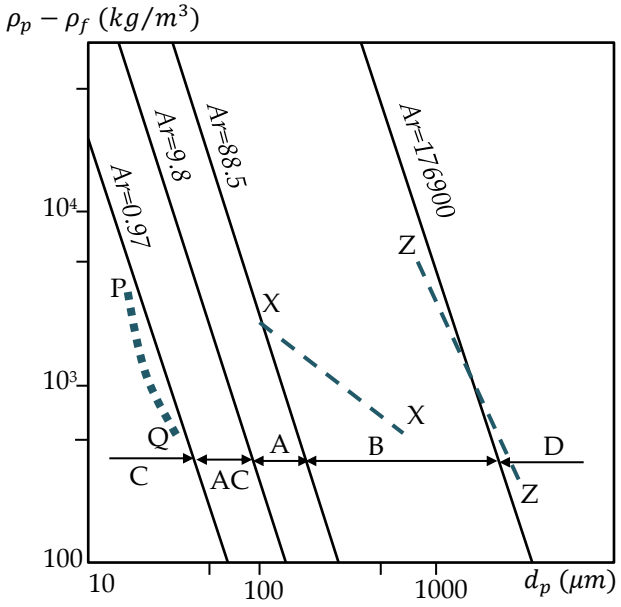

Fig. 3.5 Comparison with Geldart's classification (dashed lines).

In fact, the beginning of bubbling for larger particles is more difficult to observe. This issue was also reflected by Geldart's [65] in the empirical equation for minimum bubbling ($U_{mb} = 100\ d_p$). However, it seems that the Ar = 88.5 criterion has to be preferred to the XX line. The base of this criterion is that when the turbulent effects are one-thousandth of the laminar effects, the bubbling starts. Linking the bubbling to turbulent phenomena could be a plausible interpretation of the first principles of the hydrodynamics of particle-fluid systems. Indeed, when Reynolds number is of the order of one [61], the flow separates and a toroidal eddy has been observed. This condition is matched with Ar = 88.5.

Finally, the good qualitative agreement between the Archimedes criteria classification method and the Geldart method allows applying Geldart's terminology in the various classes.

In Fig. 3.6, the dashed lines show the Molerus classification [61] considering adhesion forces and heat transfer. Molerus defined the K_1 zone as the result of the hypothesis that the maximum drag force at entrainment conditions has reached a critical value, K_1, which is experimentally determined, in comparison to the adhesion force. Experiments showed that the adhesion force of soft particles is about 4 times larger than that of hard particles. The restricted dashed zone for hard and soft particles indicates the transition from not fluidizable cohesive powders to fluidizable ones; the AC/A boundary. The Ar = 0.97 line matches well in this zone.

In theory, the Ar = 0.97 line is related to the hard particles. Therefore, it should be equivalent to the K_1 hard line. However, Fig. 3.6 shows a deviation. This discrepancy suggests higher adhesion forces than those experimentally measured. As the Ar = 0.97 criterion is on the safe side, Goossens [62] proposed to rely on it.

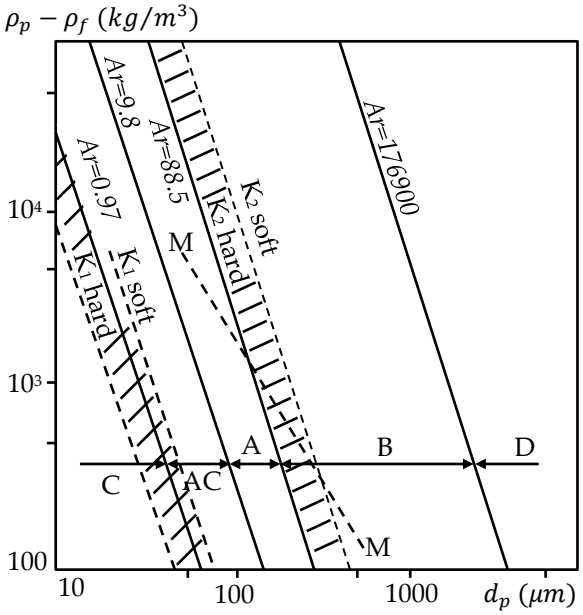

Fig. 3.6 Comparison Archimedes number criteria with Molerus' classification method (dashed lines).

In addition, Molerus [61] suggested that the transition from Group B to Group A particles is controlled by the ratio between the apparent weight and the adhesion force, a critical value K_2. The critical value K_2 is calculated based on the experimental proof that "the 100 μm glass particles with density 2500 kg/ m^3 show bubbling behavior immediately for the

gas velocities greater than the minimum fluidization". This condition matches the upper point (left) of the XX line for the Geldart classification diagram (Fig. 3.5). Again, in Fig. 3.6, the K_2 boundary zone is finally revealed based on the adhesion force of hard and soft particles. The Ar = 88.5 line coincides with the K_2 dashed line for hard particles considering the assumption that the turbulent effects become one-thousandth of the laminar effects at minimum fluidization point.

Molerus [61] employed heat transfer phenomena to obtain the criteria for the discrimination of various types of gas fluidization in his second method. Molerus revealed that when Ar < 100, the particle convective heat transfer is dominant and from Ar > 100,000, the gas convective heat transfer prevails. The pure particle convective heat transfer, the upper limit of Ar = 100, is set sharper by the Ar = 88.5 criterion, conforming to the K_2 boundary for hard particles. Similarly, the pure gas convective heat transfer, under the limit of Ar = 100,000, is formulated sharper by the Ar = 176,900 criterion.

Furthermore, Molerus [61] showed that for fine particles that show a low permeability inhibiting bubble growth, the particle convective heat transfer is characteristic. Molerus also derived a criterion plotted as MM dashed line in Fig. 3.6 cutting the K_2 boundary zone based on the maximum heat transfer attainable from such fluidized particles. From an empirical viewpoint, the MM criterion deserves more interest than the K_2 boundary. In fact, quantifying the bubbling starting point is difficult by visual observation and depends on the Archimedes number and the particle properties. However, Goossens [62] showed that the Ar = 88.5 criterion is defined in a practical method considering that turbulent flow phenomena is larger than one-thousandth of the laminar ones and could be a good criterion for classifying the group A and B. Consequently, the Archimedes number criteria of Goossens are qualitatively confirmed by the criteria of Molerus.

3.1.3 Particle adhesion forces between fine particles

In 1976, Massimilla and Donsi [4] studied the importance of van der Waals and capillary inter-particle forces with respect to particle weight. They indicated that the evaluation of solid-solid interaction base on particle size leads to enormously high effects of cohesive forces. They used electron scanning microscopy to investigate the characteristics of the particle surface of a number of catalytic powders. In fact, there are surface irregularities even in the case of apparently perfect microspheres.

Particle adhesion is caused by surface and field forces (van der Waals, electrostatic and magnetic forces), material bridges between particle surfaces (liquid and solid bridges, flocculants) and interlocking. These forces are the main forces induced between particles of a bed [13,66–68] and are the main reasons for the agglomeration of particles. They are

summarized as [35]:

- *Surface and field forces at direct contact:*
  - Van der Waals forces; all dry powders consisting of polar, induced polar and non-polar molecules, e.g. minerals, chemicals, plastics, pharmaceuticals, food.
  - Electrostatic forces:
    - Electric conductor (metal powders).
    - Electric non-conductor (polymer powders, plastics, detergents).
  - Magnetic force (iron powder).

- *Material bridges between particle surfaces:*
  - Hydrogen bonds of adsorbed surface layers of condensed water (powders).
  - Organic macromolecules as flocculants in suspensions (in wastewater).
  - Liquid bridges of
    - Low viscous wetting liquids by capillary pressure and surface tension (moist sand),
    - High viscous bond agents (resins).
  - Solid bridges by
    - Re-crystallization of liquid bridges which contain solvents (salt),
    - Solidification of swelled ultrafine gel particles (starch, clay),
    - Freezing of liquid bridge bonds (frozen soil),
    - Chemical reactions with adsorbed surface layers (cement hydration by water) or cement with interstitial pore water (concrete),
    - Solidification of high viscous bond agents (asphalt),
    - Contact fusion by sintering (aggregates of nanoparticles, ceramics),
    - Chemical bonds by solid-solid reactions (glass batch, mechanically activated metal alloys).

- *Interlocking by macromolecular and particle shape effects:*
    - The interlocking of chain branches at macromolecules (proteins),
    - The interlocking of contacts by overlaps of surface asperities (rough particles),
    - Interlocking by hook-like bonds (fibers).

Figure 3.7 reveals a schematic of these forces between particles.

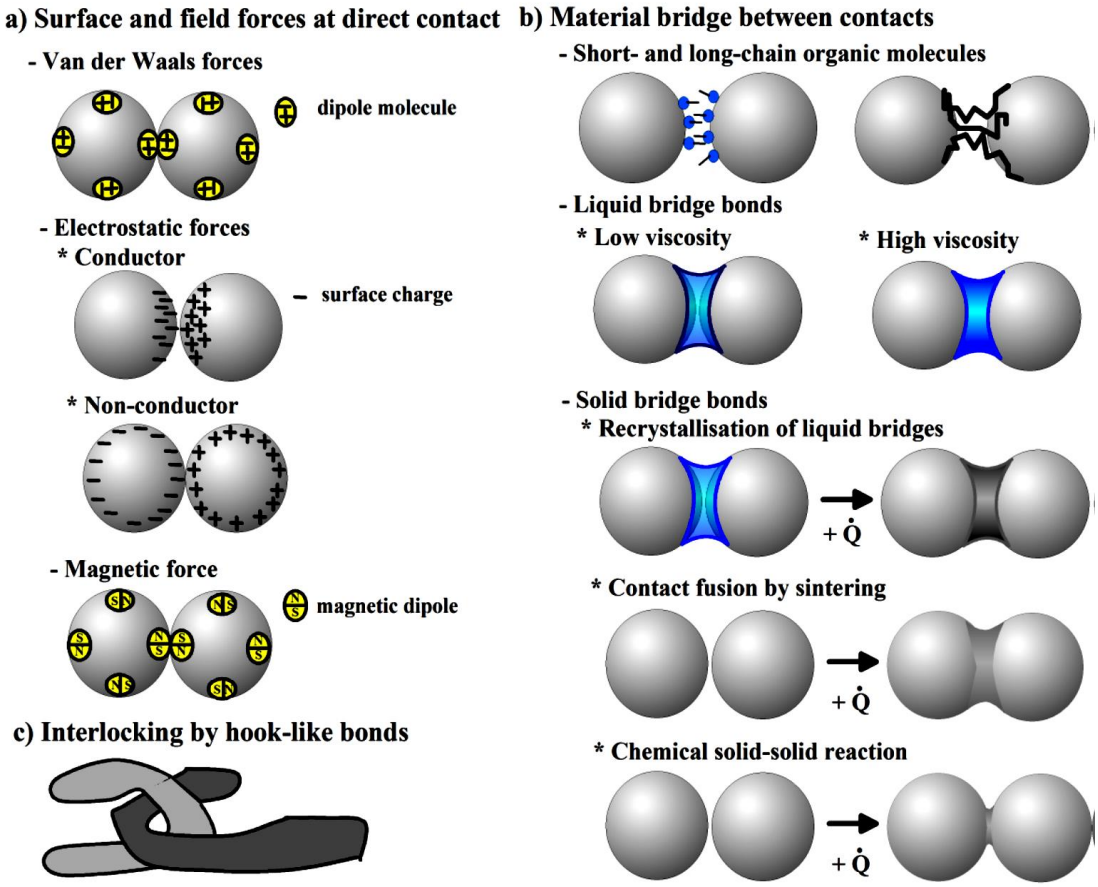

Fig. 3.7 Particle adhesion and micro-processes of particle bond effects in contact [35].

In 2000, Seville et al. [69] wrote a review paper on the inter-particle forces in fluidization. Because of the balance of forces in fluidized beds, particle interactions can have a strong effect on their microscopic and macroscopic behavior, leading to agglomeration and de-fluidization. In their paper, three types of particle interactions are reviewed: van der Waals forces, liquid bridge forces, and sintering. Sintering is a time-dependent process and qualitatively different in its effects. The effects of these three types of interactions on fluidization behavior are described and explained in terms of simple models. In this review, the focus of the study will be on liquid bridges, electrostatic and especially the van der Waals forces.

3.1.3.1 Van der Waals forces

Van der Waals force is a general term used for the dipole-dipole, dipole-non polar and non-polar - non-polar dispersion forces between molecules [66]. The inter-molecular and inter-particle van der Waals forces have some differences. The intermolecular van der Waals force declines with molecular separation, a, as a^{-7}, when the pair potentials are

integrated between macroscopic molecules. However, for spherical particles, the van der Waals force is much less sensitive to separation, declining as ${D_s}^{-2}$:

$$F_{vw} = \frac{C_H R}{12{D_s}^2} \tag{3-6}$$

where R_n ($R_n = R_1R_2/(R_1 + R_2)$) is the equivalent sphere radius, C_H is the Hamaker constant and D_s is the surface separation. The inter-particle forces depend more on the surface properties of the particle than on its bulk. Therefore, considering the surface roughness and using this parameter to determine the required curvature in the equation may be more plausible. As a result, the van der Waals force depends on this curvature instead of R_n. This result suggests that spherical particles of a diameter of order 100 μm should exhibit inter-particle van der Waals forces to equal their single-particle weight (see Fig 3.8). However, if the equivalent particle radius (R_n), as in Eq. (3-6), is taken as the controlling factor, the corresponding diameter is about 1 mm, which is less reasonable. Commonly, 100 μm particles adhere to surfaces and resist the gravity force, but 1-mm particles do not!

Molerus [70] suggested that the transition between different groups of Geldart classification corresponds to the ratio between the inter-particle cohesive force and the weight of the particle. For Geldart's group A, these forces are of comparable magnitude and for group B, inter-particle forces are insignificant by comparison with weight. This approach results in the boundaries between different groups in Geldart classification (Fig. 3.3). Molerus tried to obtain a value for the ratio of particle weight to cohesive force at the transition from group A to group B. Considering the values of Hamaker constants, it is about 0.16. However, since in practice, van der Waals force was determined by surface properties, taking into account experimental measurements for inter-particle forces [71], this value might fall in the range of 2.0–3.0.

3.1.3.2 Liquid bridges

From a practical point of view, since the magnitude of liquid bridges can be adjustable by altering the amount of free liquid (moisture content) and its properties (particularly surface tension and viscosity), liquid bridges are more interesting than van der Waals forces. In most of the driers, some types of reactors and bioreactors, and in agglomeration processes, liquid bridges have practical importance.

Since liquid bridges display both static and dynamic forces and are energy dissipative, they are also more complex than van der Waals forces. The static exhibit of the liquid bridge force is the result of two forces. First is the surface tension force and second is the force due to the pressure deficiency in the liquid bridge [72] (see Fig. 3.9):

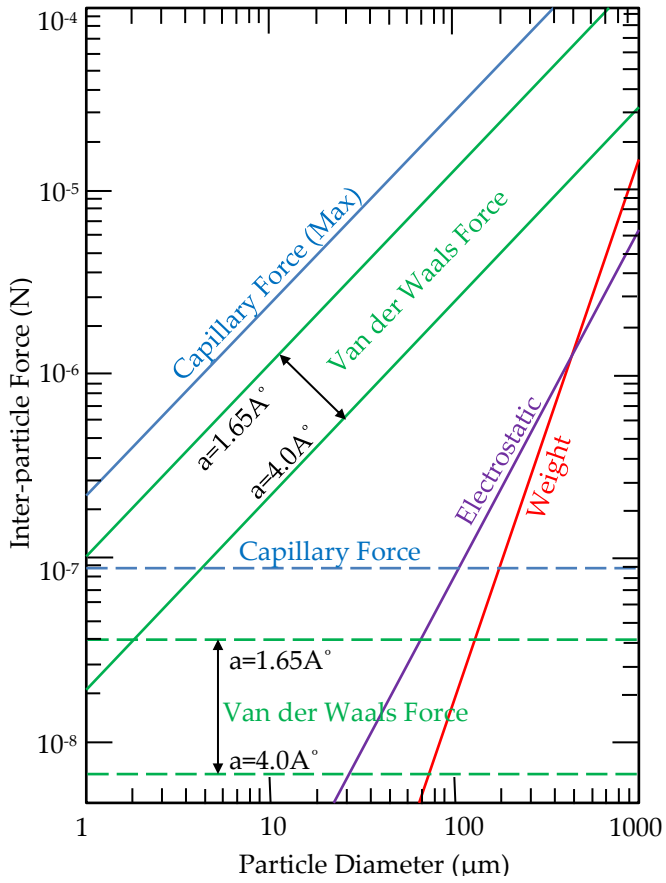

Fig. 3.8 Comparison of the magnitude of different inter-particle forces (dashed lines show forces based on surface roughness of contact). Theoretical inter-particle forces for single-point contact between equal spheres in air, with particle weight, plotted for comparison [72].

van der	(i) $C_H = 6.5\times10^{-20}$ J (quarts)
Waals	(ii) Values presented for inter-particle separations of 1.65 A° and 4.0 A°
	(iii) Dashed lines assume surface roughness in contact (asperity radius of 0.1 μm)
Capillary	(i) $\gamma = 72.8\times10^{-2}$ N m^{-1} (water)
	(ii) Values are maximum ($\beta\rightarrow0$)
	(iii) Dashed lines indicate surface roughness in contact as above
Electrostatic	(i) maximum force (opposite sign)
	(ii) ε_r =1; $\varepsilon_0 = 8.9\times10^{-12}$ C^2 N^{-1} m^{-2}
	(iii) Charge density =10 μC m^{-2}
Weight	$\rho_p = 3\times10^3$ kg m^{-3}

$$F_{ls} = 2\pi r_2\gamma + \pi r_2^2 \Delta P_{lb} \tag{3-7}$$

where F_{ls} is the static exhibit of liquid bridge force, γ is liquid-vapor surface energy, and ΔP_{lb} is the pressure reduction within the bridge with respect to the pressure of its surroundings. Exact calculation of the magnitude of this force, even for spheres, is difficult, because the bridge forms a gas-liquid interface with constant curvature to satisfy the Laplace equation:

$$\Delta P = \gamma \left[\frac{1}{r_1} - \frac{1}{r_2}\right] \tag{3-8}$$

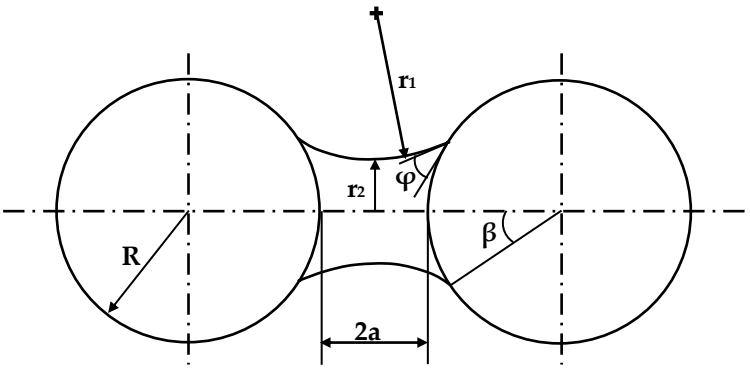

Fig. 3.9 Liquid bridge between two equal spheres. a = half particle separation

In Fig. 3.9, since r_1 is a variable for a given bridge volume, so that r_2 must also be a variable. However, according to the toroidal approximation of Fisher [73], r_1 was considered as a constant and a simple and reasonably accurate result can be calculated. The maximum static liquid bridge force at contact, is

$$F_{ls,max} = 2\pi R\gamma \tag{3-9}$$

This maximum force was plotted in Fig. 3.8 considering the particle diameter and also again for the force which would arise if the contact was dominated by surface roughness. For water, the maximum van der Waals force is rather smaller than the static liquid bridge force. According to Fisher approximation for surface contact, liquid bridge force decreased with increasing liquid loading. It is the opposite of what one would inherently expect. Pietsch [74] made an effort to resolve this problem. He suggested that all real contacts have roughness. Therefore, an effective surface separation needed to be considered. If Fisher's suggestion is used, separations of order 10^{-3} times of the radius of a spherical particle are enough to reduce the liquid bridge force significantly for bridge half-angles below 5^{o}. Consequently, the liquid bridge force reveals a maximum at a bridge volume which increases with the separation (Fig. 3.10).

By viscous flow away from the contact area on approach and departure, the liquid bridge also dissipates energy. The viscous force, unlike the surface tension force, always resists relative movement. During separation, the pressure reduction around the closest approach point may easily lead to cavitation in the liquid [75]. The force is given, to a first approximation, by Reynolds' lubrication equation [71,76]:

$$F_{ld} = 6\pi\mu_f R^2\, v_{p-p}/D_s \tag{3-10}$$

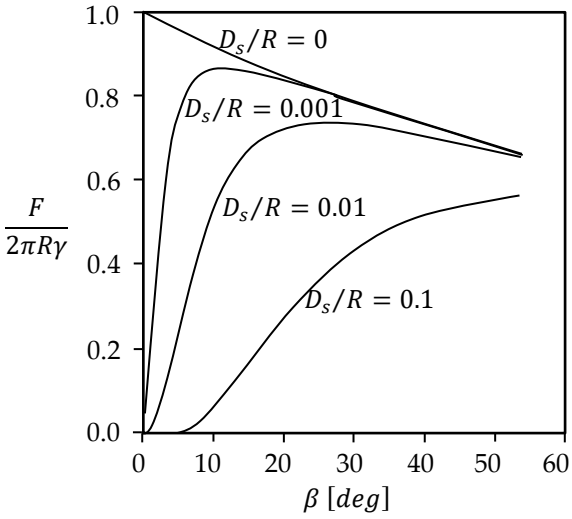

Fig. 3.10 The effect of D_s/R (dimensionless half particle separation distance), on the attractive force as a function of bridge half-filling angle, β, calculated from the Fisher's toroidal approximation.

where μ_f is the dynamic viscosity of the fluid (water) and v_{p-p} is the particle-particle relative velocity. This equation has a singularity at contact (D_s = 0). In the actual application, the surfaces have roughness. Therefore, the minimum separation, D_{s_0}, always is a non-zero value. For the following variable values, the ratio of viscous to static liquid bridge forces has been calculated as a function of separation rate: $\beta = 5°$ and 30°, $D_s = 1$ and 10 μm, $2R = 922$ μm, $\gamma = 0.072$ N m^{-1} m, and $\mu = 0.001$ kg m s^{-1} (water at 25°C). The results are plotted in Fig. 3.11. It shows that the importance of viscous forces by comparison with capillary forces can increase for separation rates above about 1 cm/s if the particle separation is small ($D_s = 1$ μm), and increase to about 1 m/s for larger separations ($D_s = 10$ μm).

The conditions under which particles impacting a thin liquid layer will be captured have been considered in detail by Barnocky and Davis [75]. They have used Reynolds' lubrication equation to estimate the forces during the impaction process. They showed that the value of an impaction Stokes number, $m_p v_{p-p}/6\pi\mu R^2$ determines whether capture occurs, where m_p is the mass of the particle. The third and most significant energy dissipation mechanism is the stretching and concluding rupture of the bridge. It can be imagined that in a fluidized bed, bridges are continually rupturing and reforming.

The dissipated energy depends on the rupture distance [77],

$$D_{s_{max}} = (0.5 + 0.25\beta){V_{lb}}^{1/3} \tag{3-11}$$

where V_{lb} is the volume of the liquid bridge.

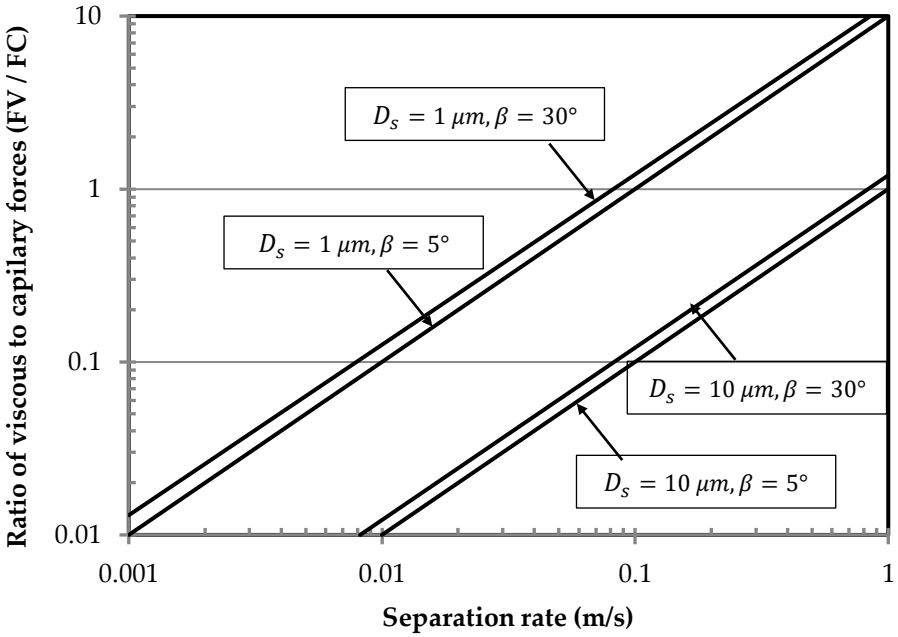

Fig. 3.11 Ratio of viscous to capillary forces as a function of separation rate for water 25°C; diameters of spheres 922 μm.

3.1.3.3 Electrostatic

The triboelectrification (static electrification of solids) in fluidized beds was first reported around 70 years ago [78] when many researchers started to observe abnormal electric behavior in their studies on fluidized beds. The mechanism of generating the static charge was seemingly quite complex. Generally speaking, when two bodies come into contact, electrons transfer from one to the other. These electrons form an "electrical double layer" that consists of two layers of charge of opposite sign. These electrical layers are located on or close to each surface and the distance between them is only a few molecular diameters.

If the bodies are abruptly pulled apart, the existing electric equilibrium cannot be re-established. One of the surfaces holds more electrons and the other will present a deficiency, compared to the situation before establishing the contact. Obviously, the total charge of the two surfaces remains constant. However, due to the better conductivity of one of the surfaces or earthing a surface, this surface could lose its obtained charge. Of course, the above description is a very simple method of discussing the phenomenon of static electrification.

A more complete description of the whole process can be found in [78,79]. The nature of fluidization processes includes continuous motion and rubbing among particles of the

bed. Therefore, a static charge generation is almost inescapable when there are particles made by an insulating material in the bed. The first references to static electrification in fluidized beds were reported by authors as abnormal behavior of the bed that they had faced in their experiments; e.g., in solids elutriation [80], type of fluidization [81], heat transfer [82], or fluid dynamics [83]. How electric charge is escalated in a fluidized bed or how it is affected by the operational parameters is of interest.

There are two different reasons for these interests: (1) the need for decreasing electrical charge in some operations such as preventing any sparks and subsequently explosions and facilitating the bulk material handling; and (2) the need for increasing the static electrification in some operations such as de-dusting of the exhaust gas stream in industries, and separation of a solid among a binary mixture. The controlling parameters for generating the electrical charge when two particles come into contact include the size and shape of the bodies, bulk chemical composition of particles, state of electric charge before contact, condition of both surfaces, and relative velocity of bodies.

For understanding the electrostatic phenomenon, measuring the degree of electrification in a fluidized bed is required. In addition, the parameters such as fluidization velocity, relative humidity, column diameter, bed height, and particle diameter should also be measured. The experimental measurement must also consider the height of the electric probe used for measuring the degree of static electrification. The effect of geometry related parameters such as bed height, column diameter, and electric probe height has already been investigated [84].

Contact electrification and electrostatic interactions between particles are ordinary phenomena in the gas-solid fluidized beds [85]. The charge transfer process between particles or particles and walls during collisions is named contact electrification. When the transferred charge onto particles is adequately strong, the induced attractive and repulsive electrostatic forces between objects can cause agglomeration [86], dispersion [87] and segregation [88], which will notably affect the dynamic behavior of particles and the fluidization performance. The fluidization process involves vigorous interactions between particles and the fluid.

Effective contact electrification and resulting electrostatic interactions are the results of the repeated collisions between particles and the intensive mixing of particles [89–93]. The electrification during fluidization of various sizes of glass beads at different gas velocities and relative humidity was investigated by Guardiola et al. [91]. The potential difference, as a criterion for measuring the electrification, between the earthed distributor and the particulate bed could attain a constant value under different conditions as the fluidization continues.

They reported that the degree of electrification increased with increasing superficial gas velocity at relatively low humidity [91]. In fact, a higher gas velocity made the motion of the particles in the fluidized bed easier, resulting in more particle collisions. In addition, the lower relative humidity restrained the dissipation of charge. Wolny and Kaźmierczak [89,90] experimentally revealed that polymer particles could gain both negative and positive charge and form agglomerates during fluidization. This process is the cause of developing micro-channels, decreasing pressure drops and increasing the minimum bubbling velocities.

When the electrostatic interactions are strong, especially at lower superficial gas velocities (closer to the minimum bubbling velocity), the behavior of the fluidized bed is a non-Newtonian fluid. Furthermore, at lower relative humidity, the adhesion of particles onto walls was also reported by Zhang et al. [93]. Liu et al. [92] studied the electrostatic charging behaviors of insulating particles in pressurized fluidized beds and proposed that the electrification of the particle could be increased by increasing the gas velocity. Understanding the relationship between the charging behavior of particles and the hydrodynamic pressure of the fluidized bed is hard due to the interplay between fluidization and electrification.

Pei et al. [94] implemented a contact condenser model into a coupled CFD-DEM simulation and investigated the charge accumulation and distribution during fluidization. They revealed that the charge accumulated exponentially during fluidization and finally reached an equilibrium value. The charge began from the contact between particles and walls and developed from the near-wall region to the center of the column. Their simulation results were in agreement with the experimental results of Guardiola et al. [91] and LaMarche et al. [95].

Guardiola et al. [91] have also studied the influence of fluidization velocity, U_{sg}, particle size, d_p, and relative humidity, RH, on the electrification degree reached by glass beads fluidized bed. By the measuring method of the potential difference between an electric probe and the metallic distributor, they measured the static electrification of the bed. The relative humidity effect is linked to the quality of fluidization either bubbling or slugging; thus, it is complex. In their study, the electrification vs. humidity characteristic curve has been suggested. This curve included five zones. Their measurements revealed that when the relative humidity is lower than a critical value (RH_c), the static electrification of the bed cannot be measured accurately. In fact, particles that adhere to the probe lead to irreproducible voltage values. They reported these five zones by increasing the relative humidity as shown in Fig. 3.12:

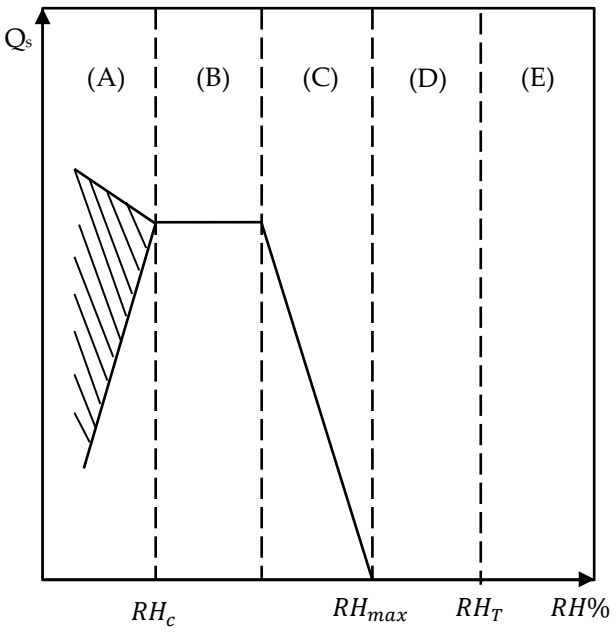

Fig. 3.12 Generalized characteristic curve- Variation of the charge on the capacitor plates with relative humidity.

Zone A: For low relative humidity (smaller than a critical value, RH_c), particles adhere strongly to the wall of the fluidization column and also to the electric probe. Therefore, the direct contact between the probe and other particles in the bed is hindered. Although the strong adhesion of particles to probe and wall indicates a very high level of bed electrification, the stationary voltage measured is usually very low and always unstable.

Zone B: Relative humidity has a limited effect on the stationary charge. Adhesion of particles to either the wall or the probe is not observed. Humidities within this range produce the highest levels of bed electrification.

Zone C: Relative humidity has a strong influence on the degree of electrification. Therefore, small increases in humidity make a sharp decrease in the produced charge. In this zone, particle adhesion is also not observed.

Zone D: During fluidization, for relative humidities greater than a certain value, RH_{max}, charge production is not observed at all.

Zone E: At high humidities above RH_T, due to high moisture content in the bed, fluidization is impossible (wet quenching). In fact, because of glass hydrophilicity [96], an ultra-thin liquid layer around the particles is formed that strengthens their mutual cohesion [97]. Preliminary experiments run with smaller glass beads (d_p = 177-210 μm) determined the value of RH_T as 70%. However, for the three particle sizes studied in [91], this value is greater than 85%.

The difficulty in fluidizing of the ultra-fine particles (group C) can be described as follows. It seems that the value of RH_T decrease with particle size. Thus, zones B, C, and D would be very thin for group C powders (it means, $RH_c \approx RH_T$). As a result, due to the very high cohesion forces (the electrostatic effect), for $RH < RH_c$, and the effect of the bed moisture (for $RH > RH_T$), the fluidization of ultra-fine powders will become difficult at any RH value. Also, increasing the air velocity and decreasing the particle size increase the degree of electrification. In their study, the relationship between electrification and the average velocity of solid circulation is also studied.

For non-conducting particles, the distribution of charge on the surface of the particle is also likely to be non-uniform. As a result, it is generally not easy to estimate the magnitude of the electrostatic force acting between pairs of particles or particles and surfaces [57]. For two charged particles, the following equation may be used to estimate the electrostatic force experienced by each particle:

$$F_{el} = -\frac{q_1 q_2}{4\pi\varepsilon_0\varepsilon_r {D_s}^2} \tag{3-12}$$

where q_i (C) is the charge on the particle i, ε_0 is the permittivity of vacuum, 8.85×10^{-12} F/m, ε_r is the relative permittivity of the material in which the charges are immersed, and D_s (m) is the distance between the particle centers.

3.1.4 Agglomeration formation mechanism and states

In 2000, Zhou and Li [98] developed a model of force balance to estimate the formed agglomerates' size in fluidized beds of cohesive particles. For group C powders, normal fluidization was extraordinarily difficult. However, cohesive particles could be fluidized in some cases in the form of agglomerates [8]. The behavior of cohesive particles in the agglomerating fluidization was studied widely in the 1980s [99,100]. By using external forces, vibration, acoustic or magnetic fields, adjusting the cohesiveness of particles by modifying the surface of particles or by adding other particles, the fluidization quality of cohesive particles is improved. Investigating the mechanism of agglomerate formation and breakup in the fluidization of cohesive particles has been the focus of attention in the 1990s.

Gidaspow [101] also explained the kinetics of two particles collision and introduced relations for the velocity of particles before and after the collision. In a cohesive particle fluidized bed, the probability of collision between agglomerates is high. Zhou and Li [98] developed a model of force balance for the collision between two different sizes agglomerates and analyzed the collision kinetics of agglomerates through the balance of forces acting on one of them. They considered three possible cases for two agglomerates to come into collision: straightforward (opposite direction), different velocities in the

same direction, and collision with an angle. In addition, after the collision, they imagined again three conditions: agglomeration, separation, and disintegration.

The force balance when two agglomerates collide in a fluidized bed includes drag force, the difference between gravity and buoyancy, the cohesive force between agglomerates and collision force. The drag force for a particle or agglomerate in a turbulent flow is $F_D = 0.055\pi\rho_f d_{a1}^2 u^2 \varepsilon^{-4.8}$, the gravity-buoyancy force is $F_{g-b} = \pi/6\left(\rho_a - \rho_f\right)d_{a1}^3 g$, the cohesion force is $F_{vdw} \cong (C_H/12a^2).(d_{a1}d_{a2}/(d_{a1}+d_{a2}))$; where ρ_a is the agglomerate density, d_{a1} and d_{a2} are the diameters of two colliding agglomerates.

For collision force, they considered the elastic collision of the two vertically aligned particles with relative velocity v. In a fluidized bed of cohesive particles, the separation, coalescence, or breakage of two colliding agglomerates depends on the properties of the cohesive particles; such as the density of primary particles, material cohesiveness, size, the operating condition and the ratio of two colliding agglomerates diameters, etc. Through the model analysis, they showed that high superficial gas velocity, low cohesion particles, high fluid density, and the collision between different sizes of agglomerates are beneficial for the agglomerating fluidization of cohesive particles.

Agglomeration is the adhering of particles to form larger ones resulting in an increase in particle size [102]. Increasing the particle size may be desirable for industrial applications such as pellet-making in the pharmaceutical industry, granulation, compacting, sintering of ores, and briquetting. On the other hand, agglomeration and growing the particle size can sometimes result in de-fluidization and losses in a bed, if it proceeds in an uncontrolled procedure [103]. Accidental bed agglomeration is a crucial concern in processes (e.g., combustion and gasification of solid fuels).

Unscheduled shut down of a reactor due to de-fluidization of the bed caused by the agglomeration of particles results in serious problems and losses. In addition, in some cases, operational changes to avoid agglomeration can also make unfavorable effects. For example, while trying to prevent agglomeration by decreasing temperatures in a reaction, a notable decrease in feed conversion efficiency may be encountered. In addition, where a sorbent like limestone particles in fluidized bed combustion is used for emissions control, mineral species derived from the sorbent can also play an important role.

An experimental study of agglomeration problems is also challenging. Agglomeration can be difficult to control. Predictions at the real industrial scale cannot be based on laboratory-scale experimental results. In addition, it is inconvenient, expensive and difficult to do this kind of experiment. Moseley and O'Brien [104] and Wank et al. [105] have reported that agglomeration has a very close relation with particle density, size and

surface properties; also the system's operating temperature, gas velocity, physical and chemical characteristics, reaction mechanism and particle size distribution have an important effect on agglomeration [106].

The effects of some of these parameters have been studied in the laboratory scale in isolation (experiments are normally reported in the literature). A model to predict the agglomeration process for a given set of raw material and a set of process parameters could provide a manner for improved operational efficiency of a plant using fluidized bed technology. Due to such reasons, theoretical means of predicting agglomeration under a given set of operating conditions is important. Normally, studies show the basic physics of agglomeration developed for dry particles or particles which are being sprayed with a binder. Although these models are useful for research, they may be not sufficient to make full-scale predictions. In fact, agglomeration is concurrently affected by several different parameters [107].

3.1.4.1. Agglomeration states of fine particles

The experiments of Wang et al. [3] also showed that there are three states of aggregation for fine particles (un-aggregated or single particles, natural agglomerates, and fluidized agglomerates). Fine particles tend to stick together and form spherical agglomerates when stored in a silo, kept in a stack, and during transferring from one vessel to another one. Due to the relative motion between ultra-fine particles, they form quasi-spherical agglomerates when kept in a container or during transfer to the fluidization column, which are named *natural agglomerates*. This kind of agglomerates is lightweight and breakable. Also, they have a relatively narrow size distribution.

After starting fluidization, in a competition between the transport of agglomerates by the gas flow and the cohesive forces between them, they become restructured regarding the number of constituent particles. They can be disintegrated into smaller agglomerates or even single particles. This new configuration of agglomerates is called *fluidized agglomerates*. Analysis of their experimental results indicated that:

(1) By decreasing particle size, the stability of natural agglomerates increases. For example, the large-sized natural agglomerates of talcum, zeolite, and alumina particles consist of unstable accumulated structures while the small-sized natural agglomerates of nickel particles, show chain or network structures with multi-point cohesion. For the much smaller titanium particles (0.2 μm), the natural agglomerates have a certain specific cluster structure in which the individual particles are recognizable. For the even smaller fumed silica particles (0.0086 μm), the natural agglomerates are lightweight and very stable against the motion in which the component single particles could not be easily distinguishable.

(2) Multi-sized agglomerates, such as for magnetic and fumed silica particles, result in better fluidization, while uniform size agglomerates of titanium and nickel particles, could not be fluidized so well.

(3) The fluidization behavior and quality of the fluidized agglomerates are determined by the density and stability of natural agglomerates (initial condition of the bed before fluidization). For example, nickel particles with high bulk density (970 kg/m^3) and particle density (8670 kg/m^3) form natural agglomerates with a chain of the cohesive network. Therefore, their fluidized agglomerates are unstable and high-density ($\rho_{agg} \cong \rho_b$) result in poor fluidization quality. But the natural agglomerates for fumed silica particles with low bulk density (65 kg/m^3) and particle density (2280 kg/m^3) have low density and high stability. Thus, their fluidized agglomerates are stable and low-density; result in good fluidization behavior. It suggests that lowering the density of agglomerate results in improving the fluidization quality of fine particles.

The measurements of particle size distribution inside agglomerates also show that since the smaller particles have stronger cohesive forces compared to their weight and less single-particle freedom in motion than larger particles, they form more stable agglomerates sinking to the bottom, while the larger particles stick together to form smaller agglomerates which are positioned at the top.

3.1.5 Basics of de-fluidization in fluidized beds

In a fluidization process when the gas flow rate increases in a particle bed, the pressure drop across the bed also increases. The minimum superficial gas velocity needed to avoid de-fluidization is called the minimum fluidization velocity [76]. At this point, the pressure drop across the bed equals the weight of the bed. When the gas velocity falls below the minimum fluidization velocity, the bed de-fluidizes. Particles in group C are very fine while the ones in group A are larger and allow more stable fluidization. Group B particles are normally both larger and heavier than group A particles. Group D is comparatively the largest and heaviest particles and requires high minimum fluidization velocities [77]. When agglomeration starts, particles transfer from one Geldart's group to another one. This change in the distribution can lead to segregation and thus unfavorable temperature distribution [78]. De-fluidization is also one of the issues that happens due to agglomeration. In fact, the agglomeration process increases the size distribution of fluidizing objects. Therefore, they need more kinetic energy (superficial gas velocity) for fluidization. Thus, at lower gas velocities, de-fluidization may occur.

When a collision occurs between two particles, different forces are available on each of

them. To model the resultant force on a particle during a collision, the balances of these different forces are used. Depending on this force balance, two colliding particles may either stick or may rebound after a collision. Depending on the collision velocity, colliding particles possess their own kinetic energy. This kinetic energy gets dissipated by several modes of collision. A collision between two particles may be completely elastic, plastic or elastic-plastic [79]. The coefficient of restitution is normally used for quantifying the particle elasticity. In a plastic collision, the initial kinetic energy is dissipated during the deformation [80]. In an elastic collision, a repulsive Hertzian force can be used for a recoverable deformation.

Van der Waals cohesive force is also available between colliding particles and promotes adhering. This kind of cohesive force is weak and is sufficient to hold only small-size particles together. Besides these forces, the drag force due to the processing fluid may influence the particle velocity, thus promoting agglomeration. In addition, the gravity force and buoyancy also influence the agglomerate formation [56]. In several conditions, a liquid layer coats the colliding particles. In these situations, the magnitude and properties of the liquid bridge force are also crucial in the agglomeration process. Due to the presence of the liquid bridge, the capillary force, viscous dissipation force, and surface tension force influence agglomeration. When two solid particles come close to each other, the liquid bridge between them is squeezed outwards. This process continues until the point of closest approach. Therefore, the kinetic energies of the approaching particles are dissipated [26].

When liquids have high viscosities, the viscous dissipation forces are dominant (amongst liquid bridge forces) [81]. In summary, the impact force due to kinetic energy is dissipated by forces such as cohesion forces, viscous dissipation forces, capillary forces, and surface tension forces. The particles stick together after the collision if the sum of the impact and elastic repulsive force is less than the sum of these dissipative forces. The particles may experience either a normal, head-on collision or at some angle. In an oblique collision, additional tangential forces are involved. They induce sliding, slipping or rolling resistance force on the particles [82].

3.1.6 Elutriation of fine particles

Elutriation of the particles from fluidized beds is a complex event. The mechanisms of occurrence of the elutriation are not well understood even for free-flowing particles. The ejection of particles into the freeboard is done by collisions, hydrodynamic effects (shielding), and momentum interchange between particles, by bubbles, wall effects, and agglomeration.

Considering the trend of elutriation data of group A, the elutriation rate constant, R_i increases by decreasing the average of the bed particle size, $R_i \propto 1/d_m$. The poor fluidization of the bed could be responsible for higher elutriation. However, for ultra-fine particles, Yerushalmi and Cankurt [60] argued that in the case of fast fluidization, forming considerable agglomeration in the freeboard results in a larger effective size of particles. In addition, when the more cohesive particles reach the low-velocity area near the walls, they form agglomerates with each other and stick to the wall. Thus they do not become involved effectively in the elutriation. According to the visual observation, the bubble eruption happens far fewer in the cohesive powder beds. When they did, the ejected agglomerates disengage in short height. The measurement of elutriation shows that the entrainment rates may approach those of group A particles at higher gas velocities when the agglomeration is suppressed by the high turbulence in the system.

Elutriation of fine particles from a fluidized bed is one of the important parameters for the application of fluidized bed techniques. Li and Kato [108] worked on a correlation for the elutriation rate constant of Geldart's group C particles. Due to differences in experimental conditions, the results obtained by different investigators are not the same. The experimental conditions include particle sizes and distribution, superficial gas velocity, gas humidity, column diameter, column height above the gas distributor, and type of particles. The size of the particle is especially important for the elutriation of cohesive particles during fluidization.

Extensive studies have been performed on the elutriation of groups A or B particles. The elutriation of group C particles usually leads to unusual results. Due to increasing the application of cohesive powders in industry, the understanding of the process of elutriation of group C particles has increasingly been the focus of attention in recent years. Geldart and Wong [109] found that the entrainment flux of alumina first increases as the particle size becomes finer and then decreases. They qualitatively explained that the low entrainment rate of cohesive powders is due to the strong effect of cohesive forces between particles.

By considering the effect of agglomeration of fine particles, Baron et al. [110] also reported that the most easily elutriated particles from a fluidized bed of mixed silica sand, FCC and polyethylene particles are not the smallest ones. They indicated that the smallest particles may be attached to the larger one as an agglomerate. Baeyens et al. [111] also worked on entrainment for mixtures of group C and group A particles. They found that the elutriation rate increased as the particle size decreased and at a critical size became constant. They defined and presented a method to estimate the critical particle size from the balance of inter-particle forces and hydrodynamic forces [111]. The particles whose

sizes are smaller than the critical size are called cohesive particles. They also suggested that the fine particles adhere to larger particles rather than agglomerate with each other.

Ma et al. [112] and Ma and Kato [113] indicated that the elutriation rate of powders (limestone, 9.5–88 μm as fines; silica, 331 μm as coarse) reach a maximum at a certain particle size that almost corresponds to the boundary between groups A and C particles. It shows that elutriation mechanisms for group A (or B) particles are different from the mechanism of group C particles. These findings are contrary to the assumption made by existing models for the prediction of the elutriation rate of groups A or B particles and may be due to the powder cohesion. The particle size at which the elutriation rate is the maximum value was defined as the critical size. Based on the experimental results, an empirical correlation was obtained to predict the critical size.

It is found that the elutriation rate does not increase with the decreasing of the elutriated particle sizes when the elutriated particle size is smaller than the critical size. Furthermore, the calculated values of the critical size are in good agreement with each other by Baeyens et al. [111] and Ma and Kato [113]. Geldart [65] has derived the correlations of elutriation rate based on two categories of superficial gas velocity and slip velocity, respectively. The majority of correlations for estimating the elutriation rate were based on the slip velocity [114–118].

Li et al. [119] showed that the elutriation rate constant of Geldart's group C particles is not only affected by the properties of the elutriated particles and fluidizing gas but also affected by the bed particles. Li and Kato [108] investigated the elutriation of group C and group A particles from a fluidized bed in a steady state. They reported the following results. The elutriation rate of group A particles was affected by the properties of the elutriated particles and gas and by the operating conditions such as gas velocity. However, the elutriation rate of group C particles was not only affected by the above conditions but also by the size of bed particles; i.e., the mean diameter of bed particles. They showed that if the mean diameters of particles in the bed are different, with a constant gas velocity, the same-sized group C powder particles give different elutriation rate. This result is completely different from the elutriation rate of groups A or B particles. The elutriation rate of group C particles decreases with the increase in the mean diameter of particles in the bed. It also decreases with the decrease in the particle size of group C particles. Inter-particle adhesion forces have a great influence on the elutriation rate for cohesive powders. The coarse particles in the bed strongly affected the elutriation of group C particles. However, the elutriation rate of group C particles was hardly affected by the density of coarse particles in the bed.

The elutriation rate correlations used normally for particles belonging to groups A and B

are not suitable for group C particles for which inter-particle forces have a marked effect. Li and Kato [108] proposed a correlation of elutriation rate constant for cohesive particles. Their proposed correlation well-predicted values of the elutriation rate constant of the cohesive particles:

$$R_i = 6.64 \times 10^6 C_{ps} \left[\frac{\rho_g U_0 g}{\rho_p}\right]^{2.64} \quad \text{for} \quad d_{pi} \leq d_{crit}, \tag{3-13}$$

where

$$C_{ps} = \begin{cases} 1 & d_p \leq 60\ \mu m \\ \left[\frac{200 - d_p}{150}\right]^{\alpha} + \left[\frac{d_p - 60}{150}\right]^{\alpha} \left[\frac{d_{pi}}{d_{crit}}\right]^{1.4} & 60\ \mu m \leq d_p \leq 200\ \mu m \\ \left[\frac{d_{pi}}{d_{crit}}\right]^{1.4} & d_p \geq 200\ \mu m \end{cases} \tag{3-14}$$

$$\alpha = \left[\frac{d_{crit}}{d_{pi}}\right]^{0.3} \tag{3-15}$$

$$d_{crit} = \frac{1.01 \times 10^5}{\rho_p g^{0.731}} \tag{3-16}$$

3.1.7 Fluidization behavior of Geldart groups A and C

The behavior of gas-fluidized beds of fine particles in the homogeneous expansion was investigated by Abrahamsen and Geldart [11]. In this work, the minimum bubbling velocity has been corrected. They found that this velocity is a function of the mean sieve size of the powder and the fraction of fines less than 45 μm as well as the density and viscosity of the fluidizing gas. For predicting U_{mb}/U_{mf}, an improved equation was presented in their work. This ratio also correlates with the maximum non-bubbling bed expansion ratio H_{mb}/H_{mf} which is used for the calculation of the maximum voidage of the dense phase ε_{mb}. In addition, based on the Carman-Kozeny theory, bed voidages between incipient of fluidization and bubbling can be predicted.

They worked on fine particles (Geldart group A [8]) with a diameter of 20-100 μm [11]. They showed that this kind of particles has several fluidization characteristics as:

(a) They are aeratable; it means that they expand homogeneously between the incipient fluidization velocity, U_{mf}, and the bubbling velocity, U_{mb}. In addition, if the fluidizing gas is interrupted, their collapse rate is slow.

(b) There is a maximum stable bubble size in the fluidization of this kind of material. This maximum size is advantageous for chemical conversion. Because the rates of bubble coalescence and splitting balance each other, the maximum size is reached. Due to the limitation of the bubble size, fluidization is smooth; It means that slugging is unlikely, and pressure fluctuations are small.

(c) The increased reacting surface by using fine particles increases the heat transfer coefficient in the operations.

The work of Massimilla and Donsi [4] was part of a study on the fluidization behavior of fine particles (d < 100 μm), such as catalyst powders used in chemical processes. Their study was directed to the characterization of the dense phase of the bed. The range of gas velocities was between the minimum fluidization velocity and the minimum incipient bubbling velocity. It has been discovered that bed expansion in the bubble-free range of fluidization takes place through the nucleation of microscopic cavities, whose size ranges between a few to about ten particle diameters. Changing gas velocities within the bubble-free range of fluidization varies the size but not the number of cavities [120].

Particle-particle interaction forces have an influence on how the fine particle bed expands. The cohesive forces preserve the cavities walls and cavity expansion develops by a detachment of particles with a weak bond [121]. In [4], only van der Waals and capillary forces are considered.

One of the best studies on the fluidization of cohesive powders has been reported by Geldart et al. [2]. This study is about the fluidization behavior of fine powders (< 70 μm). It has revealed big differences between cohesive group C and free-flowing group A particles. They found that relatively small changes in the size of particles or other parameters (affecting the inter-particle attraction forces) could change the behavior from fine free-flowing particles to cohesive powders. This change in the behavior can be determined by measuring the ratio of tapped to aerated bulk density.

It has been known for more than 70 years that due to the cohesive properties, ultra-fine powders are difficult to fluidize. The first systematic study of interparticle forces in fluidized beds has been done by Baerns in 1966 [122]. It included fine particles that are naturally cohesive because of their small size as well as larger particles made artificially cohesive with additives.

The phrase of “fine particles” are normally used for free-flowing Geldart group A and easy-to-fluidize particles. In some literature, it is also used for cohesive Geldart group C

powders with difficult-to-fluidize behavior. So, for better identification, for cohesive powders, the phrase of "ultra-fine powders" is used in what follows.

It is better to refer them as ultra-fine powders. Since most commercial fluidized bed catalytic reactors use the Geldart A group of particles, a large number of investigations have been devoted to this kind of material. The basic scientific understanding of these particles has been accelerated undoubtedly by the research of Rietema [123] and Donsi and Massimilla [124], but the fluidization behavior of group C powders has attracted much less attention. However, wishing to use them in the commercial processes is the main reason for the increasing interest in investigating this kind of powders [2,5,122,124,125].

The inter-particle forces in group A powders are not so large compared with the hydrodynamic forces acting within the fluidized bed. The influence of these inter-particle forces is beneficial since they are responsible for the expanded dense phase which limits the growth of bubbles. This is the reason that the particles of group A are called "slightly cohesive" materials. In the powders classified as group C, the interparticle forces are considerably larger than the hydrodynamic forces. Therefore, the fluidizing gas cannot easily separate particles and channeling occurs, resulting in poor fluidization.

For cohesive powders, because the bed pressure drop was non-reproducible and is a time-varying parameter due to the creation, destruction, and re-formation of channels, any meaningful measurement of minimum fluidization velocity U_{mf} became impossible [2]. In a free-flowing group A powders, the pressure drop across the fluidized bed is within 1-2% of the theoretical value; that is $P_{wb} = W/A$, where W is the total weight of the bed and A is the cross-section area of the bed.

For group A particles, the dense phase volume in the bubbling bed is reduced more quickly than the bubble holdup increases. Since the inter-particle contacts are steadily disrupted by the passing bubbles, the voidage of the dense phase is decreased; consequently, the overall powder circulation is increased. For more cohesive powders, the stronger inter-particle forces allow the micro-voids to increase in number and/or size (also described by Massimilla and Donsi [4]). Many horizontal and sloping cracks or channels form, and there is not any true bubble formation during the expansion of the bed. Sometimes, some small bubbles form and destroy the cracks near the walls. However, the cracks reform in the bed with a different angle and length.

Wang et al. [3] conducted experiments on ultra-fine powders (Geldart group C) fluidization and reported one of the most comprehensive studies on the behavior of different types of ultra-fine particles in fluidization. In their study, the mean sizes of

particles were between 0.01 and 18.1 μm and their densities were between 100 and 8600 kg/m^3. The particles used in this work were titanium dioxide, alumina, glass fiber, limestone, amorphous silica, fumed silica, Quartz, goethite, talc, magnetite, nickel, zeolite, and aerogel. Their results show that the fluidization of fine particles usually involves plugging, channeling, disrupting, and agglomerating. When this kind of particles fluidized, the fluidized objects generally consist of agglomerates varying in size from the smallest at the top (some even unassociated to individual particles) to the largest at the bottom of the bed (some even de-fluidized).

The agglomerates which have reached a uniform equilibrium size after repeating the circulation of particles are the best to fluidize. Decreasing the density of agglomerates improves the fluidization quality of ultra-fine particles. The fluidization behavior of agglomerates compared with that of individual particles is illustrated in their study. They considered different methods for comparing the fluidization behavior of different particles. They performed their experiments with the same static bed height of 145 mm (loosely poured) for all the particles. First of all, most of the tested materials show a hysteresis effect with increasing (fluidization loading) and then decreasing (fluidization unloading) the gas velocity.

Wang et al. [3] showed that with a gradual increase in the gas velocity, the goethite particles initially formed a plug with a high-pressure drop. This pressure drop was much greater than the weight of the particles. Then, the plug collapsed and the bed pressure suddenly dropped to a low value. By increasing the gas velocity, the pressure drop rose again suddenly to a higher pressure drop (similar to plugging part), and by starting the fluidization, the bed disrupted itself. With further increase in the gas velocity, the bed expands, while the pressure drop remains constant. The fluidization behavior of magnetic powders, amorphous silica and zeolite are similar to goethite.

For some materials, like titanium, the bed disruption occurred regionally and stepwise with an increase in the gas velocity, with a progressive increase in the pressure drop and slow expansion of the bed. Their observations showed that the fluidized particles form agglomerates. For amorphous silica, with increasing the gas velocity, particles initially make a channel and the bed pressure drop fluctuated, and the height of the bed increased increasingly. However, for fumed silica, with an increase in the gas velocity, particles channeled initially while the height of the bed remains almost constant, and the bed pressure drop decreased instantly from a high value to low value, then increased stepwise even after the bed disruption at a higher gas velocity.

For talcum and aerogel particles, with increasing gas velocity, they initially made a channel and their beds expanded suddenly at a small gas velocity. Then, they reached

homogeneous fluidization. For glass fiber particles, with increasing gas velocity, they initially made a channel at very small gas velocity and thereafter the bed pressure drop fluctuated notably. It should be noted that for goethite, talcum, zeolite and glass fiber particles, the loading and unloading curves for expansion of the bed and the bed pressure drop indicated hysteresis effect while those of amorphous silica particles did not. For nickel and limestone, channeling occurred at low gas velocities and pressure drop fluctuated as gas velocity further increased, while bed heights remained almost constant.

In summary, the process of fluidizing ultra-fine particles usually involves plugging, channeling, disrupting and agglomerating, and their combinations. Therefore, each property and characteristic of the particles or processing fluid is important and could play a notable role in the fluidization. Generally, ultra-fine particle beds could be disrupted abruptly at some characteristic gas velocity, called the disruptive velocity, $U_{disrupt}$. The disruptive velocity may apparently depend on the cohesive force between particles.

When an ultra-fine particle bed is fluidized, three main characteristics are obvious in the bed expansion of these particles:

(1) Drastic channeling. With increasing gas velocity, not only small channels were formed near the fluidizing column wall but also large channels were formed in the center of the bed. For fluidization of titanium powders, they first spouted, and then channels formed. Due to these phenomena, bed pressure drops were highly fluctuating and very unstable. Although the bed surface still remained unstable, only at high gas velocities (0.16 m/s) the bed could be disrupted.

(2) When the bed was abruptly disrupted, the bed surface rose suddenly. With further increase of the gas velocity, it followed by homogeneous bed expansion. For example, for aerogel particles, at a gas velocity of 0.04 m/s, the bed surface rose suddenly from 160 to 440 mm, but the bed pressure drop remained more or less constant, and the particles were fluidized smoothly.

(3) As soon as the ultra-fine particle bed fluidized, with increasing the gas velocity, the ratio of the bed expansion did not change much. For example, when the gas velocities changed from 0.02 to 0.22 m/s, the bed height of limestone particles only increased by 20 mm.

Wang et al. [3] also showed that in the bed collapsing processes for most ultra-fine particles which formed agglomerates while fluidized, the three-stage characteristics of collapsing of Geldart group A particles (the bubble escape, solids consolidation, and the hindered sedimentation stages) emerged. They noted that, when the laminated talcum

particles or the relatively coarse alumina particles were fluidized, neither large agglomerates nor plugs were formed. Very low bulk densities particles such as fumed silica and aerogel particles had very high expansion ratios, and no large bubbles were observed. For this kind of particle, channels were formed instead of plugs. By using circulating fluidized bed, goethite, magnetic powder, amorphous silica, and zeolite particles could have homogeneous fluidization, proving that fluid dynamic action could suppress the cohesion of these agglomerates.

For ultra-fine particles, the bed collapsing behavior was classified into two classes. In the first class such as titanium, nickel, and limestone particles, the expansion ratio was very small and the particles in the bed formed channels. The second class was related to particles with a considerable expansion ratio. For these particles, different sizes of agglomerates were formed and the three-stage characteristics of the bed collapsing similar to the Geldart group A particles were observed. For example, for zeolite particles, all three collapsing stages are short, but for goethite, alumina, fumed silica, amorphous silica, talcum, and aerogel particles, although the bubble escape and solids consolidation stages were short, the hindered sedimentation stage was long.

They also indicated that magnetic, aerogel, and zeolite powders had almost the same equilibrium size of formed agglomerates (200 μm), but their expansion ratios and the lengths of their hindered sedimentation stage were completely different [3]. It indicated that other significant factors were affecting the fluidization behavior and quality of the formed agglomerates. For ultra-fine particles with multi-size agglomerates or particles, if the fluidization behavior and fluidization quality are identical as narrow size distribution single Geldart group A particles, these two particulate systems can be considered equivalent in fluidization behavior.

Their experimental results also showed that during fluidization, particle agglomerates formed in the bed. Then, a fixed-bed region of large agglomerates established at the bottom of the bed, a fluidized region of smaller agglomerates in the middle and a dilute-phase region of even smaller agglomerates, including single, unassociated particles further up in the fluidized bed (see Fig. 3.13).

Their results for amorphous silica also showed that, at a gas velocity of 0.104 m/s, the agglomerate layer height first increased rapidly. Then, the height of this layer decreased by breaking large agglomerates into smaller ones and elutriating the smaller agglomerates out. With collecting and recycling the elutriated agglomerates into the bed, the average of the agglomerates size would decrease to around 2 - 3 mm. Continuing these processes (further fluidization, elutriation, collection, and recycling) for the second time reduced the size of agglomerates to even smaller sizes. With progressive fluidizing,

collecting, and recycling, the agglomerates' size finally became almost constant at 200-300 μm. This range of agglomerates size could be fluidized homogeneously. This procedure suggested that a circulating fluidized bed increases the fluidizability of fine particles through this process.

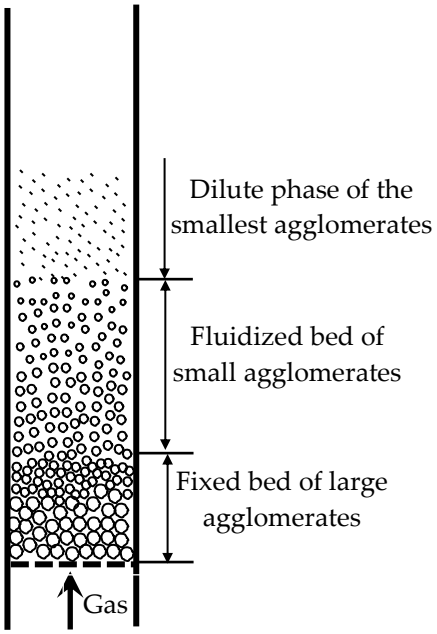

Fig. 3.13 Macro-structures of three regions of agglomerate in the ultra-fine powder fluidized bed [3].

For limestone and nickel particles, larger agglomerates around 3.0 mm were formed. These agglomerates were very friable. Therefore, after cutting the gas off, they easily fragmented under the weight of the bed to form a fixed bed of large agglomerates at the bottom of the bed. For flaky particles of talcum, at some gas velocities, some visible agglomerates sometimes formed, but due to collision and crushing by adjacent particles, they broke very fast. So, the sizes of these agglomerates could not be characterized. In addition, no dead region was established in their fluidized bed.

As the titanium particles agglomerated, winding channels were formed inside the bed. Forming these channels resulted in alternating fixed and fluidized regions and was accompanied by bubbling. For fumed silica and aerogel particles, with increasing gas velocity, channels formed initially. At the disruptive gas velocity, non-spherical and multi-sized agglomerates with a size of about one millimeter to tens of microns were formed. The size of the agglomerates decreased from the bottom to the top of the bed. The bed showed stable fluidization. For fumed silica particles, with increasing gas velocity, the bed continuously expanded, showed completely particulate fluidization.

After comparing the particle properties, characteristics of bed collapsing and fluidization behavior for different ultra-fine particles, the ultra-fine particles could be classified into four types according to their fluidization characteristics:

First type: Due to the considerable cohesive force normally available between ultra-fine particles and between their agglomerates, channeling and slugging took place during their fluidization. For this type of fluidization, there were two cases. In the first case, for particle size ranging from several microns to tens of microns and without enough cohesion to agglomerate, channels were directly formed from single fine particles, like quartz particles. In the second case, for particle size smaller than 1 μm and demonstrating strong cohesion between agglomerates, channels or plugs were formed by the agglomerates of fine particles, like titanium particles. Experiments showed that using external forces, such as tapping and vibration of the bed, the formed channels or plugs could be broken and stable fluidization could be obtained.

Second Type: Agglomerates such as were formed by fumed silica and aerogel are similar to Geldart group A particles when they were fluidized. The fluidization behaviors of these agglomerates were very similar to those of the Geldart group A particles. Generally, the size of the second type of particles was much less than 1 μm and belongs to nonmetallic oxide. They formed stable agglomerates rather than exist individually.

Third type: The agglomerates, such as were formed by nickel and limestone when fluidized, were large agglomerates similar to the size of Geldart group B or D particles. The fluidization behaviors of these large agglomerates were similar to those of the Geldart group B or D particles. These particles were smaller than 5 μm, and usually belong to metallic and ionic compounds; their formed natural agglomerate was generally not stable.

Fourth Type: With smaller agglomerates at the top of the fluidized bed and larger agglomerates at the bottom, some of them might even be de-fluidized, such as goethite, magnetic and amorphous silica powders. After repeating solids recirculation, the dissimilar sizes of these agglomerates could generally reach some steady and relatively uniform value. Therefore, it could lead to relatively homogeneous fluidization. The range of these particles was from several microns to tens of microns; they normally were oxides and their bulk densities were usually less than 0.8 g/cm^3. Generally, they formed stable natural agglomerates.

They finally concluded that the ultra-fine particles are seldom fluidizable as a single particle but only as agglomerates. If the minimum fluidization velocity of agglomerates is smaller than operating fluid velocity ($U_{mf,agg} < U_0$), these agglomerates can be

homogeneously fluidized [3]. Experiments show that the size of agglomerates is a function of single particle size, particle density, cohesive force, and dynamic factors.

3.1.8 Influence of the particle size distribution (PSD) on the fluidization regime

In 1999, Gauthier et al. [126] presented their results of an experimental study on the influence of the particle size distribution (PSD) on the fluidization regime. They showed that the particle size distribution (PSD) had an important influence on the hydrodynamics and related characteristics of gas-solid fluidized beds (e.g., mixing, conversion, etc.). In most cases, a narrow cut enhanced the bed stability thus facilitating its operation (decreasing the effect of de-fluidizing, segregation, and entrainment), although in some cases a wide PSD was found to be advantageous for fluidity and chemical conversion. However, the process of wide PSD powders is practically and economically interesting when working with mineral materials. In fact, because grinding and sievings are time- and energy-consuming processes, using a narrow PSD or classifying only a fraction of existing materials would be too expensive.

They used different river sands classified in Geldart group B and D. Five mean diameters were considered in this study are d_1=282.5 μm; d_2=450 μm; d_3=900 μm; d_4=1425 μm; d_5=1800 μm. Particles with the average diameter of d_1 and d_2 belong to Geldart's Group B, while the other three powders belong to Group D. In addition, four PSD cases were studied for each of mean diameter as a narrow cut (reference) powder, a Gaussian-distribution, a binary mixture, and a wide PSD powder. For each specific diameter, they considered:

1. A reference narrow-cut powder (R); it was a narrow cut between two standard sieves; the average between both sieve openings determined the mean diameter.

2. A Gaussian-distribution powder (G), prepared from five proportions of measured and adjusted powders that followed a centered bell shape. The peak of the bell was near the resulting mixture mean diameter. About 1/3 of the weight of material had a diameter equal to the average diameter of the powder. Each of both extreme-sized proportions was about 10% of the weight of the particulate material. In this way, the ratio of standard deviation over average diameter (σ/d_p) was always equal to 0.34.

3. A binary mixture (B), was prepared by mixing of two measured and adjusted sets of particles, each one had about 50% of the material weight.

4. A wide PSD powder (W), which was prepared from five to six measured and adjusted powders in almost equal proportions.

In each case, all mixtures have the same Sauter mean diameter. The Sauter diameter is calculated as:

$$d_p = 1 \Big/ \left(\sum_i x_i / d_i \right) \tag{3-17}$$

where x_i is the mass fraction of particles having the average diameter of d_i.

The Gaussian distribution powders were fluidized almost at the same incipient fluidization velocities as the narrow cut powders. Therefore, the minimum fluidization velocity of a Gaussian distribution powder could be calculated roughly by any relationship suitable for powders with a uniform size distribution. Contrariwise, wide PSD and binary mixtures had a completely different hydrodynamic behavior. However, their behavior was similar to each other. To describe the behavior of these mixtures, two characteristic velocities of the incipient and the complete fluidization velocities were required. The domains between the transition of incipient and complete fluidization were also investigated in their study for particles classified in Geldart groups B and D (Fig 3.14) [126].

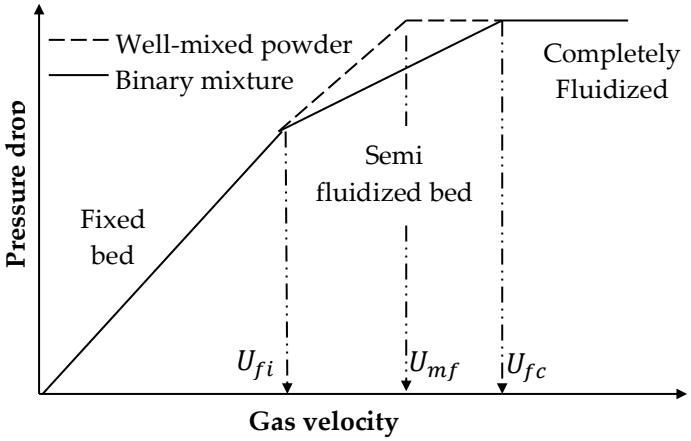

Fig. 3.14 The bed pressure drop versus gas velocity profile, for both homogeneous powders and mixtures (U_{fi} is the incipient fluidization velocity, U_{mf} is the minimum fluidization velocity, and U_{fc} is the complete fluidization velocity) [126].

Their experimental results showed that the behavior in this domain also depended to a great extent on the PSD: Binary and wide PSD mixtures were normally segregated, whereas Gaussian mixtures and narrow range reference powders were hardly segregated. They compared the experimental results for incipient fluidization and complete fluidization velocities with the minimum fluidization velocity (U_{mf}) considering several existing correlations for U_{mf} of binary mixtures. For average diameters smaller than 1.5 mm, most of them were correct, but for larger diameters, only one of them was satisfactory. Therefore, they proposed two correlations between Re and Ar to predict the

incipient and complete fluidization velocities. These correlations matched with their experimental results obtained in a wide range of average diameter.

$$\mathrm{Re}_{fi} = 2.2 \times 10^{-3}\mathrm{Ar}^{0.818} \text{ with } 0.78 < \mathrm{Re}_{fi} < 78 \text{ and } 1800 < \mathrm{Ar} < 5 \times 10^{5}$$
$$\mathrm{Re}_{fc} = 5.2 \times 10^{-3}\mathrm{Ar}^{0.777} \text{ with } 1.35 < \mathrm{Re}_{fc} < 113 \text{ and } 1800 < \mathrm{Ar} < 5 \times 10^{5} \quad (3\text{-}18)$$

where Re_{fi} and Re_{fc} were Reynolds numbers for incipient and complete fluidization, respectively. When the average diameter increased for binary powders, it was experimentally found that the complete fluidization velocity was decreased with respect to the minimum fluidization of large particles. This behavior could be explained by an increasing influence of interactions between the small and large particles when increasing the average diameters. For five considered binary powders cases, the results of calculations for the particle-particle (particle collisions) and gas-particle interactions showed clearly that as soon as the average diameter of the mixture was larger than 1 mm, the interparticle forces became significant.

3.1.9 Effects of adding different size particles on fluidization of cohesive particles

Zhou and Li [25] in 1999 studied the effects of adding different size particles on the fluidization of cohesive particles. The powders used in their experiments were different sizes of SiC. The fluidization behavior of SiC was evaluated by the expansion and collapse of the bed. The change of the intensity of cohesive stress (c) was not very great for SiC15 (d_p = 13.26 μm, packed density = 1235 kg/m^3, trapped density = 1765 kg/m^3, intensity of cohesive stress = 243.39 N/m^2) and SiC10 (d_p = 10.3 μm, packed density = 1099 kg/m^3, trapped density = 1622 kg/m^3, intensity of cohesive stress = 257.88 N/m^2). However, the intensity of cohesive stress increased significantly from SiC10 to SiC5 (d_p = 4.99 μm, packed density = 680 kg/m^3, trapped density = 1213 kg/m^3, intensity of cohesive stress = 770.34 N/m^2). The intensity of inter-particle cohesive shear stress was measured by using a shear cell, as:

$$\tau = \sigma \tan\varphi_i + c \quad (3\text{-}19)$$

where φ_i is the angle of internal friction, τ is the shear stress, σ is the normal stress, and c is the intensity of cohesive stress.

First, they studied on the fluidization behavior of single-component powders [25]. They reported that for SiC15 and SiC10, channeling was formed at gas velocities less than 0.005 m/s. Although the bed was in an expanded state, there was no actual fluidization (only partial fluidization in the channeling region). The elutriation was very little. However, for SiC5, the bed formed horizontal or sloping cracks at superficial gas velocities less than 0.0325 m/s. Cracks moved upward to the expanded section of a bed. Then, the cracks collapsed and the broken cracks fell to the bottom of the bed. Channels were detectable at

a velocity of 0.0325 m/s. When increasing the gas velocity, the fixed bed of larger agglomerates (de-fluidized region) was established at the bottom of the bed. However, smaller agglomerates were fluidized in the top of the bed. At a certain velocity, the de-fluidized region grew with time.

The formed agglomerates of SiC5 were loose and fragile. At the velocity of 0.45 m/s, the turbulent fluidization was observed all over the bed. The surface of the bed was not clear due to severe turbulence. The loss of particles due to elutriation was also very appreciable. The bed expansion of SiC15 and SiC10 was noticeable. It reached twice the initial bed height at a velocity of 0.039 m/s and 0.085 m/s, respectively. Contradictory, the bed expansion of SiC5 was relatively smaller than for the two other materials.

The graph of the bed pressure drop versus superficial gas velocity showed that the highest bed pressure drop was for SiC15, and the lowest one was related to SiC5. The bed collapsing curves showed that SiC15 and SiC10 had a great capability of holding gas, but that of SiC5 had a relatively insignificant capability. The diameters of SiC15 and SiC10 were greater than 10 μm. They could be completely fluidized at a superficial gas velocity far greater than the minimum fluidized velocity, which was in agreement with the experimental results of Chaouki et al. [99] and Morooka et al. [100]. However, for finer SiC5 particles, it was difficult to be fluidized by increasing superficial gas velocity. In fact, the elutriation loss increased with increasing the superficial gas velocity. Therefore, for fluidizing SiC5 cohesive particles, other methods (fluidization aids) should be considered.

In the work of Zhou and Li [25], the method of adding different particles was used to motivate the ultra-fine particles to fluidize. They added iron oxide yellow (α-FeO(OH), 0.6 μm) in SiC5 cohesive particles (11.1% of the total mixture weight). At the superficial gas velocity of 0.2 m/s, the mixture was initially fluidized. However, at the bottom of a bed, agglomerates formed with time resulting in a de-fluidized region. Increasing the amount of iron oxide yellow to 20% of the total weight of mixture resulted in the same experimental phenomena as mentioned above. Consequently, iron oxide yellow could improve the fluidization behavior of SiC5 particles, but it was not an ideal additive.

In the second case, they added white carbon (SiO_2, 4.6 μm) in SiC5 and the amounts of additive were 11.1%, 20%, and 27%, respectively. The experimental results showed that for the cases with additive amounts of 20% and 27%, the mixture could be fluidized at a superficial gas velocity of 0.33 m/s. However, in the bottom of the bed, agglomerates became visible with time. In addition, there was an elutriation loss by increasing the gas velocity. CLC catalyst (180–200 mesh) was the third additive that they added to improve the fluidization quality. CLC was a kind of FCC catalyst and was added to SiC5. The amounts of additive in the mixtures were 20%, 27% and 33% of weight percent. They

found that the mixture of SiC5 and 33% of CLC additive could be fluidized at a velocity of 0.33 m/s, but there were elutriation losses.

Then, they added an FCC catalyst of 180–200 mesh in SiC5. The amounts of additive in the mixtures were 16.67%, 23.08%, 33.33%, and 45% of weight percent, respectively. Their results showed a decrease in the required superficial gas velocity for fluidizing the mixtures of SiC5 and FCC. Moreover, with increasing the amount of additive, the elutriation loss decreased. However, when the weight percentage of additive was greater than 33.33%, the improvement in the fluidized behavior was not evident.

The fluidized behavior is significantly affected by the sizes of particles. By decreasing the size of particles, the required superficial gas velocity for fluidizing cohesive particles increases, the collapsing time decreases, and the elutriation loss increases. The reason is the increased inter-particle cohesion by decreasing the sizes of particles. They also showed that the intensity of cohesive stress of the mixtures of SiC5 and FCC decreased with increasing the amount of additive [25]. It proved that choosing the right additive could decrease the cohesive force. For a mixture of SiC5 and FCC, they found that the intensity of cohesive stress of binary mixtures could be calculated as the following law:

$$1/C_M = \sum_{i=1}^{2} x_i/c_i \tag{3-20}$$

3.2. Own Experimental results and discussion

3.2.1 Determination of the range of superficial gas velocity

The fluidization starts when the pressure drop across the bed is equal to the weight of the bed divided by its cross-section area (P_{wb}). Before fluidization, in the fixed primary condition, the bed pressure drop (ΔP_b) linearly increases when increasing the superficial gas velocity (U_{sg}). According to theory [12], when ΔP_b approaches P_{wb}, it begins to saturate, that is, there is no change in ΔP_b when increasing gas velocity. However, when inter-particle adhesive forces are dominant, actual practices [12] show that the pressure drop balances P_{wb} at a theoretical level of U_{mf}, but that inter-particle forces prevent the particle bed from fluidization albeit the gas velocity is increased above U_{mf}. Then, there is a peak in the bed pressure drop, which is observed due to the extra pressure required to overcome these forces. This behaviour can also happen due to a pre-compaction of the bed, or due to wall effects for a small bed diameter.

The U_{mf} is defined as the intersection point obtained by linearly extrapolating the fixed bed line (in ΔP_b vs. U_{sg} curve) and the fully fluidized state line. By considering the well-known Ergun equation [63] for the pressure drop of a gas stream across a packed bed and

assuming negligible cohesive force between particles, the pressure drop at U_{mf} should be equal to the weight per cross section area of the particle bed. By substituting this equation and after some simplifications, Wen and Yu [127] indicated that the Reynolds number at minimum fluidization condition (Re_{mf}) is given for a wide range of particle Reynolds numbers (0.001 < Re < 4000) as:

$$\mathrm{Re}_{\mathrm{mf}} = \sqrt{33.7^2 + 0.0408\mathrm{Ar}} - 33.7 \tag{3-21}$$

Then, U_{mf} can easily be given by

$$U_{mf} = \frac{\mathrm{Re}_{\mathrm{mf}} \cdot \vartheta_g}{d_p} \tag{3-22}$$

Grace [128] proposes 27.2 instead of 33.7 suggested by Wen and Yu (Equation (3-21)) to improve the results for fine particles. His equation is then

$$\mathrm{Re}_{\mathrm{mf}} = \sqrt{27.2^2 + 0.0408\mathrm{Ar}} - 27.2 \tag{3-23}$$

Another helpful empirical equation for calculating U_{mf} was proposed by Leva [129] as

$$U_{mf} = \frac{7.169 \times 10^{-4}\left(\rho_p - \rho_g\right)^{0.94} d_p^{1.82} g}{\rho_g^{0.06} \mu_g^{0.88}}, \quad \mathrm{Re}_{\mathrm{mf}} < 30 \tag{3-24}$$

where μ_g is the dynamic gas viscosity. Note that all these equations were obtained based on experimental observations for particles with d_p > 20 μm.

For smaller particles, by considering the van der Waals cohesive force between particles, Xu and Zhu [130] offered a new equation for Group C-particles as

$$\mathrm{Re}_{\mathrm{mf}}^2 + \frac{85.71\left(1 - \varepsilon_{mf}\right)}{\varphi_s}\mathrm{Re}_{\mathrm{mf}} = E_G + E_c \tag{3-25}$$

where ε_{mf} is the void fraction in minimum fluidization condition and φ_s is particle sphericity. In addition, E_G and E_c represent the gravitational and cohesive effects, respectively. Considering mechanical vibration as a fluidization aid, they offered the following equation for estimating ε_{mf} as

$$\varepsilon_{mf} = 0.77\left(d_p \times 10^6\right)^{-0.124} \tag{3-26}$$

In addition, E_G and E_c can be calculated as

$$E_G = 0.57\varphi_s \cdot \varepsilon_{mf}^3 \cdot \mathrm{Ar} \tag{3-27}$$

$$E_c = 4.79 \times 10^{-9} \frac{\varphi_s \cdot \varepsilon_{mf}^{0.52} \cdot \rho_g \cdot d_p}{L_0 \cdot \mu_g^2} \tag{3-28}$$

where L_0 is the settled bed height (initial bed height). When the initial bed height is not measured, it can be estimated by

$$L_0 = \frac{m_s}{A(1-\varepsilon_{mf})\rho_p} \tag{3-29}$$

where A is the bed cross-section area and m_s is the total mass of the particle bed.

Using Equations (3-21), (3-23) and (3-24) for fine particles, the minimum fluidization velocities are calculated as 0.128, 0.159 and 0.157 cm/s, respectively. Using Equation (3-25), U_{mf} is predicted as 0.01185 cm/s for ultra-fine particles. However, since the ε_{mf} in Equation (3-28) is obtained by considering mechanical vibration—a feature that is not used in the present study, the value of U_{mf} calculated with Equation (3-25) is expected to be much smaller than the real U_{mf} for a bed consisting of ultra-fine powders without any fluidization aid.

It should be noted here that any meaningful quantification of U_{mf} is practically impossible for ultra-fine cohesive powders (as already clear from previous studies [2,3]). In fact, due to the formation, destruction, and re-formation of cracks and channels, measurements of the bed pressure drop for ultra-fine cohesive powders are non-reproducible, showing highly unsteady features. The bed structure of this kind of material can become suddenly disrupted at some characteristic velocity. After disruption, a superficial gas velocity that matches the maximum bed pressure drop is observed. Hereafter, the corresponding velocity is called after-disruption velocity, U_{ad}. The point where the process reaches the after-disruption condition is also called the peak point, since it corresponds with the maximum of ΔP_b. In Reference [3], the use of this velocity U_{ad} instead of U_{mf} is suggested for comparison between different fluidization processes.

When increasing the superficial gas velocity, it is expected that the smaller particles start to elutriate before the coarse particles. At the same time, at higher superficial gas velocity, it is expected that notable aggregation occurs between ultra-fine cohesive powders. The ratio of the effective size of these agglomerates to the size of the single particles increases with the decreasing size of the single particles. The density and the effective mean size of the formed clusters (agglomerates) are such that U_{mf} for the mixture will be far higher than U_{mf} for a single particle class. This explains why a bed of ultra-fine particles remains unfluidized at gas velocities that are several times the U_{mf} corresponding to the mean diameter of the individual particle. Turki and Fatah [131] reported that, for nanoparticles, this can be up to 3×10^6 times the gas velocity for fluidizing the single particles. The measurements of the portion of elutriated particles from the bed in this study show that the range of the minimum fluidization velocity ratio for ultra-fine (micron size) powders is not so large.

The measured superficial gas velocities for starting partial fluidization combined with the measurement of particle size distribution and weight of material remaining in the column after fluidization, show that the loss of particles due to elutriation and their exit from the fluidization column is negligible even up to about 1200 times the calculated U_{mf} of single particles. This is due to the formation of agglomerates at higher velocities and dominant cohesive forces. Nevertheless, by increasing superficial gas velocity to achieve ultra-fine fluidization, the elutriation losses generally increase. Considering all these issues together, the velocity range for all fluidizations lies between 0–15 cm/s. The superficial gas velocity is increased from zero to the maximum velocity in 35 equal steps for all the fluidization loading processes and is decreased in 18 steps for all unloading processes.

3.2.2 Fluidization of fine and ultra-fine particles separately

The experimental tests start with the results of fluidization tests for fine and ultra-fine particles separately, before investigating the effect of the presence of some specified percentage of ultra-fine powders on fluidization of a fine-particle bed. Figures 3.15 and 3.16 show the fluidization curve, that is, the variation of bed pressure drop (ΔP_b) when increasing superficial gas velocity (U_{sg}), for two independent fluidization tests for CALCIT MVT 100 (fine material) and CALCIT MX 10 (ultra-fine material), respectively. For each superficial gas velocity, ample time (up to 5 min) is considered to ensure that the bed pressure drops have reached stable values before recording is started. In fact, for fine particles, steady-state conditions are really obtained. However, for ultra-fine powder, the fluctuations in the bed pressure drop can remain relatively high. Here, the pressure drops presented in this work are the mean value, averaged over the last minute of the recording for each superficial gas velocity (it means, if the ample time is 5 min for each record, the averaging has been done during the fifth minute, not for whole five minutes).

3.2.2.1. Fine particle bed fluidization

a. Loading: The fine (Group A) particles fluidization at U_{mf} shows an almost homogeneous non-bubbling fluidization followed by bubbling fluidization as gas velocity increases. Before U_{mf}, in the fixed bed state, the pressure drop increases linearly when increasing the superficial gas velocity. According to Ergun's equation [63], the gas pressure drop during the passage of a fluid through a porous medium (fixed bed) is calculated as

$$\frac{\Delta P_b}{L_0} = 150\frac{\mu_g U_{sg}(1-\varepsilon)^2}{d_p^2\varepsilon^3} + 1.75\frac{\rho_f U_{sg}^2(1-\varepsilon)}{d_p\varepsilon^3} \tag{3-30}$$

In the fixed bed zone, the superficial gas velocities are very low. Therefore, the first term on the right side of the Ergun Equation (viscous term), which corresponds to the Blake-Kozeny equation for laminar flow is much larger than the second term (kinetic term), which corresponds to the Burke-Plummer equation for turbulent flow. Consequently, the

variation of bed pressure drop with gas velocity is almost linear. The fluidization curve smoothly saturates at the fully fluidized state (Fig. 3.15). This is because the fine material used in this study has a wide particle size distribution (PSD), from 1 μm to about 200 μm (Fig. 2.10). The wide size distribution of particles has different effects on the fluidization behavior, such as smaller void sizes [132], a greater air retention capacity [133], enhanced fluidity, increased segregation and partial mixing [126].

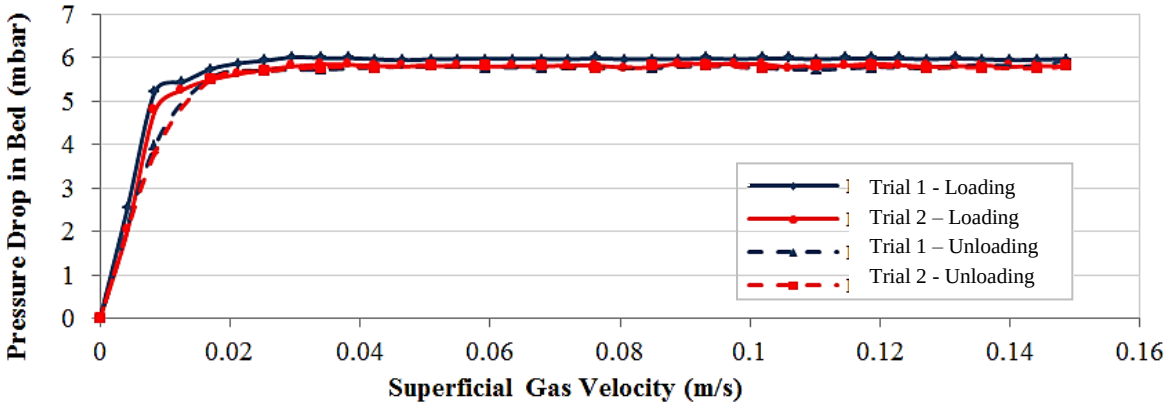

Fig. 3.15 Two independent fluidization tests - Loading (—) and Unloading (– –) of fine powder bed (CALCIT MVT-100).

A wide PSD also reduces the bubble size in bubbling fluidization mode [134]. Fluidization starts as an increase in bed height. The expansion of the bed before starting bubble formation is a result of the nucleation of micro-cavities in the bed. The size range of these cavities is between one and ten particle diameters. For this condition (bubble-free), by increasing the gas velocity, the number of cavities does not change, but their size starts to increase [4]. The cohesive force between particles fixes the cavities' walls and the disconnection of weakly-bonded particles is the reason for developing cavity growth. After that, when increasing gas velocity, bubbling occurs. It should be recalled here that the Archimedes number for the used fine material is about 5.315 and the bed height to diameter ratio is $L_0/D_b < 1$. Thus, when increasing gas velocity, only bubbling happens and there is no slugging behavior [135]. However, the dissipation of energy during the bubbling condition is very low and it does not lead to important changes in the bed pressure drop. Therefore, after starting fluidization, the pressure drop is almost constant.

b. Unloading: Figure 3.15 also shows that the fluidization loading and unloading curves follow one another closely; only a slight hysteresis effect is evident. In fact, for this kind of material, weak cohesive forces between particles result in decreasing extra-energy for overcoming such forces in fluidization loading. Small hysteresis effects in this material are due to collisions between particles, some irreversible deformations [136] and limited segregation effects [137].

3.2.2.2. Ultra-fine powder bed fluidization

a. Loading: For the fluidization of ultra-fine cohesive powder, it is clear from Fig. 3.16, that there are strong fluctuations in the bed pressure drop when looking at the loading curves. This figure shows two independent fluidization tests for the same ultra-fine powder. For a fixed bed condition, by increasing the gas velocity, the pressure drop also increases. However, there is not any change in the bed height. Again, a linear trend is observed between the rising bed pressure drops and increasing gas velocity. Focusing on the first trial fluidization curve (dark blue), the general behavior of the loading curve of ultra-fine cohesive powders can be discussed qualitatively. As a complementary source of information, Fig. 3.17 also shows pictures corresponding to three different behaviors of ultra-fine particle fluidization during the first fluidization test as shown in Fig. 3.16.

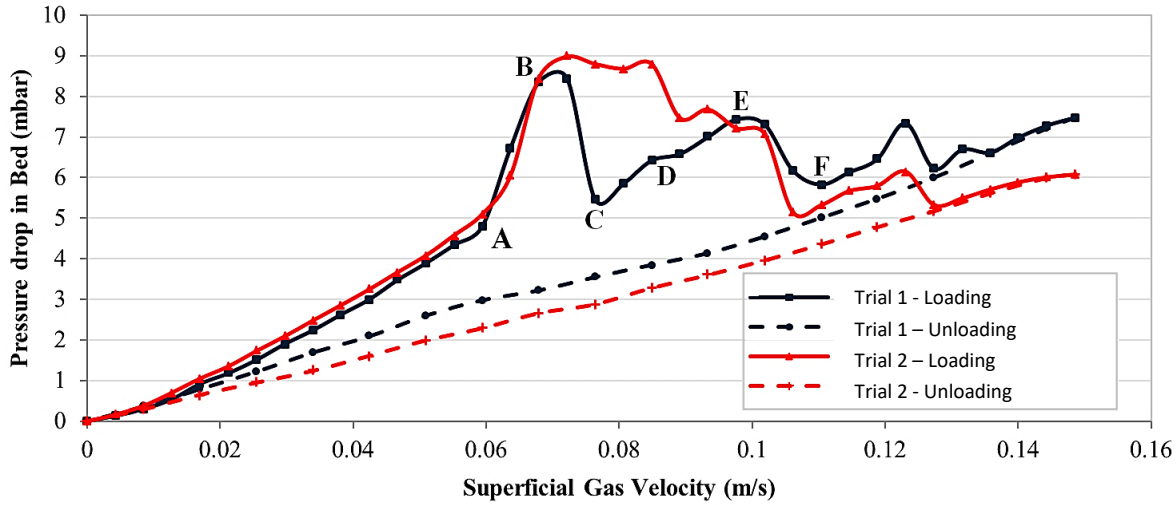

Fig. 3.16 Two independent fluidization tests - Loading (—) and Unloading (– –) of ultra-fine powder bed (CALCIT MX-10).

By increasing the gas velocity, some horizontal or sloping cracks first begin to form. At point A, the formed cracks have been broken down and, due to this phenomenon, the slope of the changes in the bed pressure drop increases when increasing the superficial gas velocity. This behavior continues up to point B. At this point, at which enough kinetic energy becomes available in the gas, the available voids between cohesive powders and their adjacent cracks connect and build vertical channels. This leads to a finite expansion of the bed, but without the formation of a real bubble. Then, some small bubbles (unlike the bubbling behavior seen in fluidization of Group A-particles) form.

Due to the motions of these small bubbles, the cracks formed near the wall disappear. The moving bubbles re-shape the cracks until they take the form of vertical channels. After starting of channeling, the pressure drop decreases suddenly to point C. In fact, because of channels, the gas stream now has a shortcut to pass the powder bed and needs a lower pressure drop to cross the porous medium.

Increasing the superficial gas velocity further, the available gas in the cracks and adjoining voids escape the bed and the cracks break and fall down. The ratio at which the available gas in micro-voids can leave a vertical channel will control the rate of collapse [2]. After the channels collapse, the pressure drop again increases. The collapsed bed forms a network of adhered powders and a large horizontal crack is formed near the bottom of the bed. When further increasing the gas velocity, due to retention of air under the upper part of the powder bed, this upper part starts to rise in the column as a slug flow, as long as the flow rate of the air entering into this gap is higher than the flow of air passing through the upper part of the powder bed. The formation of some small channels in the upraised part of the bed after point D is the reason of increasing pressure drop with a different slope (lower) up to point E. Increasing further the gas velocity, a large channel is activated, causing the collapse of the raised part of the bed at point F. Finally, the fluidization continues in the channeling regime.

This first trial fluidization curve (the dark blue one) reveals all essential features of fluidization for Geldart's Group C-powders. However, as revealed by a second independent test (red curve), not all features will be systematically observed. For the second fluidization test, the fluctuations in the pressure drop are due to activation and collapse of cracks or channels, but the rising bed, as seen in the previous test between points C and E, was not observed. Figure 3.17 shows three photos taken during the first test and illustrating the key features of ultra-fine fluidization at the macro-scale.

Figure 3.17 shows that there are a lot of random phenomena during fluidization of ultra-fine particles, such as formation and disruption of cracks and channels, agglomeration, slug flow, spouting behavior of channels, the sticking of powder to the column walls, and movements of active channels, fluidized and de-fluidized zones when increasing or decreasing the superficial gas velocity. All these features are a direct function of the exact initial conditions of the bed before starting fluidization; though the bed properties are statistically identical for all tests, the exact local distribution of the particles at an initial time varies from realization to realization and also depends on the previous state of the bed (the condition of the bed for each level of gas velocity) during fluidization loading and unloading (history effect). Thus, the behavior of ultra-fine fluidization is different for each independent test even when using the same material, as shown in Fig. 3.16.

b. Unloading: The unloading curves of ultra-fine powder fluidization show a substantially different (almost linear) behavior compared to the loading curves (Fig. 3.16). The pressure drop measurements during unloading lie entirely below the loading. Based on Darcy's law, the total volumetric flow rate of the fluid passing through a porous medium formed by particles, $\dot{V}$, can be represented using the height and cross-section area of the powder bed as:

$$\dot{V} = k \cdot A \cdot HG, \qquad HG = \Delta h_w / \Delta h_b \tag{3-31}$$

where HG is the hydraulic gradient, Δh_w (m) is the pressure drop across the bed, Δh_b (m) is the height of the bed, A is the total cross-sectional area of the bed and k is a constant depending on the physical properties of the particle bed and fluid (permeability). Then, the mean velocity of the fluid (U_{sg}) is defined as:

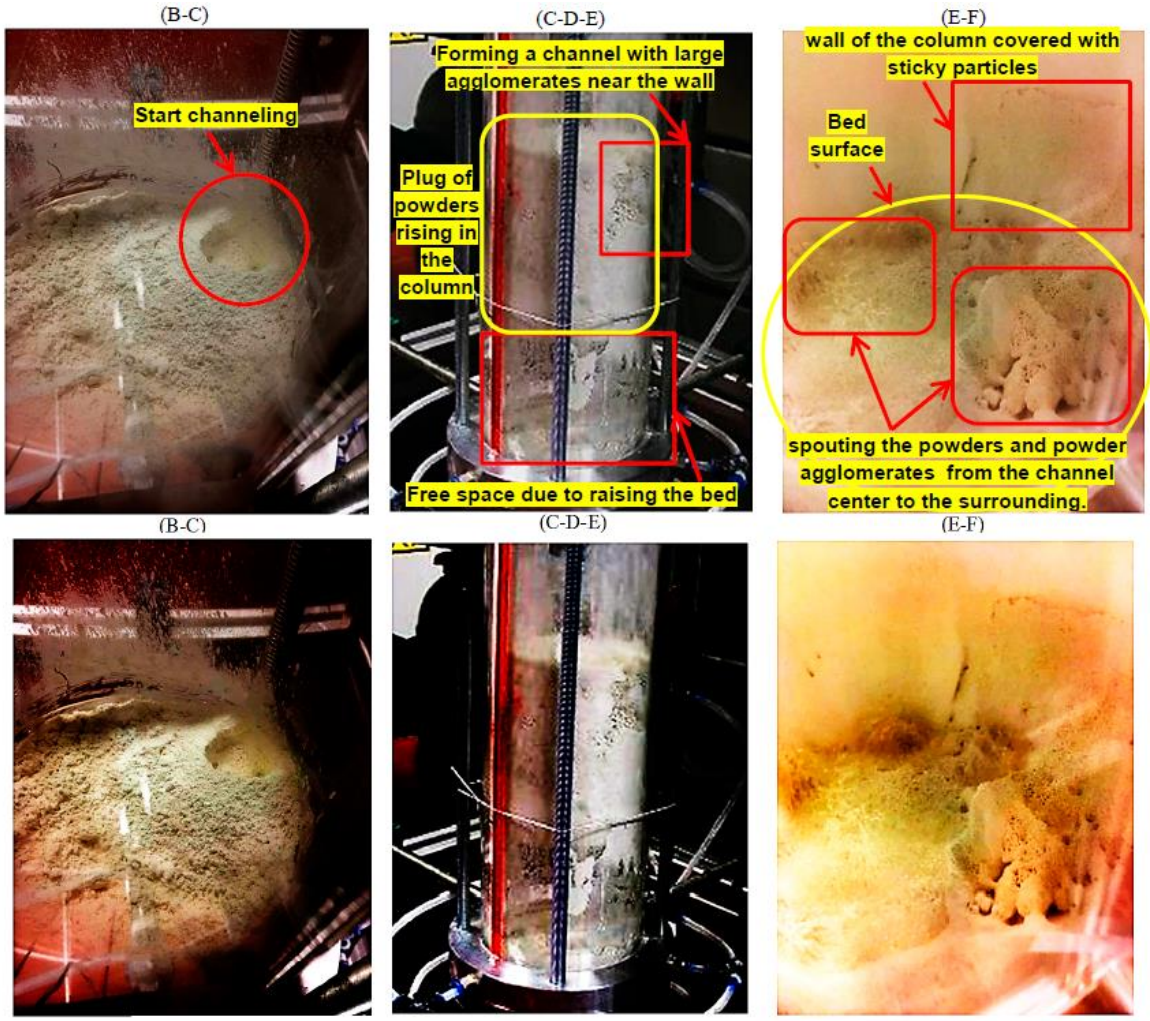

Fig. 3.17. Three different behaviors of ultra-fine particle fluidization during the first test shown in Fig. 3.16: First row: (B-C) start channeling and decrease of bed pressure drop; (C-D-E) rising of the upper part of the bed as a plug-in the fluidization columns, accompanied by competition between formation and destruction of some small channels in the raised bed; (E-F) top view of bed surface showing the wall of the column covered with sticky particles and some large channels after the collapse of the raised bed, spouting the powders and powder agglomerates from the channel center to the surrounding—Second row: High-contrast pictures for better observations.

$$\dot{V}/A = U_{sg} = k \cdot \Delta h_w / \Delta h_b \quad \Longrightarrow \quad k \propto U_{sg} / \Delta h_w \quad and \quad \Delta P_b = \rho_f g \Delta h_w \tag{3-32}$$

where ΔP_b is the bed pressure drop.
Considering that the slope of the ΔP_b-U_{sg} graph is inversely proportional to permeability, k (refer to Equation (3-32)), the linear behavior of the unloading curve shows a constant permeability in the powder bed during unloading. It means that for ultra-fine material, although permeability of the bed during loading changes several times due to competing phenomena taking place at this stage (as discussed before), the unloading process is much simpler and permeability is almost constant (Fig. 3.16).

On the other side, the permeability of the fine particle bed increases in the loading process with almost the same rate as it decreases during the unloading process, as mentioned in connection with Fig. 3.15. It is worth noting that for the ultra-fine material, observations never show a fully fluidized bed; a partially-fluidized bed is systematically seen, involving cracking, channeling, plugging (slugging), collapsing and agglomeration of the powders. Similar observations are also reported by Wang et al. [3]. This shows that the fluidization behavior of the ultra-fine material is not stable and is very sensitive to the initial conditions and history of the bed before starting (initial arrangement of particles) and during fluidization tests. Therefore, a considerable effort has been spent to ensure identical initial conditions (in a statistical sense) for all fluidization tests.

3.2.2.3. Using agglomeration number to evaluate the fluidization behavior of cohesive particles

One criterion for describing the fluidization behavior of cohesive powders involves the interaction of formed agglomerates with peripheral adhered powders. When the size of particles is reduced down to the micrometer range, particles try to build agglomerates to reduce their surface energy. Zhou and Li [25] defined the particle agglomeration number (Ae) as a criterion that indicates whether particles fluidize or not:

$$\mathrm{Ae} = F/\mathrm{Re} = \frac{c \cdot \mu_g}{U_{sg} \cdot \rho_g \cdot \rho_{ag} \cdot d_p^2 \cdot g} \tag{3-33}$$

where F comes from the ratio of F_c/F_g. F_c is the cohesive force between agglomerates and their peripheral adhered powders and F_g is the gravity of the peripheral adhered spherical powders. In addition, Zhou and Li [25] estimated the density of the agglomerates (ρ_{ag}) as 1.15 times that of the packed bed density; they concluded that the cohesive particles can be fully fluidized if Ae ≤ 40,000. Using the particle properties in this study, Ae is much larger than 40,000 for the ultra-fine material in the range of gas velocities considered here (0–15 cm/s).

The critical value of 40,000 would be obtained for a huge gas velocity of 2700 cm/s, at which all particles (agglomerates) would be pneumatically transported out of the fluidization column. Thus, increasing the gas velocity to such a high value is impossible. The fact that the criterion of Zhou and Li [25] is not valid here shows that the ultra-fine

material is a very cohesive powder and never reaches full fluidization. Therefore, if the fluidization of such ultra-fine materials is necessary for an industrial process, some kind of fluidization aids, as discussed in the introduction section, is required to reduce the agglomeration number. For our fine particles, Ae is smaller than 40,000, even at low gas velocities, explaining the easy and full fluidization of fine particles in the experiments.

3.2.3. Fluidization of binary mixtures, as a combination of fine and ultra-fine particles

The first point of investigating the binary mixtures is to find the suitable weight percentages of ultra-fine materials in the mixtures. For this purpose, a series of initial tests were carried out with increasing the proportion of ultra-fine particles in the mixtures by 5% in each step and checking the fluidization behavior. These experiments showed that increasing the portion of ultra-fine particles to more than 20% by mass results in partial fluidization (cracking, channeling or slug flow). For all blends containing more than 20% of ultra-fine particles, the mixture could not be fluidized completely. For a mixture with 20% of ultra-fine powders, the full fluidization happens first at high gas velocities, leading to elutriation loss. Below 20% of ultra-fines, the behavior of the mixture changes due to the presence of ultra-fine material. However, reaching fluidization is still possible by increasing the gas velocity; a higher percentage of ultra-fine powders requires a higher superficial gas velocity for fluidization.

These observations can also be explained by looking again at the particle agglomeration number, Ae. For a mixture of two material (binary mixture), Ae can be calculated by [25]:

$$\mathrm{Ae} = \frac{c_M \cdot \mu_g}{U_{sg} \cdot \rho_f \cdot \rho_{ag} \cdot d_{st,M}^2 \cdot g} \tag{3-34}$$

where c_M is the intensity of cohesiveness for the binary mixture (as measured in the shear cell for each mixture) and $d_{st,M}$ is the Sauter mean value of particle diameters in the mixture, which is given by

$$1/d_{st,M} = \sum_{j=1}^{2} w_j/d_{p_j} \tag{3-35}$$

where d_{p_j} is the mean particle size and w_j is the weight fraction of the sample particle j in the mixture.

The values of Ae according to equation (3-34) reveal that a mixture containing 20% of ultra-fines is expected to be fluidized for superficial gas velocities higher than 39.5 cm/s (i.e., this gas velocity corresponds to Ae < 40,000 [25]).

Therefore, in this study, only portions (mass-weighted ratio) of ultra-fine particles above the critical value (20%) are considered in what follows. Finally, three percentages of ultra-fine powders (30%, 50% and 68% of the total weight of the mixture) in the mixtures will be employed. Following [25], for the lowest percentage of ultra-fine powders (30%), the velocity where Ae < 40,000 would be 115 cm/s, which is already much larger than the acceptable velocity for avoiding elutriation loss.

Table 3.1 shows the properties of all mixtures used in the experiments. The values of ρ_b, c_M and ff_c are measured by the same shear cell test device used for the measurements in Table 2.10. The parameter d_M is calculated according to equation (3-35). Considering the relative density of solid and gas as well as the value of d_M, all mixtures belong to the very cohesive Geldart Group C. However, increasing the ultra-fines in the mixture decreases flowability and increases the intensity of cohesiveness. For a higher percentage of ultra-fines, saturation is observed: c_M for compositions containing 50% and 68% of ultra-fine particles is only 6% and 2% smaller than pure ultra-fine powder, respectively. Figure 3.18 shows the increase in c_M when increasing the ultra-fine powders in the binary mixtures.

Table 3.1 Properties of the powder mixtures used in this study.

Powder Combination (% Fine–% Ultra-Fine)	$d_{st,M} \times 10^6$ (m)	ρ_b (kg/m^3)	ρ_p (kg/m^3)	c_M (N/m^2)	ff_c
70–30	5.67	1149	2700	572	1.9
50–50	3.51	1053	2700	862	1.40
32–68	2.62	926	2700	903	1.35

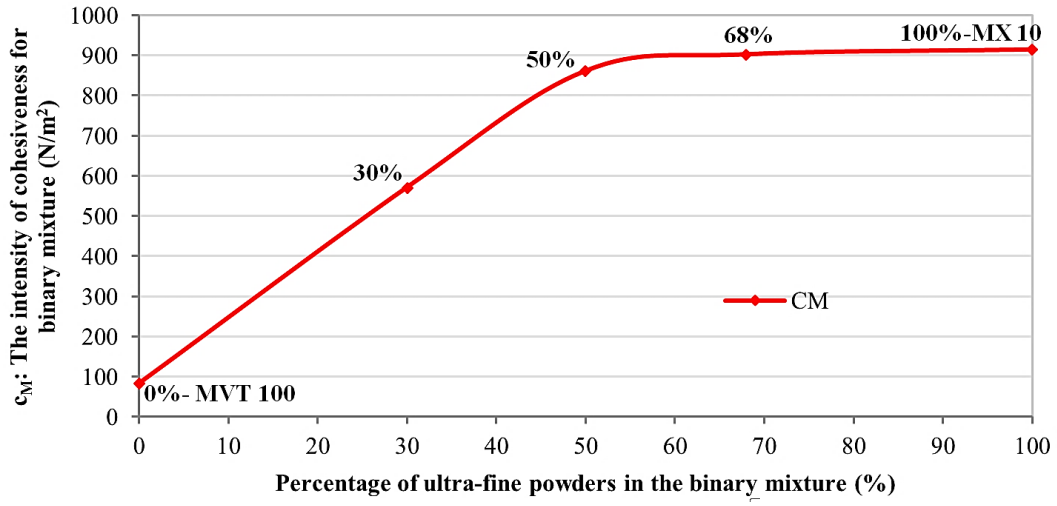

Fig. 3.18 Change in the intensity of cohesiveness for a binary mixture when increasing the percentage of ultra-fine powders.

This graph includes pure fine and ultra-fine particles as two mixtures containing 0 and 100% of ultra-fine powder, respectively.

In addition, Fig. 3.19 shows the cumulative distribution function and probability density function of the particle size for a binary mixture of 50% ultra-fine and 50% fine particles, illustrating the typical distribution of particle size in such binary mixtures. Figures 3.20–3.22 show two independent repetitions of the fluidization tests (ΔP_b-U_{sg} graphs) for the three different mixtures of fine and ultra-fine particles, with weight percentage combination (fine%–ultra-fine%) of 70%–30%, 50%–50% and 32%–68%, respectively.

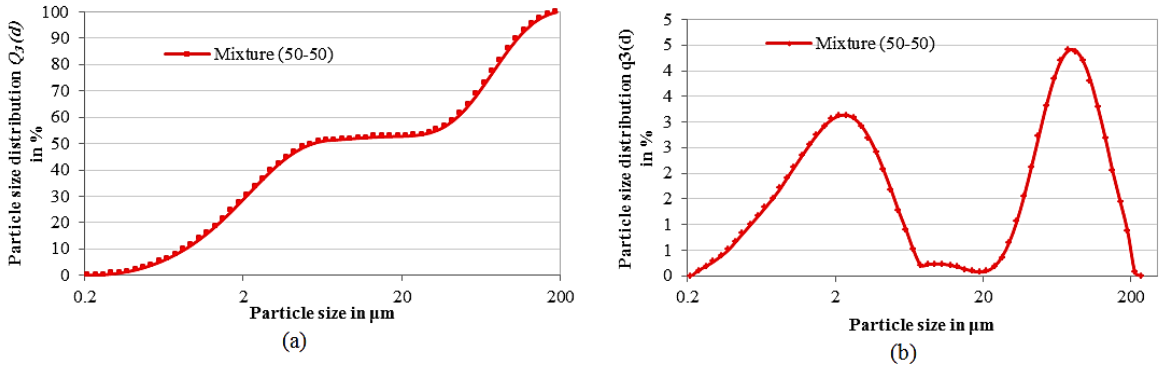

Fig. 3.19 (a) Cumulative distribution function (b) Probability density function of the particle size for a binary mixture of 50% of ultra-fine + 50% of fine particles (laser Mastersizer 2000).

These figures show that the fluidization curves of loading and unloading are qualitatively similar to the fluidization curve for ultra-fine cohesive powders discussed previously; strong fluctuations in bed pressure drop are observed during loading, with an almost linear behavior during the unloading stage. These figures show that the presence of ultra-fine cohesive powders can change entirely the fluidization behavior of the fine particle bed. It is again clear that the fluidization tests for all these mixtures are not reproducible. Changes between two different repetitions of fluidization tests with the same material (as observed in Figures 3.20–3.22) are due to differences in the initial conditions, to the history of the particles regarding applied forces and to the stochastic formation and collapsing of cracks and channels. These factors will change the fluidization curve in each test repetition (history-dependent).

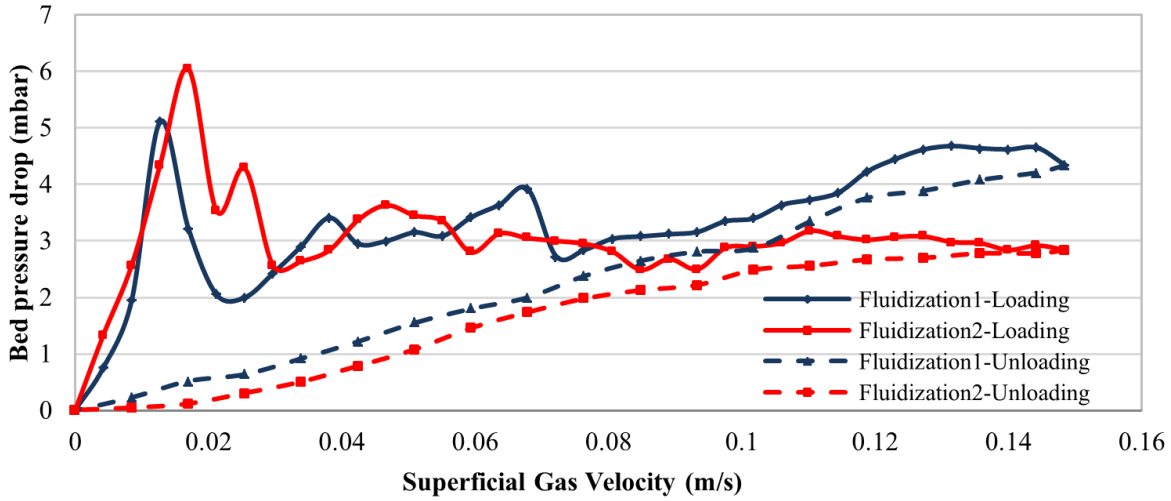

Fig. 3.20 Two independent fluidization tests—loading (—) and unloading (– –) of mixed material—(30% of ultra-fine + 70% of fine particles).

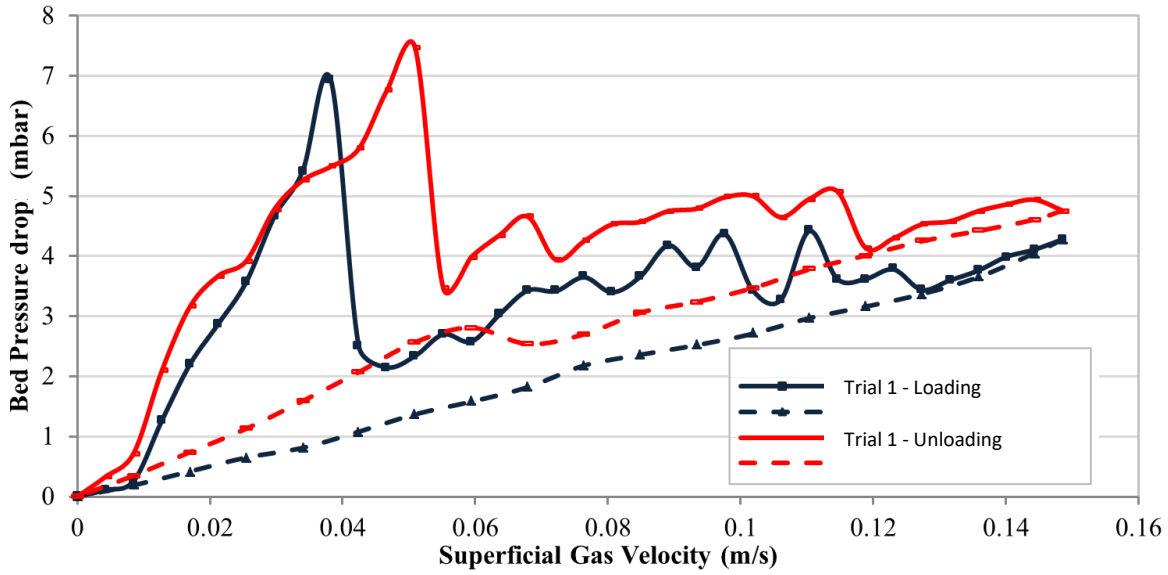

Fig. 3.21 Two independent fluidization tests—loading (—) and unloading (– –) of mixed material—(50% of ultra-fine + 50% of fine particles).

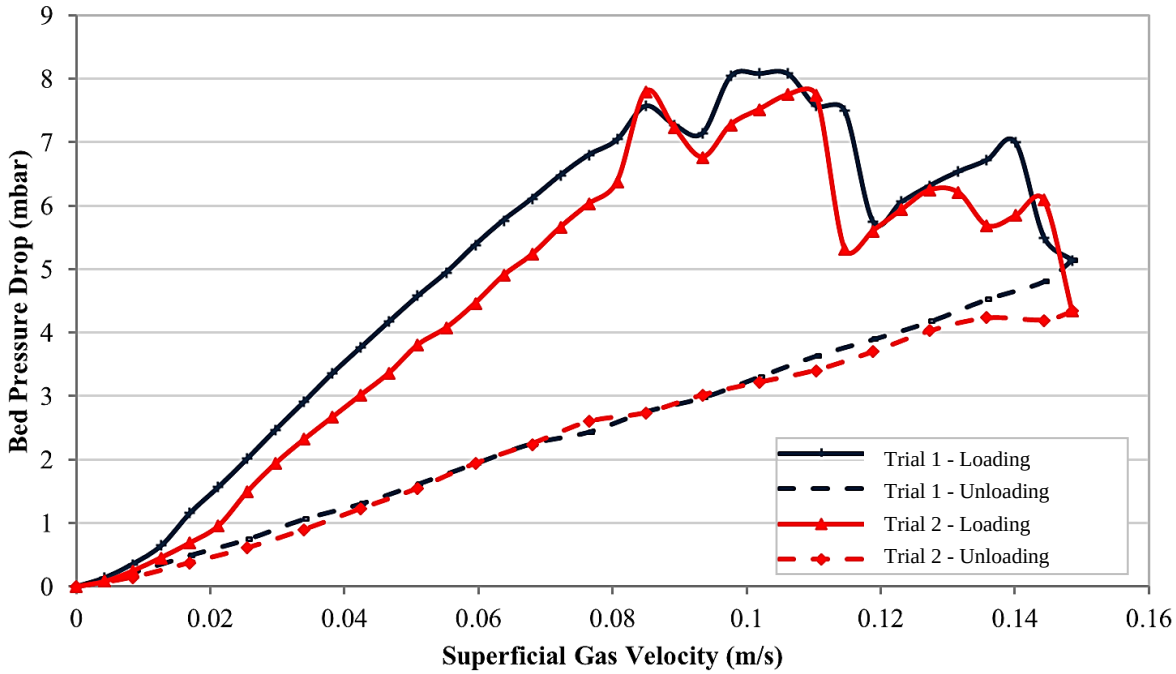

Fig. 3.22 Two independent fluidization tests—loading (—) and unloading (– –) of mixed material—(68% of ultra-fine + 32% of fine particles).

3.2.4 Using the mean value of bed pressure drop as a criterion for comparing non-reproducible fluidization processes

In this study, several independent fluidization tests were performed for the three combinations of fine and ultra-fine particles. Considering that each test takes about eight working hours (including discharging the previous material, cleaning, preparation, charging the new material, loading to fluidization and unloading), the number of tests for each mixture was restricted by time: ten tests have been carried out for each combination of materials. Given that $\Delta P_b(U_{sg})$ is different for each repetition of the measurements, the mean value of bed pressure drop at each superficial gas velocity for all repetitions of the same process will be used for further discussion.

For a better understanding of the averaging process, figures 3.23 and 3.24 show the mean values (symbols) and the standard deviations (indicated graphically by vertical error bars, although they are not errors) of the measured bed pressure drop of fine and ultra-fine materials for each gas velocity and all repetitions, respectively. It is clear, that the fluidization of fine particles (Fig. 3.23) is stable, with a negligible effect of initial conditions; the only noticeable variation appears at the fluidization point but is still very small.

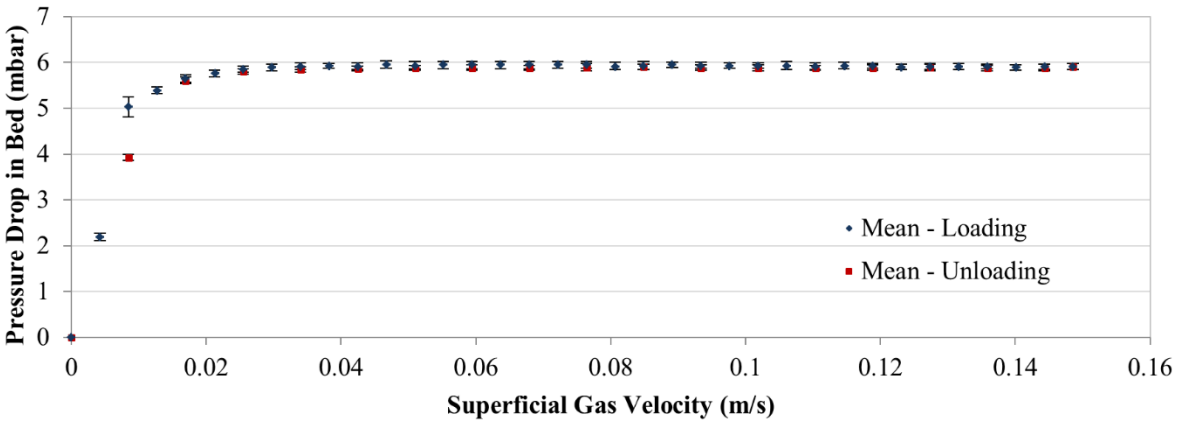

Fig. 3.23 Mean value (symbols) and standard deviation (vertical bars) of $\Delta P_b(U_{sg})$ when repeating fluidization tests for fluidization loading and unloading of fine particle bed (CALCIT MVT-100).

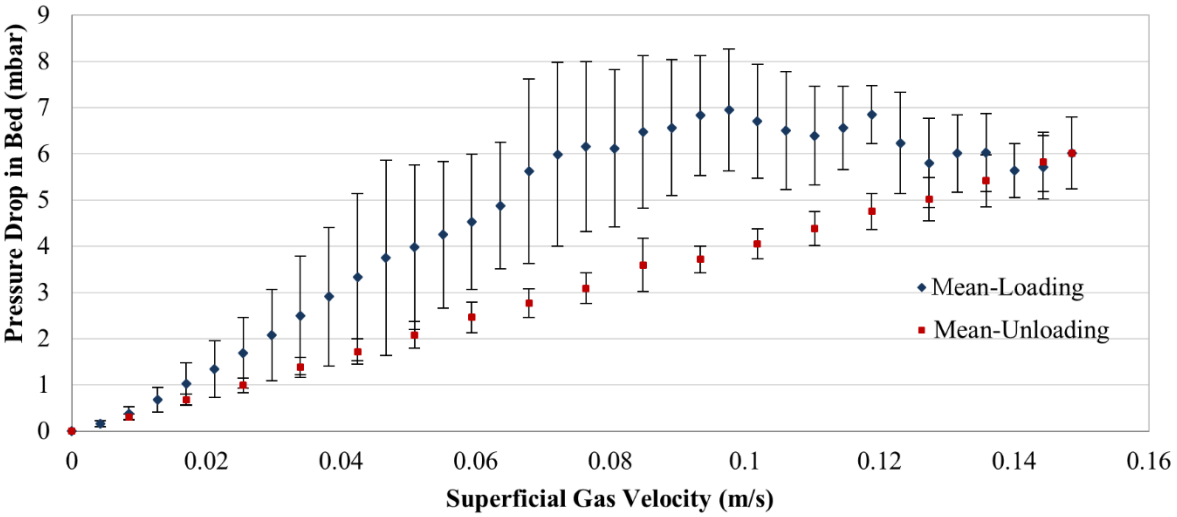

Fig. 3.24 Mean value (symbols) and standard deviation (vertical bars) of $\Delta P_b(U_{sg})$ when repeating fluidization tests for fluidization loading and unloading of ultra-fine powder bed (CALCIT MX-10).

On the other hand, although all experiments correspond to the same initial conditions in a statistical sense, as discussed previously, for ultra-fine powders (Fig. 3.24), very large variations in the bed pressure drop are observed for most superficial gas velocities.

Using the mean value of ΔP_b, it becomes possible to check and compare the overall fluidization behavior for each mixture. For this reason, for each superficial gas velocity, only the mean value of the bed pressure drops calculated from the experimental results of all repetitions will be presented and discussed in what follows. Again, the investigation starts with the mean value of the experimental results for the fluidization of fine and ultra-fine cohesive materials (Figures 3.25 and 3.26), separately.

In the case of fine particles (Fig. 3.25), the process is stable, as discussed previously. Only negligible fluctuations are observed concerning ΔP_b and the system shows a fully fluidized bed behavior.

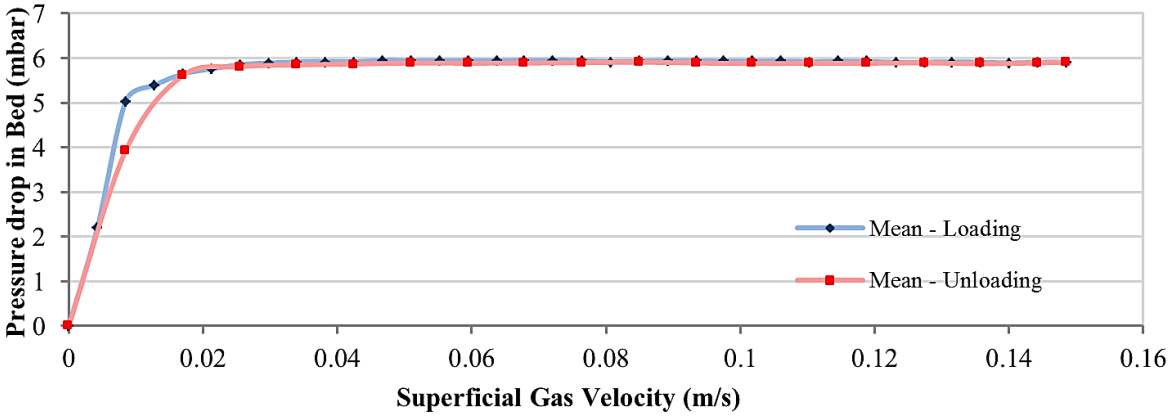

Fig. 3.25 Mean value of $\Delta P_b(U_{sg})$ when repeating fluidization tests for fluidization loading and unloading of fine particle bed (CALCIT MVT-100).

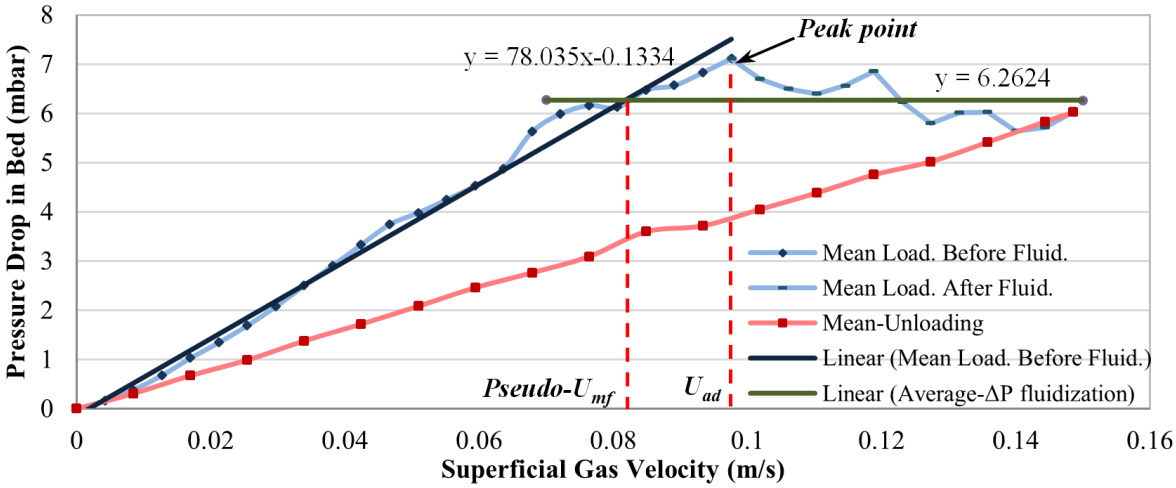

Fig. 3.26 Mean value of $\Delta P_b(U_{sg})$ when repeating fluidization tests for fluidization loading and unloading of ultra-fine powder bed (CALCIT MX-10).

On the other hand, the results of Fig. 3.26 show that the fluidization of ultra-fine particles is not a fully fluidized behavior and that considerable pressure drop fluctuations occur during the loading stage. According to the previous definition, the superficial gas velocity corresponding to the peak point is called the after-disruption velocity (U_{ad}). Figure 3.26 indicates that for ultra-fine material, U_{ad} = 9.76 cm/s and the peak of bed pressure drop is 7.11 mbar.

An accurate definition of U_{mf} is impossible here, since the fluidization tests are not reproducible. However, using the mean value curve, a pseudo-U_{mf} can be extracted from Fig. 3.26, based on the intersection of the extrapolated line of fixed bed condition and the

mean-value line of the fluctuations of the bed pressure drop in the partial fluidization condition. This method leads to a pseudo-U_{mf} of 8.19 cm/s for this case.

The previous conditions correspond to the two extremum conditions of only fine or only ultra-fine particles. For different combinations of the primary materials, Figures 3.27–3.29 depict the behavior of the mean bed pressure drop averaged over all realizations.

The figures also show the peak point (corresponding to the maximum of ΔP_b), the after-disruption velocity U_{ad} related to this point and the fitting lines used for estimating pseudo-U_{mf} velocities. Comparing the average curves in the loading stage, it appears that by increasing the ultra-fine material in the mixture, the peak value of ΔP_b increases (4.407, 5.04 and 7.05 mbar for 30%, 50% and 68% of the ultra-fine material in the total weight of the mixtures, respectively). The superficial gas velocities corresponding to these peak points (U_{ad}) also increase when increasing the percentage of ultra-fine powders in the mixture (they are 5.5, 6.79 and 8.49 cm/s, respectively).

In addition, the results show that by increasing the percentage of ultra-fine powder in the mixtures, the obtained pseudo-U_{mf} velocities also increased (2.6, 4.06 and 7.32 cm/s for 30%, 50% and 68% of ultra-fine material in the mixtures, respectively). Generally speaking, increasing the percentage of ultra-fine materials in the mixture causes a delay in the onset of partial fluidization (it appears first at higher superficial gas velocities), an increase in the bed pressure drop, as well as a delay in reaching the peak point.

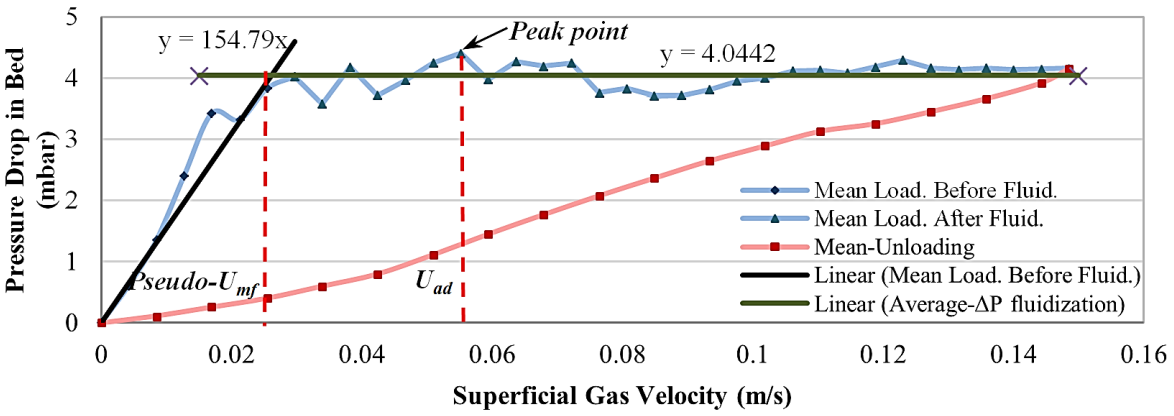

Fig. 3.27 Mean value of $\Delta P_b(U_{sg})$ when repeating fluidization tests for fluidization loading and unloading of mixed material—(30% of ultra-fine + 70% of fine particles).

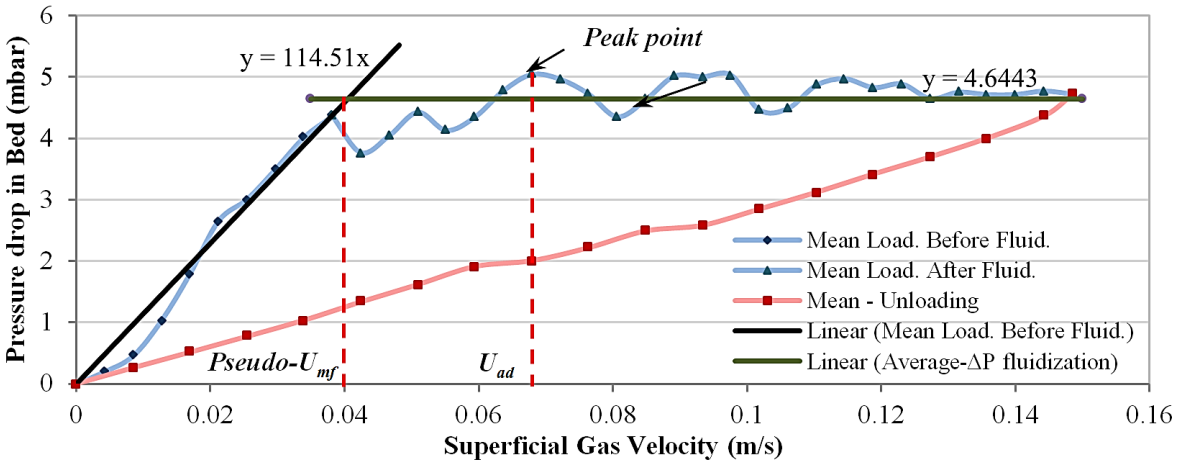

Fig. 3.28 Mean value of $\Delta P_b(U_{sg})$ when repeating fluidization tests for fluidization loading and unloading of mixed material—(50% of ultra-fine + 50% of fine particles).

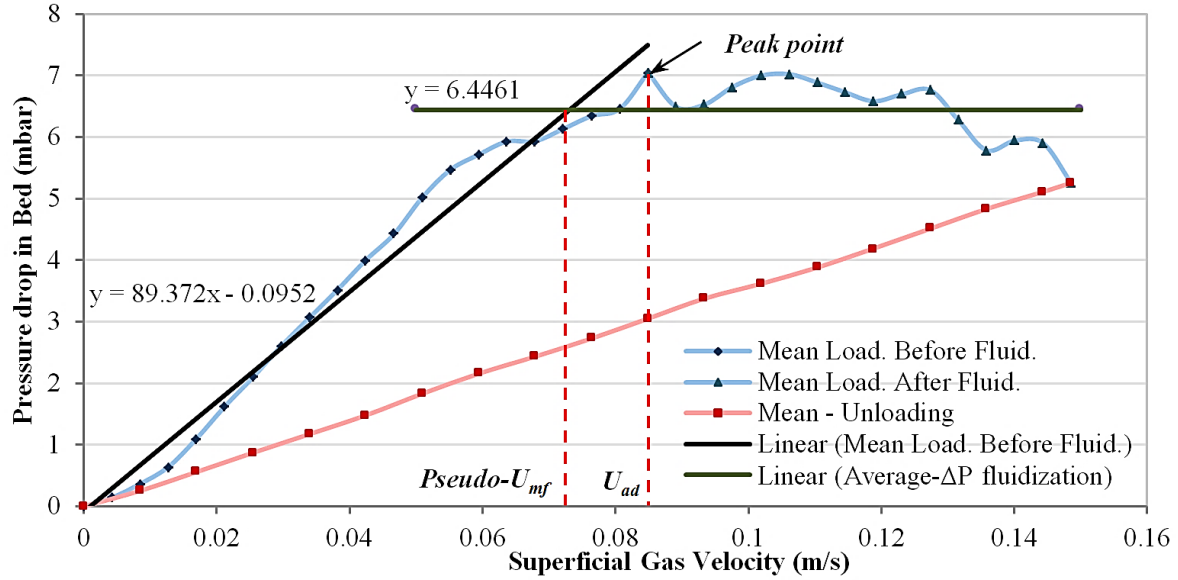

Fig. 3.29 Mean value of $\Delta P_b(U_{sg})$ when repeating fluidization tests for fluidization loading and unloading of mixed material—(68% of ultra-fine + 32% of fine particles).

3.2.4.1. Bed expansion ratio

To understand better the behavior of different mixtures of materials during fluidization, Fig. 3.30 shows the bed expansion ratio (%) of the bed when increasing the superficial gas velocity.

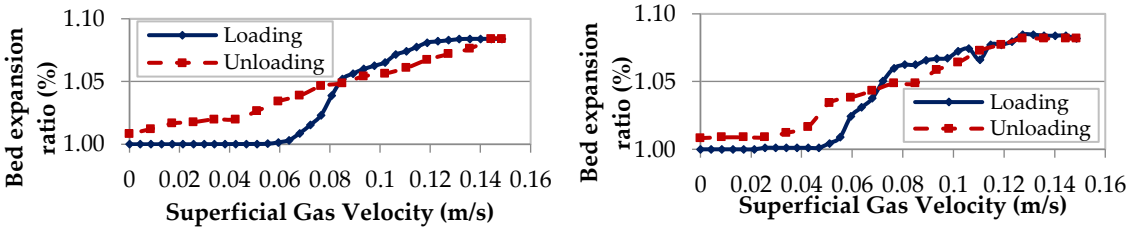

(**a**) MX-10 (100% ultra-fine) (**b**) 68% ultra-fine–32% fine

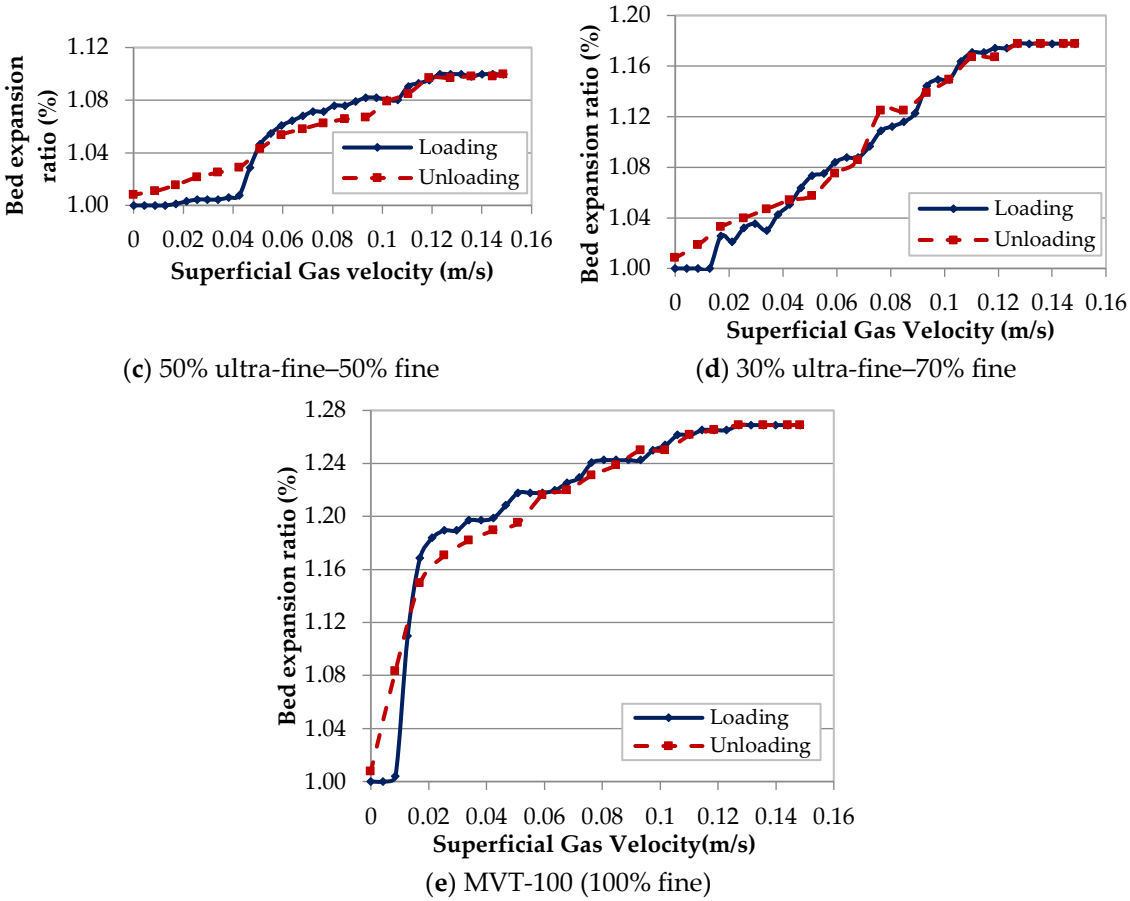

Fig. 3.30 Bed expansion ratio ($\Delta h_b/L_0$, where Δh_b and L_0 are the current and the initial height of the bed, respectively) as a function of superficial gas velocity for different mixtures of materials.

This figure shows that at the beginning of the unloading stage (right part of the figures), the height of the bed during loading conditions is always higher or equal than during unloading for a given value of the superficial gas velocity. During fluidization, due to the spouting particles from the channels, the height of the central part of the channel decreases and the height of its peripheral part increases. In addition, the location of the channels also changes when changing the superficial gas velocity. As a consequence, a non-level surface is observed. For this reason, an average height calculated over the whole surface (see chapter 2 for the methodology) has been used as height in Fig. 3.30.

At lower superficial gas velocities (left part of the figures), the bed height for unloading is higher than for loading. It is noted that the loading and unloading curves cross each other at a velocity near the calculated pseudo-U_{mf} for all mixtures. In addition, by increasing the percentage of ultra-fine particles in the mixture, the bed expansion ratio (%) decreases and the total expansion of the bed after unloading increases. Table 3.2

shows the values for the bed expansion ratio (%) and the total expansion of the bed for better comparison.

Table 3.2 The bed expansion ratio (%) and the total bed expansion of the used powder mixtures.

Mixture Material	Bed Expansion Ratio (%)	Total Expansion of the Bed (mm)
CALCIT MVT-100	126.89	0.51
70% Fine–30% Ultrafine	117.77	0.5825
50% Fine–50% Ultrafine	109.97	0.69
32% Fine–68% Ultrafine	108.47	0.8333
CALCIT MX-10	108.40	0.9375

3.2.4.2. Aggregation states of cohesive powders

For describing the observed behavior, the fluidization of ultra-fine cohesive powders is studied first. Cohesive powders usually show three different states of aggregation, that is, individual particles (agglomerate-free), natural agglomerates, as well as fluidized agglomerates [3]. Due to the relative motion between ultra-fine particles, they form quasi-spherical agglomerates when kept in a container or during transfer to the fluidization column, which are named natural agglomerates. This kind of agglomerates is lightweight and breakable. Also, they have a relatively narrow size distribution.

Figure 3.31 shows the natural agglomerates of fine, ultra-fine and different mixtures of these two materials. The shape, size, and structure of the formed natural agglomerates of each mixture have been captured by a KEYENCE digital microscope system VH-Z250R (real zoom lens from 250× to 2500×).

MVT-100 (100% Fine)

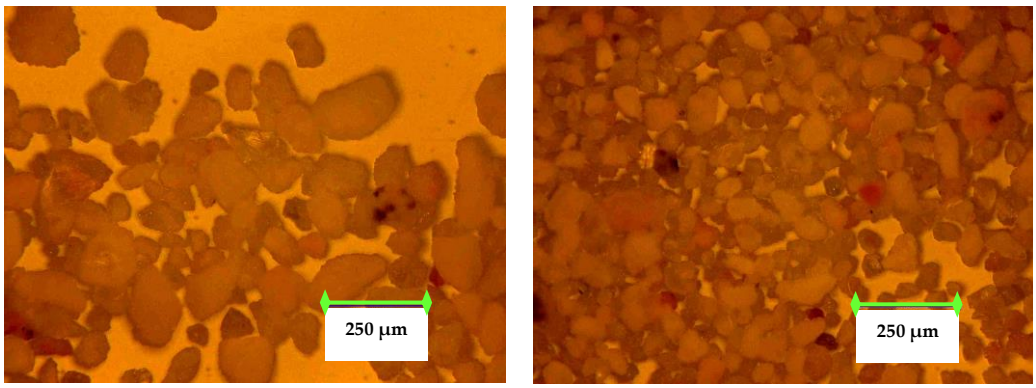

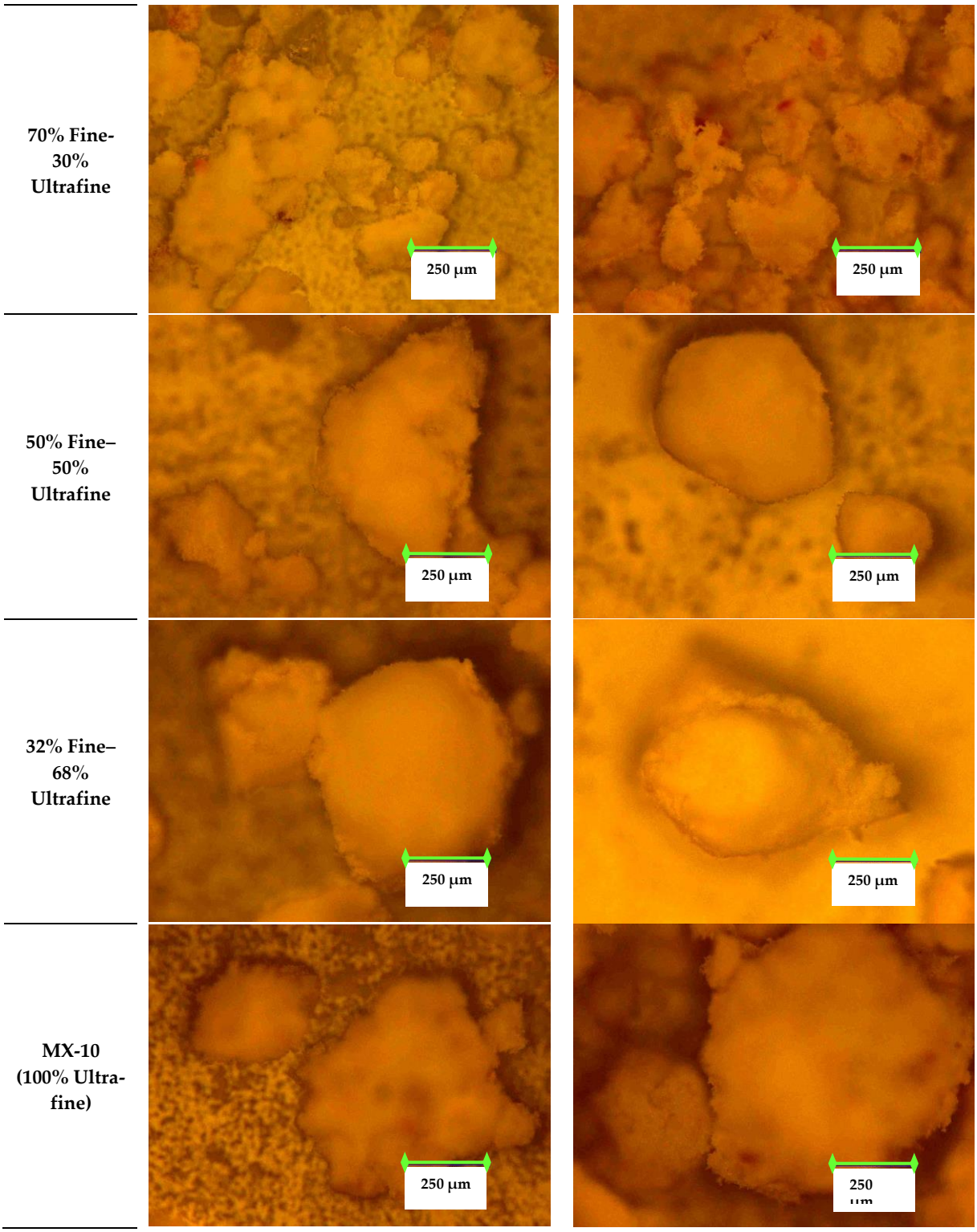

Fig. 3.31 Pictures that are taken from the microscope for formed natural agglomerates on the microscope slides. Each row shows two exemplary pictures for each material or material mixtures.

These pictures taken from the microscope show that for fine particles, almost all of the particles are single particles with different shapes and sizes according to the size distribution of this material. The natural agglomerates of the mixture of 70% of fine and

30% of ultra-fine particles show some small agglomerates, mostly with fine particles in the core. This means that the ultra-fine powders stick to the surface of fine particles and form agglomerates. By increasing further the percentage of ultra-fine powders to 50, 68 and 100 percent, thus increasing the value of cohesiveness, the size of natural agglomerates increases. The pictures also show that the sphericity of the agglomerates is increased when increasing the ultra-fine particles in the mixture.

After starting fluidization, in a competition between the transport of agglomerates by the gas flow and the cohesive forces between them, they become restructured regarding the number of constituent particles. They can be disintegrated into smaller agglomerates or even single particles. This new configuration of agglomerates is called fluidized agglomerates. Due to considerable cohesive forces between the agglomerate and peripheral adhered particles, some larger agglomerates may be created. When increasing the size of agglomerates due to high cohesive force between particles, more kinetic energy (superficial gas velocity) and larger forces (bed pressure drop) are needed to reach the disruption point and start fluidization (even partial). Therefore, due to the high intensity of cohesiveness, the maximum bed pressure drop (peak point) during the fluidization process is expected to move toward a higher superficial gas velocity for pure ultra-fine powders, as confirmed by the present measurements.

Figure 3.32 shows the fluidized agglomerates formed in the ultra-fine powder fluidized bed for three different superficial gas velocities. Due to the sticking of the ultra-fine particles to the walls leading to the build-up of an opaque layer, a detailed optical analysis is not possible in general. However, these images reveal the general morphology of semi-spherical fluidized agglomerates. Considering the size distribution of the powders for this material (<10 μm), all of the observed semi-spherical objects in this figure are the formed agglomerates during the fluidization process. The size of agglomerates varies from almost 3 mm at the bottom of the de-fluidized region to dozens of micrometers for the spouting agglomerates in the channel opening. The fluidized and de-fluidized zones are separated by red lines in each picture.

3.2.4.3. Effect of mixing fine and ultra-fine materials on the agglomerates

Mixing fine particles with ultra-fine powders improves the fluidization behavior of ultra-fine powders for two reasons. First, the smaller fine particles can form new agglomerates; that is, ultra-fine particles stick to the surface of fine particles to form some stable agglomerates. Baeyens et al. [111] reported that the ultra-fine powders adhere to larger particles, rather than they agglomerate with each other. Second, crushing and breaking of the formed agglomerates occurs due to friction or collisions; this is particularly frequent in the presence of larger fine particles [27] and changes the size distribution.

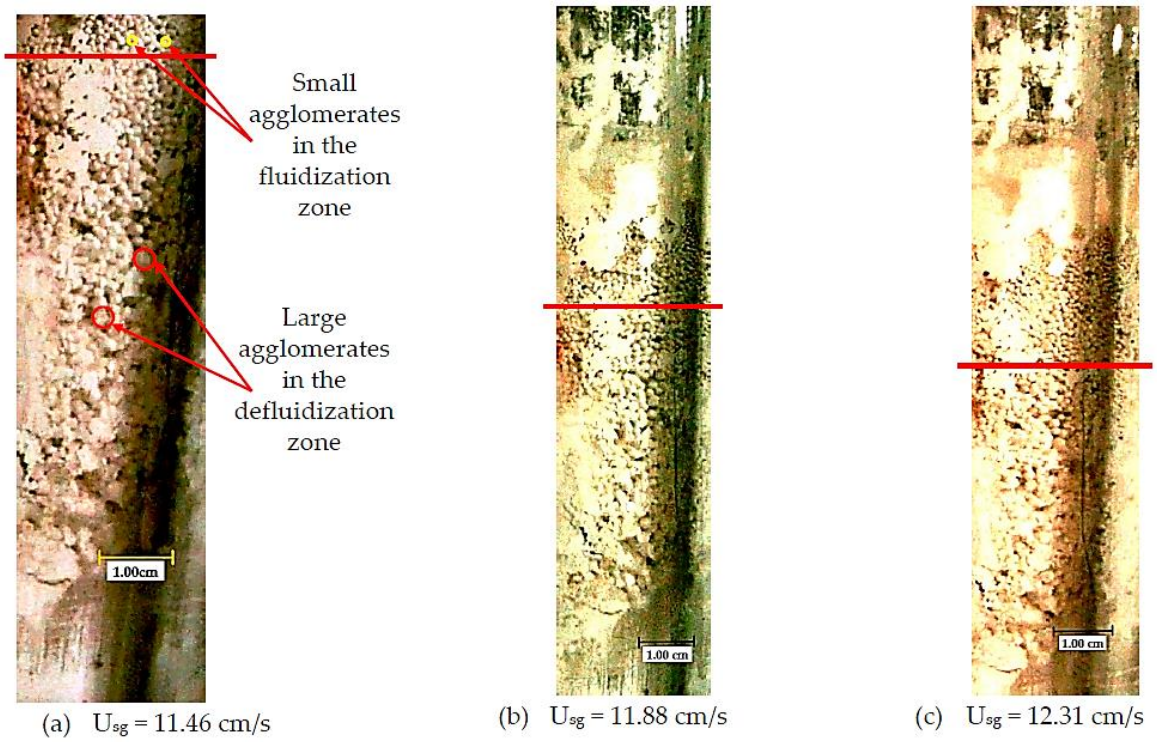

Fig. 3.32 Cropped sections of an active channel near the wall during a fluidization test of ultra-fine material for three different values of superficial gas velocity. The red line is used as a separator of two fluidized and de-fluidized zones (Above the line: fluidized; Below the line: de-fluidized). (a) This figure is a zoomed-in capture for a better view of formed agglomerates at lower velocity, 11.46 cm/s; (b) Formed agglomerates for the whole domain at 11.88 cm/s; (c) Changes in the agglomerates' size, shape, and the thickness of de-fluidized zone by increasing the superficial gas velocity to 12.31 cm/s.

Agglomerates containing fine particles are not necessarily bigger but can reach a far higher weight than those containing only ultra-fine powders. Therefore, they can get more kinetic energy and more easily disintegrate by collision or friction. Thus, the size of these agglomerates becomes smaller. After each collision, depending on agglomerate density, on the relative collision velocity, on the distance between agglomerates or particles, some new agglomerates are created. This process increases the variety of agglomerate sizes (leading to a wide size distribution for the formed agglomerates) and their structure becomes denser (as discussed before).

Shear cell tests already showed that the intensity of cohesiveness decreases when increasing the portion of fine particles (see Table 3.1). Thus, by increasing the percentage of fine particles in the mixture, the fluidization behavior in such a mixture (partial fluidization) is further improved, so that the disruption point is reached at a lower superficial gas velocity and lower bed pressure drop. In parallel, by increasing the percentage of fine particles in the mixture, the probability of the breakage of agglomerates increases in two ways. First, forming some new agglomerates with fine particles in the core; these have more weight and more kinetic energy than the agglomerates formed

during collisions by ultra-fine particles only. The second way is the existence of some larger fine particles (up to 200 μm) in the bed. The larger fine particles have a bulk density near the particle density. Then, they have more weight and more kinetic energy than any agglomerates formed by finer particles.

A wide size distribution results in the smaller void sizes [132] and enhanced fluidity [126]. This wide distribution increases the chance of filling the available voids between larger particles (agglomerates) by finer ones. Therefore, the size of micro-voids is decreased, hindering the growth of cracks between particle layers. In addition, decreasing the intensity of cohesiveness decreases the ability to form arches between particles [36], resulting in a denser mixture.

According to Geldart et al. [2], a strong intensity of cohesiveness leads to an increase in the number and size of micro-voids, as also described by Massimilla and Donsi [4]. Numerous horizontal and sloping cracks or channels form; then, the bed expands without true bubble formation. Conversely, decreasing the intensity of cohesiveness when increasing the number of fine particles decreases the size and number of micro-voids, limiting the growth of cracks and increasing the probability of small bubble formation. In fact, by decreasing the inter-particle forces, the small bubbles form, grow and disrupt the dense structure of the bed. Rising bubbles in the bed are the main reason for the conversion of horizontal or sloping cracks to vertical channels. Thus, the formed cracks in the bed are converted much easier to vertical channels, leading to a further improvement in fluidization behavior. In fact, this conversion increases the particles-air contact and forms the agglomerates.

For all mixtures, the observed fluidization is partial fluidization and the airflow does not fluidize the whole particle bed. Therefore, the air doesn't need to move the entire bed and overcome its weight. This fact can explain the decrease in the level of bed pressure drop at the peak point for mixtures containing a higher portion of fine particles, to lower values than the P_{wb} of the bed.

On the other hand, the wide range of the size of agglomerates, as well as reduced cohesion level in the compositions containing more fine particles, lead to a denser structure (similar to the structure of fine particles only). Then, the bed resistance increases against the gas flow. In other words, by increasing the portion of fine particles in the mixture, the bed pressure drop corresponding to each superficial gas velocity increases (packed bed condition). Therefore, the slope of the ΔP_b versus U_{sg} graph increases in the packed bed section of the loading curve.

However, for the case with 68% ultra-fines, increasing the portion of ultra-fine powders leads to increasing the inter-particle forces (Table 3.1 shows only 2% difference in the intensity of cohesiveness between this mixture and ultra-fine material only). This can explain the increase in the peak of bed pressure drop. The mixture containing 68% of ultra-fines has properties very close to pure ultra-fine powders; thus, it is conceivable that it mimics ultra-fine fluidization behavior. For this mixture, due to increasing inter-particle forces as well as forming agglomerates with a more uniform size distribution, the mixture has a lower bulk density and higher porosity (proved by the bed initial height for the same weight of the material). Therefore, in the packed bed condition, due to the lower bulk density and higher permeability, the bed pressure drop for each specified gas velocity is lower than for the two other mixtures; the slope of the loading curve is reduced. However, this mixture needs a higher bed pressure drop for disrupting and overcoming the inter-particle forces.

To estimate the size of the formed agglomerates in each part of the fluidization tests of different mixtures of materials, the Ergun equation (Equation 3-30) along with Wen & Yu equation (Equation 3-21) can be used to calculate the mean value of agglomerates' size. Considering the Ergun equation for the linear part (packed bed condition) of the fluidization curve, the mean value of agglomerate size in the three conditions (1. the initial phase of loading (near-zero velocity), 2. at slightly higher gas velocities in the fixed bed condition of loading, as well as 3. near to rest (near-zero velocity) state in the unloading condition), can be calculated as:

$$d_p = \sqrt{\frac{150\mu L_0(1-\varepsilon)^2}{\varepsilon^3}\frac{U_{sg}}{\Delta P_b}} \tag{3-36}$$

In addition, using the Wen & Yu equation, the agglomerate sizes can also be estimated at the fluidization point. Substituting the needed parameters in this equation, the mean value of agglomerates size can be obtained from

$$d_p = 0.00055546\left(U_{mf}^2 + \sqrt{U_{mf}^4 + 3.696U_{mf}}\right) \tag{3-37}$$

In these equations, the calculated pseudo-U_{mf} is used as U_{mf}. For the low-velocity condition, these equations predict slightly larger agglomerates for mixtures containing a higher portion of fine particles (it increases from 91 to 100 μm). On the contrary, at the minimum fluidization velocity point and due to increased kinetic energy (increasing gas velocities), the mean value of agglomerates' size is decreased (from 274 to 154 μm) when increasing the portion of fine particles, as already discussed previously.

After starting channeling, the small channels grow to a bigger one when increasing further the gas velocity and two distinct regions are established; that is, fixed and

fluidized (active channel) zones. When the gas velocity increases further, these zones alternate in an unsteady manner during the experiment. In some cases, this is accompanied by moving and bursting of bubbles.

Figures 3.27–3.29 also show that increasing the ultra-fine material in the mixture increases the hysteresis effect between loading and unloading curves. The hysteresis can be the result of the following three factors:

a) the need for a greater force to overcome the cohesion forces between the particles,
b) increase in the irreversible deformation of particulate materials in the fluidization process,
c) energy dissipation during collisions or friction between particles or agglomerates.

According to Tomas [138]: "Obviously, the finer the particles the "softer" are the contacts and the more cohesive is the powder." It means that for ultra-fine particles, due to a high level of cohesive inter-particle forces and even without direct contact, there are some plastic, irreversible deformations for the particles close to each other. In the fluidization process, due to the kinetic energy provided by the fluidizing gas, the number of contact and collision increases. Therefore, due to softer contact behavior, the irreversible deformations are higher for the mixtures with a higher proportion of ultra-fine particles. This induces a stronger hysteresis effect compared to mixtures with a lower amount of ultra-fine powders.

In addition to some irreversible deformation of ultra-fine particles due to cohesive forces, the formation and collapse of the channels and cracks in the powder bed and avalanching of different particle layers on each other can explain most of these irreversible deformations. The probability of irreversible deformation increases when increasing the proportion of ultra-fine particles.

3.3 Final remarks

In this study, different fluidization tests were conducted for fine particles, ultra-fine particles and mixtures of these two materials in order to study the effect of the presence of ultra-fine particles on the fluidization of a fine-particle bed. The investigations concentrated on 30%, 50% and 68% (weight percentage) of ultra-fines; all show only partial fluidization. The fluidization behavior of fine material (Geldart A) is characterized by an easy, aggregative (bubbling) and full fluidization. For fine material, experimental results also show smooth fluidization with a slight hysteresis effect.
When mixing with ultra-fine powders, the experimental results show that the presence of ultra-fine powders can change the full fluidization of fine particle bed severely. The measured physical properties (e.g., ρ_b, c_M, d_M and ff_c) of the mixtures of fine and ultra-fine particles are close to those of ultra-fine powders only. Similar to ultra-fine powders,

the fluidization behavior of these mixtures is partial, non-reproducible, significantly different for each realization, and includes cracking, channeling and agglomeration. Initial conditions have significant impacts on fluidization behavior. There are many fluctuations in the bed pressure drop when increasing gas velocity (loading process). Therefore, to have a better overview of the fluidization process for these mixtures, the fluidization tests have been repeated and the mean value of the bed pressure drop for each gas velocity has been used for analyzing the fluidization behavior. When decreasing the fluidization air velocity (unloading curve), the change in the bed pressure drop shows an almost linear behavior, corresponding to an approximately constant permeability.

Briefly, increasing the portion of ultra-fine powders in the fluidized material causes a delay in starting partial fluidization, an increase in the bed pressure drop, a delay in reaching the peak point, a decrease in the bed expansion ratio (%), an increase in the total expansion of the bed after unloading as well as an increase in the hysteresis effect between loading and unloading curves. To understand these phenomena, the effect of mixing fine particles with cohesive ultra-fine powders and their roles in modifying the size distribution of agglomerates have been discussed. In the next chapter, the effect of compression on re-fluidization will be studied.

3 Fluidization Test

CHAPTER 4

Fluidization, Compression, and Re-fluidization Test

In this chapter, the results of the second class of tests performed in this study will be reported and discussed. The results and discussion of this chapter were partly published in the article "The Effect of Very Cohesive Ultra-Fine Particles in Mixtures on Compression, Consolidation, and Fluidization", Processes, 2019, 7,439; DOI:10.3390/ pr7070439.

4.1 Introduction

Considering the complex microscopic behavior of fine particles and their interactions, understanding the compression process for particulate materials is far more difficult than for fluids [36]. Experimental studies on the compression of solid particles go back to the early 20th century when Walker [139] used a logarithmic-law to fit his empirical data as $(1/\varphi) = (1/\varphi_J) - n \log(\sigma_{ca}/\sigma_{c0})$. In this equation, φ is the particle volume fraction (packing density), n is the compressibility index, σ_{ca} is the applied compression stress, and σ_{c0} and φ_J are two empirical parameters. The ratio σ_{ca}/σ_{c0} is normally shown as the dimensionless applied pressure ($\hat{\sigma}_c$). In civil engineering, when the powder bed has a loose structure and the rearrangement of particles is the main phenomenon occurring during compression, this logarithmic equation is satisfactory. However, for fine and ultra-fine particles, the cohesive inter-particle forces are essential. Experimental results for cohesive particles indicate that the compressibility index increases when increasing the void fraction of the particle bed at the initial condition (unconsolidated state) [140].

The compressibility and compactability of powders are affected by their mechanical properties and the inter-particle forces at the macro and micro-scale. The mechanical properties of bulk materials can be analyzed using a shear-cell. The compression function relates changes in the bulk density of the powder to increase in the applied pressure. The equation for isotropic compaction of a random powder bed packing is approximated by [30]:

$$\frac{d\rho_b}{\rho_b} = n \cdot \frac{dP}{P} = n \cdot \frac{d\sigma_{M,st}}{\sigma_{M,st} + \sigma_0} \tag{4-1}$$

where ρ_b is the bulk density, n is the compressibility index, σ_0 is isostatic tensile strength for a loose random packing, and $P = \sigma_{M,st} + \sigma_0$ is the total pressure (according to Mohr's circle [141]). In addition, $\sigma_{M,st}$ is the average pressure ($\sigma_{M,st} = (\sigma_1 + \sigma_2)/2$, where σ_1 and σ_2 are the major and minor principal normal stresses of Mohr's circle, respectively). The compression function is obtained by integrating Eq. (4-1) with the initial condition: for $\sigma_{M,st} = 0$, $\rho_b = \rho_{b,0}$.

$$\frac{\rho_b}{\rho_{b,0}} = \left(1 + \frac{\sigma_{M,st}}{\sigma_0}\right)^n \tag{4-2}$$

where $\rho_{b,0}$ is the bulk density for a loose packing without any compaction. The compressibility index, n, characterizes how the volume of a cohesive powder reduces under a compressive force. Figure 4.1 shows the compression function for different compressibility indices ($n = 0$ shows the behavior of an incompressible solid material, and $n = 1$ indicates an ideal gas compressibility index) [58]. The compressibility indices of different particulate materials are summarized in Table 4.1 [30].

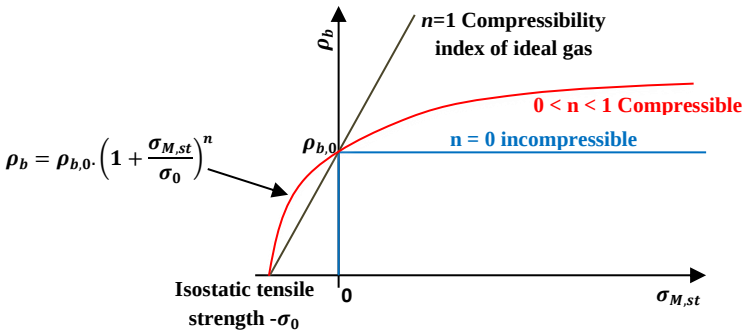

Fig. 4.1 Compression function of a cohesive powder.

Table 4.1 Classification of the particulate materials based on their compressibility indices [30]

Index n	Evaluation	Examples	Flowability
0–0.01	Incompressible	Gravel	Free-flowing
0.01–0.05	Low compressibility	Fine sand	Free-flowing
0.05–0.1	Compressible	Dry powder (Calcite)	Cohesive
0.1–1	Very compressible	Moist powder	Very cohesive

The focus of this study is on the behavior of two fine (d < 100 μm) and ultra-fine (d < 10 μm) materials as well as of their mixtures in a series of compression tests. For the fine particles, the ratio between inter-particle attractive force and weight (called the granular Bond number (B_{og}) [36]) is in the range of 1 to 100 [13]. Consequently, they correspond to slightly adhesive particles with aggregating or bubbling fluidization (classified as group

A in Geldart classification [8]). However, for ultra-fine powders which are categorized in the group C of Geldart's classification, this ratio (B_{og}) is in the range of 100 to 10^4, and they are cohesive or very cohesive materials [13]. These powders are characterized by poor flowability and noticeable compressibility.

Consequently, storage, mixing, and discharge of this kind of bulk solids are difficult. Fine and ultra-fine particles tend to agglomerate and form bridges or stable ratholes around the outlet of a silo. These problems can only be solved effectively using discharge aids. Fluidization is one of the modern methods for mixing and discharge of stored fine particles with diameters between a few microns and 200 μm using injecting air. After discharging, the remaining fine particulate solids continue to gain strength if stored at rest under compressive stress for a long period [142]. This effect is called time consolidation. The time consolidation is the result of adhesive forces. Discharging the consolidated material using fluidization is not like the first fluidization (before consolidation) and the behavior of the bulk material is entirely different. Such processes often happen in chemical, pharmaceutical, and food industries, where the fine and ultra-fine particulate materials are used in different compositions for getting different final products.

The fluidization of particles in a fluid is a result of the force balance between hydrodynamics, gravitational, and inter-particle forces [50]. For ultra-fine cohesive powders, the attractive inter-particle forces greatly affect the fluidization behavior. Since the adhesion is often stronger than the forces that the fluid can exert on the particles, these powders are difficult to fluidize. In a dry bulk material, when the size and the distance between the particles are tiny, the dominant and controlling interaction force is the van der Waals force. For this condition, the contact between particles is the key particle-particle interaction mechanism [131].

In most applications, the initial conditions include some level of consolidation stress due to the weight of the upper layer of particles acting on the lower layers. The ideal initial condition of a compaction process is defined as unconsolidated condition ($\sigma_{ca} \approx 0$, where σ_{ca} is the applied compression stress). In this study, to control the inter-particle cohesion force and to ensure a loose structure of particle beds (with minimum initial consolidation effect), the bed was initially fluidized with gas (dried air at ambient temperature). After fluidization of the bed (in that case, σ_{ca} is near zero), the airflow rate was decreased gradually. In this manner, the transition of a fluidized bed to the jamming condition takes place under very small applied stress [143]. The fluidization tests of cohesive ultra-fine and also mixtures of fine and ultra-fine particles show a size enlargement due to agglomeration [50] (new agglomerate size is d_{ag}). In this process, increasing the size of agglomerates is related to the granular Bond number [36] as $K \sim \mathrm{Bo}_{\mathrm{g}}^{1/(D_f+2)}$. In this

equation, K is the ratio of size enlargement (d_{ag}/d_p) and D_f is the fractal dimension of the formed agglomerates.

When unloading (decreasing the gas velocity) the fluidized bed, the agglomerates are jammed in a loose packing that is very close to the random loose packing of particles obtained when cohesion effects are negligible [144]. The agglomerate Bond number for the formed agglomerates during fluidization is small [36]. Thus, the agglomerates are practically low-cohesive, quasi-spherical particles; then, the effect of inter-particle forces can be neglected. In this condition, if some low pressure (<10 Pa) is applied to the particle bed, a small level of consolidation first happens for agglomerates (without any breakage). The arrangement of the formed agglomerates in the packed system changes from loosely packing to close packing. A further increase in the pressure (more than $\sigma_{c0} \approx 10$ Pa) [36] leads to a new regime of compaction; i.e., disruption of the formed agglomerates and filling the voids between agglomerates with single particles or fragmented agglomerates. This regime is called the logarithmic-law regime [139].

Valverde and Castellanos [36] showed that a further increase in the applied pressure up to a few dozen kPa could be the cause of a new transition in the compaction regime. In this condition, the compression takes place by rearranging the single particles. This process does not depend on the agglomerates' distribution in the initial state [36] and leads to a different logarithmic law regime.

The effect of adding fine particles to improve the fluidization of ultra-fine cohesive beds has been investigated by other researchers. In previous publications (e.g., [9,25–27]), the authors considered the addition of coarser particles with different origins leading in particular to a different density, size, and surface properties. In contrast, this study considers only mixtures of the same material; the fine and ultra-fine material fractions have the same origin, and they differ only in the particle size distribution. The present series of tests involving fluidization, compression, and re-fluidization after applying different pressure levels should deliver useful information for a better understanding of the underlying processes. The knowledge about the behavior of mixtures of materials in different processes also helps to improve the manufacturing and process efficiency of a variety of products in particle-based industries [1]. Practically, most of the bulk materials are mixtures of different size distributions of the same material (multimodal particle size distributions). However, the effect of increasing the amount of ultra-fine materials in a fine particle bed on the compression process and re-fluidization of the compressed bed is still not fully understood.

The main goal of this study is to investigate the behavior of different mixtures of fine and ultra-fine particles during compression tests and also to evaluate the re-fluidization

behavior of the compressed bed to investigate the history effect, i.e., the effect of the compression on (re-) fluidization. In the next section, the methodology of performing the experiments will be introduced. Thereafter, experimental results of initial fluidization, compression, and re-fluidization of compressed bed will be discussed, in particular regarding the effect of the presence of ultra-fine powders in a fine particle bed. This chapter will close by remarks in Section 4.4.

4.2 Experimental methodology

In this study, each experiment involves three steps: (1) initial fluidization, (2) compression of the bed (starting from a low level of consolidation), and (3) re-fluidization of compressed and consolidated particle bed, as depicted in Fig. 4.3.

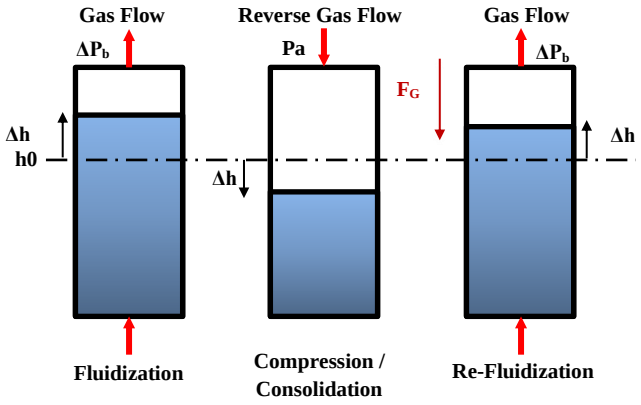

Fig. 4.3 Working principle for each experiment, involving three steps (Fluidization, Compression, and Re-fluidization).

In the fluidization and re-fluidization process, the dried air used as fluidization gas enters the system from the bottom of the bed and, after passing through the bed, exits from the top of the bed. Conversely, for the compression tests, the dried compressed air comes to the system from the top side and there is not any exit. During compression (realized in four equidistant sub-steps), the propagation of pressure waves in the bed results in a decrease in total volume. The pressure waves, classified as elastic waves, are transmitted from the top to the bottom of the bed by particle contacts [145]. Considering the free movement of particles relative to other ones, the force chains in the bed can deform or collapse. Previous experiments [146] have depicted the capability of these force chains to induce the rearrangement of the particles. The volume decrease is affected by the amount of pressure as well as by the arrangement of particles.

In this series of tests, similar to the first class of tests (only fluidization), two mixtures with a dominant mass fraction of either fine or ultra-fine particles and a mixture of these two materials in the same weight fraction were considered; i.e., the portions of ultra-fine powders in the mixtures were 30%, 68%, and 50%, respectively.

4.3 Results and discussion

The effect of the presence of ultra-fine particles on a fine particle bed fluidization has been previously discussed in chapter 3. Therefore, these findings are not repeated here. Considering the results of the previous chapter for the initial fluidization of different mixtures of fine and ultra-fine particles, this section will start by the results of the compression tests (second step in Fig. 4.3).

4.3.1 Compression test results

The jamming transition is a crucial slowing down of system dynamics far from equilibrium as a result of the overcrowding of particles. The dynamics of the system is stopped by reducing possible particle movements; this condition is referred to as jamming [147]. According to Castellanos et al. [143], at jamming transition, the dynamics of the agglomerates of fine particles after fluidization show a critical behavior, characterized by a power law relating the increase of particle volume fraction with consolidation stress ($\hat{\sigma}_c \propto (\Delta\varphi)^{\beta}$) where $\Delta\varphi = \varphi - \varphi_J$ and φ_J is particle volume fraction in jamming condition. For fine cohesive powders, $\beta \approx 1$ is normally obtained for soft particle granular systems [36]. At a critical pressure ($\sigma_{c0} \approx 10$ Pa), agglomerates begin to break, and one obtains a logarithmic law ($\Delta\varphi = \vartheta \log\hat{\sigma}_c$), similar to the situation in silos.

Sederman et al. [148] used Magnetic Resonance Imaging (MRI) and considered statistical distributions of the pores' characteristics to show that the logarithmic law during the consolidation of particles can also be anticipated considering statistical mechanics of non-cohesive spherical particles. During consolidation, the large pores become filled and the distribution of voids undergo an irreversible change (rearrangement of pores). Simultaneously, the number of small pores is increased, the number of large pores is decreased, and the relative size of pore space is decreased. Therefore, the overall porosity is also decreased during consolidation, which will alter the characteristics of the bed hydrodynamics [149]. According to the maximum entropy principle, the volume distribution of the pores shows an exponential law. Its reduction becomes slower when increasing the compaction of the system [150].

The logarithmic law is also valid for the behavior of cohesive particle beds [143]. However, the compressibility index is a material-dependent index and increases almost linearly with the ratio of void-to-particle fractions of unconsolidated particle bed [140]. A looser packed bed yields higher compressibility.

In this study, three levels of applied pressures were tested for each mixture of fine and ultra-fine particles. The equidistant sub-steps used for increasing the applied pressure (compression) in each experiment are summarized in Table 4.2. The same sub-steps were

used for decreasing the pressures (decompression) in the opposite direction. Peak pressure levels are 20, 40, and 80 kPa, respectively. They were chosen in such a way to be large enough for getting a logarithmic law compaction regime, but also low enough to avoid getting a deformed structure with stable consolidated regions hindering re-fluidization.

Table 4.2 Applied air pressures (kPa) at each sub-step of compression tests.

	Sub-Step 1	Sub-Step 2	Sub-Step 3	Sub-Step 4
Level 1 (Low)	5	10	15	20
Level 2 (Intermediate)	10	20	30	40
Level 3 (High)	20	40	60	80

The focus of this study is on the logarithmic law compaction regimes. At the end of the initial fluidization, the consolidation stress in the system at rest is already higher than the limit of the power-law regime ($\sigma_{ca} \geq \sigma_{c0}$).

4.3.1.1 Effect of applied pressure on the specific volume fraction of particles

The behaviors of fine, ultra-fine, and different mixtures of fine and ultra-fine particles in the compression tests are shown considering a logarithmic scale of the horizontal axis in Fig. 4.4, in which the specific volume fraction of particles in the bed ($1/\varphi$) is plotted as a function of dimensionless compression stress. For each mixture of materials, three sets of data are plotted, corresponding to the three pressure levels listed in Table 4.2. The maximum variation coefficient of repeated experiments for these tests is related to the CALCIT MX 10 (100% of ultra-fine material). It is equal to 7.22%. The dashed lines show the best fits for the data related to each set of pressures. The fitted graphs are well fitted to a logarithmic law as $1/\varphi \approx 1/\varphi_J - n \log(\sigma_{ca}/\sigma_{c0})$ [36]. In these fitted graphs, the factor of the log-function is the compressibility index, n, while the constant indicates the specific jammed particle volume fraction (inverse of φ_J). Table 4.3 summarizes the compressibility indices for different mixtures of fine and ultra-fine particles as well as for different pressure levels. In addition, the obtained jammed particle volume fractions are also shown in this table.

By comparing the results of Table 4.3 with the compressibility indices of different classes of materials introduced in Table 4.1, it can be confirmed that the fine particle bed (CALCIT MVT 100) is a low compressible material with free-flowing behavior. However, adding the ultra-fine particles increases the compressibility index and changes the mixtures' behavior toward compressible and cohesive materials. Pure ultra-fine powders correspond to a very cohesive and very compressible material.

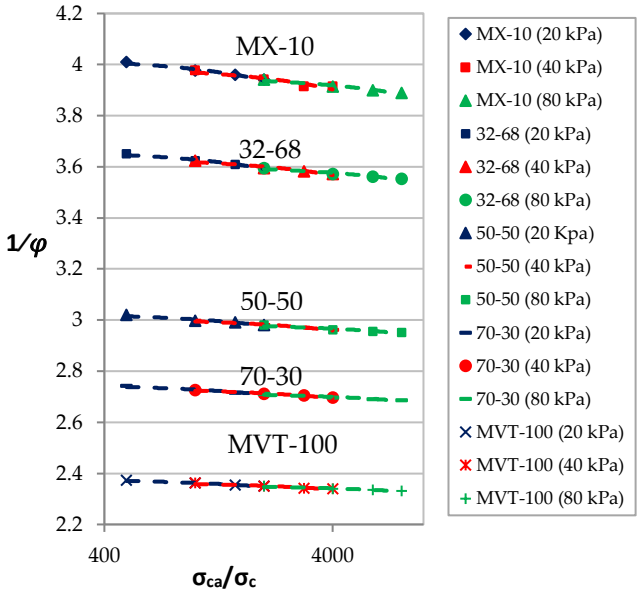

Fig. 4.4 Specific particle volume fraction ($1/\varphi$) as a function of dimensionless applied consolidation stress.

Table 4.3 Compressibility index and calculated jammed particle volume fraction of different mixtures during various sets of applied pressures

Material Name	Pressure level	n	φ_J
CALCIT MVT-100 (100% fines)	Low	0.039	0.403
	Intermediate	0.037	0.403
	High	0.030	0.408
70% -30% (fine – ultrafine)	Low	0.050	0.346
	Intermediate	0.048	0.347
	High	0.041	0.350
50% -50% (fine – ultrafine)	Low	0.062	0.313
	Intermediate	0.060	0.314
	High	0.048	0.318
32% -68% (fine – ultrafine)	Low	0.090	0.256
	Intermediate	0.085	0.256
	High	0.071	0.260
CALCIT MX-10 (100% ultrafines)	Low	0.110	0.231
	Intermediate	0.104	0.232
	High	0.088	0.235

Additionally, Table 4.3 shows that the compressibility index is almost the same for the low and intermediate pressure level. However, increasing the applied pressure to the highest level (80 kPa) leads to a noticeable decrease in the compressibility index. For ultra-fine materials, although the material behavior at low and intermediate pressure corresponds to a very compressible and very cohesive material, it changes under high pressure to only compressible and cohesive.

At low and intermediate pressure, compaction of the materials is mostly controlled by the distribution of pore areas within the porous media formed by particles and agglomerates. For the high-pressure level, it seems that the agglomerates are broken, so that compaction is controlled by the distribution of pores between individual particles. In this condition, the bed has lost the memory of its initial fluidization, as in [36]. In addition, as mentioned before, when increasing the compaction of the system, the changes in the volume distribution of the pores show an exponential law and its reduction becomes slower [150]. This argument can also explain the cause of a reduction in the compressibility index at higher compression pressures.

4.3.1.2 Effect of applied pressure on the volume fraction of particles

Another form of the logarithmic law can also be used to describe the compaction regimes. This form is remarkably similar to the empirical equation usually employed to describe the compaction of granular materials such as soils in the rearrangement regime [151]. It is written as $\varphi \approx \varphi_J + \vartheta \log \hat{\sigma}_c$ [36]. Figure 4.5 shows the volume fraction of particles in the bed (φ) as a function of the dimensionless applied consolidation stress for the three pressure levels applied on different mixtures of fine and ultra-fine particles.

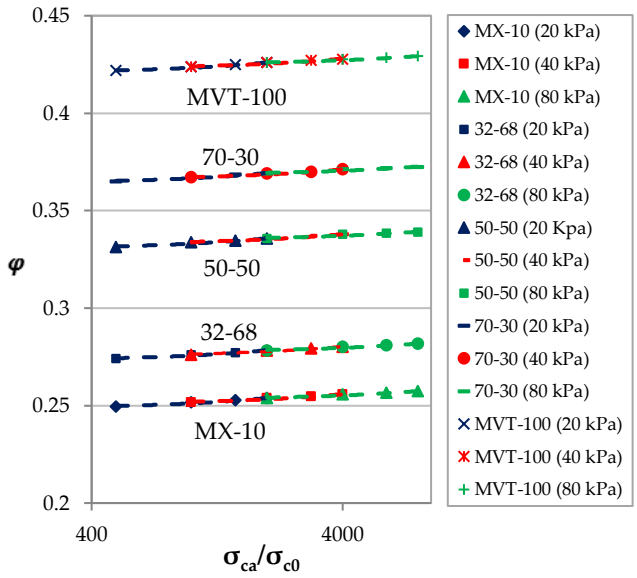

Fig. 4.5 Particle volume fraction as a function of dimensionless applied consolidation stress

Again, the dashed lines show the best fits for the data related to each set of pressures. Considering this form of logarithmic law, as it is clear from all graphs, the slopes of the particle volume fraction versus logarithmic display of dimensionless stress (ϑ) are the same for the different mixtures of fine and ultra-fine particles. For the first set of applied pressures (low-pressure level), this slope is ϑ = 0.0069 for all material combinations. For the second set of applied pressures (intermediate pressure level), the slope is slightly

decreased to 0.0067 (a 3% decrease relative to the first case). However, the third sets (high-pressure level) show a noticeably different slope and ϑ decreases to about 0.0056 (more than 18% change relative to the first case).

Therefore, it can be concluded that the slope of particle volume fraction versus the dimensionless applied stress (ϑ) does not depend on the particle size distribution of the material, but it depends on the type of material itself. This behavior is also reported by Castellanos et al. [143] for toner particles. On the other hand, this slope decreases when increasing the applied pressure level during the compression tests. For the three considered pressure levels, the decrease in the slope seems to be non-linear, being faster at a higher applied pressure. Table 4.4 summarizes the extracted particle volume fraction of different mixtures in the jammed state ($\sigma_{ca} \approx 0$) to compare with the results of Table 4.3. These results are based on the best logarithmic fit of the data shown in Fig. 4.5.

Table 4.4 Jammed particle volume fraction of different mixtures for different pressure levels.

Material Name	Pressure level	φ_J
CALCIT MVT-100 (100% fines)	Low	0.403
	Intermediate	0.403
	High	0.408
70% -30% (fine – ultrafine)	Low	0.346
	Intermediate	0.347
	High	0.350
50% -50% (fine – ultrafine)	Low	0.313
	Intermediate	0.314
	High	0.318
32% -68% (fine – ultrafine)	Low	0.256
	Intermediate	0.256
	High	0.260
CALCIT MX-10 (100% ultrafines)	Low	0.231
	Intermediate	0.232
	High	0.235

The results show that the particle volume fraction in the jammed state decreases when increasing the percentage of ultra-fine powders in the mixtures. It means that a higher ratio of ultra-fine particles results in a looser pack structure (higher fraction of voids). At the same time, the applied pressure level only shows a negligible effect on the jammed particle volume fraction extracted from the best fit of the curves. In fact, the particle volume fraction in jamming condition does not correlate with the amount of applied compression pressure after it.

Combining the two forms of logarithmic laws, $n \approx \left(1/\varphi_J\right)^2 \vartheta$ or $\vartheta \approx n\varphi_J^2$. Therefore, it can

be concluded that although the jammed particle volume fraction is reduced by increasing the ratio of ultra-fine powders in the mixture, the compressibility index increases in such a way that the reduction of φ_J is counterbalanced and ϑ remains constant. As mentioned before, there is a noticeable decrease in the compressibility index (n) of different mixtures of materials due to controlling the pore distribution by individual particles and slowing down the rate of reduction in volume distribution of the pores by increasing the applied pressure to a higher one (80 kPa). This decrease could be the main reason for a noticeable decrease in ϑ (from 0.0069 to 0.0056).

4.3.1.3 Decompression phase

The compression step is followed by a decompression phase. The applied pressure is decreased in four steps, identical to those used during compression until reaching back atmospheric pressure. Studies concerning the decompression phase are very scarce. However, the decompression phase is found in many industrial applications or processes and has an important effect on the final results. For instance, in a tableting process, the rate of loading and unloading can have crucial effects on the quality of final products [32].

From the total work delivered during the compression phase, only a small portion is recoverable. The rest of the work is dissipated due to friction, particle deformation, heat, and other irreversible processes during compression [152]. After decompression, as a result of an elastic recovery in the bed, the stresses within the bed change, and the height of the bed increases slightly. However, most of the bed height reduction during compression is irreversible, as a result of irreversible plastic deformation, rearrangement of particles or agglomerates from a loosely packed bed to a close-packed bed [36].

Therefore, the re-fluidization of the bed will start from a different height (compared to the end of the initial fluidization) due to the compression process. A lower bed height results in a higher bulk density, higher interparticle cohesion effects, and lower flowability.

4.3.2 Re-fluidization tests

Re-fluidization was performed after compression tests as the last step of each experiment to investigate the history effect and to compare the behavior of different mixtures of materials after consolidation. As explained previously, three different pressure levels were systematically considered. The results of the re-fluidization tests will be shown on the diagrams for the intermediate pressure level (40 kPa); the additional results related to low and high pressures will be reported in tables in the interest of space.

4.3.2.1 Re-fluidization of pure materials (macro-scale)

First, results for pure materials (100% of fine and 100% of ultra-fine) are discussed. Figures 4.6 and 4.7 show the fluidization curves (bed pressure drop versus superficial gas velocity (U_{sg})) for initial fluidization and re-fluidization of pure ultra-fine and pure fine particle beds, respectively.

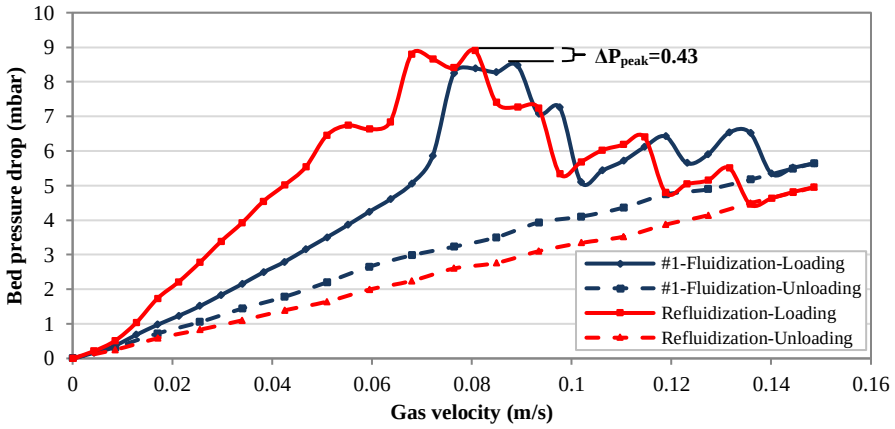

Fig. 4.6 Fluidization and re-fluidization behaviors (after compression at 40 kPa, intermediate pressure) for ultra-fine powder (CALCIT MX-10).

The fluidization, compression, and re-fluidization (FCR) experiments were repeated three times each, in order to increase the statistical significance of the analysis. Though the individual repetitions differ when involving ultra-fine powders in the beds [50], these repetitions show that the key quantities discussed in what follows, the increase in bed pressure drop at the peak point ΔP_{peak} and the corresponding superficial gas velocity, are nearly the same for all three repetitions. As a consequence, only the average values are listed in what follows.

The history effect can be quantified by measuring the increase in bed pressure drop between the peak points of the initial fluidization curve and the curve showing re-fluidization after compression (denoted ΔP_{peak} in Figures 4.6 and 4.7). In all these figures, loading means the variation of the bed pressure drop during the increment of the gas velocity (solid lines) and unloading means the variation of the bed pressure drop during the reduction of the gas velocity (dashed lines). The corresponding results when

compressing at different pressure levels are presented in Table 4.5.

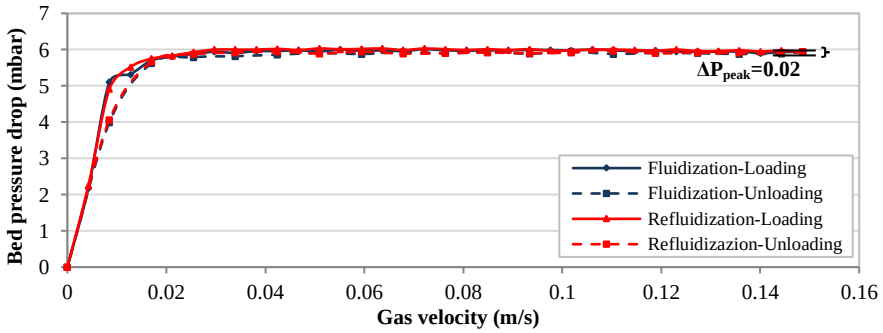

Fig. 4.7 Fluidization and re-fluidization behaviors (after compression at 40 kPa, intermediate pressure) for fine powder (CALCIT MVT-100).

Table 4.5 reveals the impact of the pressure applied during the compression step on ΔP_{peak} for the two pure materials (CALCIT MVT-100 and CALCIT MX 10). Increasing the applied pressure results in increasing ΔP_{peak} for both materials. However, the increment of ΔP_{peak} for the ultra-fine cohesive powder bed is an order of magnitude larger than for the fine particle bed.

After the initial fluidization, the powder bed of ultra-fine particles shows a loosely packed condition with low consolidation; the height of the bed denotes a lower bulk density, resulting in higher compressibility. During compression, decreasing the distance between particles results in an increase in the cohesive forces between them. For the fluidization of a consolidated bed, the applied force should be enough to overcome the extra forces due to the consolidation effect in the bed.

Table 4.5 Differences between peaks of pressure drop (ΔP_{peak}) in fluidization and re-fluidization after compression, in mbar (Mean ± Standard deviation)

FCR test	MVT-100	MX-10
Applied pressure (kPa)	ΔP_{peak} (mbar)	
20	0.01±0.006	0.27±0.025
40	0.02±0.006	0.43±0.035
80	0.04±0.006	0.69±0.035

For the case of fine particles, due to the weaker cohesive forces between them, the arrangement of particles after initial fluidization is denser; this leads to a higher bed bulk density and lower compressibility index. Thus, the effect of compression on the fine particle bed is much lower.

4.3.2.2 Re-fluidization of different mixtures of fine and ultra-fine particles materials (macro-scale)

In the following, the effect of the presence of some percentage of ultra-fine particles in a fine particle bed on ΔP_{peak} is investigated. Figures 4.8, 4.9, and 4.10 show the results of initial fluidization along with re-fluidization after compression at the intermediate pressure (40 kPa) for mixtures containing 30%, 50%, and 68% (weight ratio) of ultra-fine materials, respectively.

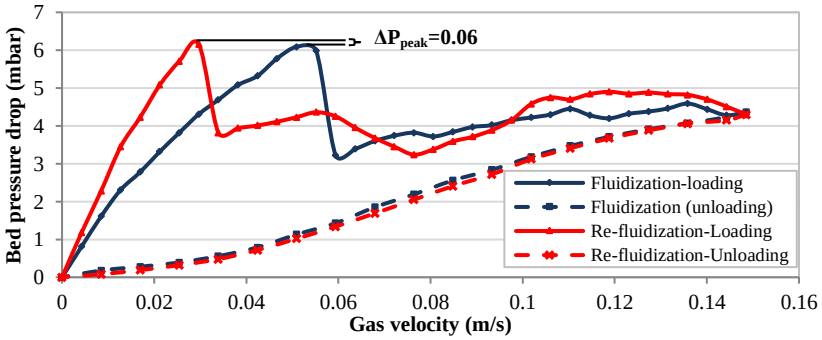

Fig. 4.8 Fluidization and re-fluidization behaviors (after compression at 40 kPa) for a mixture of 30% of ultra-fine + 70% of fine particles.

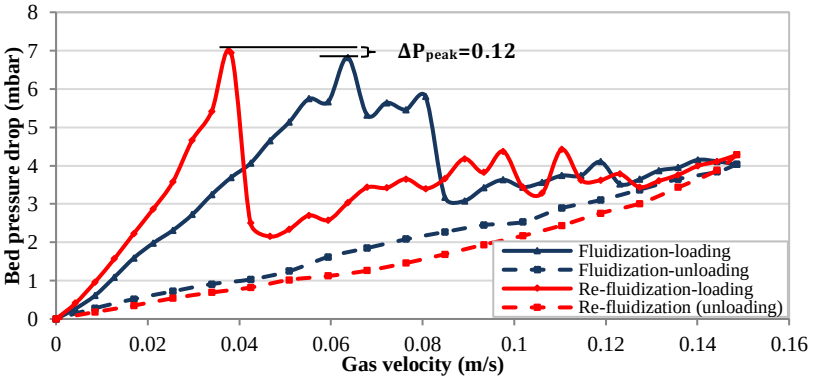

Fig. 4.9 Fluidization and re-fluidization behaviors (after compression at 40 kPa) for a mixture of 50% of ultra-fine + 50% of fine particles.

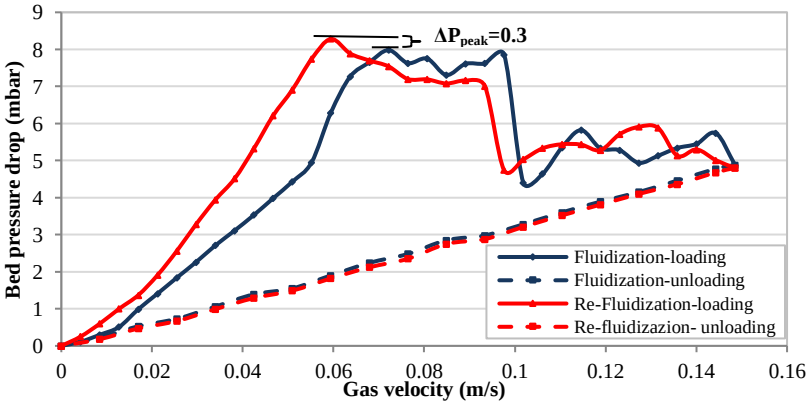

Fig. 4.10 Fluidization and re-fluidization behaviors (after compression at 40 kPa) for a mixture of 68% of ultra-fine + 32% of fine particles.

The results of increasing the peak of bed pressure drop (in the loading process) due to applying the other sets of compression pressures are summarized in Table 4.6. As can be seen from Table 4.6, when increasing the portion of ultra-fine particles, ΔP_{peak} increases monotonously; the lowest value of ΔP_{peak} is always related to the pure fine particles, the highest one to the pure ultra-fine powder (Table 4.5).

Table 4.6 Differences between peaks of pressure drop (ΔP_{peak}) in initial fluidization and re-fluidization after compression, in mbar (Mean ± Standard deviation)

	Mixture Ratio (% of Fine − % of Ultra-Fine)		
Applied pressure during compression (kPa)	70 − 30	50 − 50	32 − 68
	ΔP_{peak} (mbar)		
20	0.03 ± 0.01	0.06 ± 0.01	0.18 ± 0.015
40	0.06 ± 0.012	0.12 ± 0.012	0.30 ± 0.015
80	0.11 ± 0.012	0.21 ± 0.015	0.49 ± 0.025

Figure 4.11 shows the evolution of the normalized value of ΔP_{peak} (extracted from Tables 4.5 and 4.6 and normalized by the value of ΔP_{peak} for CALCIT MX 10 for the same applied pressure) for different mixtures. It can be seen that ΔP_{peak} does not rise linearly with increasing the portion of ultra-fine particles. It first shows a slow increase (with a small slope) with increasing the portion of ultra-fines until about 50% in the mixture. Then, a region with a rapid increase is found, between 50% and 70% of ultra-fine particles. Afterward, the slope decreases again. The normalized results are very close to each other for three different pressure levels employed during compression.

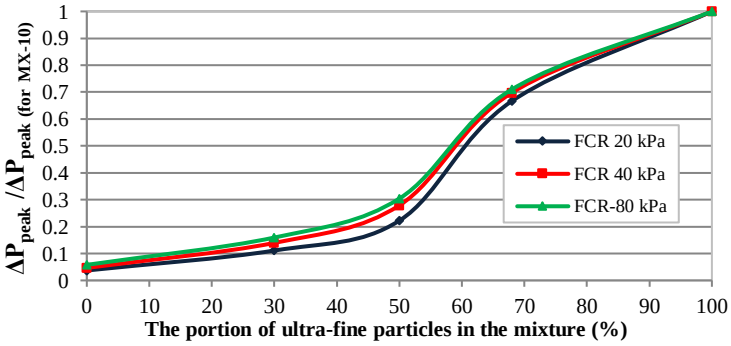

Fig. 4.11 Normalized value of ΔP_{peak} (using the value of ΔP_{peak} of ultra-fine particles for each pressure level) for fluidization, compression, and re-fluidization (FCR) tests at 20, 40, and 80 kPa compression pressure.

4.3.2.3 Analysis of the re-fluidization behavior at micro-scale

To interpret these measurements, micro-processes taking place during FCR tests should be considered. For the fine materials, after fluidization, the particles are close to each other and build a relatively dense arrangement. In addition, the resistance to the deformation of fine particles is higher than for ultra-fine powders (the decrease in particle size offers a

larger surface area and greater contact points [153]). As clearly stated previously, a similar phenomenon was reported by Tomas [138]: "Obviously, the finer the particles, the "softer" are the contacts and the more cohesive is the powder." Taking into account the initially denser arrangement as well as the reduced number of contacts, it can be concluded that the effect of compression is less marked for fine particles than for ultra-fine powders.

For different mixtures, taking into account the results discussed in [50] and using the Kozeny–Carman equation [154] for the unloading curve of initial fluidization shortly before reaching rest ($\mathrm{Re_p} < 1$), the mean value of the particle (agglomerate) size in the fluidization region can be estimated as:

$$d_a = \sqrt{\frac{150\mu L_0(1-\varepsilon)^2}{\varepsilon^3}\frac{U_{sg}}{\Delta P_b}} \tag{4-3}$$

where L_0 is the settled bed height (initial bed height), μ is the dynamic viscosity of the fluidizing gas, ε is the porosity of the particle bed and d_a is the mean value of the formed agglomerate size in the fluidization zone. By increasing the amount of ultra-fine powders in the mixture, L_0 is increased and ε is increased. Therefore, the ratio of $(1-\varepsilon)^2/\varepsilon^3$ sharply decreases. Considering the unloading curves near rest (left part of the diagram) in Figures 4.8-4.10, it is seen that the slope of $\Delta P_b/U_{sg}$ is also noticeably increased when increasing the portion of ultra-fine powders.

Consequently, Eq.(4-3) predicts a decrease in d_a when increasing the ultra-fine material in the mixture; the mean value of calculated agglomerates' size is decreased from 284 µm for 30% of ultra-fine portion in the mixture to almost 100 µm for pure ultra-fine powders during unloading (near to rest condition). In other words, at the end of the unloading process of the initial fluidization, the mean value of agglomerate size is predicted to be larger for the mixtures with a higher ratio of fine particles. In addition, due to fluidization, segregation might occur. Then, the coarser particles or agglomerates are positioned at the bottom of the bed and their available pores are filled by finer particles or agglomerates. The top part of the bed is preferentially formed by the finer agglomerates and particles.

Increasing the size of agglomerates, filling the pores by smaller ones, and decreasing the intensity of cohesiveness by increasing the portion of fine particles are the main reasons for a denser particle bed, as confirmed by the measurement of the bed height (or particle volume fraction). As a consequence, the effect of compression is decreased when the proportion of fine particles is increased; ΔP_{peak} for the mixtures with a higher ratio of fine materials is smaller. As long as there are less than 50% of ultra-fine powders in the mixture, ΔP_{peak} increases only slowly (see Fig. 4.11).

However, when the ultra-fine powders become dominant in the mixture, decreasing the

agglomerate size, increasing the intensity of cohesiveness, and decreasing the bulk density, lead to a much stronger impact of the compression process; ΔP_{peak} increases rapidly.

4.3.2.4 The role of ultra-fine powders in the mixture on the value and the corresponding superficial gas velocity of the peak point

Considering the superficial gas velocities corresponding to the maximum pressure drop (see Table 4.7) for each mixture of fine and ultra-fine particles (macro-scale), it is observed that the peak of bed pressure drop occurs at higher gas velocities when increasing the amount of ultra-fine particles in the mixture. This behavior is observed as well for the re-fluidization step. It can also be seen that the peak of bed pressure drop during re-fluidization systematically happens at a superficial gas velocity smaller than for the initial fluidization test. In other words, as visible in Fig. 4.8-4.10, the slope of the corresponding loading curve is much higher; the peak of the bed pressure drop is larger and obtained for a lower superficial velocity.

Table 4.7 Value and corresponding gas velocity of the peak in bed pressure drop (FCR test results) for the applied pressure of 40 kPa during compression.

	MVT 100	**30 – 70**	**50 – 50**	**68 – 32**	**MX 10**
FCR-Fluidization	6.01 mbar at 0.0467 m/s	6.09 mbar at 0.0509 m/s	6.82 mbar at 0.0637 m/s	7.98 mbar at 0.0722 m/s	8.47 mbar at 0.0891 m/s
FCR-Refluidization	6.03 mbar at 0.0255 m/s	6.15 mbar at 0.0297 m/s	6.94 mbar at 0.0382 m/s	8.28 mbar at 0.0594 m/s	8.90 mbar at 0.0806 m/s

From figures 4.8-4.10, it is observed that the opposite behavior occurs during the unloading process; i.e., the slope of the unloading curve is larger for the initial fluidization and (at least slightly) lower for re-fluidization after compression. Again, based on Darcy's law and according to the discussion of section 3.2.2.2 part b (unloading), the slope of the ΔP_b versus U_{sg} graphs is inversely correlated to the permeability of the particle bed.

Table 4.8 gives the corresponding values of the slope of all $\Delta P_b - U_{sg}$ curves for loading and unloading conditions, for initial fluidization, as well as for re-fluidization after compression test. All these results correspond to the intermediate pressure level (40 kPa) during compression. Table 4.8 indicates that the trends concerning the slopes (and thus bed permeability) are similar for initial fluidization and re-fluidization after compression. However, the compression step increases the slopes for loading condition, while decreasing them for unloading.

Table 4.8 Slope of $\Delta P_b - U_{sg}$ curves for fluidization and re-fluidization and for different mixtures (mbar·s/m)

		MVT 100 (100% Fine)	Mixture Ratio (% of Fine – % of Ultra-Fine)			MX 10 (100% Ultra-Fine)
			70 – 30	50 – 50	32 – 68	
Fluidization (FCR)	Loading	569	173	87	55	49
Fluidization (FCR)	Unloading	362	16	28	36	41
Re-fluidization (FCR)	Loading	583	259	125	78	73
Re-fluidization (FCR)	Unloading	359	13	22	28	33

Increasing the slope of the loading curve in re-fluidization is a result of the compression process; decreasing the distance between particles, decreasing the porosity, and consequently permeability and increasing the inter-particle cohesive forces, as occurs during consolidation. It results in a larger resistance to the airflow through the bed, particularly so for the mixtures containing ultra-fine powders.

Usually, agglomerates in cohesive powders (Geldart C) are not formed through a dynamic aggregation process between initially single particles [7] in the micro-scale. The enhancement of the interparticle attractive force by visco-plastic deformation at inter-particle contacts [155] gives rise to compact and strong agglomerates in the settled powders that cannot be easily broken by the kinetic energy of the gas flow, thus impeding the development of dynamic aggregation in the fluidized bed. Cohesive aggregation is responsible for heterogeneous fluidization behavior (Geldart C) [7]. After the re-fluidization loading, the unloading process starts. Then, the activated channels start to deactivate. When decreasing gas velocity, a new arrangement of particles forms.

When applying compression pressure, some of the particles' contact areas become flattened due to cohesive forces between close particles. For ultra-fine particles, these flattened contact areas share more contact surfaces with each contact; resulting in intense cohesive forces between them. Therefore, they can form greater agglomerates, leading to a more permeable bed. However, increasing the size of the agglomerates during the unloading stage is limited by the breakage of agglomerates due to the weight of the upper layers and collisions. On the other hand, in the mixtures with a higher portion of fine particles, increasing the number of coarser fine particles along with forming agglomerates by ultra-fine particles increase the permeability of the bed (decrease the slope of $\Delta P_b - U_{sg}$ curves).

4.4 Concluding remarks

This study is a comprehensive investigation about the effect of the presence of ultra-fine powders in a fine particle bed on compression and consolidation processes and also on the re-fluidization of the compressed and consolidated bed of a binary mixture. The

compression and fluidization of compressed beds are very important for the storage and flow of bulk materials. Discharging the consolidated material by fluidization aid is not like the fluidization of a loosed packed bed and the behavior of the bulk material is entirely different. These kinds of processes often happen in chemical, pharmaceutical, and food industries where the fine and ultra-fine particulate materials are used for producing different products.

- *Methodology:* Systematic measurements of the compression and re-fluidization behavior were conducted for different mixtures of fine and ultra-fine material fractions. The first step of each experiment (initial fluidization) was performed to minimize the initial level of stresses in the bed, before compression. Then, a compression step was carried out, using three different pressure levels. Finally, re-fluidization was the last step of the experiment to evaluate the effect of compression on the fluidization behavior of a compressed bed.
- *Compression:* The results of the compression step show that the compression behavior follows the logarithmic law for all three pressures levels (20, 40, and 80 kPa). The compressibility index is almost the same for the low and intermediate pressure levels. However, for higher pressures, the compressibility index decreases strongly due to a change in the compaction regime. Similarly, for the higher pressure, the slope of the particle volume fraction versus logarithmic display of dimensionless stress is noticeably different. The results of compression experiments further reveal that this slope does not depend on the size distribution of the mixtures but on the type of material itself.
- *Re-fluidization:* When analyzing the re-fluidization test results, history effects are observed leading to an increase in the bed pressure drop at peak point (ΔP_{peak}) between initial fluidization and re-fluidization of compressed bed. While the peak of the bed pressure drops increases, the superficial gas velocity corresponding to the peak point is smaller for re-fluidization after compression, compared to initial fluidization; consequently, the slope of the loading curve is much larger for re-fluidization. The opposite is observed for the unloading curves. When increasing the proportion of ultra-fine particles in the binary mixture, ΔP_{peak} increases as well, particularly strongly in the intermediate range of 50% to 70% of ultra-fine particles, when the ultra-fine powders start to be dominant in the mixture.

4 Fluidization, Compression, and Re-fluidization Test

CHAPTER 5

Fluidization, Compression, Permeation, and Re-fluidization Test

In this chapter, the results of the third class of tests performed in this study will be reported and discussed. To better understand the concepts and interpretation of the results, in the first part of this chapter, a targeted review on the permeation process and related phenomena will be presented. Then, the results of the tests will be thoroughly discussed.

5.1 Introduction

In this section, first, some important concepts of fluid flow through particulate or granular media, like porosity will be discussed. Then, Darcy's law and different mathematical or empirical models of fluid flow through particle beds will be introduced. Finally, these concepts and models will be utilized to evaluate the test results. Fluid flow through porous media is an important division of fluid mechanics. To scrutiny this issue, a combination of porous media theory, physical chemistry, surface physics, and even in some cases biology should be considered. Due to the large specific surface area and strong surface effect in particle beds, the viscous effect should be taken into consideration at all times.

Particle bed is a space occupied by a multiphase physical matter. In this matter, the solid phase is called particle fraction and the vacant space is called pore volume; which can be filled with gas, liquid or multiphase fluid. The pore space is normally interconnected so that the fluid can flow in them. The interconnected pore space is called effective pore space, while disconnected pore space is called dead pore space. For the flow of a fluid in a particle bed, pore space is considered as the void fraction. The shared pore structure is the inter-particle pore structure. It consists of solid particles with different shapes and sizes.

Pore structure in the particle bed provides free volumes for fluids to store and flow in. Porosity is a measure of the voids in the particle bed. The total volume V_t consists of pore volume V_p and solid particle volume V_s,

$$V_t = V_p + V_s \tag{5-1}$$

Porosity, ε, defines as the ratio of the pore volume to the total volume as:

$$\varepsilon = V_p/V_t = (V_t - V_s)/V_t = \left(1 - (V_s/V_t)\right) \tag{5-2}$$

Many-particle beds are made of discrete fine and coarse particles with a loose structure (unconsolidated particle bed). The consolidated bed is obtained from an initially unconsolidated bed after applying a compressive force and making durable interaction between particles in contact. Early studies on the porosity were led to a large extent by the study on the fields of chemical engineering, groundwater geology, and ceramics. In most of these studies, much interest was focused on the study of the porosity of unconsolidated beds. Their results showed that the porosity of unconsolidated beds depended on particle shape, packing, sorting, size distribution, as well as the compaction effects. The porosity of consolidated beds depends mainly on the degree of consolidation but also on the above-mentioned parameters for unconsolidated beds [156].

The cubical packing with a porosity of 47.6% is the minimum compact arrangement of uniform spheres. The maximum compact packing is related to the rhombohedra or close-packed arrangement of particles, where the porosity is only 26.0%. For equal size spherical particles, the porosity is independent of the diameter of particles. Figure 5.1 shows the mentioned packing arrangement. In addition to the arrangement, the particle size distribution may also affect the resulting porosity. Naturally, fine particles can occupy pores formed between coarser ones. Therefore, the porosity of packings consisting of both fine and coarse particles is reduced. On the other hand, sometimes due to the placement of fine particles in the contacts of coarser particles, the porosity increases during a phenomenon called bridging. In nature, for sub-millimeter particles, the porosity of particulate materials increases by decreasing the particle sizes. An increase in the range of particle size tends to decrease porosity [156].

Cubic arrangement of particles Rhombohedra arrangement of particles

Fig. 5.1 Two extremum arrangement of mono-size particles in the packing.

During compaction also a significant reduction in porosity may take place. Since compressive forces vary with depth, porosity will also vary with the depth of the bed. Krumbein and Sloss [157] showed a decrease in sand-stone and shale porosity from 52% to 41% and from 60% to 6% as depth increases from 0 to 2000m, respectively. Most of the pore decrease was due to the inelastic, accordingly irreversible effects of inter-particle movement. The external stress could lead to the compaction of the particle bed. Krumbein and Sluss [157] showed that the porosity of the sedimentary rocks is a function of the degree of compaction of the rock (Fig. 5.2).

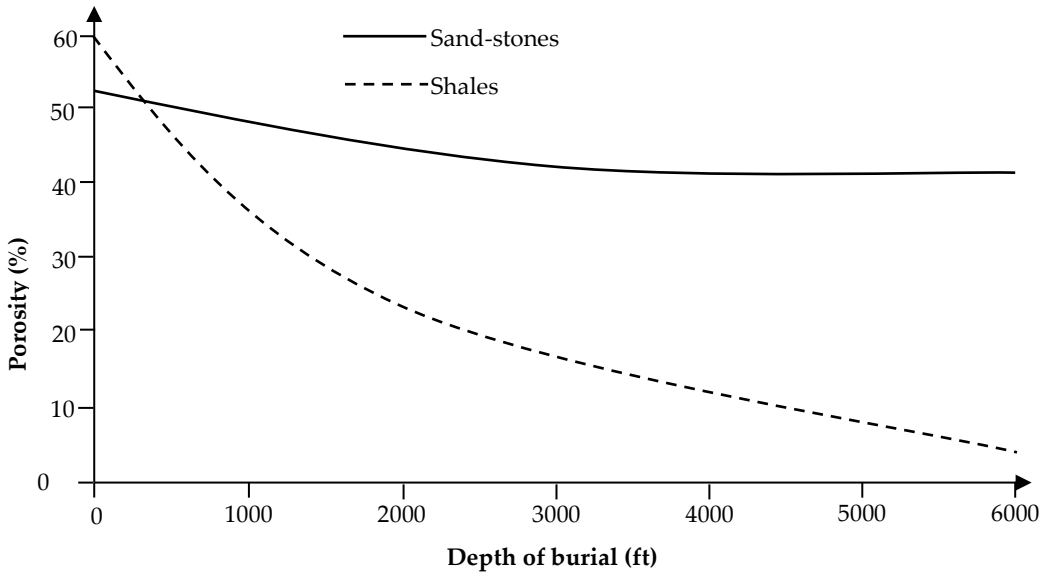

Fig. 5.2 Effect of compaction increment by depth on porosity decrease for two different materials in terms of size distribution. Reprinted from [157].

Porosity reduction due to the compaction effect is principally due to the packing rearrangement after compaction. The porosity is greatly decreased by compaction because the bridging phenomenon is suppressed by the greater forces.

The laws of the flow of fluids through porous media have several aspects of practical importance [158]. They are crucial in the movements of groundwater, petroleum, and natural gas through the soil and rock calculation, in determining the permeability of concrete and other building materials, and in deciding the extent of seepage through the subsoil of dams and of large buildings. Chemical engineers use such laws as the basis of the design of converters containing granular catalysts, as in the contact process for sulfuric acid, and of packed towers. These laws allow the interpretation of data extracted from small models used in the design of a full-scale plant [159]. Further, the study of flow through porous media is also used as the fundamental laws of filtration, both for the cake and for the filter medium. Therefore, the knowledge about the governing laws of fluid flow through a particle bed or porous media is of fundamental importance in many industrial, natural and constructional processes.

The fundamental equation of permeability is that of Darcy [160]. According to this law, when a fluid flows through a particle bed, there is energy loss due to the viscous effect. Darcy proposed [160] a fundamental relationship between fluid velocity and energy loss. Darcy law is an empirical equation based on measurements of the flow of water through sands and sandstones.

A schematic of the test rig of Darcy is shown in Fig. 5.3. The main part of the test rig is a vertical cylinder filled partly by sand particles as a particle bed (porous medium). Two manometers are connected to its wall. A filter is fixed at the bottom of the column, on which there are homogeneous sands. Water flows through the particle bed from the top, then flows out from the bottom into a container that is used to measure the flow rate; by measuring the volume of water collected in the container considering time. The overflow pipe at the upper side of the column is used to keep the water level constant in the column.

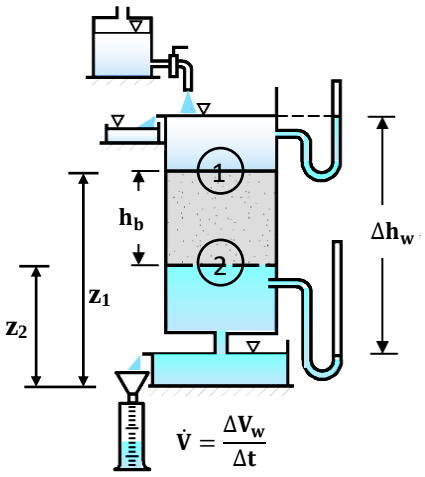

Fig. 5.3 Darcy experimental test rig.

After a given time, the flow rates of the output water are fixed and the water levels in manometers are also unchanged, which show that the flow is steady. Since the water velocity is moderately small, the head loss due to velocity is negligible. Therefore, the total head was equal to the revealed head of manometers and head loss Δh_w was equal to the difference between the two manometers' head. In fluid dynamics, Bernoulli's principle states that an increase in the velocity of a fluid in a specified section of the fluid flow occurs simultaneously with a decrease in the pressure or a decrease in the fluid's potential energy. Then, using Bernoulli's principle,

$$\Delta h_w = h_1 - h_2 = \left(z_1 + \frac{p_1}{\rho_f g} + \frac{v_1^2}{2g}\right) - \left(z_2 + \frac{p_2}{\rho_f g} + \frac{v_2^2}{2g}\right) \tag{5-3}$$

where Δh_W is the bed pressure drop; h_1 and h_2 are the manometer heads, p_1 and p_2 are static pressures, v_1 and v_2 are the fluid flow velocities at the top and the bottom of the column, respectively. In addition, ρ_f is the density of the fluid and g is the acceleration due to gravity. In this case, the velocity of the fluid on both sides of the bed are equal. Hydraulic gradient, HG, can be expressed using the bed pressure drop measured by manometers,

$$HG = \frac{\Delta h_W}{h_b} = \frac{(z_1 - z_2) + \frac{p_1 - p_2}{\rho_f g}}{h_b} = \frac{h_b + \frac{p_1 - p_2}{\rho_f g}}{h_b} = 1 + \frac{p_1 - p_2}{\rho_f g h_b} \tag{5-4}$$

where h_b is the height of the bed. Based on the analysis of experiment data, Darcy found that the flow rate $\dot{V}$, was directly proportional to the bed section area A and hydraulic gradient HG. Furthermore, it was relevant to sand properties, and which may be represented as:

$$\dot{V} = K \cdot A \cdot HG \tag{5-5}$$

where K is the hydraulic conductivity, which reflects the particle bed properties. Its dimension is the same as the velocity (m/s). In some studies, the hydraulic conductivity of the bed is called permeability. However, in this chapter, the permeability of the bed will be defined in what follows in accordance with most literature. The average velocity of the fluid in the cross-section area of the column (u) is defined as $(dV/dt)/A$, where A is the cross-section area of the bed, V is the volume of fluid flowing in time t. Thus, u can be calculated as

$$u = \frac{\dot{V}}{A} = K \cdot HG \tag{5-6}$$

In addition, experiments indicated that hydraulic conductivity, K_c, is directly proportional to the specific weight of the fluid $\rho_f g$ and inversely proportional to fluid dynamic viscosity, μ. Therefore,

$$K_c = \frac{k \rho_f g}{\mu_f} \tag{5-7}$$

where k is the ratio coefficient and normally named as permeability in most of the literature. Its dimension is the square of the length (m^2). Substituting Equations (5-5) and (5-7) in Equation (5-6),

$$u = \frac{k}{\mu_f}\left(\frac{\partial p}{\partial z} + \rho_f g\right) \tag{5-8}$$

In the horizontal cases, ignoring the gravity effect, Darcy's law can be simplified as

$$u = \frac{k}{\mu_f}\frac{p_1 - p_2}{h_b} = \frac{k}{\mu_f}\frac{-\Delta P_b}{h_b} \tag{5-9}$$

where ΔP_b is the pressure drop across the bed. In addition, k (permeability) is a constant depending on the physical properties of the fluid and bed. The negative sign in equation (5-9) is necessary as the pressure increases in one direction while the length increases in the opposite direction. "Darcy" is a practical unit of permeability. In a particle bed, the permeability is equal to 1 Darcy, if a pressure difference of 100 kPa (1 atm) causes a fluid flow rate of 1 cm^3/sec with 1 centipoise (cP) viscosity through a cube with 1 cm side length. The Darcy law is closely analogous to Poiseuille's law for the flow of a viscous fluid through a circular capillary tube as,

$$u = \frac{D_e^2}{32\mu_f}\frac{-\Delta P_b}{h_b} \tag{5-10}$$

where D_e is the equivalent diameter of the tube. This is the reason for considering the assumption that a particular bed is analogous to a group of capillary tubes parallel to the direction of flow and diameter, D_e, in many studies.

The first continuation of the Darcy law was made by Dupuit [161]. He realized that the apparent velocity, u, must be less than the actual velocity in the pores. If the pore-space in the bed is considered as a uniformly distributed voids between particles, the porosity of a layer of extremely small thickness normal to the direction of flow will be equal to the porosity, ε, of the bed as a whole. As, for such a layer, the fractional free volume will be equal to the fractional free area, the true velocity of flow must be u/ε. Therefore, the Darcy law could be re-written as:

$$u = \varepsilon\frac{k_1}{\mu_f}\frac{-\Delta P_b}{h_b} \tag{5-11}$$

The importance of porosity was later found out by Slichter [162]. He supposed that the average of cross-sections of the equivalent channels is triangular. Then, he derived the required expressions for the cross-section area and the length of these channels in terms of particle size and of porosity. Thereafter, considering a correcting factor to Poiseuille's law (for flow through a triangular cross-section channel), the permeability of the bed was calculated. The resulting equation was:

$$u = 10.2\frac{d^2}{K_2\mu_f}\frac{-\Delta P_b}{h_b} \tag{5-12}$$

where K_2 is a function of porosity. This parameter varies from 12.8 for $\varepsilon = 0.48$ to 84.3 for $\varepsilon = 0.26$. In the correlation of flow through smooth circular pipes, Stanton et al. [163], following on the work of Osborne Reynolds, have shown that a unique plot is obtained if

the dimensionless groups, $R/\rho_f u^2$ and $\rho_f u d_e/\mu_f$, are plotted against one another, where $R =$ frictional force per unit area, and $\rho_f u d_e/\mu_f$ is called the Reynolds number. For non-circular pipes, Schiller [164] has shown that, in the turbulent region, the correlation is still in place if $R/\rho_f u^2$ is plotted against $\rho u r_h/\mu_f$. The factor $r_h = \frac{\text{cross-section area normal to flow}}{\text{perimeter presented to fluid}}$ is called mean hydraulic radius. For a circular pipe, $r_h = d_e/4$. Considering a uniform cross-section of the pipe, an alternative expression for r_h is $\frac{\text{volume of fluid in the pipe}}{\text{surface presented to fluid}}$.

The resistance to the flow of a fluid through a pipe had been shown by Stanton and Parnell [163], using dimensional analysis, to be:

$$\frac{\Delta p}{h_b} = k_1 \frac{u^2 \rho_f}{D_h} \left[\frac{D_h \cdot u \cdot \rho_f}{\mu_f}\right]^{n-2} \tag{5-13}$$

or in another form,

$$\frac{\Delta p \cdot D_h}{h_b u^2 \rho_f} = k_1 \left[\frac{D_h \cdot u \cdot \rho_f}{\mu_f}\right]^{n-2} \tag{5-14}$$

Where D_h is the hydraulic diameter. Blake [165] used dimensional analysis in a similar procedure and revealed that for the flow of fluid through particle beds follows:

$$\frac{\Delta p \cdot d_p}{h_b u^2 \rho_f} = k_2 \left[\frac{d_p \cdot u \cdot \rho_f}{\mu_f}\right]^{n-2} \tag{5-15}$$

Passing different fluids such as water or air through beds of glass beads and rings, Blake [165] indicated that for a given particle bed (with the particle diameter, d_p):

$$\frac{\Delta p}{h_b u^2 \rho_f} = k_3 \left[\frac{u \cdot \rho_f}{\mu_f}\right]^{n-2} \tag{5-16}$$

By plotting values of $\frac{\Delta p \cdot d_p}{h_b u^2 \rho}$ against $\frac{d_p \cdot u \cdot \rho}{\mu_f}$, the points did not lie on the same curve. It revealed that the pressure drop is affected by particle diameter and hence voidage. Blake [165] tried to account for the effect of change in voidage on the resistance by replacing d_p by the mean hydraulic radius of the packing ($r_h = \varepsilon/S$), and accepting Dupuit's assumption that the interstitial velocity u_e equals u/ε (where S is the surface of packed bed per unit volume of bed and ε is the void fraction of the bed). By substituting the new relations in equation (5-15) for conditions in the streamline region where $n = 1$:

$$\frac{\Delta p}{h_b} = k_K \cdot \mu_f \cdot u \cdot {S_0}^2 \frac{(1-\varepsilon)^2}{\varepsilon^3} \tag{5-17}$$

(where S_0 is the surface to volume ratio of the particles and $S = S_0\,(l-\varepsilon)$ is the surface of the packed bed per unit volume and of bed). Equation (5-17) can be rearranged as:

$$k_K = \frac{\Delta p \cdot \varepsilon^3}{h_b \cdot \mu_f \cdot u \cdot {S_0}^2 \cdot (1-\varepsilon)^2} \tag{5-18}$$

where k_K is known as the Kozeny constant. Equation (5-18) was discussed by Kozeny [166]. Carman [158] reviewed the work of Blake, Kozeny, and others. He demonstrated the general applicability of Blake's method of dimensional analysis. For the special case of streamline flow, from permeability measurements, he independently derived the Kozeny equation. Carman's correlation of the data showed that for streamline flow

$$\frac{\Delta p \cdot \varepsilon^3 \cdot \rho_f}{h_b \dot{m}^2 S} = k_K \left[\frac{\dot{m}}{\mu_f \cdot S}\right]^{-1} \tag{5-19}$$

where $\dot{m}$ is the mass flow rate of fluid flow through the bed. For the turbulent flow region, Carman found that $k_K = 0.4$. In addition, the power of the closed brackets on the right side of the equation is also changed to (-0.1). For spherical particles, using the following geometrical relationship, Carman correlated specific surface (S) to particle diameter (d_p):

$$S = 6\frac{1-\varepsilon}{d_p} \tag{5-20}$$

By considering the particle bed as a group of similar parallel channels with the same total internal surface and total internal volume as particle surface and pore volume, Kozeny [166] had derived the same equation. In addition to the previous assumption, Kozeny assumed further that the tortuous passage length (L_e) is longer than the height of the bed (h_b), and the fluid velocity in the channel correspondingly higher than if there was a straight vertical channel. The general law of streamline flow through a channel was derived as

$$u_e = \frac{-\Delta P_b}{L_e}\frac{{r_h}^2}{k_0 \mu_f} \tag{5-21}$$

where k_0 depended upon the shape of the cross-section of the channel and had the given values in Table 5.1 for various shapes [167,168]. This table revealed that in the region of streamline flow, the hydraulic radius does not affect the correlation. On the other hand, independent of the shapes, k_0 varied only in the range of 1.8 to 2.5. It is interesting to note that k_0 = 2.0 does not necessarily characterize a circular cross-section or even a shape similar to a circle. This fact could explain the success in applying Poiseuille's law for channels in the particle beds.

Table 5.1 Values of k_0 for streamline flow in various cross-sections.

Shape	k_0	Remark
I. Circle	2.0	Poiseuille's law.
2. Ellipse		
(a) Major axis = twice minor axis.	2.13	—
(b) Major axis = 10 by minor axis.	2.45	—
3. Rectangles		
(a) Length = breadth, i.e., square.	1.78	—
(b) Length=2 by breadth	1.94	—
(e) Length = 10 by breadth	2.65	—
(d) Length is infinite	3.0	—
4. Equilateral Triangle	1.67	—
5. Pipes with Core		
(a) Core set concentrically	2.0-3.0	—
(b) Core set eccentrically	1.7-3.0	Eccentricity <0·7
(c) Core set eccentrically	1.2-2.0	Eccentricity >0·7

Considering all of the mentioned assumptions, the Carman-Kozeny equation was derived to predict the pressure drop of fluid flow through spherical particles as:

$$\frac{\Delta p \cdot \varepsilon^3 \cdot \rho_f \cdot d_p}{6 h_b \dot{m}^2 (1-\varepsilon)} = f\left[\frac{d_p \cdot \dot{m}}{6\mu_f \cdot (1-\varepsilon)}\right]^n = f_{K-C} \tag{5-21}$$

When a fluid flows through a particle bed, McCabe et al. [169] recommended the Carman-Kozeny equation for predicting the pressure drop. Leva [170,171] did a considerable literature review as well as an experimental investigation of the flow of different fluids through packed particle beds. He found that an empirical correlation of data for a Carman-Kozeny type equation is possible. The resulting equation was:

$$-\Delta p = \frac{2f \cdot \dot{m}^2 \cdot h_b \cdot \lambda_L^{1.1} \cdot (1-\varepsilon)^2}{\varepsilon^3 \cdot \rho_f \cdot d_p} \tag{5-22}$$

where λ_L is Leva particle shape factor (dimensionless) and the friction factor can be calculated as:

$$f = \frac{-\Delta p \cdot \ \varepsilon^3 \cdot \rho_f \cdot d_p}{2 \cdot \dot{m}^2 \cdot h_b \cdot \lambda_L^{1.1} \cdot (1-\varepsilon)^2} \tag{5-23}$$

From fluid mechanics, it was found that the friction factor, f, is a function of the particle Reynolds number and also the particle roughness. For viscous flow, Leva found that equation (5-22) reduced to the form:

$$\Delta p = \frac{K \cdot \dot{m} \cdot h_b \cdot \mu_f \cdot \lambda_L^2 \cdot (1-\varepsilon)^2}{\varepsilon^3 \cdot \rho_f \cdot {d_p}^2} \tag{5-24}$$

Chilton and Colburn [172,173] used particle diameter d_p, as a measure of particle size and the superficial fluid velocity, u, as the measure of velocity. The pressure loss of fluid flow in a bed is a combination of enlargements and contractions of the passages and also surface friction. However, the required expressions to deal with these factors could not be measured. In their study, Chilton and Colburn used the following equation:

$$\frac{\Delta p}{h_b} = 2\Phi \left[\frac{d_p \cdot u \cdot \rho_f}{\mu_f}\right]\left[\frac{\rho_f \cdot u^2}{d_p}\right] \tag{5-25}$$

The variations in the voidage of the bed were not considered in their equation. The next works showed that the bed pressure drop is a function of the bed voidage. Using dimensional analysis to include the voids, ε, the surface roughness, the shape, and the size distribution of the particles in the bed as well as the wall effect, Rose [174,175] modified the method of Chilton and Colburn. He developed the following equation:

$$\frac{\Delta p}{\rho_f \cdot h_b} = \Phi \left[\frac{\mu_f}{d_p \cdot \rho_f \cdot u}\right]\left[\frac{u^2}{d_p}\right] f_1(\varepsilon) \cdot f_2\left(\frac{D}{d_p}\right) \tag{5-26}$$

where D is the bed column diameter. For very fine particles, Brownell and Katz [176] obtained correlated results and suggested that by using a modified Reynolds number and a proper friction factor, the curve of Reynolds number against friction factor for packed particle beds could be superimposed on the corresponding curve for pipes. They tried to perform this suggestion by including the void fraction value raised to different powers in both the Reynolds number and the friction factor.

$$\frac{-\Delta p}{\rho \cdot h_b} = \left[\frac{d_p \cdot u \cdot \rho_f}{\mu_f \cdot \varepsilon^m}\right]\left[\frac{\rho_f \cdot u^2}{d_p}\right]\left(\frac{1}{\varepsilon^n}\right) \tag{5-27}$$

The pressure drop of the flow of a fluid through a packed particle bed depends upon the flow rate of fluid, the fluid density and viscosity, the proximity, and orientation of the particles in the packing and the particles' size, shape and surface properties [63]. To describe the energy loss in the passage of fluid through a packed particle bed, various equations have been developed. Ignoring the kinetic energy loss, the Carman-Kozeny equation (a modified form of Eq. 5-21) is used to calculate the pressure drop for laminar flow through packed beds [177].

$$-\frac{\Delta p}{h_b} = 180\,\frac{(1-\varepsilon)^2 \cdot u \cdot \mu_f}{\varepsilon^3 \cdot {d_p}^2} \tag{5-28}$$

Ergun and Orning [178] indicated that for the fixed bed region, the ratio of the pressure gradient to superficial fluid velocity in packed beds is a linear function of fluid mass flow rate. Using the air permeability method, they investigated different methods for

determining the specific surface of powders. For fluid flow at low velocities through fine particles, they revealed that the viscous forces are accounted for through the pressure drop. While, for higher velocities, kinetic effects became more important. However, the kinetic effects did not account for the pressure drop without using some factors which in turn are functions of flow rate. By incorporating both viscous and kinetic energy losses, Ergun [63] developed another equation (5-29). This equation, thus, holds true for calculation of pressure drop for both viscous and inertial flow across packed particle beds.

$$-\frac{\Delta p}{h_b} = 150\frac{(1-\varepsilon)^2 \cdot u \cdot \mu_f}{\varepsilon^3 \cdot {d_p}^2} + 1.75\frac{(1-\varepsilon)}{\varepsilon^3} \cdot \frac{\rho_f \cdot u^2}{d_p} \tag{5-29}$$

5.1.1 Parameters of packed bed

The correlations discussed heretofore may be used to investigate the fluid flow through packings of arbitrary shapes, on the condition that the packing characteristics and also bed parameters are obtainable. These parameters include particle diameter, sphericity or shape of particles, the porosity, particle's orientation, and surface roughness.
Pressure drop in packed beds is highly affected by particle orientation as well as by porosity. Martin et al. [179] studied the bed pressure drop of flowing water through spherical particles. They reported that for a tetragonal arrangement of particles with a porosity of about 0.3, the measured bed pressure drop in the turbulent flow condition was more than 20 times as high as for a bed consisting of the same particles in cubic arrangement with a porosity of about 0.476. It is worth noting that in the practical applications of a particle bed, such variations in orientation do not occur in a random packing. In fact, the above-mentioned example is only used to indicate the effect of orientation on the maximum difference of porosities of two extremum cases. If this range of voidage were experienced in a randomly packed bed the bed pressure drop increases only about five times [129].

For a packing consisting of particles with a specific size in a determined container, the porosity of the bed depends upon the packing method. Generally, if the particles are transferred to the container more slowly, the bed will be denser. Also, when particles have a smoother surface, denser beds will form. However, some other phenomena such as the vibration of the container and the effect of fluid (liquid or gas) flow through the bed can also cause the particle bed to be compressed, eventually. Although the importance of particle shape on the porosity is much more than surface roughness, both of these variables behave in the same way. The lower the particle sphericity, the more open is the bed. The dependence of porosity and the packing method upon sphericity of mono-size particle beds is shown in Fig. 5.4.

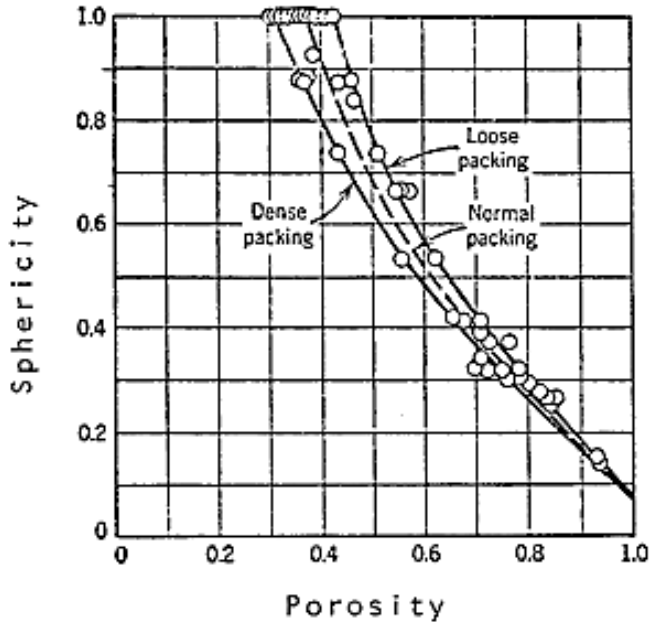

Fig. 5.4 Sphericity as a function of porosity and packing condition for randomly packed beds of mono-sized particles, reprinted from [180].

The presence of fine and coarse particles together in a packed bed results in a lower porosity than a uniform mono-sized particle bed. In fact, for the first case, fine particles fill the spaces between the larger ones. In general, the wider the range of particle sizes, the lower is the porosity obtained [181].

5.1.2 Measurement of permeability

The permeability of a porous medium can be determined from the samples extracted from the formation or by in-place testing such as well logging and well testing. Measurement of permeability in the case of isotropic media is usually performed on linear, mostly cylindrical-shaped, "core" samples [156]. Pressure applied on the surface of the sample as confining pressure. A suitable sample pressure gradient is adjusted and the rate of airflow through the sample is measured. The permeability can be found from equation (5-11). Considering experimental error, permeability can be determined for viscous flow conditions by obtaining data at several flow rates and plotting the flow rate versus pressure drop, as shown in Figure 5.5.

A linear function is fitted to the extracted data. According to Darcy's law, the slope of this line is k/μ, and this line must pass through the origin of the coordinates. However, the airflow rate does not depend on the pressure drop at ultra-low flow rates. Therefore, the extrapolation of Darcy's law to the origin is not true. At high flow rates, there is a deviation from the straight line. It is an indication of turbulent flow (Fig. 5.5). This deviation reveals that in turbulent flow condition, the pressure drop is higher than in viscous flow. By increasing the pressure drop, the flow rate is saturated to a maximum

value indicating the maximum capacity of the particle bed to pass the flow. After that flow rate will not increase by increasing the pressure drop.

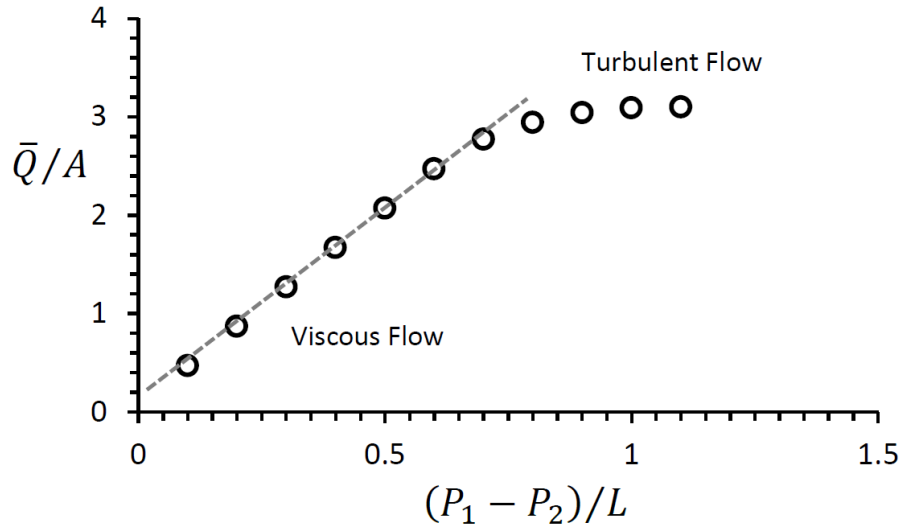

Fig. 5.5 Plot of typical data extracted from experiments for calculation of permeability

5.1.3 Effect of applied pressure

When the applied pressure exceeds the fluid pressure in the pore space, the particle bed is compacted. The porosity, permeability, and compressibility are reduced. To illustrate the effect of applied pressure, consider an unconsolidated bed. At low pressures, the bed is loosely packed, and there is a lot of space for particles to realign under pressure. Generally, the pore throats are relatively large to pass the fluid. Hence, the compressibility, porosity, and permeability are high. When the pressure increases, the particles are forced into close contact, and there is less space for the realignment. Hence, porosity and compressibility decrease. The compaction of the particles also decreases the size of the pore throats. Therefore, the permeability is also decreased.

5.2 Experimental methodology

The experimental apparatus for this study with all of its components have been already described in chapter 2; the details can be found there. In this series of tests, each experiment involves four steps: (1) initial fluidization, (2) compression of the bed (starting from a low level of consolidation), (3) permeation of air through the consolidated bed, and (3) re-fluidization of compressed, consolidated, and permeated particle bed, as depicted in Fig. 5.7.

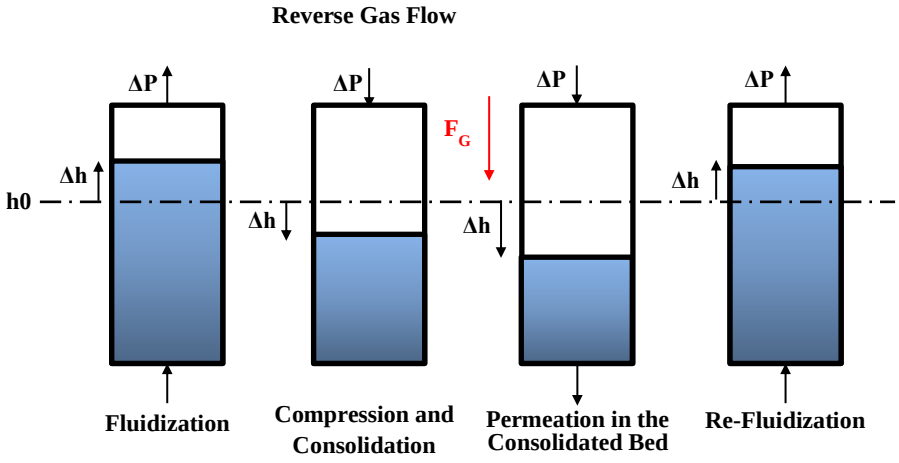

Fig. 5.7 Working principle for each experiment, involving four steps (Fluidization, Compression, Permeation, and Re-fluidization).

In the fluidization and re-fluidization process, the dried air used as fluidization gas enters the system from the bottom of the bed and, after passing through the bed, exits from the top of the bed. Conversely, for the compression and permeation tests, the dried compressed air comes to the system from the top side. Although for compression, there is not any exit for the airflow, for permeation, air exits from the bottom of the column after passing through the particle bed (from valve V3 in Fig. 2.12).

Similar to the previous chapters, in this chapter also, two mixtures with a dominant mass fraction of either fine or ultra-fine particles and a mixture of these two materials in the same weight fraction will be considered; i.e., the portions of ultra-fine powders in the mixtures are again 30%, 68%, and 50%, respectively.

5.3 Experimental results

The influence of adding ultra-fine particles on the fluidization of a fine particle bed has been previously researched in chapter 3. In chapter 4, in addition to fluidization, the effect of the presence of ultra-fine powders in a fine particle bed has been investigated in initial fluidization, compression and consolidation, and finally in the effect of compaction process on the re-fluidization process. Since the initial fluidization and compression process was described thoroughly in chapter 3, it will not be repeated here. In this chapter, the goal of the study is the investigation on the additional process of permeation of air in the compressed bed after compression (with the same level of pressure applied in the compression stage), and also on the combined effect of compression and permeation on re-fluidization of compressed, consolidated, and permeated bed.

5.3.1 Permeation of air in the consolidated bed

Permeability is a measure of the particle's resistance to fluid flow. The relative difference in air pressure between the top and the bottom of the particle bed in a column is a function of the air permeability through the bed. The tests here are designed under the same range of applied stresses as the compression tests and by measuring the airflow rates. Permeability is utilized in many applications, such as tableting and filling. For example, in a tableting process, the capability of air removal during the compression process will influence the mechanical properties of the compacted tablet. Capping or lamination may occur, therefore, if the air is maintained within the tablet due to low powder permeability. Within a filling process, the ability of the air to flow back out of the die (or container) through the particles depends on the bulk permeability. The backflow has a crucial influence on filling rate and filling consistency.

Since permeability is an important property of the bulk material in many processes and applications, it should be accurately measured. The permeation test results could help scientists and engineers to better design the process components and to troubleshoot the problems in different processes. In the permeation tests, the relative difference in air pressure between the top and bottom of the bed is set at the same values used in chapter 4 (see Table 4.2). This means that after unloading the applied pressures in the compression test, the released bed again is pressurized by the same range of applied pressures (with the same equal four sub-steps). However, in these steps, the V3 valve (Fig. 2.12) is open and after passing through the bed, the air goes out from the bottom of the column.

Simultaneously, at each step of the pressure increment, the rate of airflow through the particle bed is carefully measured and recorded. Combining with the measurement of the height of the bed in each sub-step, the permeability can be calculated from Eq. 5-11. In the following, the effect of different parameters on derived ones and on the permeability of the bed will be studied and discussed in the permeation tests.

5.3.2 Effect of the pressure difference between the two sides of the bed on the superficial gas velocity of the airflow

Figure 5.8 shows the effect of the pressure difference between the two sides of the bed (ΔP) on the superficial gas velocity of the airflow (u). In these graphs, the calculated superficial gas velocities (based on the measured flow rates of air) are drawn for different adjusted pressure levels. The graphs (a) to (e) show the results for different mixtures of the materials. In each graph, the changes of superficial gas velocities are drawn for three levels of applied (set) pressures (20, 40, and 80 kPa).

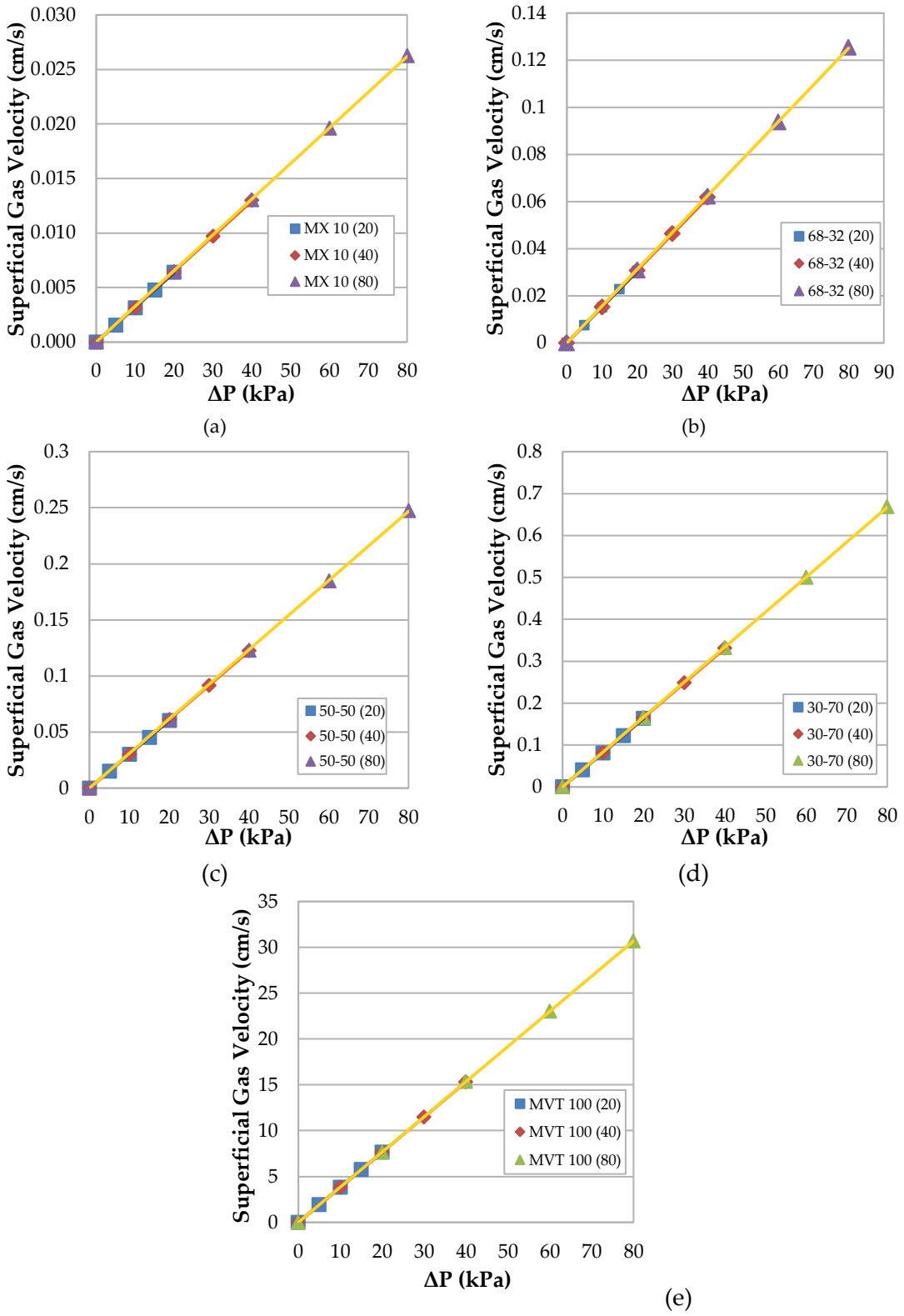

Fig. 5.8 The pressure difference between the two sides of the bed versus the superficial gas velocity of the airflow for different combinations of fine and ultra-fine particles; (a) MX 10 (100% of ultra-fine powders), (b) 68-32 (68% ultrafine-32% fine), (c) 50-50, (d) 30-70, and (e) MVT 100 (100% fine particles)

The rates of increasing air velocity in the particle beds for all levels of adjusted pressure differences (slope of the fitted lines to the experimental results) and also for different mixtures of materials are summarized in Table 5.2.

Table 5.2 The rates of increasing air velocity for all levels of adjusted pressure differences and for different mixtures of materials.

		MX 10 (100% of ultra-fine)	(% ultra-fine - % fine)			MVT 100 (100% fine)
			68-32	50-50	30-70	
		(cm/s)/kPa or 10 (m²·s)/kg				
Pressure level (kPa)	20	0.000318	0.00152	0.00302	0.00818	0.3821
	40	0.000323	0.00154	0.00306	0.00828	0.3829
	80	0.000327	0.00156	0.00308	0.00834	0.3835

The results of the graphs in Fig. 5.8 considering the value of the slope of fitted lines summarized in Table 5.2 can be summarized as follow:

The graphs show that by increasing the pressure differences between both sides of the bed at all the pressure levels, the superficial gas velocities also increase. This behavior easily could have been predicted. In fact, considering that fluid flow paths in a particle bed are equivalent to very small tubes, and also with the help of the Poiseuille's law (Equation (5-10)), increasing pressure on the two ends of the fluid carrier tube will increase the fluid velocity therein.

In addition, Table 5.2 indicates a relatively small increase in the rate of increasing air velocity by increasing the pressure difference level. Ignoring this limited increase in the slopes (rates of increasing air velocity), it can be concluded that for all levels of adjusted pressures, the slopes of the linear fitted lines related to each mixture of material are almost constant for this range of applied pressures. It shows a similar trend of increase in gas velocities for all pressure levels. The linear behavior of increasing the gas velocity by increasing applied pressure also indicates laminar flow even at the highest pressure level (as explained in Fig 5.5).

Table 5.2 also reveals that by increasing the ultra-fine powders in the mixtures, the slopes of fitted lines are decreased. It means that for the same pressure adjustment, the mixtures containing more ultra-fine powders experience a lower increment in the air velocity. In fact, due to the smaller pore diameter, the air velocity through the mixtures containing more ultra-fine powders is much smaller than to mixtures with a dominant amount of fine particles. Therefore, although the rates of decreases in the porosity and also height are larger for mixtures dominated by ultra-fine powders, limited changes in the pore sizes

and also the formation of preferred pathways of flow in this kind of beds result in a smaller change in the fluid velocity as the pressure level increases.

By adding the ultra-fine powders in the particle bed, even for only 30% of ultra-fines in the mixture, the slope of fitted linear curves indicates a fundamental change (about 50 times smaller) in the permeability of the mixture material. By increasing the ratio of ultra-fine powders in the mixture, the height and then the porosity of the bed are increased and simultaneously the mean particle diameter is decreased. Although the ratio of the volume of pores to the total volume of the bed (porosity) increases by increasing the ultra-fine particles, however, the size of the inter-particle pores becomes too small; results in increasing the bed resistance to the fluid flow. Therefore, the effect of decreasing the mean particle diameter plays a key role in reducing permeability. In fact, it causes a decrease in the slope of the curve (proportional to permeability).

5.3.3 Effect of porosity on permeability

Figure 5.9 shows the effect of porosity on the calculated permeability. In this figure, the vertical axis (permeability) is drawn based on milliDarcy (mD).

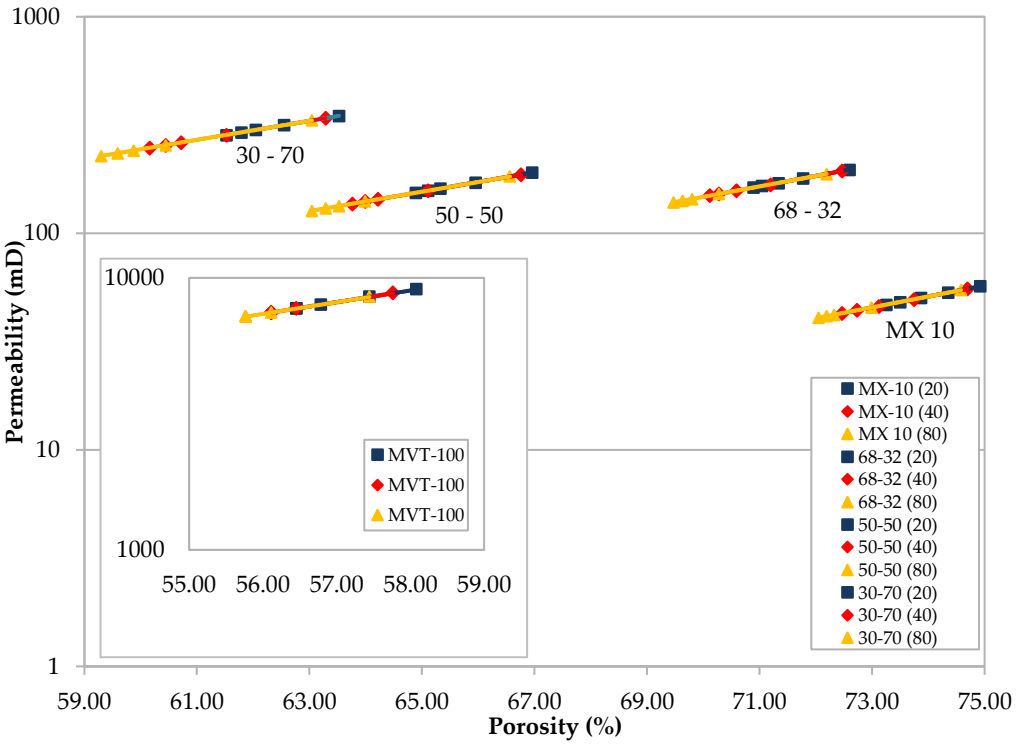

Fig. 5.9 Permeability of different mixtures as a function of porosity of the bed

According to the definition of Darcy, each m^2 (as SI dimension of permeability) is equal to 1013250273830886.6 mD. This figure reveals that by increasing the percentage of ultra-fine powders in the mixture, the slopes of permeability vs. porosity curves are increased.

It means, by increasing porosity, the change in the permeability for a certain range of applied pressure is decreased. The permeability is revealed based on a logarithmic scale. According to this figure, the logarithmic presentation of permeability shows a linear relation with the porosity of the bed. Considering this issue, their correlation can be written as follows:

$$\ln k = A\varepsilon + \ln k_0 \tag{5-30}$$

where k_0 is a constant. In this equation, permeability is based on milliDarcy and porosity is based on (%). Table 5.3 summarizes the coefficients A and k_0 for different mixtures of fine and ultra-fine particles.

Table 5.3 The coefficients of Equation (5-31)- Extracted from fitted lines.

Coefficient	Pressure level (kPa)	MX-10	68-32	50-50	30-70	MVT-100
A	20	0.1177	0.1126	0.1042	0.1014	0.0992
	40	0.1165	0.1118	0.1036	0.1009	0.09914
	80	0.116	0.1111	0.1033	0.1007	0.0991
k_0	20	0.0084	0.0553	0.1774	0.5564	28.528
	40	0.0092	0.0586	0.185	0.5728	28.604
	80	0.0096	0.0618	0.1893	0.5823	28.679

The extracted data of this table shows that the rate of changes in permeability by decreasing the porosity (A: the slope of the linear fit of Fig. 5.9) is higher for a mixture with a larger amount of ultra-fine powders. Also, the intercept of the line ($\ln k_0$), indicates three classes of behaviors. The first class is related to the ultra-fine material with k_0 in the average amount of 0.00907 (smaller than 0.01). The second class belongs to the mixtures of fine and ultra-fine particles with a mean value of k_0 in the range of 0.0586-0.571 (smaller than 1). Finally, the third class is related to the fine particle bed with k_0 in the average amount of 28.6. Although in this classification, the ultra-fine powders and three mixtures of fine and ultra-fine are classified in two different classes, their intercepts are close to each other. However, the range of intercept for fine particle bed is about two orders of magnitude greater than the results for even 30-70 mixture. It shows that adding ultra-fine powders to the fine particle bed totally changes the permeation behavior and the final behaviors of the mixtures are more similar to the ultra-fine powders.

For MX 10, the porosity is maximum and although the rate of decreasing in the permeability is higher than for other mixtures, the changes in the absolute amount of permeability by pressure increment is far less than the changes in the amount of permeability of MVT 100 (100% of fine material) for the same range of pressure increment. As mentioned before, because of establishing the preferred paths for passing the fluid in the beds with ultra-fine powders, changes in the pressure have less effect than for fine particles; where the pore sizes and the throat diameters of equivalent tubes are reduced

by increasing pressure difference. Table 5.3 indicates the classification of different materials based on their permeability.

Table 5.3 Classification of materials based on their permeability. (SGN presentation- https://www.hsl.gov.uk/media/1298372/06%20mark%20wheeldon.pdf)

Permeability	**Pervious**				**Semi-Pervious**				**Impervious**			
Unconsolidated sand and gravel	Well sorted gravel		Well sorted sand or sand and gravel		Very fine sand, silt, loess, loam							
Unconsolidated clay and organic					Peat		Layered clay		Unweathered* clay			
Consolidated rocks	Highly fractured rocks				Oil reservoir rocks			Fresh sandstone	Fresh Limestone , Dolomite		Fresh Granite	
k (cm2)	10^{-3}	10^{-4}	10^{-5}	10^{-6}	10^{-7}	10^{-8}	10^{-9}	10^{-10}	10^{-11}	10^{-12}	10^{-13}	10^{-14}	10^{-15}
k (milliDarcy)	10^{8}	10^{7}	10^{6}	10^{5}	10^{4}	10^{3}	10^{2}	10	1	10^{-1}	10^{-2}	10^{-3}	10^{-4}

* Not changed by exposure to the weather - Not changed through time, use, or exposure; as new

Figure 5.9 reveals that the range of permeability for MVT 100 is between 10^3 and 10^4 mD. According to Table 5.3, the fine material (MVT 100) is classified in the semi-pervious materials like peat (turf) or even well-sorted sands. However, adding ultra-fine powders to fine particles reduces mixture permeability to the range of 100 to 1000 mD; similar to the class of very fine sands such as silt, loess, and loam. In addition, Fig. 5.9 shows that the ultra-fine material has a permeability in the range of 10 to 100 mD. Therefore, it is classified in the semi-pervious (near to the impervious) materials such as layered clay.

5.3.4 Effect of pressure on permeability

Figure 5.10 shows the changes in the permeability of different mixtures of the particulate materials as a function of changes in the pressure difference between two sides of the bed. This figure shows that by increasing the applied pressure (the pressure difference between two sides of the bed), permeability is decreased. The trend of decreasing the permeability for all three levels of applied pressures is almost similar. For all three applied pressure levels, the rate of decreasing permeability in the first stages of applying pressures is far more than in the last stages of applying. While increasing the pressure to the maximum pressure of each level, the rate of changes in the permeability is decreased.

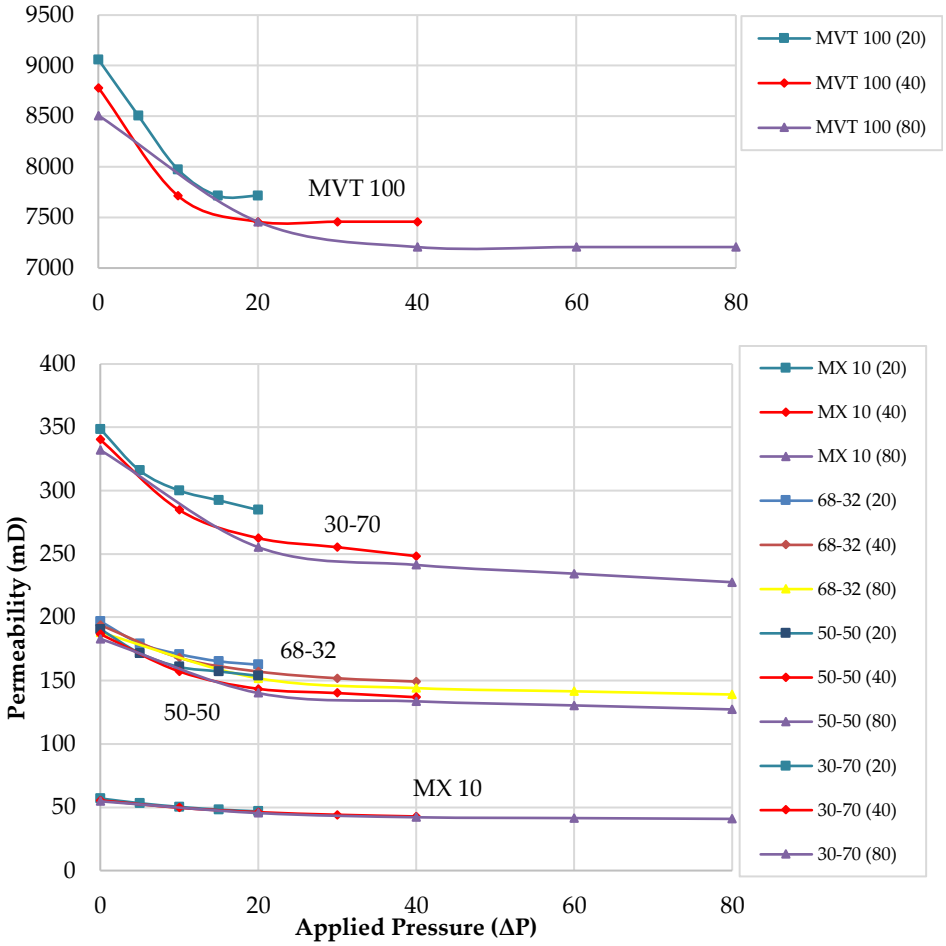

Fig. 5.10 Permeability of different mixtures as a function of the pressure difference between two sides of the bed.

At the first stage of applying pressure, the compaction of the bed is minimum. By increasing the pressure, it is going to be more compressed and consolidated; the observations revealed a larger decrease in the height of the bed for the first step of applying the pressure and a decreasing rate of changing bed height in the next steps (toward maximum pressure). In fact, by increasing the pressure, the position and orientation of particles in a more dense particle bed are in such a way that rearrangement of them and more decrease in the volume of the bed are more difficult than during the first steps.

Although it seems that by increasing the proportion of ultra-fine powders in mixtures, the permeability decreases, the experimental results show that a mixture containing 50% of ultra-fine powders has slightly smaller permeability values than a mixture with 68%. The tests related to these two mixtures were repeated five times, however, the results are the same. Considering the equations for calculation of the permeability (Eqs. (5-28) and (5-29)), it can be concluded that the sensibility of the permeability to the porosity is more

than to the mean particle size of the mixture. Figure 5.11 shows graphically the change in in the functions of $\varepsilon^3/(1-\varepsilon)^2$ and ${d_p}^2$ for the values between 0 and 1. This graph shows that the rate of change in $\varepsilon^3/(1-\varepsilon)^2$ (in the range of change in ε) is sharper than the rate of change in ${d_p}^2$ (in the range of change in d_p). Therefore, although the mean particle size for 50-50 mixture is more than for the 68-32 mixture, the porosity of 50-50 mixture decreases in such a way that the resulting permeability of the mixture of 50-50 is a little (3-6%) less than for the 68-32 mixture.

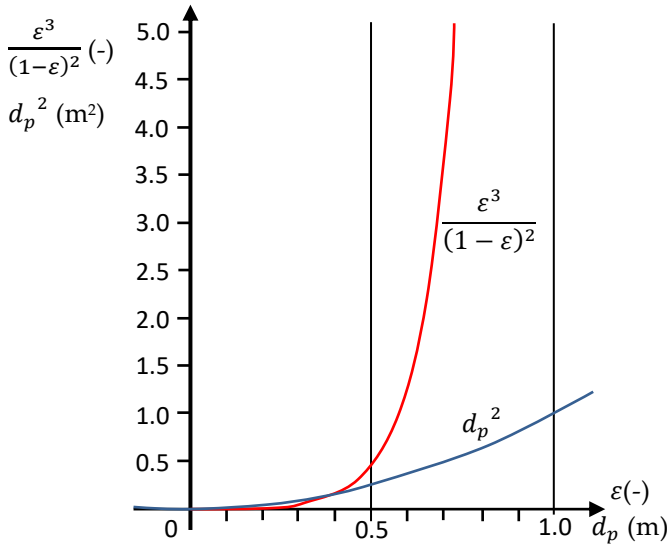

Fig. 5.11 Graph comparing the rate of changing in $\varepsilon^3/(1-\varepsilon)^2$ and ${d_p}^2$.

5.3.5 Re-fluidization tests

In these series of tests, re-fluidization was performed after permeation tests as the last step of each experiment, to investigate the history effect and to compare the behavior of different mixtures of materials after consolidation due to compression and permeation processes. As explained previously, three different pressure levels were systematically considered sequentially for both compression and permeation. Similar to the previous chapter, the results of the re-fluidization tests will be shown on the diagrams for the intermediate pressure level (40 kPa); the results related to low and high pressures will be only reported in tables in the interest of space. The analysis follows those of chapter 4.

5.3.5.1 Re-fluidization of pure materials (macro-scale)

First, the results for pure materials (100% of fine and 100% of ultra-fine) are discussed. Figures 5.12 and 5.13 show the fluidization curves (bed pressure drop versus superficial gas velocity (U_{sg})) for initial fluidization and re-fluidization of pure ultra-fine and pure fine particle beds after permeation tests, respectively.

Similar to previous sets of tests reported in chapter 4, the fluidization, compression, permeation, and re-fluidization (FCPR) experiments were repeated three times each, in order to increase the statistical significance of the analysis. Again, though the individual repetitions differ when involving ultra-fine powders in the beds [50], these repetitions show that the key quantities discussed in what follows, the increase in bed pressure drop at the peak point ΔP_{peak} and its corresponding superficial gas velocity, are nearly the same for all three repetitions. As a consequence, only the average values are listed in what follows.

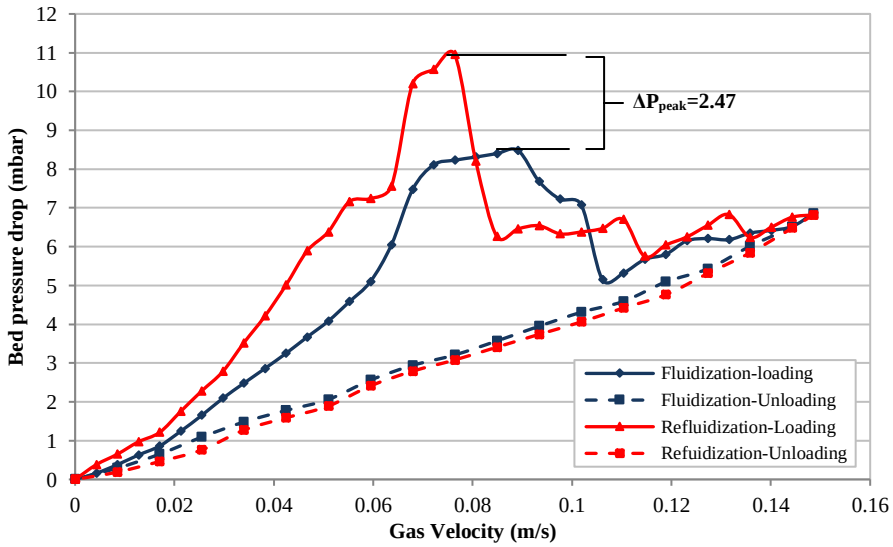

Fig. 5.12 Fluidization and re-fluidization behaviors (after compression and permeation at 40 kPa, intermediate pressure) for ultra-fine powder (CALCIT MX-10).

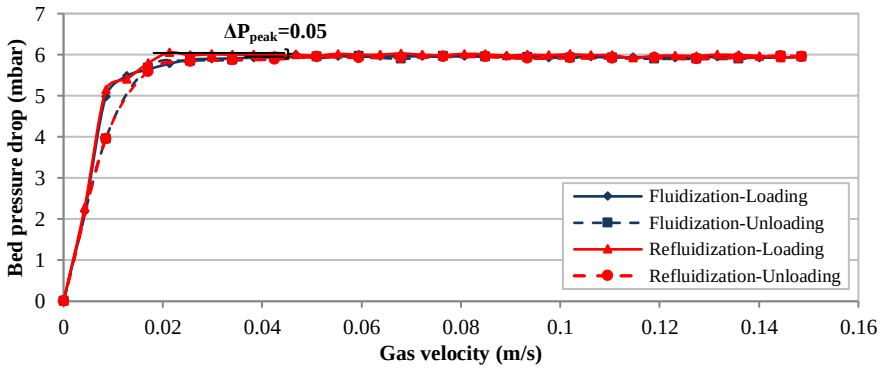

Fig. 5.13 Fluidization and re-fluidization behaviors (after compression and permeation at 40 kPa, intermediate pressure) for fine powder (CALCIT MVT-100).

The history effect can be quantified by measuring the increase in the bed pressure drop between the peak points of the initial fluidization curve and the curve showing re-fluidization after permeation (denoted ΔP_{peak} in Figures 5.12 and 5.13). In all these figures, loading means the variation of the bed pressure drop during the increment of the

gas velocity (solid lines) and unloading means the variation of the bed pressure drop during the reduction of the gas velocity (dashed lines). The corresponding results of ΔP_{peak} at different pressure levels are presented in Table 5.4.

Table 5.4 Differences between peaks of pressure drop (ΔP_{peak}) in fluidization and re-fluidization after compression and permeation, in mbar (Mean ± Standard deviation)

FCR test	MVT-100	MX-10
Applied pressure (kPa)	ΔP_{peak} (mbar)	
20	0.02±0.003	1.06±0.025
40	0.05±0.006	2.47±0.035
80	0.08±0.01	3.83±0.035

Table 5.4 reveals the impact of the pressure applied during the compression and permeation steps on ΔP_{peak} for the two pure materials (CALCIT MVT-100 and CALCIT MX 10). Increasing the applied pressure results in increasing ΔP_{peak} for both materials. However, similar to the results of chapter 4 for the compression effect on re-fluidization, the increase of ΔP_{peak} for the ultra-fine cohesive powder bed is much larger than for the fine particle bed.

After the initial fluidization, the powder bed of ultra-fine particles shows a loosely packed condition with low consolidation. During compression, decreasing the distance between particles results in an increase in the cohesive forces between them. What happens in permeation is something like a big compression. The most important factor for this effect is the rearrangement of particles due to the pressure difference between two sides of the bed and also the passing airflow through the bed. In fact, during permeation tests for every mixture, there is a larger change (decrement) in the height and (increment) in the bulk density than for the compression tests under the same level of applied pressure. Decreasing the height again results in decreasing the distance between particles and increasing the consolidation effect. For fluidization of a consolidated bed after compression and permeation, the applied force should be enough to overcome the extra forces due to the consolidation effect in the bed.

For the case of fine particles, due to the weaker cohesive forces between them, the arrangement of particles after initial fluidization is denser than ultra-fine powder bed; this leads to a higher bed bulk density and lower compressibility index. Thus, the effect of compression and then, permeation on the fine particle bed (denser bed) is much lower.

5.3.5.2 Re-fluidization of different mixtures of fine and ultra-fine particles materials (macro-scale)

In the following, the effect of the presence of some percentage of ultra-fine particles in a fine particle bed on ΔP_{peak} is investigated. Figures 5.14, 5.15, and 5.16 show the results of initial fluidization along with re-fluidization after compression and permeation at the intermediate pressure (40 kPa) for mixtures containing 30%, 50%, and 68% (weight ratio) of ultra-fine materials, respectively.

The results of increasing the peak of bed pressure drop (in the loading process) due to applying the other sets of compression and permeation pressures are summarized in Table 5.5. As can be seen in Table 5.5, when increasing the portion of ultra-fine particles, ΔP_{peak} increases monotonously; the lowest value of ΔP_{peak} is always related to the pure fine particles, the highest one to the pure ultra-fine powder (compare to Table 5.4).

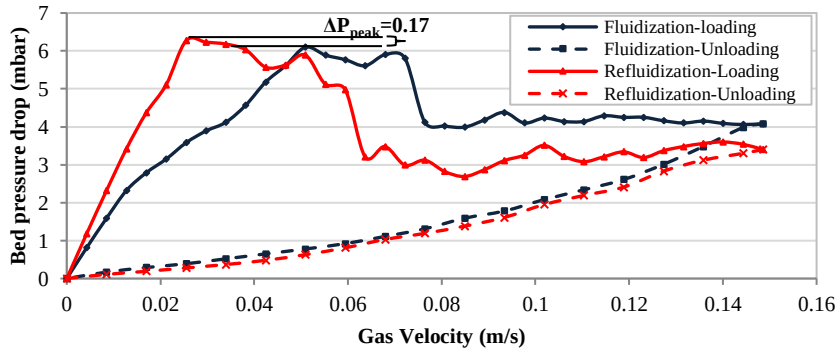

Fig. 5.14 Fluidization and re-fluidization behaviors (after compression and permeation at 40 kPa) for a mixture of 30% of ultra-fine + 70% of fine particles.

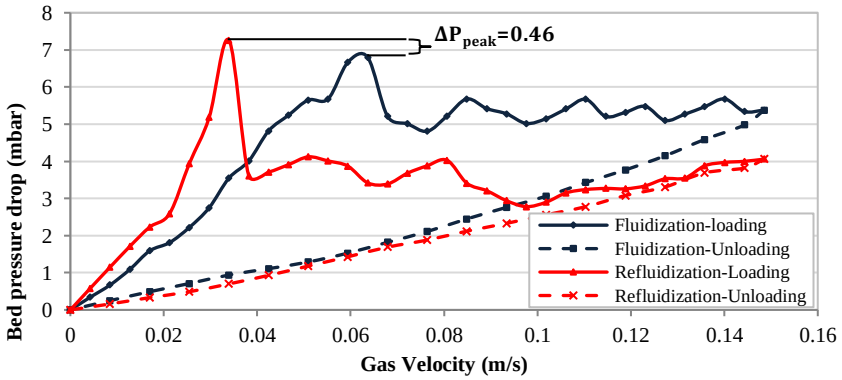

Fig. 5.15 Fluidization and re-fluidization behaviors (after compression and permeation at 40 kPa) for a mixture of 50% of ultra-fine + 50% of fine particles.

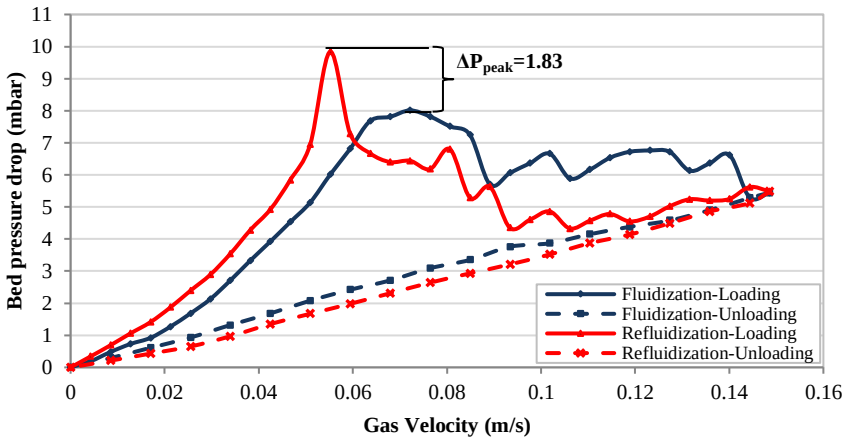

Fig. 5.16 Fluidization and re-fluidization behaviors (after compression and permeation at 40 kPa) for a mixture of 68% of ultra-fine + 32% of fine particles.

Table 5.5 Differences between peaks of pressure drop (ΔP_{peak}) in initial fluidization and re-fluidization after compression and permeation, in mbar (Mean ± Standard deviation)

	Mixture Ratio (% of Fine – % of Ultra-Fine)		
Applied pressure during compression (kPa)	70 – 30	50 – 50	32 – 68
	ΔP_{peak} (mbar)		
20	0.06 ± 0.01	0.19 ± 0.015	0.77 ± 0.02
40	0.17 ± 0.015	0.46 ± 0.015	1.83 ± 0.025
80	0.31 ± 0.015	0.76 ± 0.025	2.85 ± 0.03

Figure 5.17 shows the evolution of the normalized value of ΔP_{peak} (extracted from Tables 5.4 and 5.5 and normalized by the value of ΔP_{peak} for CALCIT MX 10 for the same applied pressure) for different mixtures.

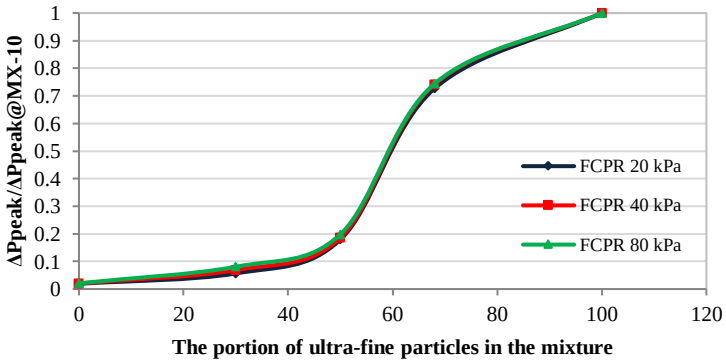

Fig. 5.17 Normalized value of ΔP_{peak} (using the value of ΔP_{peak} of ultra-fine particles for each pressure level) for fluidization, compression, permeation, and re-fluidization (FCPR) tests at 20, 40, and 80 kPa compression pressure.

It can be seen that again, similar to the compression tests, ΔP_{peak} does not rise linearly with increasing the portion of ultra-fine particles. The behavior of the evolution of the normalized value of ΔP_{peak} is completely similar to the behavior of compression tests

only. Again, it first shows a slow increase (with a small slope) when increasing the portion of ultra-fines until about 50% in the mixture. Then, a region with a rapid increase is found, between 50% and 70% of ultra-fine particles. Afterward, the slope decreases again. Although the trends of the normalized curves are similar to the trends of normalized curves for compression tests only, here, the slope of increasing normalized ΔP_{peak} for the first part (below 50% of ultra-fines in the mixture) and also for the last part (more than 68% of ultra-fines) is smaller. Therefore, the rate of increase in the normalized ΔP_{peak} between 50% and 68% is much sharper than the results for compression tests only. The normalized results are very close to each other for the three different pressure levels.

To interpret these measurements, it can be mentioned that increasing the size of agglomerates, filling the pores by smaller ones, and decreasing the intensity of cohesiveness by increasing the portion of fine particles are the main reasons for a denser particle bed, as confirmed by the measurement of the bed height (or particle volume fraction). As a consequence, the effects of compression and also permeation processes are decreased when the proportion of fine particles is increased; ΔP_{peak} for the mixtures with a higher ratio of fine materials is smaller. As long as there are less than 50% of ultra-fine powders in the mixture, ΔP_{peak} increases only slowly (see Fig. 5.17).

However, when the ultra-fine powders become dominant in the mixture, decreasing the agglomerate size, increasing the intensity of cohesiveness, and decreasing the bulk density, lead to a much stronger impact of the compression and also permeation process; ΔP_{peak} increases rapidly.

5.3.5.3 The role of ultra-fine powders in the mixture on the value and the corresponding superficial gas velocity of the peak point

Considering the superficial gas velocities corresponding to the maximum pressure drop (see Table 5.6) for each mixture of fine and ultra-fine particles (macro-scale), similar to the results of re-fluidization for compression tests in the previous chapter, it is observed that the peak of bed pressure drop occurs at higher gas velocities when increasing the amount of ultra-fine particles in the mixture. This behavior is observed as well for the initial fluidization step. Again, it can also be seen that the peak of bed pressure drop during re-fluidization systematically happens at a superficial gas velocity smaller than for the initial fluidization test. In other words, as visible in Figs. 5.12-5.16, the slope of the corresponding loading curve is much higher; the peak of the bed pressure drop is larger and obtained for a smaller superficial gas velocity.

Table 5.6 Value and corresponding gas velocity of the peak in bed pressure drop (FCR test results) for the applied pressure of 40 kPa during compression.

	MVT 100	30 – 70	50 – 50	68 – 32	MX 10
FCR-Fluidization	5.98 mbar at 0.0467 m/s	6.1 mbar at 0.0509 m/s	6.8 mbar at 0.0637 m/s	8.01 mbar at 0.0722 m/s	8.48 mbar at 0.0891 m/s
FCR-Refluidization	6.03 mbar at 0.0212 m/s	6.29 mbar at 0.0255 m/s	7.26 mbar at 0.034 m/s	9.84 mbar at 0.0552 m/s	10.95 mbar at 0.0764 m/s

From figures 5.12-5.16, it is observed again that the opposite behavior occurs during the unloading process; i.e., the slope of the unloading curve is larger for the initial fluidization compared to the re-fluidization after compression. Table 5.7 gives the corresponding values of the slope of all $\Delta P_b - U_{sg}$ curves for loading and unloading conditions, for initial fluidization, as well as for re-fluidization after compression test. All these results correspond to the intermediate pressure level (40 kPa) during compression. As mentioned before, this slope is inversely proportional to the permeability. Table 5.7 indicates that the trends concerning the slopes (and thus bed permeability) are similar for initial fluidization and re-fluidization after compression. However, the combined steps of compression and permeation increase the slopes for loading condition, while decreasing them for unloading.

Table 5.7 Slope of $\Delta P_b - U_{sg}$ curves for fluidization and re-fluidization and for different mixtures (mbar·s/m)

		MVT 100 (100% Fine)	Mixture Ratio (% of Fine – % of Ultra-Fine)			MX 10 (100% Ultra-Fine)
			70 – 30	50 – 50	32 – 68	
Fluidization (FCR)	**Loading**	572	173	89	55	49
Fluidization (FCR)	**Unloading**	361	16	28	36	41
Re-fluidization (FCR)	**Loading**	592	264	133	83	74
Re-fluidization (FCR)	**Unloading**	356	11	19	25	29

Increasing the slope of the loading curve in re-fluidization is a result of the compression and especially permeation processes; decreasing the distance between particles, decreasing the porosity, and consequently permeability and increasing the inter-particle cohesive forces, as occurs during consolidation. It results in a larger resistance to the airflow through the bed, particularly so for the mixtures containing ultra-fine powders. However, comparing the results of this table with Table 4.8 shows that in this case (combined effect of compression and permeation), due to the higher effect of permeation process in decreasing the height, porosity, and then permeability, the slopes for loading is higher than the slopes for the case of compression only and the slopes of unloading is lower.

Similar to the previous case, when applying the pressure during compression and

permeation processes, some of the particles' contact areas become flattened due to cohesive forces between close particles. For ultra-fine particles, these flattened contact areas share more contact surfaces with each contact; resulting in intense cohesive forces between them. Therefore, they can form greater agglomerates, leading to a more permeable bed. However, increasing the size of the agglomerates during the unloading stage is limited by the breakage of agglomerates due to the weight of the upper layers and collisions. On the other hand, in the mixtures with a higher portion of fine particles, increasing the number of coarser fine particles along with forming agglomerates by ultra-fine particles increase the permeability of the bed (decreasing the slope of $\Delta P_b - U_{sg}$ curves).

5.4 Final Remarks

In this chapter, the results of the third and lost class of our tests, i.e., Fluidization, Compression, Permeation, and Re-fluidization (FCPR), have been compared and assessed for five different mixtures of fine and ultra-fine particles; similar to the previous chapters. During permeation, rearrangement of fine and ultra-fine particles in porous media causes a reduction of permeability and formation of preferred flow pathways. The observations show a permanent decrease of permeability which was attributed to structural changes in the pore network, such as sealing of pore channels or expansion and realignment of particles within the pores.

The results show that by increasing the pressure differences between two sides of the bed at all the retained pressure levels, the superficial gas velocities are also increased. The results also reveal that by increasing the ultra-fine powders in the mixtures, the slopes of fitted lines to the (Superficial gas velocity vs. Δp) graphs are decreased. It means that for the same pressure adjustment, the mixtures containing more ultra-fine powders experience a lower increment in the air velocity. In addition, by adding the ultra-fine powders in the particle bed, even for only 30% of ultra-fines in the mixture, the slope of fitted linear curves indicates a sharp change in the permeability of the mixture material compared to the fine particle bed (about 50 times smaller).

For MX 10, the porosity is maximum and although the rate of decrease in the permeability is higher than for other mixtures, the changes in the amount of permeability by pressure increment is far less than the changes in the permeability of MVT 100 (100% of fine material) for the same range of pressure increment. The results also reveal that the trend of decreasing permeability for all three levels of applied pressures are almost the same. However, the rate of decreasing the permeability in the first stages of applying pressure is far more than in the last stages, for all three pressure levels. In fact, for each pressure level setting, when increasing the pressure toward the maximum pressure, the rate of changes in the permeability is decreased.

When analyzing the re-fluidization test results, history effects are observed leading to an increase in the bed pressure drop at peak point (ΔP_{peak}) between initial fluidization and re-fluidization of compressed and permeated bed. While the peak of the bed pressure drops increases, the superficial gas velocity corresponding to the peak point is smaller for re-fluidization after compression and permeation, compared to the initial fluidization; consequently, the slope of the loading curve is much larger for re-fluidization. The opposite trend is observed for the unloading curves. When increasing the proportion of ultra-fine particles in the binary mixture, ΔP_{peak} increases as well, particularly strongly in the intermediate range of 50% to 70% of ultra-fine particles, when the ultra-fine powders start to be dominant in the mixture. However, comparing the results of the combined effect of compression and permeation (FCPR) with only compression (FCR) shows that in FCPR tests, due to the higher effect of permeation process in decreasing bed height, porosity, and then permeability, the slopes for loading are higher than the slopes for FCR tests, while the slopes for unloading are lower.

CHAPTER 6

Toward the development of a CFD-DEM model for fluidization of fine particles

In this chapter, the results of the developed model for simulating the gas-solid interaction during a fluidization process for the fine particle bed will be reported and discussed. The chapter will start with an introduction covering the Discrete Element Method (DEM) for simulating the particle motion, an introduction to Computational Fluid Dynamics (CFD) for simulating the fluid motion, as well as a description for coupling of CFD and DEM for simulating the interaction of solid particles and fluid during the fluidization process. This chapter will finish with the simulation results and conclusions.

6.1 Introduction

In the previous chapters, it has been revealed that the fluidization of fine and ultra-fine particles is a complex process in which the cohesive effects play a very important role. The cohesive behavior strongly influences the gas resistance of the bed. According to the experimental tests, the fluidization behavior of ultra-fine particles is an unpredictable, time-varying behavior. However, for fine particles, the results show aggregative fluidization, which is a stable and predictable behavior.

Since the costs for preparing an industrial-scale test rig or even a scale-down prototype of it are very high, and also because of the difficulty of testing and monitoring all of the parameters for such a complex process in an apparatus, it could be helpful if a simulation method would reduce the corresponding costs and difficulties. This was the reason for starting the simulations in this study. The main purpose of this chapter is to check the feasibility of a numerical method to simulate the fluidization process for fine and even ultra-fine particles.

There are several methods for simulation of particle-fluid interaction. The fluid equations are normally computed using an Eulerian frame of reference, while the particle transport could be computed using either Eulerian or Lagrangian frames of reference. There are two main modeling approaches for dispersed multiphase flows. They are known as

Eulerian-Lagrangian model (e.g., Discrete Particle Method (DPM), Discrete Element Method (DEM), Multiphase Particle-In-Cell (MP-PIC) method, etc.), or Eulerian–Eulerian model (e.g., Eulerian multiphase (EMP), Two-Fluid Model (TFM), etc.).

In the Eulerian-Lagrangian approach, the Navier–Stokes equations are solved for the continuous (Eulerian) phase, or fluid phase. In addition, for solid particles, each individual particle is tracked using a Lagrangian approach. The Eulerian-Lagrangian approach has some advantages. This model provides detailed information for each particle; such as position, velocity, acceleration, temperature, components, etc. Some features such as particle-wall impact (used in the study on erosion), particle-particle collision, heat and mass transfer between particles and also between particle and fluid, turbulence interactions between particles and produced eddies in the continuum phase, as well as the size distribution of particles can be handled practically. On the contrary, this method has also its disadvantages. Unless when a DEM approach used, the particle volume fraction could not exceed 0.4 [182]. Therefore, except for DEM, this approach is limited to a smaller concentration of the solid phase. In addition, it is a computationally demanding approach. In fact, tracking all of the particles in the domain in each time step requires a statically meaningful representation of the flow and increase the computational cost of this model. In other words, DEM's major imperfection is its computational requirement. This problem is due to the explicit nature of the simulation method. In explicit methods, many time steps are required to ensure numerical stability. Therefore, with the increasing number of particles, the amount of required simulation time increases significantly.

In the Eulerian-Eulerian method, both phases exist side by side everywhere in the domain. The volume fraction represents the portion of the volume occupied by each phase. It means that the solid phase is also treated as a continuous fluid. In the Eulerian-Eulerian model, the conservation equation for mass, momentum, energy, and turbulence are solved for each phase. Eulerian-Eulerian models have also their advantages and disadvantages. Considering turbulence in each phase has only little extra computational costs. The mean value of velocity, pressure, volume fraction, temperature, etc. can be directly calculated as the simulation results. A full range of volume fraction can be considered for each phase. However, using this model, it is complex when the particles with a specific particle size distribution are involved. Also, the interactions of particles with each other and with walls are not simulated directly, and must be modeled separately.

In this study, since the particle interactions and also inter-particle forces are important, the Lagrangian frame of reference is used for the particle phase. In addition, since the particle volume fraction is normally very high for a particle bed before starting the

fluidization (packed bed condition), the DEM model is selected among other Lagrangian models. Therefore, the gas-solid two-phase flow will be simulated by a coupling between the Eulerian model for the gas phase using computational fluid dynamics (CFD) and the Lagrangian model (DEM) for the particle phase. In the next sections, DEM modeling, CFD method, as well as the coupled CFD-DEM method will be thoroughly discussed.

In this study, most of the Discrete Element Modelling was done using the EDEM® software from DEM Solutions [183]. EDEM®, first released by DEM Solutions Ltd. in 2006, is a discrete element method (DEM) engineering software used for the simulation, analysis, and visualization of particle flow, providing high-resolution information on particle kinematics, momentum, and heat and mass transfer. The simulation used in this study was based on EDEM® versions 2.7 and 2018 provided by DEM Solutions Ltd., Edinburgh, Scotland, UK.

For the Computational Fluid Dynamics part, ANSYS Fluent, the ANSYS software for simulating fluid flow, was used [184]; for the coupling between DEM and CFD, the EDEM Coupling module [185] was employed. Figure 6.1 shows a schematic structure of EDEM software and coupling possibilities for more complex particle processes. The coupling between EDEM and other codes is carried out through the EDEM Application Programming Interface (API).

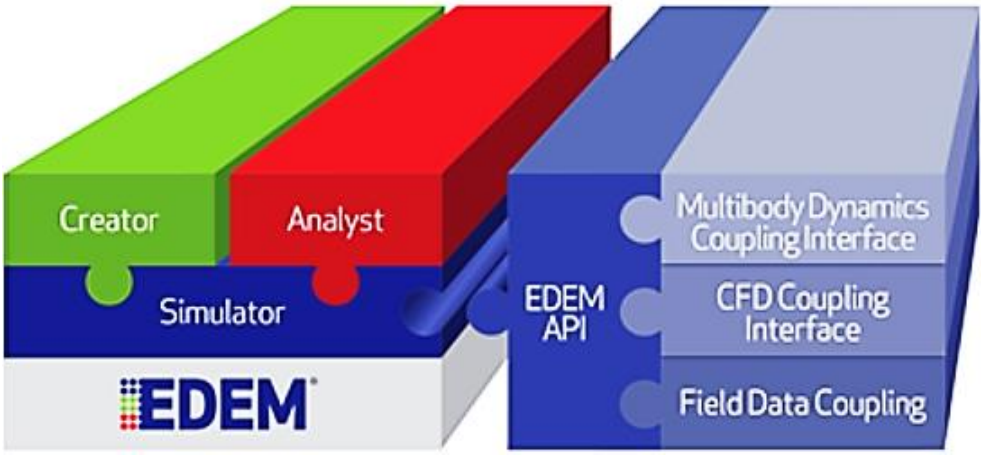

Fig. 6.1 A schematic of EDEM structure and its possibilities for coupling with other modules (see https://www.edemsimulation.com).

6.2 Discrete Element Method (DEM)

In a discrete model, the discrete phase is considered as a discontinuous phase such as a granular or particulate media. It requires different models for the behavior of individual objects. The overall system behavior is the result of interactions between all individual

objects. This kind of method is suitable for a study on most phenomena occurring at the length scale of particles.

In August 1956, a large conference on the statistical mechanics of irreversible processes was held in Brussels. Among all of them, one stood out just from its title: Molecular dynamics by electronic computers, by Livermore scientists Berni Alder and Tom Wainwright [186]. This contribution contained a new expression for a discrete phase with its own identity (molecular dynamics). For the first time, they proved that advances in the study of the time evolution of many-body discrete systems could be achieved by computation with computers. Alder and Wainwright addressed issues such as the behavior of Boltzmann's H-function, self-diffusion coefficients, collision rates and velocity autocorrelation for simple systems of about 100 hard spheres. They also convincingly showed the effectiveness of computer simulation for such investigations. They also discussed further possibilities opened by the prospect of more powerful machines [187].

However, the principles of the Discrete Element Method, also called the Distinct Element Method, were first developed by Cundall and Strack [188]. Their method was based on the use of an explicit numerical scheme. In their scheme, the interaction of the particles is monitored contact by contact and the motion of the particles modeled particle by particle. The Discrete Element Method (DEM), as a discrete approach, can precisely determine the displacements and rotations of finite particles while it detects the particles' contact for an assembly of particles. This approach is very appropriate for modeling the bulk behavior of materials. The simulations of discontinuous particulate material provide an enhanced understanding of the processes. It often reduces the number of physical experiments required.

By applying suitable contact models and using proper contact detection algorithms, DEM software calculates the forces acting on particles. Using Newton's laws of motion and numerical integration, accelerations, velocities, and positions are then computed. For better understanding the main principles of the DEM approach, Fig. 6.2 shows a flow diagram of a calculation cycle of this method. For particle-particle interactions (collisions), two main methods are used normally in the literature [189,190]: hard-sphere and soft-sphere approach. In a hard-sphere approach, the interaction forces between particles are assumed to be impulsive. In addition, only momentum exchange happens through collisions of particles. The particle-particle and particle-wall forces are not explicitly calculated during the simulation. The trajectories of particles are determined by momentum conservation during only binary collisions. The interactions between particles are assumed to be instantaneous. Therefore, these interactions occur by putting two particles together only, and considering multiple collisions at the same moment is not

possible. For not too dense systems (i.e., a dilute particle-laden flow) where the number of particle collisions with their neighbors is not high, the hard-sphere models are significantly faster than the soft-sphere models.

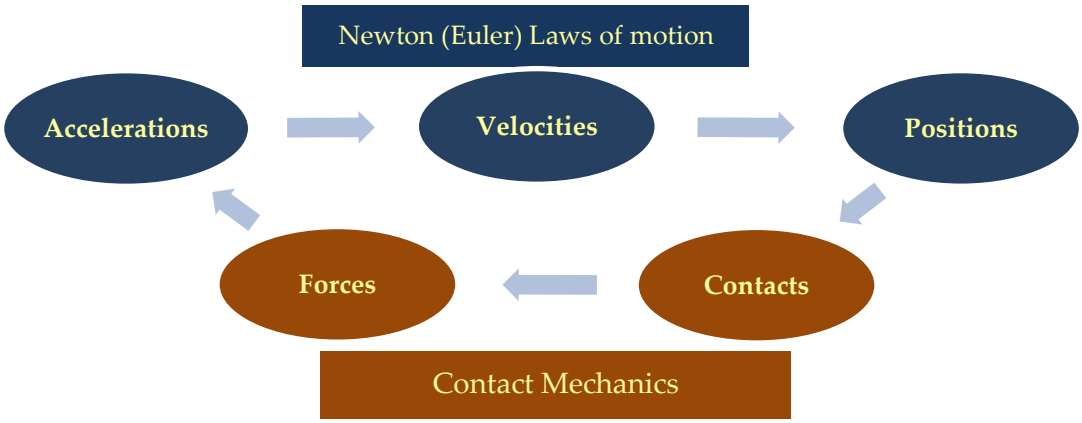

Fig. 6.2 The main principles of DEM calculation algorithm

In this study, the well-known "soft-sphere" model [183,188,191] is used, where particles may interact via short or long-range forces. In this model, the trajectories of particles are determined by integrating equations of motion. In this approach, particles are also assumed to be rigid. However, small overlaps are allowed. This model uses particle overlaps to calculate contact forces based on the magnitude of overlaps and also the relative velocity of particles in contact. This overlap represents the particles' deformations during contact. Elastic models express the relations between the amount of overlap and the resulting contact force; like the linear contact model or the Hertz contact model. The soft-sphere method is the most common and accurate approach. It is used in most DEM packages, including EDEM. The concept of the soft-sphere approach and the overlap of particles in the collision are shown in Fig. 6.3. The small overlaps are used to calculate the magnitudes of the forces acting on particles.

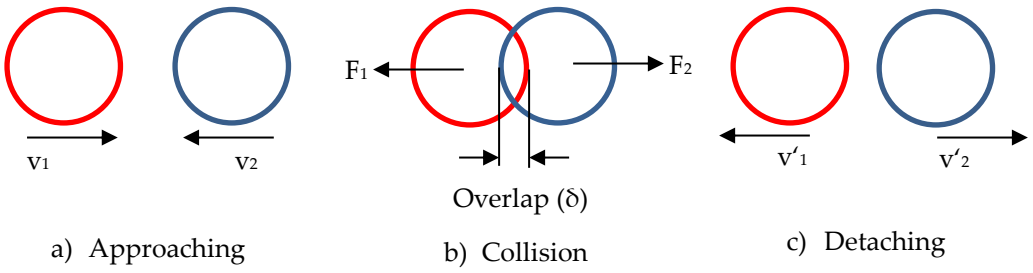

Fig. 6.3 The concept of soft-sphere approach and the overlap of particles in the collision.

6.2.1 DEM modeling

The normal overlap represents the normal deformation for a particle. The normal overlap δ_n between two particles i and j at positions p_i and p_j with radii R_i and R_j is defined as:

$$\delta_n = (r_i + r_j) - (p_i - p_j) \tag{6-1}$$

The overlap is typically less than 1% of the particle diameter in the simulations.

6.2.2 Equations of motion

Each particle within a particular flow has six degrees of freedom. Therefore, there are two canonical types of motion for it: translational and rotational. Newton's second law is used to calculate the translational and rotational accelerations in DEM simulations. To update particle velocities and positions, the accelerations are then numerically integrated over a time step. In the Discrete Element Method, every individual particle is tracked. Figure 6.4 shows a schematic illustration of applied forces on a particle from other neighbor particles.

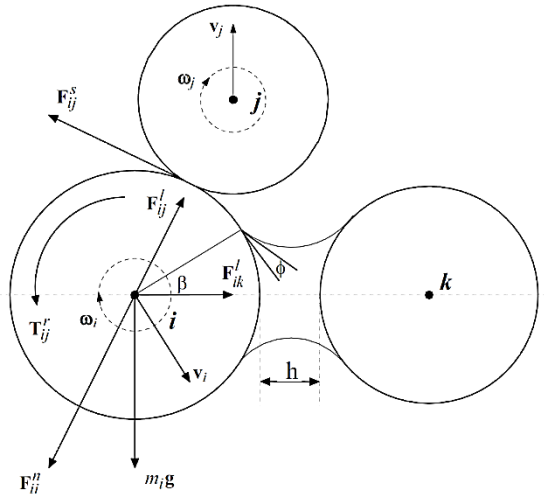

Fig. 6.4 A schematic of acting forces on the particle (i) from contact particle (j) and non-contact capillary force due to particle (k). Reprinted from [192]

The governing equation for the translational motion can be written as:

$$m_i \frac{dv_i}{dt} = m_i \frac{d^2 x_i}{dt^2} = \left(F_n + F_n^d\right) + m_i g + F_D \tag{6-2}$$

where particle i has a velocity v_i, position x_i and mass m_i. In the right-hand side of the force balance equation, the indicated forces are related to the contact including cohesive and collision forces, gravity and drag forces (particle-fluid interaction), respectively. This equation for the particle motion is solved in EDEM [183]. In equation (6-1), the collision (contact) forces are calculated using different contact models such as Hertz-Mindlin (no-

slip) and Linear Spring [193,194], Hertz-Mindlin (no-slip) with Rvd Rolling Friction [195,196], Hertz-Mindlin with JKR Cohesion [197], Linear Cohesion [198], Hertz-Mindlin with Bonding [199], Hertz-Mindlin with Archard Wear [200], Hertz-Mindlin with Heat Conduction [201], and Hysteretic Spring [202]. The rotational equation of motion for particle i is given by

$$I_i \frac{d}{dt}\omega_i = T_i \tag{6-3}$$

where I_i is the moment of inertia for particle i, ω_i is its angular velocity and T_i is the total torque acting on it.

Between all of the available contact models in EDEM, two of them are more common and are used in this study. The descriptions of other models are accessible in [203]. Here, the focus of the rest of this section will be on these two models; i.e., Hertz-Mindlin (no-slip) for cohesionless particles and Hertz-Mindlin with JKR Cohesion for cohesive particles. Hertz-Mindlin (no-slip) is the default contact model in the EDEM software [203]. In 1881, Hertz [204] proposed a model for the contact of two elastic spherical particles in contact. This was a non-linear normal force-displacement relationship between particles. To complete this model, about 70 years later, Mindlin and Deresiewicz [205] modified the model by considering an incremental tangential force-displacement model under a frictional contact (for elastic spherical particles). The Hertz-Mindlin contact model is a combination of these two models. The Hertz-Mindlin (no-slip) model [193] is one of the models used in this chapter.

In this model, two governing forces of the contact model are the normal force and the damping force. The normal force is a function of the equivalent Young's modulus E^* according to Eq. (6-4) defined as $1/E^* = \left(1-\nu_i^2\right)/E_i + \left(1-\nu_j^2\right)/E_j$; where, E_i, E_j, ν_i, and ν_j are Young's modulus and Poisson's ratios of two particles i and j, respectively. The Young's modulus is the relationship between stress (force per unit area) and strain (proportional deformation) in a material in the linear elasticity regime of uniaxial deformation. In this equation, R_n ($1/R_n = 1/R_i + 1/R_j$) and δ_n are the equivalent radius and normal overlap, respectively [203]. Figure 6.5 shows a schematic of the Hertz-Mindlin (no-slip) model for both normal and tangential directions.

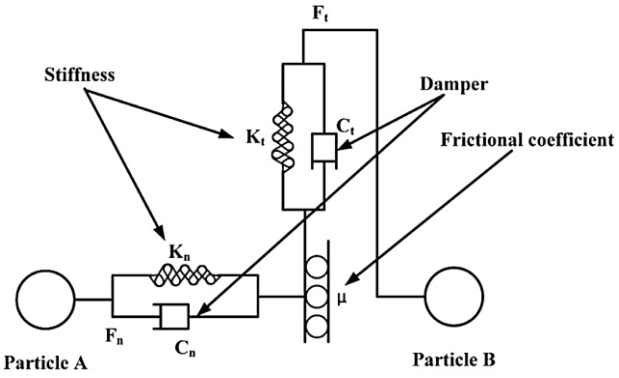

Fig. 6.5 Contact model diagram of Hertz-Mindlin. Reprinted from [206].

$$F_n = \frac{4}{3} E^* \sqrt{R_n} \delta_n^{3/2} \tag{6-4}$$

The damping force represented in equation (6-5) is a function of the particle and also material properties. In fact, it has a relation with equivalent mass m^* ($1/m^* = 1/m_i + 1/m_j$) and the normal component of the relative velocity $V_n^{\overrightarrow{rel}}$ as particle properties, and also the normal stiffness k_n and the coefficient of restitution (e) as material properties.

$$F_n^d = -2\sqrt{\frac{5}{6}} \psi \sqrt{k_n m^*}\ V_n^{\overrightarrow{rel}} \tag{6-5}$$

where ψ and k_n are defined as:

$$\psi = \frac{\ln e}{\sqrt{(\ln e)^2 + \pi^2}} \quad , \qquad k_n = 2E^* \sqrt{R_n \delta_n} \tag{6-6}$$

The tangential force, F_t, depends on the tangential overlap δ_t and the tangential stiffness k_t.

$$F_t = -k_t \delta_t \tag{6-7}$$

where $k_t = 8G^* \sqrt{R_n \delta_n}$ and G^* is the equivalent shear modulus. Accordingly, tangential damping is given by

$$F_t^d = -2\sqrt{\frac{5}{6}} \psi \sqrt{k_t m^*}\ v_t^{\overrightarrow{rel}} \tag{6-8}$$

In this equation, $v_t^{\overrightarrow{rel}}$ is the relative tangential velocity. In addition, the tangential force is limited to the Coulomb friction force defined as $\mu_s F_n$; where μ_s is the coefficient of static friction. Considering rolling friction in the contacts of particles, the applying torque could be calculated as

$$\tau_{ri} = -\mu_r F_n R_{ci} \omega_i \tag{6-9}$$

where μ_r is the rolling friction coefficient, R_{ci} is the distance of the center of mass to the contact point, and ω_i is the angular velocity of the particle at the contact point.

The second model to be discussed is Hertz-Mindlin with JKR Cohesion. Hertz-Mindlin with JKR (Johnson-Kendall-Roberts) Cohesion is a contact model for cohesive particles. In this model, the van der Waals forces within the contact zone are taken into account. Using this model, modeling of very cohesive particulate materials such as ultra-fine dry powders or wet fine particles is possible. In this model, the normal elastic contact force is based on the JKR model as first proposed by Johnson-Kendall-Roberts in 1971 [197]. For Hertz-Mindlin with JKR Cohesion, the tangential elastic force, normal dissipation force, and tangential dissipation force is the same as the Hertz-Mindlin (no-slip) contact model. However, the normal force is based on the JKR model. According to Johnson et al. [197], the mechanical work required to overcome the adhesive forces between two cohesive particles creates new surfaces and energy. The overlap caused by the additional surface force is as follow

$$\delta_{JKR} = \frac{a^2}{R_n} - \sqrt{\frac{2\pi\Delta\gamma_{JKR} a}{E^*}} \tag{6-10}$$

where a is the contact radius, and $\Delta\gamma_{JKR}$ is the surface energy of the contact ($\Delta\gamma_{JKR} = \gamma_1 + \gamma_2 - \gamma_{1,2}$). For two identical materials (as is in the case of this study), $\Delta\gamma = 2\gamma$. Therefore, JKR normal force as a function of the overlap δ_n and the surface energy $\Delta\gamma$ is given by

$$F_{JKR} = -4\sqrt{\pi\Delta\gamma E^*} a^{3/2} + \frac{4}{3}\frac{E^*}{R_n} a^3 \tag{6-11}$$

where the contact radius is $a_{JKR} = \sqrt[3]{\frac{3R^*}{4E^*}\left(P_{pull} + 3\pi\Delta\gamma R_n + \sqrt{6\pi\Delta\gamma R^* P_{pull} + (3\pi\Delta\gamma R_n)^2}\right)}$ and P_{pull} is the pull of force. This model provides attractive cohesion forces; even if the particles are not in physical contact. The maximum gap between particles with non-zero force is given by $\delta_c = \frac{a_c^2}{R_n} - \sqrt{\frac{2\pi\Delta\gamma a_c}{E^*}}$, where $a_c = \sqrt[3]{\frac{9\pi\Delta\gamma {R_n}^2}{2E^*}\left(\frac{3}{4} + 1/\sqrt{2}\right)}$. For $\delta < \delta_c$, the model returns zero force. When particles are not in physical contact, the maximum value of the cohesion force occurs for a separation gap less than δ_c. The value of maximum cohesion force, called pull-off force, is given by

$$P_{JKR} = -\frac{3}{2}\pi\Delta\gamma R_n \tag{6-12}$$

Figure 6.6 reveals a comparison between Hertz-Mindlin with JKR cohesion model results and Hertz-Mindling (no-slip) model results. In this figure, the negative overlap shows the gap between two separate particles.

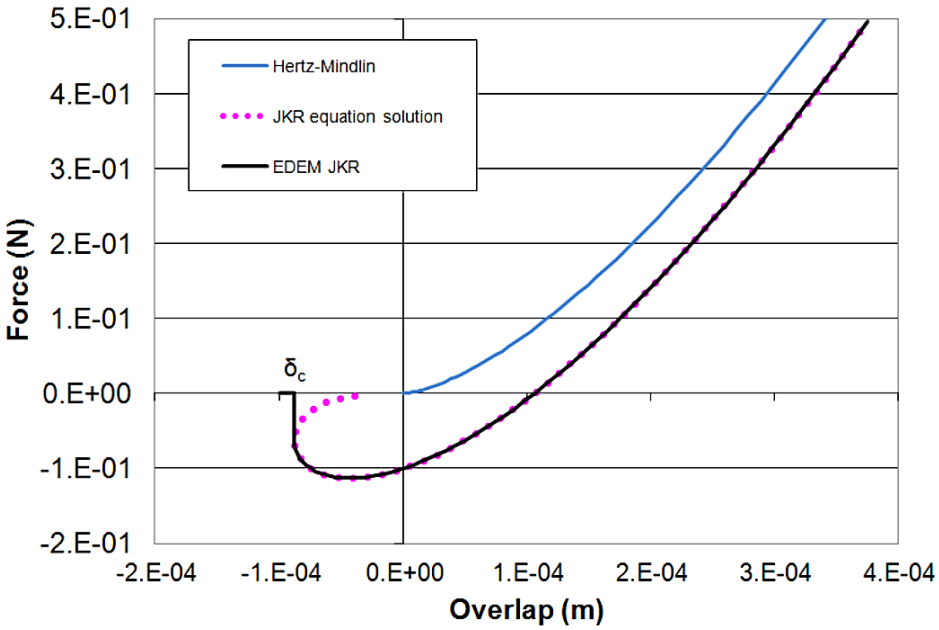

Fig. 6.6 The variation of normal force as a function of normal overlap. Reprinted from [203].

It is clear that in the case of zero surface energy ($\gamma = 0$), the JKR model reverts to the Hertz-Mindlin model. In the Hertz-Mindlin (no-slip) contact model, the friction force calculation is different. It depends only on the positive repulsive part of the JKR normal force. Therefore, the EDEM JKR friction model results in a higher friction force when the cohesion component of the contact force is higher.

6.2.3 Contact detection

Processes containing a very large number of discrete particles, make DEM simulations algorithmically complex. The most challenging part (computationally) in DEM is related to finding the neighbor particle pairs. For spherical particles, contact is detected if the distance between two spheres is less than the summation of their radii. Undoubtedly, the overall efficiency of DEM simulations depends on the efficiency of solving the geometrical problem of finding close particles to each reference particle in a solution domain. Therefore, the contact detection involves checking the distance between all the particles in the system. This process is computationally expensive and together with the force calculations takes about 70-80% of the DEM computational effort. Since in each collision, particles change their associated position from one time-step to another, collision detection must be run at every time-step. Therefore, a tiny time-step is required to detect

more often the contacts and to update forces, velocities, and positions. The smaller the time-step, the slower the simulation.

Contact detection is one of the most time-consuming parts of a DEM simulation. It needs an algorithm to create an adequately tight set of neighbor particles and to apply the contact models only to this set. In fact, when the number of particles is large, it is inefficient to simply loop through every single particle and check the distance between two particle surfaces at each time step. Using this method leads to $O(n^2)$ complexity where n is the number of particles. To improve the performance of the contact detecting method, either reducing the number of neighbors checked or by decreasing the number of time-steps that all particles are checked, three main types of schemes are used: 1) Verlet Neighbor Lists; 2) Link or Grid Cells; 3) Lattices.

In the first method, a list of particles within a certain search radius, typically 2-3 particle radii, is prepared. Therefore, instead of all particles, only this list is searched for contact. The list is updated every 20-50 time-steps or if large displacements happen. In the second method, the simulation domain is divided into a number of equally sized cells which are larger than a certain number of particle diameters. For each cell, a list of all the particles and their positions is retained. Contact detection is only done for particles within the same cell and the neighboring cells. In the last method, the simulation domain is divided into a number of equally sized cells. However, in this method, the size of each cell is the size of a particle. Therefore, each cell can possess only one particle. If the particle size distribution of the used material is a poly-disperse distribution, the cell size is related to the size of the smallest particle. Each particle is related to a grid point. Contact detection is done by creating a neighbor list for all cells containing a particle.

The contact detection procedure used in EDEM is a hybrid method of the second and third methods. The user determines the size of the grid considering the recommended range of 2 or 3 times of particle radius of the smallest particle. For twice the radius, it is the lattice method, while for larger values (3-5 times of particle radius), it becomes the link/grid cell method. Each cell is checked for more than one particle, and if found, these are checked first for contacts [183]. At a grid size of twice the particle radius, EDEM Simulator is most efficient. However, it needs large amounts of memory for computation. If the memory used for this size of cells is greater than the available memory of the simulating system, the grid radius should be increased properly to ensure that the used memory is within the available memory.

Practically, in EDEM, the calculation domain is usually discretized into 3D cells to help the contact detection algorithms to be applied on a smaller scale and reduce the computational time. The grid size must be chosen based on the particle size distribution,

dynamics, and others. A grid size of 3-5 times the smallest particle radius is usually found to be optimum. Once the domain has been discretized, the cells containing particles are marked active and are checked for contacts. The forces acting on each colliding particle are then calculated. Finally, the elements are repositioned as the result of the forces acting upon them and the active cells are again identified. The process repeats until the last time step of the simulation [207]. Figure 6.7 reveals the steps of a typical contact detection algorithm.

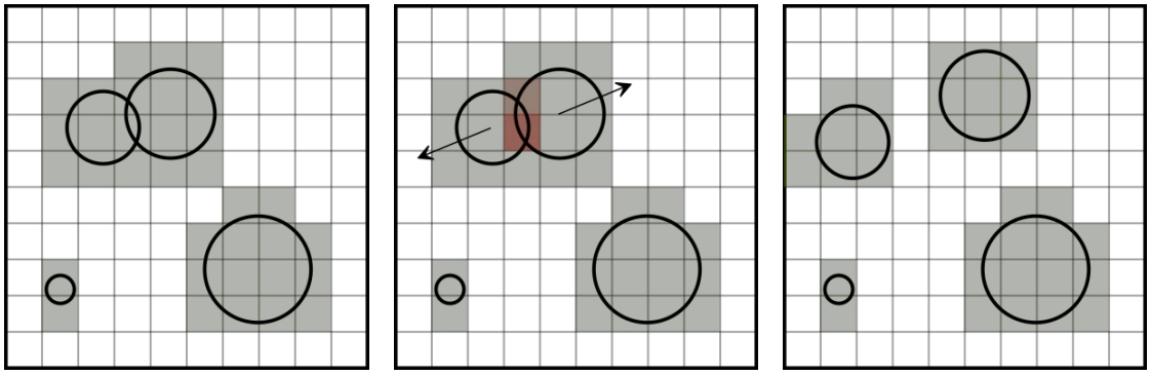

Fig. 6.7 Steps of a typical contact detection algorithm: discretize domain and identify active cells, check for contacts and calculate forces, update particle positions and add/remove active cells. Similar principles are applied in 3D and for particle-geometry contacts.

6.2.4 DEM integration scheme

DEM uses a time integration scheme for iterating through the time steps of the simulations. For the selection of time steps, a balance between two main parameters (performance and accuracy) should be considered. Cundall and Strack [188] proposed a computationally efficient, explicit central-difference time integration scheme. This scheme or a slight variation of it is mostly used in different DEM codes. Verlet integration is a numerical method used to integrate Newton's equations of motion. It is frequently used to calculate trajectories of particles in molecular dynamics simulations. In DEM, Verlet equations are second-order schemes. It means the accuracy of this scheme is dependent on the square of the time increment. Provided that the time steps are small enough, this scheme is both accurate and stable [208]. Cundall and Strack [188] declared that the time-step chosen for DEM simulation should be sufficiently small such that in an individual time-step, any small changes in the condition of a single particle cannot propagate further to their neighbor. Failure to consider this issue causes a major instability in the system.

6.2.5 Time-step of simulation

In DEM, integrating the motion equations is performed using explicit methods. To ensure the stability of simulation by an acceptable number of time steps within each collision, a

small enough integration time step is required. If $\Delta t < \Delta t_c$, the integration scheme should be stable; Δt_c is the critical time-step. For a single mass-spring system with purely translational motion, a single-degree-of-freedom system, Δt_c is given by [209]:

$$\Delta t_c = 2\sqrt{\frac{m}{k_s}} \tag{6-13}$$

where k_s is the spring stiffness and m is the mass of the single particle. In EDEM, the time step has to be chosen adequately small for two reasons. First, prevent excessive overlaps which result in unrealistically high forces; and second, avoid effects of disturbance waves (Rayleigh waves). Figure 6.8 indicates these two conditions.

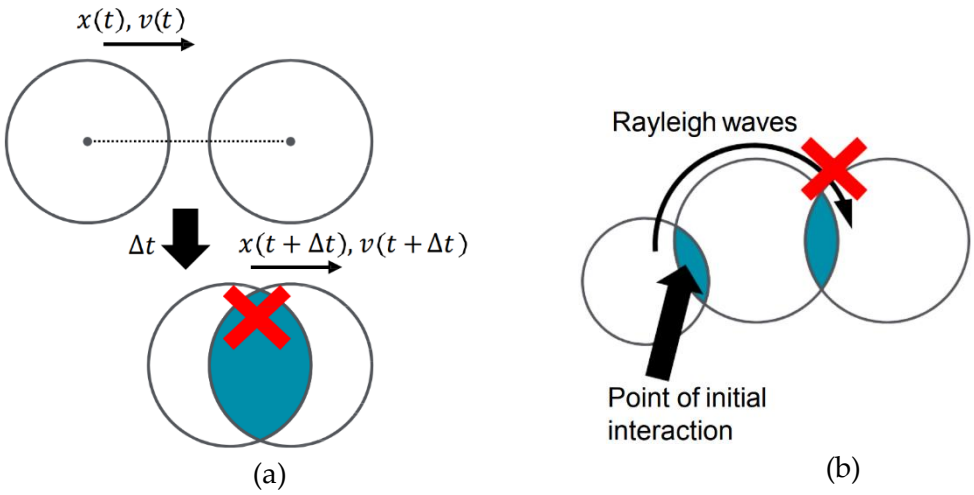

Fig. 6.8 Two reasons for choosing an adequately small time step in DEM. a) prevent excessive overlaps; b) avoid effects of disturbance waves. Reprinted from [207].

In a DEM simulation, the time steps are typically between 10^{-4} to 10^{-6} (s). This range of time steps is normally 10 to 100 times smaller than the required time steps for convergence of a CFD simulation in the same geometry [207].

In the movement of a particle in a particulate system, in addition to the effects of contacts with close neighbor particles, the effect of disturbance propagations from distant particles is also important. In DEM, disturbance waves from each particle are prevented from propagating further than its neighboring partners. This work is done by choosing a small enough time step. Approximating the Rayleigh surface wave propagation speed, the suitable time step (Rayleigh time step) has been proposed. To ensure realistic force transmission rates and prevent numerical instability, usually, a fraction of this time step is taken as the computational time-step. The Rayleigh time step can be calculated by

$$T_R = \frac{\pi R_{min}\left(\rho_p / G\right)^{0.5}}{0.1631\nu + 0.8766} \tag{6-14}$$

where T_R is the Rayleigh time step, R_{min} is the minimum particle radius, ρ_p is the particle density, G is the shear modulus, and ν is the Poisson's ratio of the particle [207].

6.2.6 Integration of motion

External forces and torques are applied to particles involved in contacts. In order to resolve and update the position and velocity of these particles, the applied forces and torques are integrated. These forces are the representative of the current translational acceleration and the torques are the representative of current angular acceleration on a particle. Motion integration is the mathematical process by which the acceleration (translational or angular) is used to update the particles' position and orientation from the current to the next time-step. However, the calculation of orientation is slightly more complex as it involves the use of rotation matrices [210], also called quaternion, to compute rotations movements.

6.3 CFD modeling

Computational Fluid Dynamics (CFD) is a numerical tool to solve the partial differential equations of fluid motion and to simulate problems related to the fluid flow. In this study, the general-purpose CFD code, ANSYS® Fluent, Release 18.1 [211] was used with ANSYS® Workbench, Release 18.1 [212] as pre-processor (meshing). A CFD problem is solved by partitioning the solution domain into a number of cells and solving a set of conservation equations for these cells, forced by defined boundary conditions. The conservation equations are a set of partial differential equations (PDE's). They describe simultaneous conservation of mass, momentum, energy and in some cases chemical species. The conservation equations control the flow of fluid and also all transport phenomena related to other fluids or solids.

In the simulations of this study, only the conservations of mass and momentum will be considered. In fact, there are not any energy or species effects in the simulation of the fluidization process of fine particles. The PDE for continuity of incompressible flow of a fluid containing particle phase (the case of this study) is given by

$$\frac{\partial \rho_f}{\partial t} + \nabla.\left(\rho_f \boldsymbol{v}\right) = S_m \tag{6-15}$$

where ρ_f is the fluid density, $\boldsymbol{v}$ is the velocity vector with three components in the main directions of the coordinate axis ($\boldsymbol{v}(x,y,z) = v_x(x,y,z).\hat{\imath} + v_y(x,y,z).\hat{\jmath} + v_z(x,y,z)\hat{k}$), and S_m is the mass source due to the existence of solid-phase beside the fluid phase. The

continuity equation represents the conservation of mass. The first term on the left side shows the rate of decrease/increase of mass, the second term reveals the net rate of flow of mass into a fluid cell (control volume). The mass added to the continuous fluid phase from a dispersed solid phase is represented by the right-hand term. Equation (6-16) shows the conservation of momentum as

$$\frac{\partial(\rho_f \boldsymbol{v})}{\partial t} + \nabla.(\rho_f \boldsymbol{v}\boldsymbol{v}) = -\nabla p + \nabla.(\rho_f \boldsymbol{\tau}) + \rho_f \boldsymbol{g} + \boldsymbol{F_b} \quad (6\text{-}16)$$

where p is the fluid static pressure, $\boldsymbol{g}$ is the gravitational acceleration, $\boldsymbol{F_b}$ is the external body forces. $\boldsymbol{\tau}$ represents the stress tensor defined as $\tau = \mu_f\big((\nabla \boldsymbol{v} + \nabla \boldsymbol{v}^T) - 2/3\,\nabla.\boldsymbol{v}\boldsymbol{I}\big)$, where μ_f is the dynamic viscosity of the fluid and $\boldsymbol{I}$ shows the unit tensor. For an incompressible Newtonian fluid, the viscous stress tensor can be simplified as $\tau_{ij} = \mu_f\big(\partial v_i/\partial x_j + \partial v_j/\partial x_i\big)$.

The rate of change of momentum equals the sum of forces acting on the control volume. This is Newton's second law which is satisfied by the Navier-Stokes (conservation of momentum) equation. On the left hand of Eq. (6-16), the terms refer to the rate of momentum increase/decrease in the control volume and the net rate of momentum into the control volume, respectively. The terms on the right hand refer to the surface force on the element due to the pressure gradient, due to viscous stress, due to gravity, and due to body forces. To close the system of fluid dynamic equations, an extra set of equations is required. These equations are called equations of state (like the ideal gas law) which are some relations between thermodynamic variables as well as between thermodynamic and transport properties.

For particle laden fluid, dimensionless numbers are used to evaluate the interaction between the fluid flow and particles. These dimensionless numbers are widely used to define the relative importance of forces acting on the involved particles. Dimensionless numbers include the dimensions and properties of the system so that they give direct information on the effect of different scales. The first dimensionless number is the particle Reynolds number ($\mathrm{Re}_p = \rho_f v_{rel} d_p/\mu_f$), the ratio of inertial forces to viscous forces. It shows the flow regime around the particles. The particle Reynolds number effects on the choice of the drag coefficient.

The second important dimensionless number is the Peclet number ($\mathrm{Pe} = v_{rel} d_p/D_0$). This value reveals the relative importance of convection to diffusion in the particle motion. In the equations of these dimensionless numbers, d_p is the particle diameter, v_{rel} is the relative velocity between fluid and particle, and $D_0 = k_b T/3\pi\mu_f d_p$ is the diffusion coefficient given by the Stokes-Einstein relation for a single spherical particle in a liquid with low Reynolds number [212]; k_b is the Boltzmann's constant, and T is temperature.

6.4 DEM-CFD coupling

A coupled DEM-CFD is an approach to model particle-fluid systems, where the particle motion is solved in Lagrangian coordination using DEM and the fluid phase is simulated using CFD. The coupling of these two phases could be done in either one or two-way coupling. In one-way coupling, considering collisions and fluid drag interactions, particle trajectories can be integrated from the data of the steady velocity field computed by CFD in the previous time step. One-way coupling is a relatively straightforward method. In fact, only the solid phase dynamics is affected by the fluid phase and the solid phase does not transfer any dynamic effects to the fluid phase. This method is normally used only for a very dilute particle phase in the fluid, where the effect of the particle phase is negligible.

Two-way DEM-CFD coupling needs to allow mutual communication between CFD and DEM (in some literature, taking into account particle collisions, this is called four-way coupling). In this case, the mutual influences (like the particle volume fraction) of the particles and the fluid are considered. By nature, the two-way coupling is an unsteady method for both phases [213]. The mutual communication between CFD and DEM processes is shown in Fig. 6.9. On the CFD side, since it requires the size of the averaging mesh cell to be larger than the particle size for non-resolved models, the mesh size depends on the particle size of the disperse phase. To study phenomena occurring at different length and time scales, a multiscale approach is necessary [214–216].

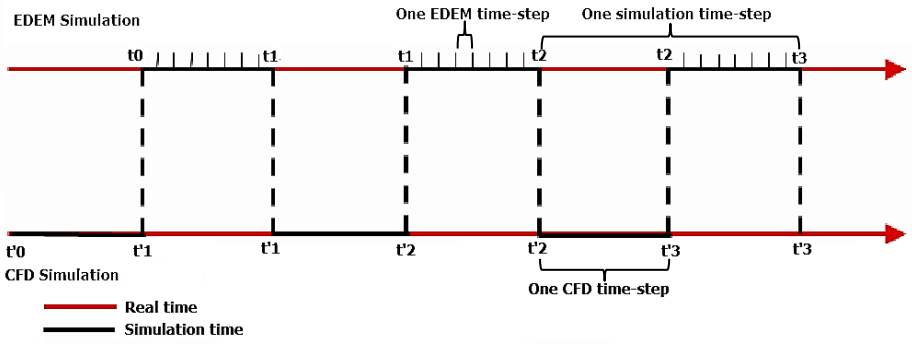

Fig. 6.9 The alternating sequence of a CFD-DEM coupled simulation. Reprinted from [217]

A CFD-DEM approach consists of a solution of the Navier–Stokes equations for the continuum fluid and Newton's equations of motion for discrete particles considering initial and boundary conditions [193,214,218–220]. Practically, in most processes, the number of particles is usually large. Therefore, a very large number of governing equations should be solved for the motion of each particle. In addition, to resolve the flow of continuum fluid through the pores among closely spaced particles, the resolution of the fluid field should be fine enough. As a result, to solve such a complex and time-

consuming simulation, some simplifications should be made depending on the existing time and length scales. In this study, the DEM-CFD coupled method is based on coupled EDEM-ANSYS Fluent codes. Fig. 6.10 shows the coupling system.

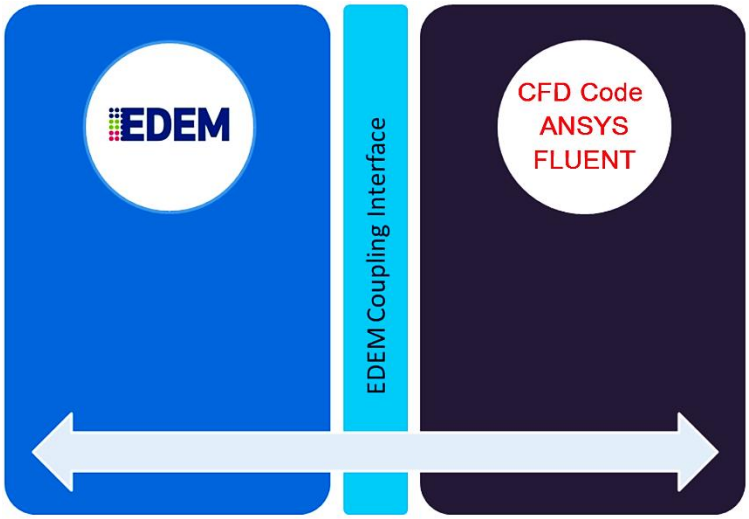

Fig. 6.10 Communication between EDEM and ANSYS Fluent code using the EDEM Coupling Interface

6.4.1 Effect of coupling with DEM on CFD equations

Tsuji et al. [193,219] were the first to propose the CFD-DEM approach. This coupled method was then further developed by other scientists. By increasing computing power of computers in recent decades and introducing parallel processing, the number of users of this method has been growing. Xu and Yu improved the proposed method of Tsuji et al. [218]. For the particle phase, the governing equations are the same as equations (6-2) and (6-3). For the fluid phase, the governing equations are the laws of conservation of mass (continuity) and momentum (Navier-Stokes) in terms of local-average variables [221]. The momentum equation is based on the model proposed by Gidaspow [222] (Model B [223]) where the pressure drop is only in the gas phase and is not shared by the solid phase as is described by Model A proposed by Arastoopour and Gidaspow [223]. For mono-sized particles, there is little difference between both models. However, considering the poly-dispersed size distribution of the used particles in this study, Model B should be preferred, as shown by Feng [224]. Using the model proposed by Gidaspow [222], assuming the pressure drop in the fluid phase only, the governing equations of the coupled CFD-DEM method are given by

$$\frac{\partial \varepsilon}{\partial t} + \nabla.\left(\varepsilon \boldsymbol{v_f}\right) = 0 \tag{6-17}$$

$$\frac{\partial}{\partial t}(\rho_f \varepsilon \boldsymbol{v_f}) + \nabla.(\rho_f \varepsilon \boldsymbol{v_f} \boldsymbol{v_f}) = -\nabla p + \nabla.(\varepsilon \boldsymbol{\tau}) + \rho_f \varepsilon \boldsymbol{g} - \boldsymbol{F^t} \tag{6-18}$$

where ε is the porosity and $\boldsymbol{F^t}$ is the total volumetric particle-fluid interaction forces. The most important volumetric particle-fluid interaction force for a gas-solid two-phase flow is the drag force. To calculate particle drag forces, the volume of particles found in each cell of the mesh must be taken into account. In each CFD time-step, the solid volume fraction data is transferred from DEM to CFD; the coupling module overrides the continuity equation for the solid phase; it is not solved by Fluent. EDEM provides an easy-to-use representation of particle volume.

The method for determining the solid fraction is the sample point method generated using Monte Carlo. In this method, regular sample points are taken within the bounding box of a particle. If the point lies within a particle bounding surface, it is stored. Figure 6.11 shows the sample point method used in EDEM.

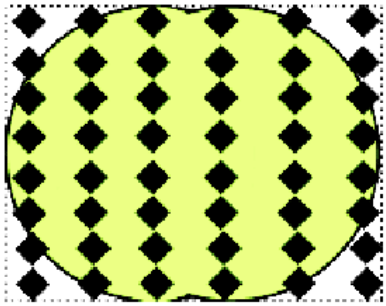

Fig. 6.11 Sample points within a particle. Reprinted from [217]

Then, the CFD cell in which the particle is located is checked. When this procedure is performed for all particles, the solid fraction within each particular mesh cell can be obtained from the percentage of the number of sample points that lie within that mesh cell, as

$$\varepsilon_s = 1 - \varepsilon = \sum_{particles} \frac{n_c}{N} V_p \tag{6-19}$$

where n_c is the number of sample points contained within the mesh cell of particle p, N is the total number of sample points of the particle and V_p is the volume of the particle. The sample points for a particle type are returned as an array of 3D values of size n. An additional force on the DEM particles based on the local drag force is required for momentum coupling. In CFD simulation, a sink of momentum is added to the momentum conservation equation of each mesh cell to display the effect of the momentum transfer to DEM particles. Considering the momentum sink, the total volumetric particle-fluid interaction forces, $\boldsymbol{F^t}$, on a mesh cell can be obtained as

$$\boldsymbol{F^t} = \frac{\sum_{all\ DEM\ iterations} \sum_{all\ paticles\ in\ cell} \boldsymbol{F}}{V_{cell}} \tag{6-20}$$

where $\boldsymbol{F}$ is the force on a particle in a particular iteration of the fluid. The sum is over the number of DEM iterations carried out between CFD iterations. Usually, CFD iterations have a larger time step than the DEM simulation (in the order of 100 times larger).

6.4.2 Particle-fluid interaction forces

In a particle-laden flow like fluidization, the particles normally interact with the surrounding fluid. As a result of this interaction, in addition to the buoyancy force, various particle-fluid interaction forces are generated. One of the most important interactions is the resistance of moving particles by stagnant fluid or moving fluid on stagnant particles (e.g., fluidization). The driving particle-fluid interaction force for fluidization is mainly the drag force. Hitherto, many interaction forces have been implemented in DEM simulation. They include drag force, pressure gradient force, and also some of the unsteady forces such as virtual mass force, Basset force, and lift forces [225–227].

The drag resistance force is well established for an isolated particle in a fluid (as Newton's equation $\boldsymbol{F}_d = C_D \pi \rho_f d_p^2 (\boldsymbol{u} - \boldsymbol{v})|\boldsymbol{u} - \boldsymbol{v}|/g$; where $C_D = f(\mathrm{Re}, \text{fluid properties})$ is the particle-fluid drag coefficient). Based on the Reynolds numbers, there are three conditions for calculating the drag force: the Stoke's Law condition, the transition condition, and Newton's law condition. There are well-established correlations for calculating the drag force for each condition. However, when the number of particles increases in a particulate system, the presence of other particles near each other makes the problem much more complicated. In this condition, reducing the space for flowing fluid between particles generates a sharp gradient in fluid velocity. Therefore, the shear stress on particle surface increases. Thus, associated with particle configuration, particle-fluid slip velocity and the properties of both particle and fluid, the drag force will change.

The drag force on the individual particles can be calculated using different drag models as shown by Zhu et al. [192]. Generally, two methods have been used to determine the drag force between particle and fluid. The first one is based on empirical correlations. The focus of these methods is normally on either bed pressure drop [63,228] or bed expansion [228] experiments. For considering the effect of other particles in the system, different suggestions have been made by different scientists; using local porosity (e.g., Ergun and Wen-Yu models [63,228]),

$$\boldsymbol{F_d} = \beta_{p-f}(\boldsymbol{u} - \boldsymbol{v})/\rho_f \tag{6-21}$$

$$\beta_{p-f} = 150\frac{(1-\varepsilon)^2}{\varepsilon}\frac{\mu_f}{\left(\varphi_s d_p\right)^2} + 1.75(1-\varepsilon)\frac{\rho_f}{\varphi_s d_p}|\boldsymbol{u}-\boldsymbol{v}| \qquad \varepsilon \le 0.8$$

$$\beta_{p-f} = \frac{3}{4}C_d\frac{|\boldsymbol{u}-\boldsymbol{v}|\rho_f(1-\varepsilon)}{d_p}\varepsilon^{-2.7} \qquad \varepsilon > 0.8$$

involving the exponent like Di Felice model [229],

$$f(\varepsilon) = \varepsilon^{-(1+\alpha)}$$
$$\alpha = 3.7 - 0.65\exp\left(-\left(1.5 - \log\mathrm{Re}_\mathrm{p}^2\right)/2\right) \tag{6-22}$$

and considering particle Reynolds number and associating the drag force to the flow regimes [230,231]. For very small Reynolds number,

$$\boldsymbol{F} = \boldsymbol{F_0}(\varphi) + \boldsymbol{F_1}(\varphi)\mathrm{Re}_\mathrm{p}^2 \qquad \mathrm{Re}_\mathrm{p} < 20 \tag{6-23}$$

where $\boldsymbol{F_0}$ is the non-dimensional Stokes-flow drag force given by [230]

$$\boldsymbol{F_0}(\varphi) = \frac{1 + 3(\varphi/2)^{1/2} + (135/64)\varphi\ln\varphi + 16.14\varphi}{1 + 0.681\varphi - 8.48\varphi^2 + 8.16\varphi^3} \qquad \varphi < 0.4 \tag{6-24}$$

And by the Carman correlation

$$\boldsymbol{F_0}(\varphi) = 10\varphi/(1-\varphi)^3 \qquad \varphi > 0.4 \tag{6-25}$$

Simulations showed that the ratio $\boldsymbol{F_1}/\boldsymbol{F_0}$ reduced when increasing the solid volume fraction (φ). For close-packed beds, the first term in Eq. 6-23 is much greater than the second one over the range of Re_p. $\boldsymbol{F_1}$ can be given by

$$\boldsymbol{F_1}(\varphi) = 0.110 + 5.10\times10^{-4}\mathrm{e}^{11.6\varphi} \tag{6-26}$$

At Re_p greater than approximately 20, $\boldsymbol{F}$ increases linearly with Re_p, and hence, the non-dimensional drag force on the spheres in random fixed beds is

$$\boldsymbol{F} = \boldsymbol{F_2}(\varphi) + \boldsymbol{F_3}(\varphi)\mathrm{Re}_\mathrm{p}^2 \qquad \mathrm{Re}_\mathrm{p} > 20 \tag{6-27}$$

where $\boldsymbol{F_2}$ is nearly the same as the Stokes-flow drag force, $\boldsymbol{F_0}$, and $\boldsymbol{F_3}$ is given by

$$\boldsymbol{F_3}(\varphi) = 0.0673 + 0.212\varphi + 0.0232/(1-\varphi)^5 \tag{6-28}$$

This expression is in good agreement with the Ergun correlation for packed beds of spherical particles for $\varphi > 0.5$.

Morgan et al. [232] showed that the exponent value is in a rather large range of −3 to 10 and finding an accurate value for this exponent is important. The second type of method is based on numerical simulations, normally DNS simulations [233] or Lattice-Boltzmann

(LB) techniques [234]. Other interaction forces between particles and the carrier fluid could also be considered, when the fluid involved is liquid rather than gas. In the case of this chapter, the fluidizing fluid is gas. Therefore, the most important particle-fluid interaction force is the drag force.

6.4.3 Coupled EDEM-CFD Simulation Overview

EDEM integrates forces and torque (due to the external forces act upon the particles in addition to any gravitational or collision forces) into the particle simulation for each individual particle [217]. Figure 6.12 reveals the stages of the EDEM simulation loop and the point at which it interacts with the CFD solver.

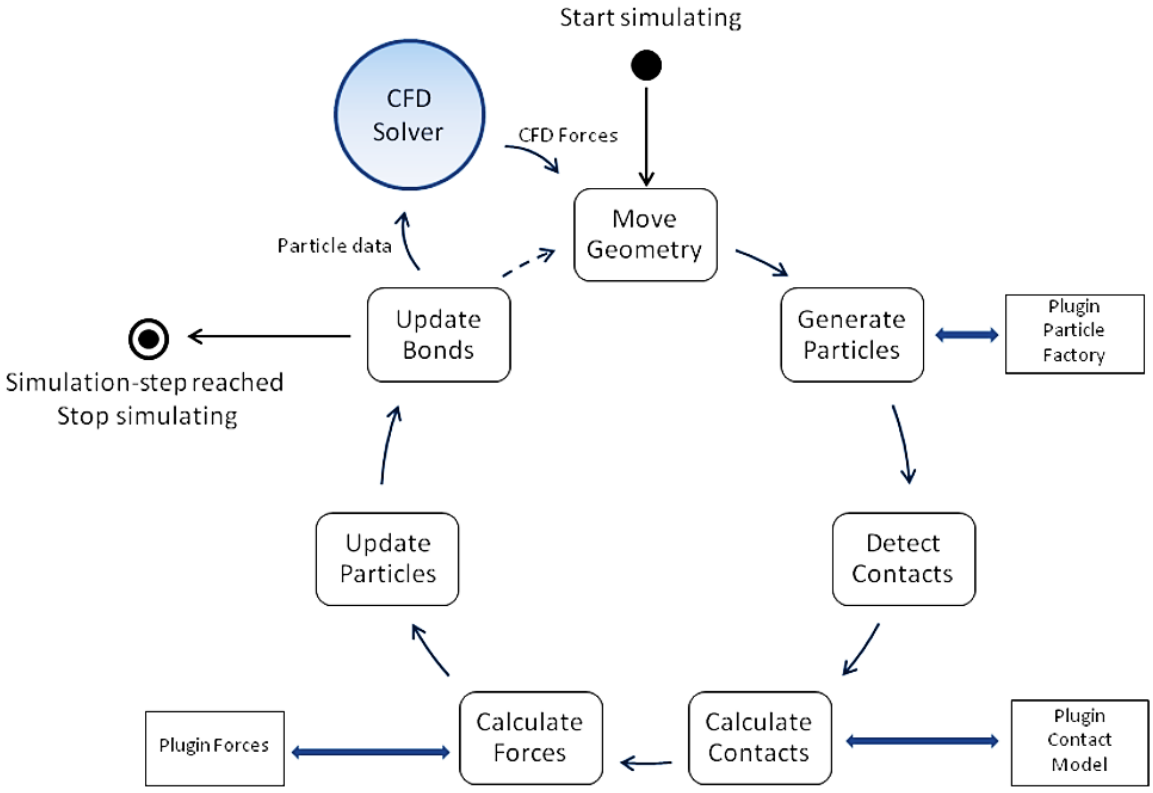

Fig. 6.12 A coupled EDEM-CFD simulation cycle. Reprinted from [217]

To complete the illustration, some Application Programming Interface (API) components, such as the Particle Factory®, Contact Model, and Particle Body Forces, have also been indicated at their interaction stages with the EDEM solver loop. Particles can have external forces and torques, calculated by the external CFD solver, applied to them before EDEM executes a simulation step. This is achieved using the setForceAndTorque method provided by the interface class, ICfdCoupling. Separate arrays exist for both force and torque. The arrays are both created as serialized 3D vectors that match the order of the particle data. Because of this, it is important that up-to-date particle data is obtained and

any force or torque is applied to the particles during one simulation step before EDEM is allowed to iterate again.

6.5 Results and discussion

6.5.1 EDEM set-up for simulation

The computer used for this study is a desktop PC with Intel Quad-Core CPU i7-4770 @3.40 GHz and 32 GB RAM. It is worth noting that although the new versions and licenses of EDEM software are capable to perform parallel computing on GPU, the license of the used EDEM software in this study was only equipped with parallel processing on PC cores. Before starting the description of the results, a short overview of the EDEM setting environment for pre-processing, simulation, and post-processing is inevitable [183].

The EDEM user interface comprises three icons for each of the simulation components: the Creator, the Simulator, and the Analyst. The creator is used to set up and initialize models. This allows the user to input bulk materials, equipment materials and set the simulation environment. Simulator tab is the place for configuring and controlling the EDEM solver engine and finally, in Analyst, EDEM simulation data can be analyzed and visualized by the available tools.

On the right-hand side of the creator page, the viewer part is used to display 3D representations of particles and geometry. Here, it is possible to control the orientation, position and zoom factor. By default, all quantities are measured in standard SI units (Système International d'Unités). However, since the size of particles in this study is very small, using SI units results in extremely small numbers for the area, volume, and moment of inertia of the particles. Using very small numbers and multiplying them in the equations, as well as the process of rounding or cutting the numbers, causes computational problems. Therefore, in this study, the CGS units are used for the definition of all materials.

In the creator tree, generally, the user defines the gravity, materials, geometry (domain, sections, the number of elements that make up each section of geometry), and particle types used in the model and their properties. In addition, the method of producing and introducing different particles in the domain by "factory" and its properties, as well as the total number of particles in the model at the current time is determined. Total specifications for each particle type are also listed. Then, different types of interactions are defined; i.e., particle-particle, particle-wall, wall-wall, etc. A list of the interaction types taking place in the model is specified in the Materials Editor. This list includes the total number of contacts in progress at the current time. The contacts are broken down into contact types. The total number of collisions that have taken place during the time

step are also listed. Also, a list of the total number of bonds, total number of intact and broken bonds and the number of bonds intact/broken between particle pairs are also specified here.

A Bulk Material contains the particle bulk material properties (Poisson's Ratio, Shear Modulus (or Young's Modulus), Solids Density and Work Function (if applicable) into the relevant fields and also the interactions of this new material with other materials and with itself), the particle shape, and size distribution. Interactions are used to define how materials act when they come into contact with each other. Interactions must be defined for all materials used in the model, including the interaction that occurs when the material comes into contact with itself. Interactions have to be set for every combination of bulk materials and their interactions with other bulk materials and equipment materials. A particle is defined using one or more spherical spheres. Multiple surface spheres can be overlapped to create multi-sphere particles.

The size distribution is set for the particle shapes in each Bulk Material. The scaling options for the size distributions are all relative to the defined particle size. If the “scale by Radius” option is used, all length dimensions will be scaled in direct proportion to the value specified. If “Scale by Volume” is specified all length dimensions will be scaled to the cube-root of the value specified. The size distribution options are classified as Fixed (an equal size and volume), Random (randomly sized within a set size range), Normal distribution (the average (mean) particle radius or volume and the standard deviation must be defined), Log-normal distribution (with the same inputs as the previous case), and User-Defined (inputs are scales and percentage of total mass to be generated at that scale).

Figure 6.13 reveals the interactions and bonds between particles (how elements behave when they come into contact with each other; using the Interaction pulldown menu). The contact models are split into Base models, Rolling Friction models, and Additional Models. A base model defines the physical collision between particle materials or particles and geometries. Typically, the base model consists of spring forces and damping forces in the normal and tangential directions. Only one base model can be used per simulation. Rotational resistance and energy loss during rotation are also significant. Most models include a Rolling Friction component to account for the material's resistance to rolling. Only one rolling friction model can be added per simulation. Additional models such as bonding, heat conduction, wear, cohesion (if it is not included in the base model) and electrostatics can be included in addition to the Base and Rolling Friction models. New interaction models can be added to the system by an API code.

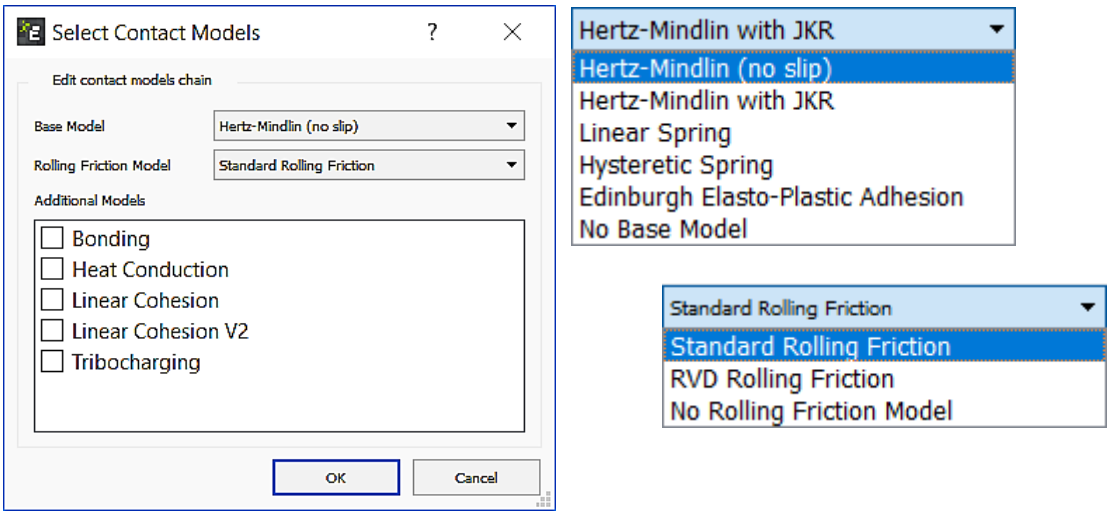

Fig 6.13 Contact model window in EDEM to describe how elements behave when they come into contact with each other.

The Simulator is where you configure and control the EDEM simulation engine, and where you can observe the progress of your simulation. The Simulator Pane is where the time step, simulation time, and grid options are set. The Viewer Controls are used to determine how items are displayed in the Viewer. In the viewer part, the grid cells, particles, geometry sections, factories, etc. can be displayed. For setting the simulator, the first step is selecting the time step. The time step is the amount of time between iterations (calculations) in the Simulator. The time step is either fixed and remains constant throughout the simulation, or the Auto Time Step option can be chosen. The value is displayed as both the actual time step (in seconds) and as a percentage of the Rayleigh time step.

As mentioned before, the Rayleigh time step is the time taken for a shear wave to propagate through a solid particle. When using a simulation with a range of particle sizes, the Rayleigh time step is calculated based on the smallest particle size. The smaller the time step, the more data points are produced. A large number of data points produce results with a very fine level of detail; however, the simulation time will be longer due to the increased number of calculations required. Typically a time-step is chosen as a percentage of the Raleigh Time Step value. The normal range is 10%-40% of the Raleigh Time-Step. The higher the particle energy in the simulation (higher forces, faster collisions), the lower the time-step value. In EDEM, 20% of the Raleigh Time-Step is the default value recommended.

Another variable to set for the simulation is the simulator grid size. EDEM calculates the smallest particle size in the simulation (R_{min}), the user then sets a grid cell size based on this particle size. 3 R_{min} is the default value, and typical ranges are 3-6 R_{min}. The grid does not impact on the simulation results, only the simulation speed. A smaller grid size results

in more memory (RAM) usage; reducing the grid cells size below 2 R_{min} results in a significant slow-down for the simulation. The main computational challenge in DEM simulation is the detection of contacts. By dividing the domain into grid cells, the simulator can check each cell and analyze only those that contain two or more elements (and therefore a possible contact), thus reducing processing time. The number of grid cells controls the compromise between memory usage and computational time. As the grid length decreases, fewer elements are assigned to each grid cell and contacts become easier to resolve. The fewer particles there are per grid cell, the more efficient the simulator regarding computational time.

The Analyst is the post-processor used to analyze and visualize the results of the simulation. It is possible to playback the simulation, graph results, save images, create videos, or export data. Particles can be represented by either default, cone, vector, stream, or template. To produce geometry and the required mesh for generating the control volumes related to the solution domain of CFD in ANSYS Fluent, the Basic Fluid Flow Analysis Workflow of Workbench is used [212].

6.5.2 Simulation results

For transient process modeling of CFD-DEM simulations, time step and mesh size are critical parameters. At first glance, it seems that the smaller the grid and time step, the more precise the results would be. However, it is not always true. In fact, the most important parameters are the convergence and efficiency of the simulation. Reasonable parameters could be determined with an analysis of the independence of results from the grid size and time step. In this manner, the reliability of the result could be checked. In addition, the basic requirement for non-resolved CFD- DEM is that the CFD grid size should be larger than the particle size. Therefore, the CFD mesh size should also satisfy this restriction. For the time step, a percentage of Rayleigh time-step is the criterion for the DEM time step and the CFD time step is considered to be a hundred times the DEM time step. It means, after every 100 time-steps of the DEM simulation, the fluid flow is updated by CFD.

Now, the simulations results performed to mimic the behavior of fine particle fluidization (experimental behavior at macro-scale) will be reported. Due to the number of particles and associated computational costs, the simulation of a real geometry is impossible. Therefore, in all simulations, a scaled-down geometry with the same aspect ratio as the main experimental set-up will be considered as a simulation domain. The air velocity changes are the same as in the experiments; the pressure drops are scaled with the height of the scaled-down geometry, and the particle size and properties are the same as in the experiments. Due to a large number of particles and related computational costs, the size distribution of particles is considered only for two cases; the other cases consider only the

Sauter mean diameter (d_{32}) as a single value of the particle size. The fluid (air) properties are the same as in the experiments.

Considering the volumes of the scaled-down geometry and the real geometry, the scale-down factor can be calculated. Using the scale-down factor, the total mass, the mass of a single particle, and the number of particles in the simulation domain can be calculated. Each simulation starts with producing the specified number of particles in a moving factory plate at a suitable height of the column, and let these particles fall down considering gravity only. Other forces such as buoyancy or drag force are ignored in this phase. After positioning the particles at the bottom of the column in this manner (considering the contact interactions between particles and also between particles and walls), the second simulation starts, using the last time-step of the first phase as the initial condition for the particles in the domain. In this second phase, EDEM software is coupled with ANSYS Fluent, enabling CFD-DEM simulations.

The velocity of air is pre-defined in Fluent as a C++ UDF velocity inlet file and increases stepwise from zero to maximum velocity (over a specified number of time-steps; and decreases again stepwise with the same procedure (in some cases). According to the calculation time, the associated velocity is considered as a boundary condition. After each increase, sufficient time is required to balance the disturbance induced by the stepwise changes in inflow velocity.

6.5.2.1 (Case 1) Geometry diameter of $25d_{50}$, cohesive particles, turbulent flow

The first simulation started using a cylinder with a diameter of 25 times the average particle size d_{50} and an aspect ratio of ($H/D = 7.6$). All particles were considered as mono-size, equal to the mean Sauter diameter of fine particles. The interaction of particle-particle was considered as cohesive, using Hertz-Mindlin with JKR Cohesion for cohesive particles. According to Bruno et al. [235], the surface energy of CALCIT ($CaCO_3$) is between 750-1050 erg/cm^2 (0.75-1.05 J/m^2). However, after some test simulations with such values of surface energy, the surface energy was considered as only one-third of the minimum; i.e., γ=0.26 J/m^2 to investigate the effect of the cohesive behavior of particles and obtain more realistic results.

In this simulation, the airflow was considered as a turbulent flow based on the $k-\epsilon$ model. Table 6.1 shows the parameters for the CFD-DEM simulation of the first case. The used values for different coefficients and parameters are according to Tomas [43,141] and other resources [236]. The total time for this simulation was about three days. The total physical time was 0.64 s for loading and unloading stages of fluidization. The results showed that the simulation behavior did not mimic the experimental observation. There

was not any fluidization; particles stuck together. The second step for this case was an increase in air velocity to reach the fluidization point. In this case, only fluidization loading was considered in the UDF of the velocity setting.

Figure 6.14 shows the behavior of the simulation results for this final case. The results showed that the particles were elutriated while some sets of particles stuck together. This behavior happened when the air velocity was 5.5 m/s and the bed pressure drop was 990.87 mbar. Figure 6.15 reveals the fluidization curve (the bed pressure drop versus the air velocity) for this case. This simulation showed that even when reducing to one-third of real surface energy for this kind of particle, wrong behavior is observed. The simulation was repeated for a surface energy of only 0.1 J/m^2. Even then, the behavior was the same. The only difference was that the elutriation of stuck particle sets occurred at a lower air velocity.

t=0.64 s, $U_{sg} = 0.1484\ m/s$ t=2.595 s, $U_{sg} = 5.5\ m/s$

Fig. 6.14 Simulation of cohesive particles in a scaled-down geometry with a cylinder diameter of 25d_{50} (case 1)

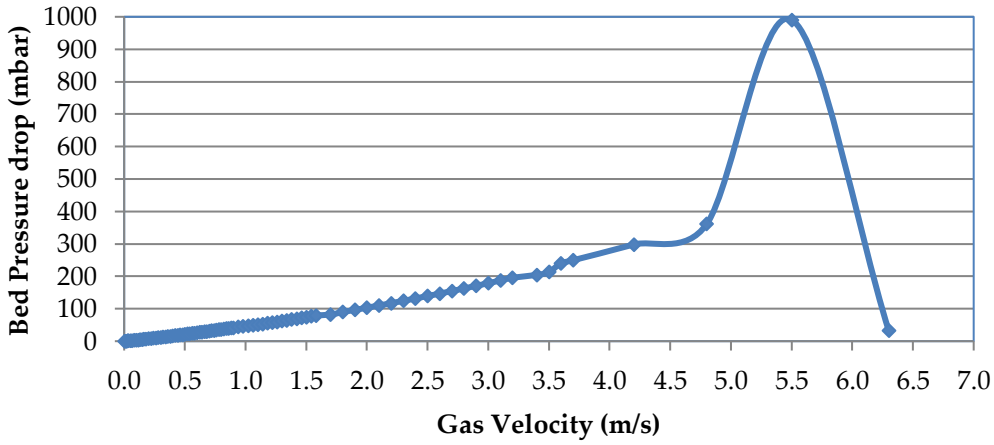

Fig. 6.15 Fluidization curve for cohesive particles in a scaled-down geometry with a cylinder diameter of 25d_{50} and turbulent airflow

Table 6.1 EDEM and ANSYS FLUENT set-up parameters for CFD-DEM simulation.

EDEM simulation set-up
Interaction:
Particle to Particle: Hertz-Mindlin with JKR Cohesion Particle to Geometry: Hertz-Mindlin (no-slip)
Gravity: -9810 mm/s^2
Material
Particle: Poisson's Ratio: 0.28 Shear Modulus: 3.4e+07 Pa (instead of 3.4e+10, to decrease the number of time steps) Density: 2.7 g/cm^3
Glass: Poisson's Ratio: 0.22 Shear Modulus: 3.0e+10 Pa Density: 2.45 g/cm^3
Interaction
Glass to Glass: Coefficient of Restitution: 0.5 Coefficient of Static Friction: 0.76 Coefficient of Rolling Friction: 0.01
Particle to Glass: Coefficient of Restitution: 0.5 Coefficient of Static Friction: 0.76 Coefficient of Rolling Friction: 0.01
Particle to Particle: Coefficient of Restitution: 0.5 Coefficient of Static Friction: 0.76 Coefficient of Rolling Friction: 0.01
Rayleigh Time step: 5.7903e-07 Time step= 25 % of Rayleigh Time step= 1.44757e-07
Smallest Radius (R min)= 0.019075 mm Cell Size: 3.5 R_{min} Approx. Number of Cells: 434372

ANSYS FLUENT simulation set-up
Solver Type: Pressure-Based Velocity Formulation: Absolute Time: Transient Gravity: -9.81 m/s^2
Models Viscous: Turbulent EDEM Coupling: Connected
Materials Fluid (Air)
Boundary Condition
Inlet Type: Velocity-inlet Momentum Velocity Specification Method: Magnitude, Normal to Boundary Reference Frame: Absolute Velocity Magnitude (m/s): UDF velocity_inlet Supersonic/Initial Gauge Pressure (Pascal): 0
Outlet Type: Pressure-outlet Momentum Gauge Pressure (Pascal): 2.74 (scaled by height) Backflow Direction Specification Method: Normal to Boundary
Wall Type: wall Zone name: wall-solid Adjacent Cell Zone: fluid Wall Motion: Stationary Wall Shear Condition: No Slip

Continue ANSYS FLUENT simulation set-up	
Reference Values	**Solution Controls**
Compute from: inlet	Under-Relaxation Factors
Area (m^2): 1	Pressure: 0.3
Density (kg/m^3): 1.225	Density: 1
Enthalpy (j/kg): 0	Body Forces: 1
Length (mm): 1000	Momentum: 0.7

Pressure (Pascal): 0 Temperature (K): 298 Velocity (m/s): 0.004 Viscosity (kg/m-s): 1.7894e-05 Ratio of Specific Heat: 1.4 Reference Zone: fluid	**Solution Initialization** Initialization Methods: Standard Initialization Compute from: Inlet Reference Frame: Relative to Cell Zone
Solution Solution Methods Pressure-Velocity Coupling Scheme: SIMPLE	**Initial Values:** Gauge Pressure (Pascal): 0 X Velocity (m/s): 0 Y Velocity (m/s): 0 Z Velocity (m/s): 0.004
Spatial Discretization Gradient: Least Square Cell-Based Pressure: Second-order Momentum: Second-order Upwind Transient Formulation: First Order Implicit	**Run Calculation** Time Stepping Method: Fixed Time Step Size (s): 100 times of EDEM time steps

6.5.2.2 (Case 2) Geometry diameter of $25d_{50}$, non-cohesive particles, turbulent flow

Considering the results of the previous simulation, in the second simulation, the particle-particle interaction was considered based on a non-cohesive behavior using the Hertz-Mindlin (no-slip) model. Again, the flow of air was turbulent and represented by the $k-\epsilon$ model. The geometry was exactly as before (diameter of the cylinder is $25d_{50}$). All particles were considered as mono-size equal to the mean Sauter diameter of fine particles. Here again, until 0.1485 m/s (the maximum velocity used in the experiments), there was not any fluidization behavior. The fluidization curve shows only the linear part (packed-bed condition) before fluidization; i.e., increasing the bed pressure drop by increasing the gas velocity without any change in the bed height or condition. However, increasing the air velocity to 0.24 m/s resulted in the fluidization of particles. Figure 6.16 shows the fluidization curve for this case. When the air velocity increased to more than the fluidization point, then, most of the particles were elutriated from the domain at 0.36 m/s, like in pneumatic conveying. Figure 6.17 reveals the simulation behavior of this case at three different velocities.

Considering Fig. 6.16, the results indicate that the rate of increasing bed pressure drop was much smaller than the experimental results. In addition, the fluidization point is reached as a much higher bed pressure drop. The lower slope of the linear part of the fluidization curve (packed bed) shows a higher permeability of the bed. It could be due to: the reduced size of geometry, considering mono-size particles instead of the real size distribution of particles, and to the initial settling process of the particles in the first stage of each simulation. The first two items will be considered in the next simulations.

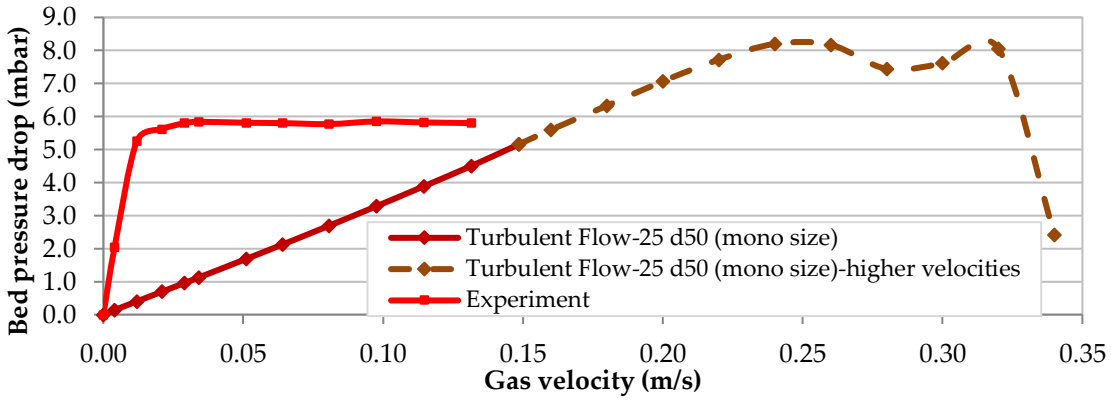

Fig. 6.16 Fluidization curve for non-cohesive particles in a scaled-down geometry with a diameter of $25d_{50}$ and turbulent airflow

Fig. 6.17 The simulation behavior of particles in different velocities (case 2).

To explain the excessive pressure drop to reach the fluidization point, the turbulent flow could be influential. In fact, considering the fine size of these particles, the particle Reynolds number $\mathrm{Re_p} = \rho v\, d_p/\mu$ is very small for a low level of air velocity (in the case of our studies and for the maximum velocity of 0.1485 m/s, it is about 0.4). According to Vallero [237], the flow condition of fluid around the particles are classified as:

- $\mathrm{Re_p} < 1$: Fluid flow around the particle is laminar. In a Stokes region, the frictional force exerted on the particle is predominant, and the inertia force is negligible.
- $1 < \mathrm{Re_p} < 1000$: Turbulence starts to occur around the particle. In the transient region, both inertial force and frictional force are important to the behavior of the particle.
- $\mathrm{Re_p} > 1000$: Fluid flow around the particle is turbulent. In a Newton region, the drag coefficient of the particle decreases as the $\mathrm{Re_p}$ increases.

Therefore, the flow should be laminar in these sets of simulations. Thus, the drag exerted on the particles may be considered as the dominant force on the particle by the airflow, and the effects of the turbulent diffusion may be ignored. This assumption was considered in Case 3.

6.5.2.3 (Case 3) Geometry diameter of 25d_{50}, non-cohesive particles, laminar flow

Considering the results of the previous simulation, in the third simulation, again, the particle-particle interaction was considered based on a non-cohesive behavior using the Hertz-Mindlin (no-slip) model. The geometry was exactly the same as before (diameter of the cylinder was 25d_{50}). All particles were considered as mono-size equal to the mean Sauter diameter of fine particles. The only difference to the previous case was that the flow of air is laminar.

The results showed that once again, the bed was not fluidized until reaching the maximum fluidization velocity of experiments (0.1485 m/s). However, increasing the velocity to 0.2 m/s results in starting the fluidization behavior in the bed. This velocity was somewhat smaller than the required velocity of the incipient fluidization of the previous case (turbulent flow). In addition, the fluidization curve for this simulation indicated that the average of the bed pressure drop after starting fluidization was decreased by 0.89 mbar for the laminar flow compared to the turbulent flow. However, it was still about 1 mbar greater than the average of the bed pressure drop after fluidization in the experiment. Figure 6.18 shows a comparison between the fluidization curves of these two last simulations. The results indicated that after fluidization, the laminar flow showed a somewhat lower bed pressure drop. However, the linear part (fixed bed) was almost the same for both cases. This showed that, even if the flow regime was an important parameter after fluidization, its effect was limited for fixed particles in the bed (before fluidization).

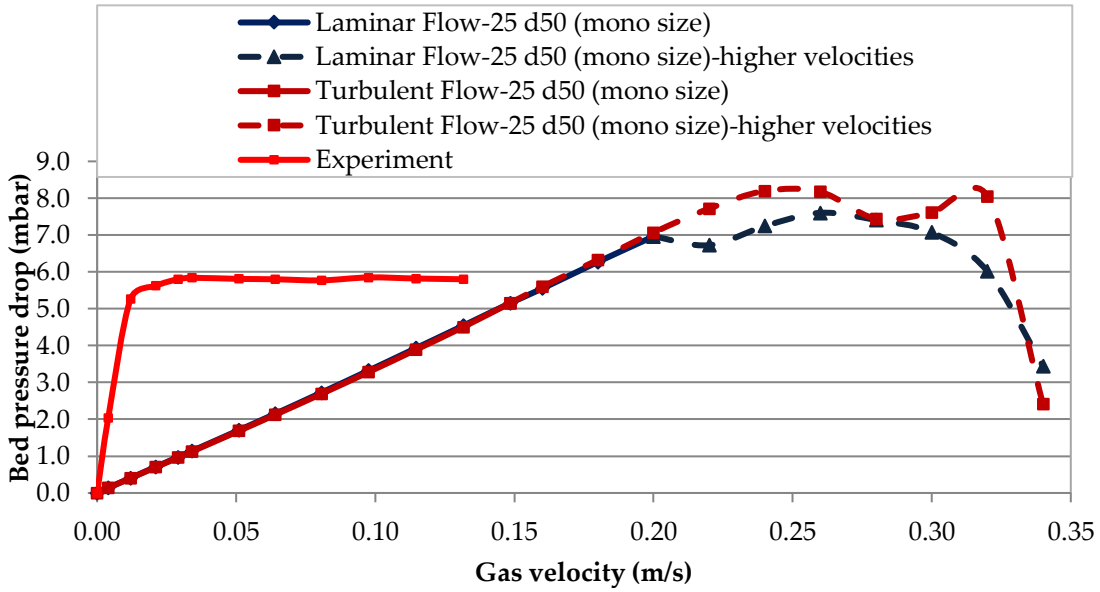

Fig. 6.18 Fluidization curve for non-cohesive particles in a scaled-down geometry with a diameter of 25d_{50} (comparison of laminar, Case 3, and turbulent airflow, Case 2)

The other difference between these two cases was that for the case of laminar flow the elutriation of a large number of particles to the output of the domain started already at about 0.28 m/s while it was initiated first at about 0.32 m/s for the case of turbulent flow.

6.5.2.4 (Case 4) Geometry diameter of 25d_{50}, non-cohesive particles, laminar flow, taking into account the size distribution of particles

The aim of this case was to investigate the effect of considering a broader particle size distribution on the simulation results. In this simulation, all settings were similar to the previous case; but, instead of using the Sauter mean size as size for all particles in the simulation domain (mono-disperse), a size distribution similar to the real particle size distribution of fine particles is considered. To control the computational costs, the ultra-fine particles are gathered together in bigger size-interval bins. In fact, according to the Rayleigh time step equation (6-14), the time scale of the DEM simulation is directly proportional to the minimum size of particles in the simulation domain. This is the reason for collecting all of the ultra-fine powders in a bigger bin with an average size of about 10 µm. Figure 6.19 shows the customized size distribution of particles pre-defined in the simulation set-up.

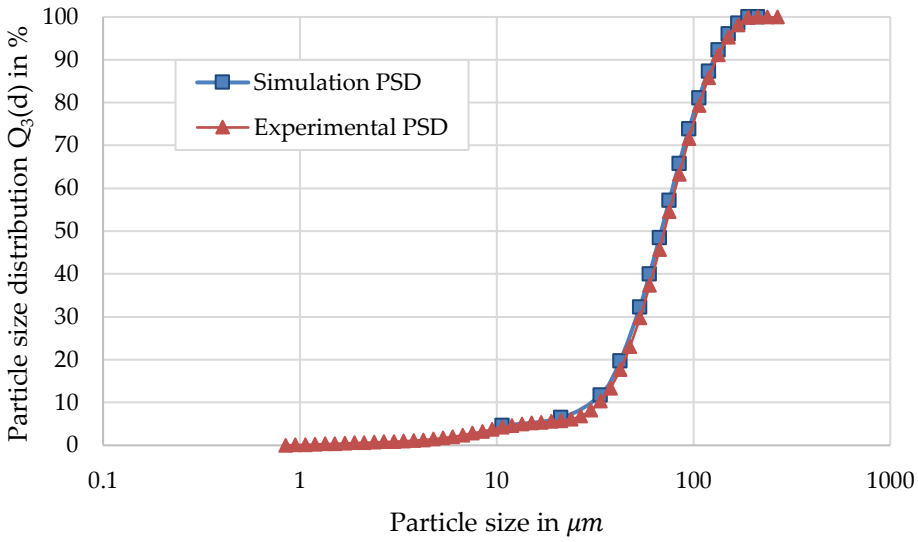

Fig. 6.19 Cumulative size distribution functions of fine material in both simulation (case 4) and experiment

In addition to the decrease in the value of time steps due to a decrease in the minimum size of the particles, considering a broad size distribution of particles causes a large increase in the number of particles (1,140,000 particles) and therefore a large increase in the total simulation time. In this case, the simulation time increased to almost 28 days for this very small geometry. However, the simulation results were qualitatively consistent with what is actually observed in the fluidization of fine particles. The results were partly

published by the DEM Solution webpage as a spotlight of EDEM software in https://www.edemsimulation.com/spotlight/cfd-dem-simulation-fluidization-compression-fine-particles/. Figure 6.20 shows some simulation results of fluidization of the complete size distribution of particles at different velocities.

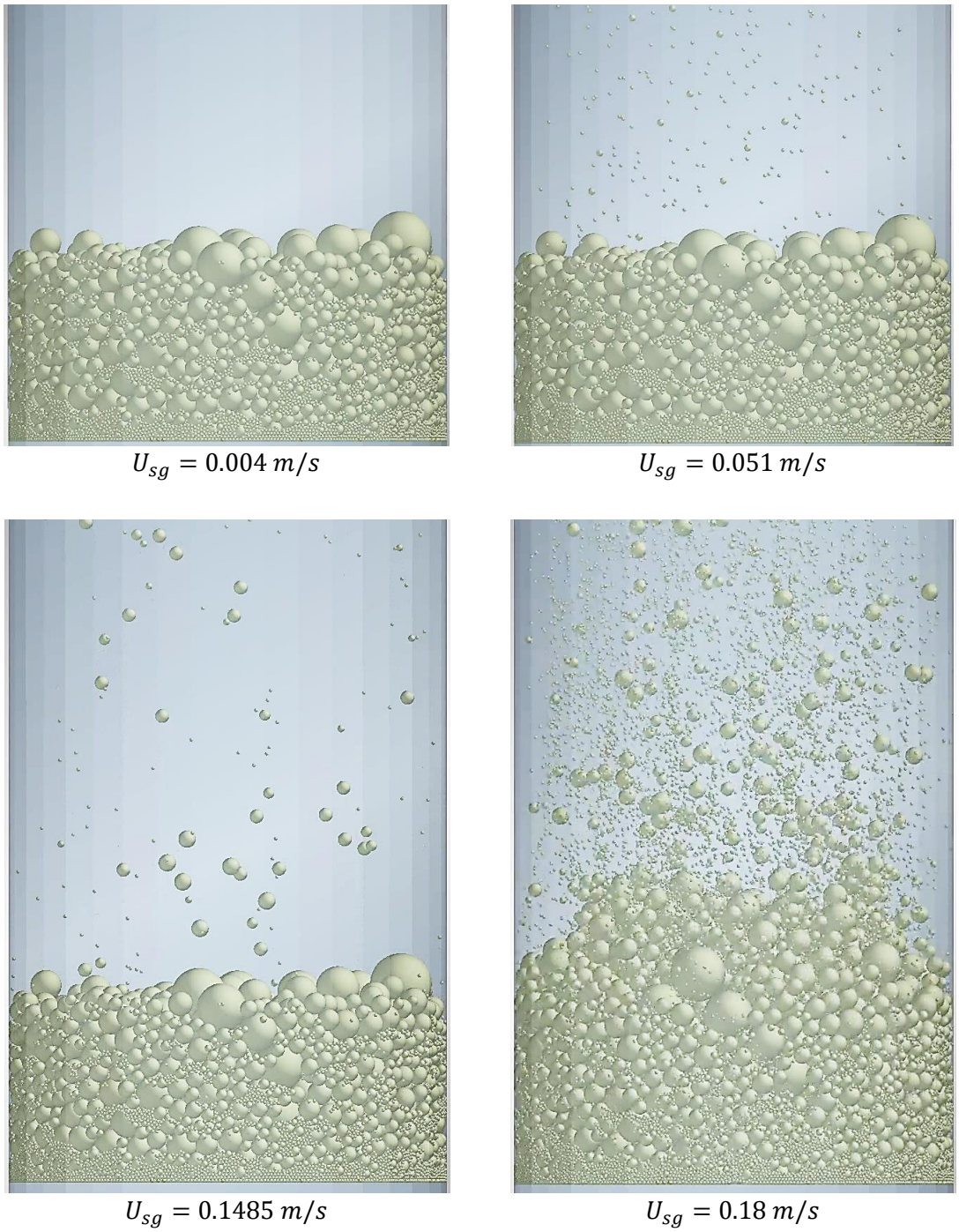

Fig. 6.20 Simulation behavior of particles with a broad size distribution at different velocities (Case 4).

Figure 6.21 shows the changes in the fluidization curve due to considering the real particle size distribution.

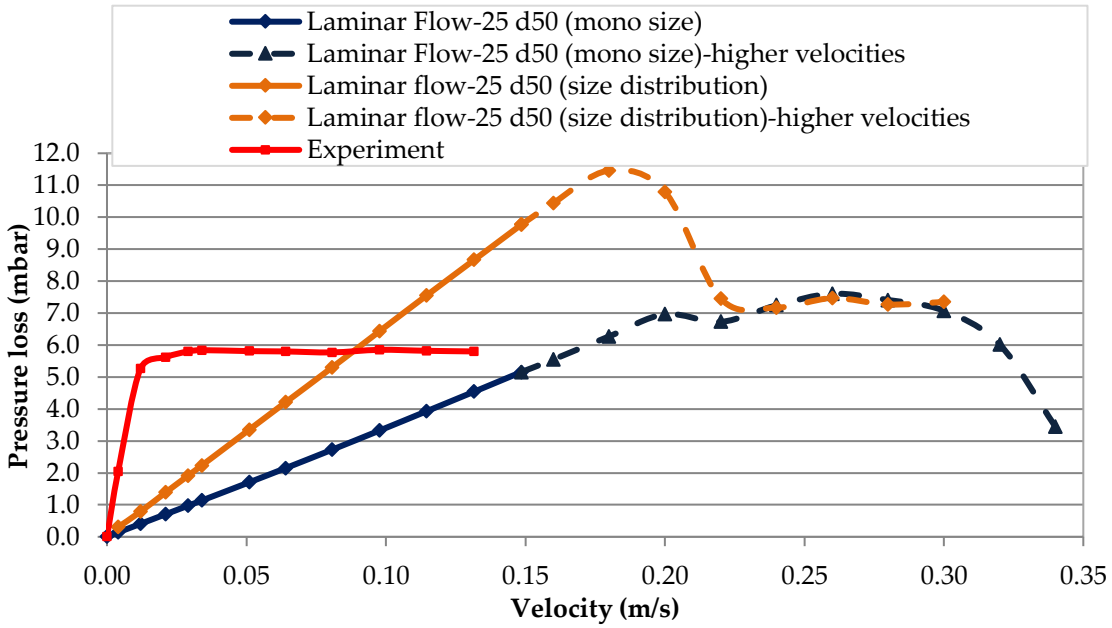

Fig. 6.21 Fluidization curve for non-cohesive particles in scaled-down geometry with a diameter of $25d_{50}$ and laminar airflow (comparison of mono-size and poly-size distribution)

This figure shows that the consideration of the real size distribution of the particles in the simulation resulted in a considerable increase in the slope of the linear part (related to the fixed bed condition) of the fluidization curve. This is equivalent to a decrease in the permeability of the bed due to positioning the smaller particles between the coarser ones. In addition, again, at the maximum velocity of the air in the experiments (0.1485 m/s), only movements of some small particles were visible. By increasing the air velocity, the fluidization started at about 0.18 m/s; which is again somewhat smaller than for the mono-size distribution. However, the bed pressure drop related to this velocity is far larger than for the case of mono-size particles (11.46 mbar). Furthermore, the mean value of the bed pressure drop after the fluidization point decreased a lot and showed an almost fixed value (average: 7.34 mbar).

Comparison the results of this simulation with experimental results indicates somewhat better conformity for the fixed bed condition and the final pressure drop after fluidization. In addition, the velocity related to the fluidization point was decreased and revealed better correspondence to the experimental results; it showed lower permeability and higher slope of linear behavior. However, the peak of the bed pressure drop was much too high at the fluidization point. The reduced size of the geometry and the effect of walls could be the source of the problem. Therefore, in the next simulation, modified conditions concern enlarging the size of the simulation domain.

6.5.2.5 (Case 5) Geometry diameter of $50d_{50}$, non-cohesive particles, laminar flow, mono-size distribution of particles

In this case, the diameter, and consequently the height of the column, were twice the previous cases. Therefore, the volume of this geometry and consequently the number of particles with the same particle size (mono-size) were 2^3=8 times those of the previous cases. In addition, from the viewpoint of the computational cost, considering the size distribution of particles was not feasible for this case. Thus, the simulation of this case was based on mono-disperse particles (Sauter diameter of fine particles). The number of particles for this case was 371,692. In addition, non-cohesive particles and laminar airflow are the other important settings.

The results of the fluidization curve for this case are shown in Fig. 6.22. In this figure, the results were compared with the smaller geometry of cases 3 and 4. For the linear behavior of the fixed bed condition, the results showed that increasing the diameter by twice resulted in a similar slope with case 4 (considering the real size distribution for a smaller geometry). It revealed that increasing the geometry reduced the permeability of the bed.

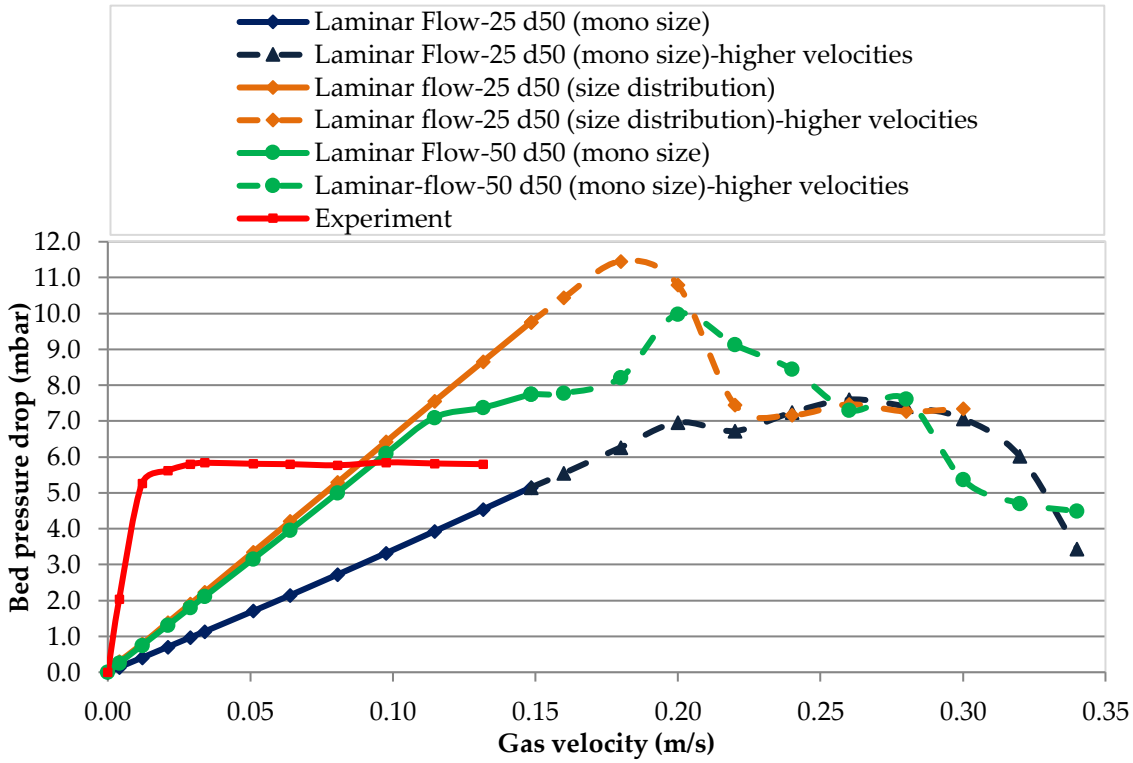

Fig. 6.22 Fluidization curve for non-cohesive particles in two scaled-down geometries with the diameters of $25d_{50}$ and $50d_{50}$, laminar airflow (comparison of mono-size and poly-size distribution of particles in a smaller geometry with mono-size particles in a bigger geometry)

In fact, the effect of walls decreased and the settling of the first simulation step resulted in a more compact bed. This case showed some fluidization from the velocity of 0.1146 m/s onward. The opening of a channel and upward movement of some particles decreased the rate of bed pressure drop increase. However, as visible in this figure, closing the channel was the reason for increasing again the bed pressure drop at 0.18 m/s. At 0.2 m/s, real fluidization occurred. This graph showed a (slightly) lower bed pressure drop before and during the start of fluidization in comparison with case 4. The computation took about 17 days.

Since the observed changes appear to go in the right direction, the next simulation was done based on an even larger computational domain.

6.5.2.6 (Case 6) Geometry diameter of $75d_{50}$, non-cohesive particles, laminar flow, mono-size distribution of particles

Following the previous case and to continue the investigation about the effect of the geometry size on the results, the sixth case was designed with exactly the same setting as the fifth case. The only difference was the size of the computational domain (geometry). In this case, 75 times of d_{50} was considered as the diameter of the fluidization domain. Accordingly, the height also increased. The geometry of this case was 3.375 times larger than the previous case and 27 times that of the first three cases. The number of particles for this case was 1,254,463. The simulation time was 38 days. This case contained also mono-size non-cohesive particles and the flow condition was laminar. The fluidization curve is shown in Fig. 6.23. For better comparison, the results of cases 3, 4, and 5 are also plotted in this figure.

The results showed that the further increase in the size of the scaled-down geometry increases also the slope of the linear part of the fluidization curve (fixed bed). Increasing the size of geometry revealed a lower permeability of the bed in the fixed bed condition, somewhat closer to that of the experiments. In addition, for this case, the fluidization point occurred for the first time before the maximum velocities of experiments (at 0.1316 m/s). This behavior also indicated a better consistency of those simulation results with experimental data.

However, although the average of the bed pressure drop after the fluidization point was in the same range as for case 5, the peak point of the bed pressure drop increased for this case. Apart from the last observation, these results indicated that the increase in the size of the scaled-down geometry results in more consistent results compared to the experiments. It means, the slope of the linear condition (fixed bed) increases, the permeability of the bed decreases, and the fluidization point moves toward the smaller velocities.

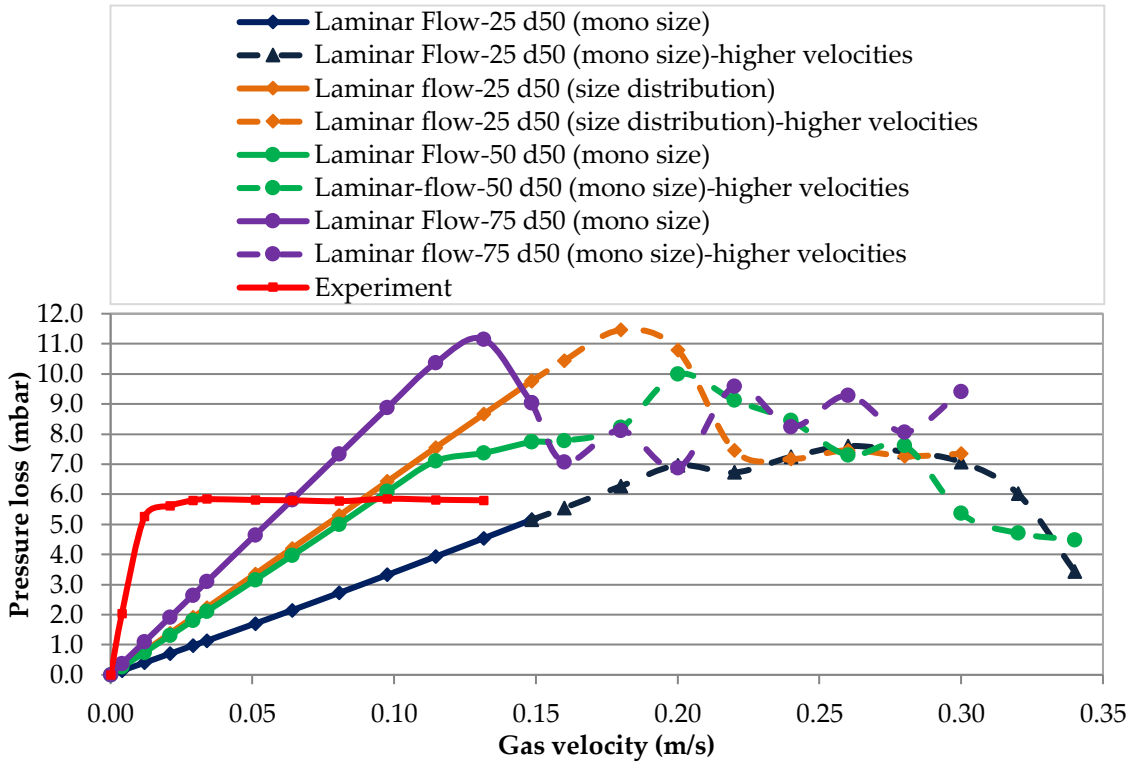

Fig. 6.23 Fluidization curve for non-cohesive particles in three different scaled-down geometries with the diameters of $25d_{50}$, $50d_{50}$, and $75d_{50}$, laminar airflow (comparison of mono-size and poly-size distribution of particles in smaller geometry with mono-size particles in two larger geometries)

6.5.2.7 (Case 7) Geometry diameter of $75d_{50}$, non-cohesive particles, laminar flow, mono-size distribution of particles, and lower friction coefficient

All settings for this case were exactly the same as for Case 6. The only difference was decreasing the coefficient of friction (0.4) for particle-particle and for particle-wall contacts. In this case again, 75 times of d_{50} was considered as the diameter of the fluidization domain. The number of particles for this case was equal to that of the sixth case. The simulation time was 28 days (this case was not continued for higher velocities). This case contained also mono-size non-cohesive particles and the flow condition was laminar. The fluidization curve is shown in Fig. 6.24. For better comparison, the results of cases 4 and 6 are also plotted in this figure.

The graph of case 7 showed very good matches to the experimental data at small velocities. However, after increasing the velocity to 0.012 m/s, and after a very small expansion in the bed, there was a sharp reduction in the slope of linear behavior. This could be the result of decreasing the friction factor (due to the mentioned initial expansion). This behavior continued until the velocity of 0.029 m/s.

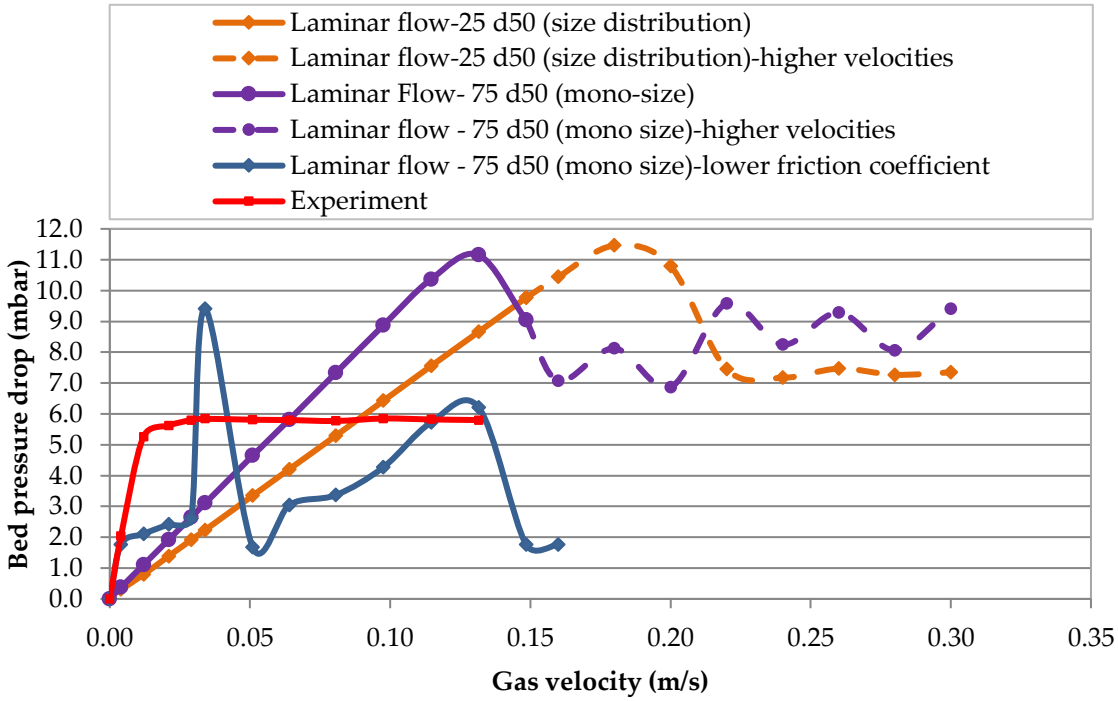

Fig. 6.24 Fluidization curve for non-cohesive particles in three different cases (4, 6, and 7) for comparison.

By increasing the velocity to 0.034 m/s, there was suddenly a big peak in the bed pressure drop, and something like spouting fluidization occurred. In this condition, some amount of particles (about 18%) were elutriated from the column and the remaining ones settled down again; then, the process of increasing the bed pressure drop by increasing the gas velocity was repeated for the remaining particles. This evolution had a similar slope as the case of considering the real size distribution of particles (case 4). Again, at 0.1316 m/s, there was a second peak and second elutriation of particles. At this point, about 81% of the particles were elutriated from the column and this was the main reason for decreasing the bed pressure drop after this velocity.

Although the behavior of fluidization, in this case, was more similar to the experimental results at very small gas velocities, decreasing the coefficient of friction, and consequently the contact forces between particles, was the cause of completely different behavior, involving spouting and elutriation of particles at higher velocities. Increasing again the coefficient of friction to 0.6 (not shown in the interest of space) also did not match with the experimental results; spouting behavior and elutriation of many particles out of the simulation domain were again observed.

6.5.2.8 (Case 8) Geometry diameter of 75d_{50}, non-cohesive particles, laminar flow, mono-size distribution of particles, lower friction coefficient, and free-slip boundary condition on walls

Increasing the size of geometry (cases 5 and 6) improved the results, showing that the wall effect is an important factor in the simulations. In case 8, the conditions were similar to case 7. The friction coefficient, was again 0.6, but the boundary condition of fluid flow on the wall was free-slip. The fluidization curve is shown in Fig. 6.25. For better comparison, the results of cases 4 and 6 are also plotted in this figure.

The no-slip boundary condition says that at the interface between a moving fluid and a stationary wall, both the normal and tangential components of the fluid velocity field are equal to zero. On the other hand, the free-slip boundary condition says that at the interface between a moving fluid and a stationary wall, the normal component of the fluid velocity field is equal to zero, but the tangential component is unrestricted. In this case, the fluid momentum near the wall is higher than in the previous cases.

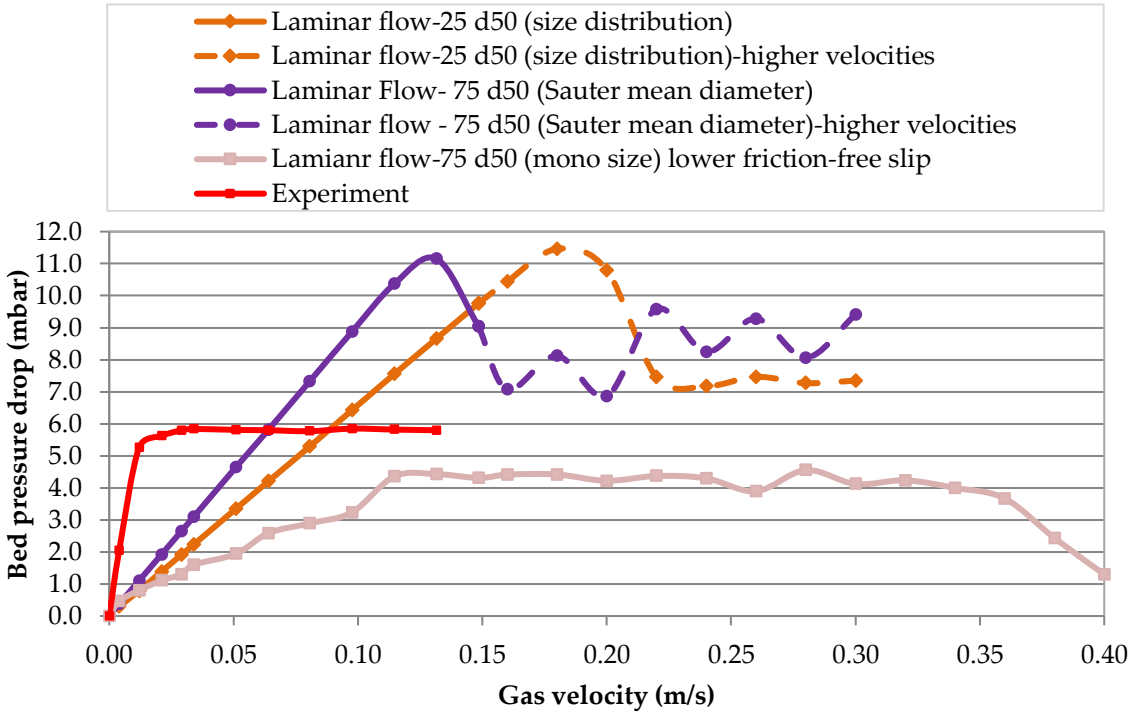

Fig. 6.25 Fluidization curve for non-cohesive particles in three different cases (4, 6, and 8) for comparison.

The results showed that the slope of the linear section (fixed bed) decreased a lot in Case 8, indicating higher permeability in the bed. A new kind of fluidization was observed in this case. The particles of one part of the bed (right-hand side) started to fluidize at 0.1146 m/s; by increasing the velocity, a circulation of particles in the bed occurred; while the bed pressure drop is almost constant. At 0.34 m/s the elutriation of particles from the simulation domain reduced the bed pressure drop. Although the fluidization curve in this

case qualitatively showed a typical fluidization curve for fine particles, the simulation results were quantitatively very far from the experimental observations.

6.5.2.9 (Case 9) Geometry diameter of $25d_{50}$, cohesive particles with smaller Hamaker constants, laminar flow, the real size distribution of particles, periodic boundary condition on walls

The simulations of these last cases were planned and performed under the guidance of Prof. van Wachem, using his in-house CFD-DEM simulation code for multi-phase flows. The aim of these simulations was the investigation of the effect of periodic boundary condition on the simulation results, and of the Hamaker constants. Therefore, in this case, a rectangle cube was considered as the computational domain instead of the cylindrical geometry of all the previous cases. Figure 6.26 indicated the results for two different Hamaker constants of 8.5×10^{-21} and 7.0×10^{-21} J.

The C_H (Hamaker constants) were decreased by about one order of magnitude. These results again showed that even considering cohesion between particles in such a small geometry could not mimic the physical behavior of the fluidization of fine particles in the experiments. The slopes of the linear part of the fluidization curve for this case lie in-between those of cases 1 and 4 and did not match the experimental results.

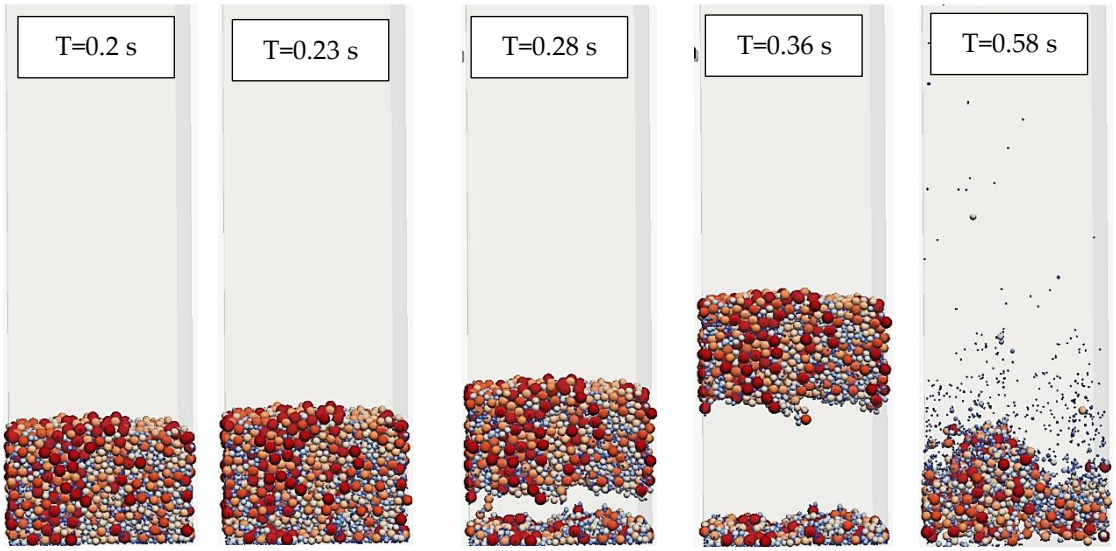

$C_H=8.5\times10^{-21}$

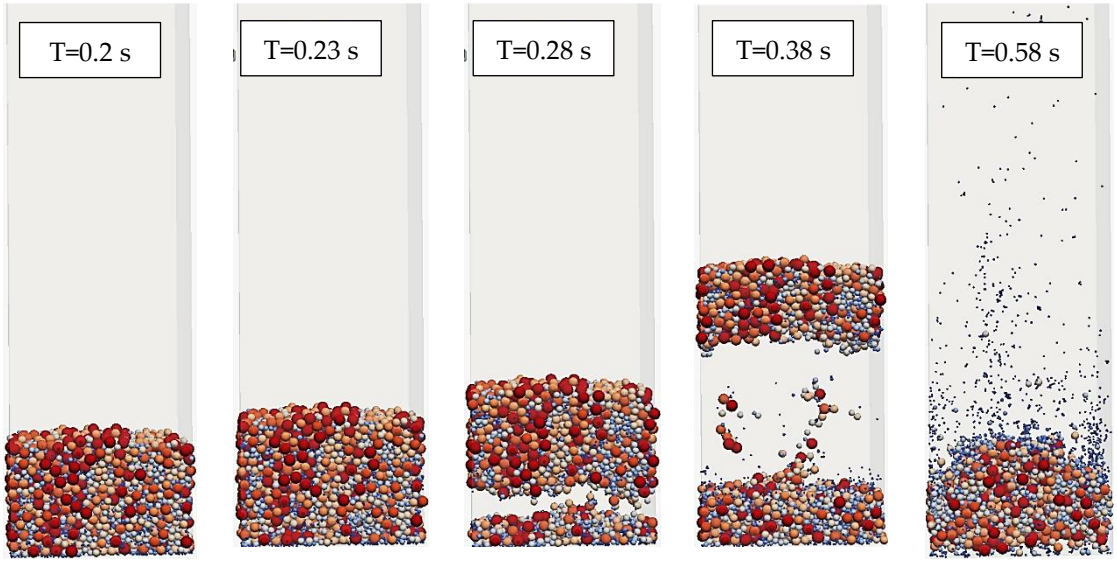

C_H=7.0×10^{-21}

Fig. 6.26 Fluidization behavior of cohesive particles with two different Hamaker constants in a rectangular geometry and periodic boundary conditions.

6.6 Concluding remarks

In this chapter, results concerning the simulation of fine particle bed fluidization under different conditions were reported. For these simulations, a coupled CFD-DEM was required to simulate the interaction of gas and solid phases. For the DEM (Discrete Element Method), EDEM software, and for CFD, ANSYS-FLUENT were used. These two software were coupled through an EDEM Application Programming Interface (API). Alternatively, the in-house code of Prof. van Wachem was also tested. Table 6.2 shows a brief comparison of nine different cases simulated in this chapter. The effects of different parameters were investigated and discussed.

Table 6.2 A brief comparison of the change in effective parameters between different simulated cases. The change made in each case (compared to the previous one) is highlighted by a green background.

Case #	Geometry Diameter scale	Representative particle size	Friction factor	Wall boundary condition	Cohesion	Used codes	Flow regimes	Remarks
1	$25d_{50}$	d_{32}	0.76	No-slip	Cohesive	EDEM-Fluent	Turbulent $k-\epsilon$	Herz-Mindlin with JKR (J=0.26 J/m^2)
2	$25d_{50}$	d_{32}	0.76	No-slip	Non-cohesive	EDEM-Fluent	Turbulent $k-\epsilon$	Herz-Midlin

3	$25d_{50}$	d_{32}	0.76	No-slip	Non-cohesive	EDEM-Fluent	Laminar	Herz-Midlin
4	$25d_{50}$	Real PSD	0.76	No-slip	Non-cohesive	EDEM-Fluent	Laminar	Herz-Midlin
5	$50d_{50}$	d_{32}	0.76	No-slip	Non-cohesive	EDEM-Fluent	Laminar	Herz-Midlin
6	$75d_{50}$	d_{32}	0.76	No-slip	Non-cohesive	EDEM-Fluent	Laminar	Herz-Midlin
7	$75d_{50}$	d_{32}	0.4 (0.6)	No-slip	Non-cohesive	EDEM-Fluent	Laminar	Herz-Midlin
8	$75d_{50}$	d_{32}	0.6	Free-slip	Non-cohesive	EDEM-Fluent	Laminar	Herz-Midlin
9	$25d_{50}$ (Rect. Cube)	Real PSD	0.76	Periodic B.C.	Cohesive	Prof. van Wachem code	Laminar	Van der Waals (C_H=8.5×10^{-21} and C_H=7.0×10^{-21})

The results show that:

a- Increasing the size of the scaled-down geometry as a representative geometry of the real experimental set-up increases the agreement of the simulation results with experimental data. In fact, many phenomena, which occur at macro scale, do not appear on the micro-scale. For example, the turbulent transport of energy has a predominant contribution over the energy transport, and important parameters as the turbulent kinetic energy vary in the inertial subrange of 1×10^{-3} m; while the scale for the dissipation of kinetic energy (Kolmogorov scale) is about 1×10^{-4} m. An even smaller scale occurs in the molecular diffusion of the species involved in the phenomenon (Batchelor scale), which is in the range of $1 \times 10^{-5} - 1 \times 10^{-6}$ m [238]. Therefore, in order to have simulation results that are consistent with experimental results, it is necessary to enlarge the simulation geometry toward real dimensions, while resolving all relevant scales, which is not possible due to the computational limitations and costs required and the limited power of the computer available in this study.

b- Considering the size distribution of involved particles (PSD) in the fluidization process could notably improve the simulation results. However, using a broad PSD causes an increase in the number of particles and also a decrease in the simulation time-step due to the decrease of the minimum size of particles in the simulation domain. Both changes result in a strong increase in computational costs.

c- Considering cohesion, even with smaller Hamaker constant or smaller surface energy than the real values, the obtained results could not mimic the behavior of fine particle fluidization observed in the experiments.

d- Considering a laminar flow condition decreases the velocity corresponding to the onset of fluidization (fluidization point) and leads to more realistic results. However, its effect on the behavior of the particulate system in the fixed bed

condition (at low velocities) is not significant, so that the overall agreement is not satisfactory.

e- Decreasing the friction coefficient in particle-particle and particle-wall contact has a strong effect on the results. However, the simulation results do not match better the experimental observations, apart from at very low velocities.

f- Changing the wall boundary condition to free slip or considering a rectangular cube geometry and periodic boundary condition instead of no-slip boundary condition on a cylindrical geometry changes the results and the behavior of the bed. However, a good agreement could not be obtained either.

g- Finally, a combination of increasing the size of the simulation domain while considering the real size distribution of the particles approves as the best method to match experimental observations. However, as mentioned in part (a), it is not possible in this study. It needs a high-performance GPU/CPU together with a powerful computer.

Overall, further studies are necessary to understand how CFD-DEM simulations could best be used to describe the fluidization of cohesive particles.

CHAPTER 7

Conclusions and perspectives

7.1 Conclusions

In this study, the effect of the presence of very cohesive ultra-fine powders in mixtures on fluidization, compression, permeation, and re-fluidization after compression or permeation was investigated. In this study, ground calcium carbonate (GCC) was used as fine material, CALCIT MVT 100 (Geldart's group A), and ultra-fine material, CALCIT MX 10 (group C). To complete this study, three classes of tests were performed. They are: 1) Fluidization test, 2) Fluidization, Compression, and Re-fluidization (FCR) tests, and 3) Fluidization, Compression, Permeation, and Re-fluidization (FPCR) tests. In addition to the three classes of experiments, a series of simulations were also done toward the development of a CFD-DEM model for the fluidization of fine particles. The results of experiments and simulations are as follow:

Fluidization test: In this study, different fluidization tests were conducted for fine particles, ultra-fine particles, and mixtures of these two materials in order to study the effect of the presence of ultra-fine particles on the fluidization of a fine-particle bed. Two mixtures with a dominant mass fraction of either fine or ultra-fine particles and a mixture of these two materials in the same weight fraction were considered. The fluidization behavior of fine material (Geldart A) was characterized by an easy, aggregative (bubbling), and full fluidization. For fine material, experimental results also showed smooth fluidization with a slight hysteresis effect.

When mixing with ultra-fine powders, the experimental results showed that the presence of ultra-fine powders can change the full fluidization of fine particle bed severely. The measured physical properties (e.g., ρ_b, c_M, d_M, and ff_c) of the mixtures of fine and ultra-fine particles were close to those of ultra-fine powders only. Similar to ultra-fine powders, the fluidization behavior of these mixtures was partial, non-reproducible, significantly different for each realization, and includes cracking, channeling, and agglomeration.

Initial conditions had significant impacts on fluidization behavior. There were many fluctuations in the bed pressure drop when increasing gas velocity (loading process). Therefore, to have a better overview of the fluidization process for these mixtures, the fluidization tests have been repeated, and the mean value of the bed pressure drop for each gas velocity has been used for analyzing the fluidization behavior. When decreasing the fluidization air velocity (unloading curve), the change in the bed pressure drop showed an almost linear behavior, corresponding to an approximately constant permeability.

Briefly, increasing the portion of ultra-fine powders in the fluidized material causes a delay in starting partial fluidization, an increase in the bed pressure drop, a delay in reaching the peak point, a decrease in the bed expansion ratio (%), an increase in the total expansion of the bed after unloading as well as an increase in the hysteresis effect between loading and unloading curves. To understand these phenomena, the effect of mixing fine particles with cohesive ultra-fine powders and their roles in modifying the size distribution of agglomerates were discussed.

Fluidization, Compression, and Re-fluidization (FCR) tests: The results of the compression step showed that the compression behavior follows the logarithmic law for all three pressures levels (20, 40, and 80 kPa). The compressibility index was almost the same for the low and intermediate pressure levels. However, for higher pressures, the compressibility index decreased strongly due to a change in the compaction regime. Similarly, for the higher pressure, the slope of the particle volume fraction versus logarithmic display of dimensionless stress was noticeably different. The results of compression experiments further revealed that this slope does not depend on the size distribution of the mixtures but on the type of material itself.

The re-fluidization test results showed that while the peak of the bed pressure drop (ΔP_{peak}) increases, the superficial gas velocity corresponding to the peak point is smaller for re-fluidization after compression, compared to initial fluidization; consequently, the slope of the loading curve was much larger for re-fluidization. The opposite was observed for the unloading curves. When increasing the proportion of ultra-fine particles in the binary mixture, ΔP_{peak} increased as well, particularly strongly in the intermediate range of 50 to 70% of ultra-fine particles, when the ultra-fine powders start to be dominant in the mixture.

Fluidization, Compression, Permeation, and Re-fluidization (FPCR) tests: The observations showed a permanent decrease of permeability by increasing the applied pressure which was attributed to structural changes in the pore network, such as sealing of pore channels or expansion and realignment of particles within the pores. Moreover, by increasing the

pressure differences between the two sides of the bed at all the retained pressure levels, the superficial gas velocities were increased. In addition, by adding the ultra-fine powders in the particle bed, even for only 30% of ultra-fines in the mixture, the results indicated a sharp change in the permeability of the mixture material compared to the fine particle bed (about 50 times smaller).

The results also revealed that the trend of decreasing permeability for all three levels of applied pressures was almost the same. However, the rate of decreasing the permeability in the first stages of applying pressure was far more than in the last stages, for all three pressure levels. In fact, for each pressure level setting, when increasing the pressure toward the maximum pressure, the rate of changes in the permeability was decreased. The re-fluidization test results showed that while the peak of the bed pressure drops increases, the superficial gas velocity corresponding to the peak point is smaller for re-fluidization after compression and permeation, compared to the initial fluidization; consequently, the slope of the loading curve is much larger for re-fluidization. The opposite trend was observed for the unloading curves. When increasing the proportion of ultra-fine particles in the binary mixture, ΔP_{peak} increased as well. However, comparing the results of FCPR tests with FCR tests showed that in FCPR tests, due to the higher effect of permeation process in decreasing bed height, porosity, and then permeability, the slopes for loading were higher than the slopes for FCR tests, while the slopes for unloading were lower.

Simulations: The simulations considering different affecting parameters shows that a combination of increasing the size of the simulation domain while considering the real size distribution of the particles approves as the best method to match experimental observations. However, it needs a high-performance GPU/CPU together with a powerful computer.

7.2 Perspectives

The experimental results considered in this work were performed for calcite ($CaCo_3$). In fact, three main processes of fluidization, compression, and permeation, as well as the history effect due to a compression phase and a combination of compression and permeation process on the re-fluidization of fine particles, are focused on the behavior of two Geldart groups (A and C) of calcite particles. Investigating the behavior of other commonly used materials in the industry and comparing the results of that series of tests with the outcomes of this study could be interesting. It could show the influence of the type of material on the outcomes.

Moreover, in this study, the effect of ultra-fine (Geldart group C) powders was investigated in mixtures containing fine (Geldart group A) particles. The results showed

several interesting outcomes concerning the mixing of different Geldart groups. To continue, it seems that the combination of other Geldart groups (e.g. Geldart groups B and D, etc.) can lead to new interesting results of combining a material with different size compositions.

Since one of the goals for this study was investigating the history effect of compression and permeation on fluidization, the range of applied pressures used in the compression and permeation is selected in such a way that the compressed bed doesn't make a durable consolidation effect. It could be helpful if, in another study, the higher ranges of applied pressures will be considered. In this manner, the effect of the presence of cohesive ultra-fine powders in different mixtures with fine particles could be studied during all of these processes. The comparison of the results with the results of this study for lower levels of applied pressures can lead to interesting results and show the effect of increasing applied pressures on these processes.

The experiments of this study were performed with a fixed test rig (as described in chapter 2). Investigating the effect of changes in the size of the column, the aspect ratio (height to diameter) of the column, the effect of changing the cylinder column with a rectangular cube, using different fluidizing gas, etc. seems also remarkable. In fact, it would be interesting to study different mixtures of ultra-fine powders and fine particles in different geometries or processing gases and compare the outcomes with the results of the present study.

For the simulation part, the simulation of a greater domain considering the real size distribution of fine particles can lead to better and more consistent results. However, with the current facilities and due to the lack of a high-performance GPU/CPU together with a powerful computer, this simulation was not possible. However, using a high-performance cluster of GPUs and the new versions of EDEM (GPU based parallel processing types), it could be possible to continue the improvement of consistency of simulation results with experimental observations in the future studies.

Bibliography

1. Tomas, J.; Kache, G. Micro- and macromechanics of hopper discharge of ultrafine cohesive powder. *Int. J. Chem. React. Eng.* **2012**, *10*, 47–65, doi:10.1515/1542-6580.A44.
2. Geldart, D.; Harnby, N.; Wong, A.C. Fluidization of cohesive powders. *Powder Technol.* **1984**, *37*, 25–37, doi:10.1016/0032-5910(84)80003-0.
3. Wang, Z.; Kwauk, M.; Li, H. Fluidization of fine particles. *Chem. Eng. Sci.* **1998**, *53*, 377–395, doi:10.1016/S0009-2509(97)00280-7.
4. Massimilla, L.; Donsi, G. Cohesive forces between particles of fluid-bed catalysts. *Powder Technol.* **1976**, *15*, 253–260, doi:10.1016/0032-5910(76)80054-X.
5. Dry, R.J.; Judd, M.R.; Shingles, T. Two-phase theory and fine powders. *Powder Technol.* **1983**, *34*, 213–223, doi:10.1016/0032-5910(83)87053-3.
6. Shaul, S.; Rabinovich, E.; Kalman, H. Typical fluidization characteristics for Geldart's classification groups. *Part. Sci. Technol.* **2014**, *32*, 197–205, doi:10.1080/02726351.2013.842624.
7. Millán, J.M.V. *Fluidization of Fine Powders*; Particle Technology Series; Springer: Dordrecht, The Netherlands, 2013; Vol. 18; ISBN 978-94-007-5586-4.
8. Geldart, D. Types of gas fluidization. *Powder Technol.* **1973**, *7*, 285–292, doi:10.1016/0032-5910(73)80037-3.
9. Ajbar, A.; Alhumazi, K.; Asif, M. Improvement of the fluidizability of cohesive powders through mixing with small proportions of group A particles. *Can. J. Chem. Eng.* **2008**, *83*, 930–943, doi:10.1002/cjce.5450830602.
10. Dechsiri, C. Ph.D. thesis - Particle transport in fluidized beds, UMCG research database, 2004.
11. Abrahamsen, A.R.; Geldart, D. Behaviour of gas-fluidized beds of fine powders part I. Homogeneous expansion. *Powder Technol.* **1980**, *26*, 35–46, doi:10.1016/0032-5910(80)85005-4.
12. Yang, W.-C. Handbook of fluidization and fluid-particle systems. In; Marcel Dekker, Inc.: New York, 2003; pp. 1–850 ISBN 082470259X.
13. Rumpf, H. Die Wissenschaft des Agglomerierens. *Chemie Ing. Tech. - CIT* **1974**, *46*, 1–11, doi:10.1002/cite.330460102.
14. Millán, J.M.V. Fluidization of Fine Powders: Cohesive versus Dynamic Aggregation. In *The 14th International Conference on Fluidization – From Fundamentals to Products*; ECI Symposium Series; Noordwijkerhout, Netherlands, 2013.
15. Horio, M. Binderless granulation - its potential, achievements and future issues. *Powder Technol.* **2003**, *130*, 1–7, doi:https://doi.org/10.1016/S0032-5910(02)00216-4.
16. Barletta, D.; Poletto, M. Aggregation phenomena in fluidization of cohesive powders assisted by mechanical vibrations. *Powder Technol.* **2012**, *225*, 93–100, doi:10.1016/j.powtec.2012.03.038.
17. Xu, C.; Zhu, J. Experimental and theoretical study on the agglomeration arising from fluidization of cohesive particles - Effects of mechanical vibration. *Chem. Eng. Sci.* **2005**, *60*, 6529–6541, doi:10.1016/j.ces.2005.05.062.
18. Mawatari, Y.; Koide, T.; Tatemoto, Y.; Uchida, S.; Noda, K. Effect of particle

diameter on fluidization under vibration. *Powder Technol.* **2002**, *123*, 69–74, doi:10.1016/S0032-5910(01)00432-6.
19. Mawatari, Y.; Hamada, Y.; Yamamura, M.; Kage, H. Flow pattern transition of fine cohesive powders in a gas-solid fluidized bed under mechanical vibrating conditions. *Procedia Eng.* **2015**, *102*, 945–951, doi:10.1016/j.proeng.2015.01.216.
20. Meili, L.; Daleffe, R. V.; Freire, J.T. Fluid Dynamics of Fluidized and Vibrofluidized Beds Operating with Geldart C Particles. *Chem. Eng. Technol.* **2012**, *35*, 1649–1656, doi:10.1002/ceat.201100546.
21. Zhu, C.; Liu, G.; Yu, Q.; Pfeffer, R.; Dave, R.N.; Nam, C.H. Sound assisted fluidization of nanoparticle agglomerates. *Powder Technol.* **2004**, *141*, 119–123, doi:10.1016/j.powtec.2004.01.023.
22. Guo, Q.; Liu, H.; Shen, W.; Yan, X.; Jia, R. Influence of sound wave characteristics on fluidization behaviors of ultrafine particles. *Chem. Eng. J.* **2006**, *119*, 1–9, doi:10.1016/j.cej.2006.02.012.
23. Shabanian, J.; Jafari, R.; Chaouki, J. Fluidization of Ultrafine Powders. *Int. Rev. Chem. Eng.* **2012**, *4*, 16–50.
24. Zhu, X.; Zhang, Q.; Huang, C.; Wang, Y.; Yang, C.; Wei, F. Validation of surface coating with nanoparticles to improve the flowability of fine cohesive powders. *Particuology* **2016**, 1–9, doi:10.1016/j.partic.2016.09.001.
25. Zhou, T.; Li, H. Effects of adding different size particles on fluidization of cohesive particles. *Powder Technol.* **1999**, *102*, 215–220, doi:10.1016/S0032-5910(98)00211-3.
26. Duan, H.; Liang, X.; Zhou, T.; Wang, J.; Tang, W. Fluidization of mixed SiO2 and ZnO nanoparticles by adding coarse particles. *Powder Technol.* **2014**, *267*, 315–321, doi:10.1016/j.powtec.2014.07.045.
27. Song, L.; Zhou, T.; Yang, J. Fluidization behavior of nano-particles by adding coarse particles. *Adv. Powder Technol.* **2009**, *20*, 366–370, doi:10.1016/j.apt.2009.02.010.
28. Ajbar, A.; Alhumaizi, K.; Ibrahim, A.; Asif, M. Hydrodynamics of gas fluidized beds with mixture of group D and B particles. *Can. J. Chem. Eng.* **2002**, *80*, 281–288, doi:10.1002/cjce.5450800213.
29. Scala, F.; Cammarota, A.; Chirone, R.; Salatino, P. Comminution of Limestone during Batch Fluidized-Bed Calcination and Sulfation. *AIChE J.* **1997**, *43*, 363–373, doi:10.1002/aic.690430210.
30. Grossmann, L.; Tomas, J.; Csöke, B. Compressibility and flow properties of a cohesive limestone powder in a medium pressure range. *Granul. Matter* **2004**, *6*, 103–109, doi:10.1007/s10035-004-0164-z.
31. Gochioco, K. The Effect of Crystalline and Amorphous Lactose on Mechanical Properties of Roller Compaction Ribbon and Tablets, Master's Thesis, University of Kansas, Lawrence, KS, USA, 2014.
32. Faldu, B.; Zalavadiya, B. Compaction Behaviour: Force Distribution Through Powder Bed. *Int. J. Pharm. Res. Dev.* **2012**, *4*, 38–50.
33. Darwin, G.H. On the Horizontal Thrust of a Mass of Sand. In *Minutes of the Proceedings of the Institution of Civil Engineers*; ICE Virtual Library: London, UK, 1883; Vol. 71, pp. 350–378.
34. Castellanos, A. The relationship between attractive interparticle forces and bulk behaviour in dry and uncharged fine powders. *Adv. Phys.* **2005**, *54*, 263–276, doi:10.1080/17461390500402657.

35. Tomas, J. Adhesion of ultrafine particles—A micromechanical approach. *Chem. Eng. Sci.* **2007**, *62*, 1997–2010, doi:10.1016/j.ces.2006.12.055.
36. Valverde, J.M.; Castellanos, A. Compaction of fine powders: From fluidized agglomerates to primary particles. *Granul. Matter* **2007**, *9*, 19–24, doi:10.1007/s10035-006-0022-2.
37. Song, H. Fundamentals of Fluid Mechanics Through Porous Media. In *Engineering Fluid Mechanics*; Springer Singapore: Singapore, 2018; Vol. 54, pp. 171–197 ISBN 9789811301735.
38. Terzaghi, K.; Peck, R.B.; G., M. *Soil mechanics in engineering practice (3rd edition)*; 3rd ed.; Petros Fekadu, 1996; ISBN 978-0471086581.
39. Ansari, M.I. *Fine particle processing - A difficult problem for mineral engineers*; National Metallurgical Laboratory, Jamshedpur, India, 1997;
40. Sivamohan, R. The problem of recovering very fine particles in mineral processing - A review. *Int. J. Miner. Process.* **1990**, *28*, 247–288, doi:10.1016/0301-7516(90)90046-2.
41. Sivamohan, R.; Forssberg, E. Recovery of heavy minerals from slimes. *Int. J. Miner. Process.* **1985**, *15*, 297–314, doi:10.1016/0301-7516(85)90047-X.
42. Sivamohan, R. A Study of Gravity Concentration with Emphasis on Surface Phenomena, Phd Thesis, Technical Universit y of Luleå, 1985.
43. Tomas, J. Micromechanics of Ultrafine Particle Adhesion – Energy Absorption At Contact. *Energy* **1979**, *29*, 2–7.
44. Kamranian Marnani, A.; Idowu, R.; Bück, A.; Antonyuk, S.; Thévenin, D.; Tomas, J. Classification of ultra-fine adhesive particles at fine cohesive powders. In *12th International Conference on Bulk Materials Storage, Handling and Transportation (ICBMH 2016)*; Darwin, Australia, 11–14 July, 2016.
45. Saravacos, G.D.; Kostaropoulos, A.E. *Handbook of Food Processing Equipment*; 2nd ed.; Springer Switzerland, 2016; ISBN 978-3-319-25020-5.
46. Juliano, P.; Barbosa-Cánovas, G. V. Food Powders Flowability Characterization: Theory, Methods, and Applications. *Annu. Rev. Food Sci. Technol. - (new 2010)* **2010**, *1*, 211–239, doi:10.1146/annurev.food.102308.124155.
47. Fu, P.; Wang, F.; Ma, L.; Yang, X.; Wang, H. Fine particle sorting and classification in the cyclonic centrifugal field. *Sep. Purif. Technol.* **2016**, *158*, 357–366, doi:10.1016/j.seppur.2015.12.044.
48. Brown, J.S.; Gordon, T.; Price, O.; Asgharian, B. Thoracic and respirable particle definitions for human health risk assessment. *Part. Fibre Toxicol.* **2013**, *10*, 1–12, doi:10.1186/1743-8977-10-12.
49. Pope, C.A.I.; Dockery, D.W. Health Effects of Fine Particulate Air Pollution: Lines that Connect. *J. Air Waste Manage. Assoc.* **2006**, *56*, 709–742, doi:10.1080/10473289.2006.10464485.
50. Kamranian Marnani, A.; Bück, A.; Antonyuk, S.; van Wachem, B.; Thévenin, D.; Tomas, J. The Effect of the Presence of Very Cohesive Geldart C Ultra-Fine Particles on the Fluidization of Geldart A Fine Particle Beds. *Processes* **2019**, *7*, 35, doi:10.3390/pr7010035.
51. Galk, J.; Peukert, W.; Krahnen, J. Industrial classification in a new impeller wheel classifier. *Powder Technol.* **1999**, *105*, 186–189, doi:10.1016/S0032-5910(99)00136-9.
52. Johansson, R. Air Classification of Fine Aggregates. *Géotechnique* **2014**, *29*, 47–65.

53. Hamaker, H.C. The London—van der Waals attraction between spherical particles. *Physica* **1937**, *4*, 1058–1072, doi:10.1016/S0031-8914(37)80203-7.
54. Zeng, Y. Colloidal Dispersions Under Slit-Pore Confinement. *Géotechnique* **2012**, *29*, 5–22, doi:10.1007/978-3-642-34991-1.
55. Lifshitz, E.M. The theory of molecular attractive forces between solids. *J. Exp. Theor. Phys.* **1956**, *2*, 73–83.
56. Bergström, L. Hamaker constants of inorganic materials. *Adv. Colloid Interface Sci.* **1997**, *70*, 125–169, doi:10.1016/S0001-8686(97)00003-1.
57. Shamlou, P.A. *Handling of Bulk Solids - Theory and Practice*; 1st ed.; Butterworth & Co.: London, 1988; ISBN 0-407-01180-3.
58. Tomas, J. The mechanics of dry, cohesive powders. *Powder Handl. Process.* **2003**, *15*, 296–314.
59. Kuni, D.; Levenspiel, O. *Fluidization Engineering (Chapter 2 - Fluidization and Mapping of Regimes)*; Brenner, H., Ed.; Second Edi.; Butterworth-Heinemann, 1991;
60. Yerushalmi, J.; Cankurt, N.T. Further studies of the regimes of fluidization. *Powder Technol.* **1979**, *24*, 187–205, doi:10.1016/0032-5910(79)87036-9.
61. Molerus, O. *Principles of Flow in Disperse Systems*; Chapman & Hall, 1993; ISBN 0 412 40630 6.
62. Goossens, W.R.A. Classification of fluidized particles by archimedes number. *Powder Technol.* **1998**, *98*, 48–53, doi:10.1016/S0032-5910(98)00027-8.
63. Ergun, S. Fluid flow through packed columns. *Chem. Eng. Prog.* **1952**, *48*, 89–94.
64. Rietema, K.; Cottaar, E.J.E.; Piepers, H.W. The effects of interparticle forces on the stability of gas-fluidized beds - II. Theoretical derivation of bed elasticity on the basis of van der Waals forces between powder particles. *Chem. Eng. Sci.* **1993**, *48*, 1687–1697, doi:10.1016/0009-2509(93)80128-D.
65. Geldart, D. *Gas fluidization technology*; John Wiley & Sons Ltd.: Chichester, 1986; ISBN 9780471908067.
66. Israelachvili, J.N. *Intermolecular and surface forces*; 3rd editio.; Elsevier Inc.: USA, 2011; ISBN 9780123919274.
67. Schubert, H. Grundlagen des Agglomerierens. *Chemie Ing. Tech.* **1979**, *51*, 266–277, doi:10.1002/cite.330510404.
68. Tomas, J. Zur Verfestigung von Schüttgütern - Mikroprozesse und Kinetikmodelle". *Chemie Ing. Tech.* **1997**, *69*, 455–467, doi:10.1002/cite.330690406.
69. Seville, J.P.K.; Willett, C.D.; Knight, P.C. Interparticle forces in fluidisation: A review. *Powder Technol.* **2000**, *113*, 261–268, doi:10.1016/S0032-5910(00)00309-0.
70. Molerus, O. Interaction of Geldart's Type A, B, C and D Powders by Taking into accoumt Interaction Cohesion Forces.pdf. *Powder Technol.* **1982**, *33*, 81–87, doi:10.1016/0032-5910(82)85041-9.
71. Briscoe, B.J.; Adams, M.J. *Tribology in particulate technology*; Adam Hilger: Bristol, 1987;
72. Seville, J.; Tuzun, U.; Clift, R. *Processing of Particulate Solids*; Scarlett, B., Jimbo, G., Eds.; First edit.; Chapman & Hall: London, 1997; ISBN 9789401071529.
73. Fisher, R.A. On the capillary forces in an ideal soil; correction of formulae given by W. B. Haines. *J. Agric. Sci.* **1926**, *16*, 492–505, doi:10.1017/S0021859600007838.
74. Pietsch, W.B. Tensile Strength of Granular Materials. *Nature* **1968**, *217*, 736–737.
75. Barnocky, G.; Davis, R.H. Elastohydrodynamic collision and rebound of spheres:

Experimental verification. *Phys. Fluids* **1988**, *31*, 1324–1329, doi:10.1063/1.866725.

76. Cameron, A.; Ettles, C.M.M. *Basic Lubrication Theory*; 3rd editio.; Ellis Horwood Ltd, 1981; ISBN 9780853121770.
77. Lian, G.; Thornton, C.; Adams, M.J. A Theoretical Study of the Liquid Bridge Forces between Two Rigid Spherical Bodies. *J. Colloid Interface Sci.* **1993**, *161*, 138–147, doi:10.1006/jcis.1993.1452.
78. Vick, F.A. Theory of contact electrification. *Br. J. Appl. Phys.* **1953**, *4*, S1–S5, doi:10.1088/0508-3443/4/S2/301.
79. Hersh, S.P.; Montgomery, D.J. Static Electrification of Filaments Theoretical Aspects. *Text. Res. J.* **1956**, *XXVI*, 903–913.
80. Osberg, G.L.; Charlesworth, D.H. Elutriation in a fluidized bed. *Chem. Eng. Prog.* **1951**, *47*, 566–570.
81. Wilhelm, R.H.; Kwauk, M. Fluidization of Solid Particles. *Chem. Eng. Prog.* **1948**, *44*, 201–218.
82. Miller, C.; Logwinuk, A. Fluidization Studies of Solid Particles. *Ind. Eng. Chem.* **1951**, *43*, 1220–1226, doi:10.1021/ie50497a059.
83. Lewis, W.K.; Gilliland, E.R.; Bauer, W.C. Characteristics of Fluidized Particles. *Ind. Eng. Chem.* **1949**, *41*, 1104–1117, doi:10.1021/ie50474a004.
84. Rojo, V.; Guardiola, J.; Vian, A. A capacitor model to interpret the electric behaviour of fluidized beds. Influence of apparatus geometry. *Chem. Eng. Sci.* **1986**, *41*, 2171–2181, doi:10.1016/0009-2509(86)87133-0.
85. Matsusaka, S.; Maruyama, H.; Matsuyama, T.; Ghadiri, M. Triboelectric charging of powders: A review. *Chem. Eng. Sci.* **2010**, *65*, 5781–5807, doi:10.1016/J.CES.2010.07.005.
86. Nwose, E.N.; Pei, C. Modelling die filling with charged particles using DEM/CFD. *Particuology* **2012**, *10*, 229–235, doi:10.1016/J.PARTIC.2011.11.010.
87. Pei, C.; Wu, C.-Y.; England, D.; Byard, S.; Berchtold, H.; Adams, M. DEM-CFD modeling of particle systems with long-range electrostatic interactions. *AIChE J.* **2015**, *61*, 1792–1803, doi:10.1002/aic.14768.
88. Pu, Y.; Mazumder, M.; Cooney, C. Effects of Electrostatic Charging on Pharmaceutical Powder Blending Homogeneity. *J. Pharm. Sci.* **2009**, *98*, 2412–2421, doi:10.1002/JPS.21595.
89. Wolny, A.; Kaźmierczak, W. Triboelectrification in fluidized bed of polystyrene. *Chem. Eng. Sci.* **1989**, *44*, 2607–2610, doi:10.1016/0009-2509(89)85204-2.
90. Wolny, A.; Kaźmierczak, W. The influence of static electrification on dynamics and rheology of fluidized bed. *Chem. Eng. Sci.* **1993**, *48*, 3529–3534, doi:10.1016/0009-2509(93)85008-D.
91. Guardiola, J.; Rojo, V.; Ramos, G. Influence of particle size, fluidization velocity and relative humidity on fluidized bed electrostatics. *J. Electrostat.* **1996**, *37*, 1–20, doi:10.1016/0304-3886(96)00002-2.
92. Liu, Z.; Bi, X.T.; Grace, J.R. Electrostatic charging behaviour of dielectric particles in a pressurized gas–solid fluidized bed. *J. Electrostat.* **2010**, *68*, 321–327, doi:10.1016/J.ELSTAT.2010.03.006.
93. Zhang, Q.; Zhou, Y.; Wang, J.; Jiang, B.; Yang, Y.; Stapf, S.; Mattea, C.; Gong, Q. Particle Motion in Two- and Three-Phase Fluidized-Bed Reactors Determined by Pulsed Field Gradient Nuclear Magnetic Resonance. *Chem. Eng. Technol.* **2015**, *38*,

1269–1276, doi:10.1002/ceat.201400659.
94. Pei, C.; Wu, C.Y.; England, D.; Byard, S.; Berchtold, H.; Adams, M. Numerical analysis of contact electrification using DEM-CFD. *Powder Technol.* **2013**, *248*, 34–43, doi:10.1016/j.powtec.2013.04.014.
95. LaMarche, K.R.; Liu, X.; Shah, S.K.; Shinbrot, T.; Glasser, B.J. Electrostatic charging during the flow of grains from a cylinder. *Powder Technol.* **2009**, *195*, 158–165, doi:10.1016/j.powtec.2009.05.026.
96. Harper, W.R. The generation of static charge. *Adv. Phys.* **1957**, *6*, 365–417, doi:10.1080/00018735700101396.
97. Seville, J.P.K.; Clift, R. The effect of thin liquid layers on fluidisation characteristics. *Powder Technol.* **1984**, *37*, 117–129, doi:10.1016/0032-5910(84)80011-X.
98. Zhou, T.; Li, H. Force balance modelling for agglomerating fluidization of cohesive particles. *Powder Technol.* **2000**, *111*, 60–65, doi:10.1016/S0032-5910(00)00241-2.
99. Chaouki, J. Chavarie, C.; Klvana, D.; Pajonk, G. Effect of interparticle forces on the hydrodynamic behaviour of fluidized aerogels. *Powder Technol.* **1985**, *43*, 117–125, doi:10.1016/0032-5910(85)87003-0.
100. Morooka, S.; Kusakabe, K.; Kobata, A.; Kato, Y. Fluidization state of ultrafine powders. *J. Chem. Eng. Japan* **1988**, *21*, 41–46, doi:10.1252/jcej.21.41.
101. Gidaspow, D. *Multiphase flow and fluidization: Continuum and kinetic theory descriptions*; 1st ed.; New York, 1994; ISBN 9780122824708.
102. Khadilkar, A.; Rozelle, P.L.; Pisupati, S. V. Models of agglomerate growth in fluidized bed reactors: Critical review, status and applications. *Powder Technol.* **2014**, *264*, 216–228, doi:10.1016/j.powtec.2014.04.063.
103. Pietsch, W.B. *Agglomeration Processes: Phenomena, Technologies, Equipment*; Wiley-VCH Verlag GmbH: Weinheim, 2008; ISBN 978-3-527-62067-8.
104. Moseley, J.L.; O'Brien, T.J. A model for agglomeration in a fluidized bed. *Chem. Eng. Sci.* **1993**, *48*, 3043–3050, doi:10.1016/0009-2509(93)80170-U.
105. Wank, J.R.; George, S.M.; Weimer, A.W. Vibro-fluidization of fine boron nitride powder at low pressure. *Powder Technol.* **2001**, *121*, 195–204, doi:10.1016/S0032-5910(01)00337-0.
106. Lin, C.-L.; Peng, T.-H.; Wang, W.-J. Effect of particle size distribution on agglomeration/defluidization during fluidized bed combustion. *Powder Technol.* **2011**, *207*, 290–295, doi:10.1016/j.powtec.2010.11.010.
107. van der Drift, A.; Olsen, A. *Conversion of biomass, Prediction and solution methods for ash agglomeration and related problems*; Petten and Roskilde, 1999;
108. Li, J.; Kato, K. A correlation of the elutriation rate constant for adhesion particles (group C particles). *Powder Technol.* **2001**, *118*, 209–218, doi:10.1016/S0032-5910(00)00404-6.
109. Geldart, D.; Wong, A.C.Y. Entrainment of particles from fluidized beds of fine powders. *AIChE Symp. Ser.* **1987**, *83*, 1–9.
110. Baron, T.; Hazlett, J.D.; Bergougnou, M.A.; Briens, C.L.; Galtier, P. Size distribution of the particles entrained from fluidized beds: Gas humidity effects. *Can. J. Chem. Eng.* **1992**, *70*, 631–635, doi:10.1002/cjce.5450700403.
111. Baeyens, J.; Geldart, D.; Wu, S.Y. Elutriation of fines from gas fluidized beds of Geldart A-type powders — effect of adding superfines. *Powder Technol.* **1992**, *71*, 71–80, doi:10.1016/0032-5910(92)88006-4.

112. Ma, X.; Honda, Y.; Nakagawa, N.; Kato, K. Elutriation of fine powders from a fluidized bed of a binary particle-mixture. *J. Chem. Eng. Japan* **1996**, *29*, 330–335, doi:10.1252/jcej.29.330.
113. Ma, X.; Kato, K. Effect of interparticle adhesion forces on elutriation of fine powders from a fluidized bed of a binary particle mixture. *Powder Technol.* **1998**, *95*, 93–101, doi:https://doi.org/10.1016/S0032-5910(97)03262-2.
114. Wen, C.Y.; Hashinger, R.F. Elutriation of solid particles from a dense-phase fluidized bed. *AIChE J.* **1960**, *6*, 220–226, doi:10.1002/aic.690060212.
115. Tanaka, I.; Shinohara, H.; Hirosue, H.; Tanaka, Y. Elutriation of fines from fluidized bed. *J. Chem. Eng. Japan* **1972**, *5*, 51–57, doi:10.1252/jcej.5.57.
116. Wen, C.Y.; Chen, L.H. Fluidized bed freeboard phenomena: Entrainment and elutriation. *AIChE J.* **1982**, *28*, 117–128, doi:10.1002/aic.690280117.
117. Kato, K.; Kanbara, S.; Tajima, T.; Takarada, T.; Ozawa, K.; Shibasaki, H. Effect of particle size on elutriation rate constant for a fluidized bed. *J. Chem. Eng. Japan* **1987**, *20*, 498–504, doi:10.1252/jcej.20.498.
118. Chyang, C.-S.; Wan, H.-P.; Liu, Y.-C. Elutriation of Fine Particles from a Vortexing Fluidized Bed. *J. Chem. Eng. Japan* **1998**, *31*, 950–959, doi:10.1252/jcej.31.950.
119. Li, J.; Yamashita, A.; Kato, K. Elutriation of Very Fine Particles from Fluidized Bed-Effect of Mean Diameter of Bed Particles. *J. Chem. Eng. Japan* **2000**, *33*, 730–739, doi:10.1252/jcej.33.730.
120. Massimilla, L.; Donsì, G.; Zucchini, C. The structure of bubble-free gas fluidized beds of fine fluid cracking catalyst particles. *Chem. Eng. Sci.* **1972**, *27*, 2005–2015, doi:10.1016/0009-2509(72)87059-3.
121. Donsì, G.; Massimilla, L. Bubble-free expansion of gas-fluidized beds of fine particles. *AIChE J.* **1973**, *19*, 1104–1110, doi:10.1002/aic.690190604.
122. Baerns, M. Effect of interparticle adhesive forces on fluidization of fine particles. *Ind. Eng. Chem. Fundam.* **1966**, *5*, 508–516, doi:10.1021/i160020a013.
123. Rietema, K. Application of mechanical stress theory to fluidization. In *International Symposium of Fluidization*; Amsterdam : Netherlands University Press: Eindhoven; p. 154.
124. Donsi, G.; Massimilla, L. Particle to particle forces in fluidization of fine powders. In *International Symposium on Fluidization and Its Applications*; Toulouse, France, 1973; p. 41.
125. Valverde, J.M.; Castellanos, A. Types of gas fluidization of cohesive granular materials. *Phys. Rev. E - Stat. Nonlinear, Soft Matter Phys.* **2007**, *75*, 47–65, doi:10.1103/PhysRevE.75.031306.
126. Gauthier, D.; Zerguerras, S.; Flamant, G. Influence of the particle size distribution of powders on the velocities of minimum and complete fluidization. *Chem. Eng. J.* **1999**, *74*, 181–196, doi:10.1016/S1385-8947(99)00075-3.
127. Wen, C.Y.; Yu, Y.H. A generalized method for predicting the minimum fluidization velocity. *AIChE J.* **1966**, *12*, 610–612, doi:10.1002/aic.690120343.
128. Grace, J.R. Fluidized-bed hydrodynamics. In *Handbook of Multiphase Systems.*; Hemisphere: Washington, 1982 ISBN 978-0070284609.
129. Leva, M. *Fluidization*; McGraw-Hill: New York, NY, USA, 1959;
130. Xu, C.C.; Zhu, J. Prediction of the Minimum Fluidization Velocity for Fine Particles of Various Degrees of Cohesiveness. *Chem. Eng. Commun.* **2008**, *196*, 499–517,

doi:10.1080/00986440802483855.
131. Turki, D.; Fatah, N. Behavior and fluidization of the cohesive powders: Agglomerates sizes approach. *Brazilian J. Chem. Eng.* **2008**, *25*, 697–711, doi:10.1590/S0104-66322008000400007.
132. Sun, G.; Grace, J.R. Effect of particle size distribution in different fluidization regimes. *AIChE J.* **1992**, *38*, 716–722, doi:10.1002/aic.690380508.
133. Khoe, G.K.; Ip, T.L.; Grace, J.R. Rheological and fluidization behaviour of powders of different particle size distribution. *Powder Technol.* **1991**, *66*, 127–141, doi:10.1016/0032-5910(91)80094-Y.
134. Sun, G. Influence of particle size distribution on the performance of fluidized bed reactors. *Can. J. Chem. Eng.* **1991**, *69*, 207, doi:10.1002/cjce.5450690512.
135. Shaul, S.; Rabinovich, E.; Kalman, H. Generalized flow regime diagram of fluidized beds based on the height to bed diameter ratio. *Powder Technol.* **2012**, *228*, 264–271, doi:10.1016/j.powtec.2012.05.029.
136. Dahneke, B. Particle Bounce or Capture—Search for an Adequate Theory: I. Conservation-of-Energy Model for a Simple Collision Process. *Aerosol Sci. Technol.* **1995**, *23*, 25–39, doi:10.1080/02786829508965292.
137. Olivieri, G.; Marzocchella, A.; Salatino, P. Segregation of fluidized binary mixtures of granular solids. *AIChE J.* **2004**, *50*, 3095–3106, doi:10.1002/aic.10340.
138. Tomas, J. Product design of cohesive powders - Mechanical properties, compression and flow behavior. *Chem. Eng. Technol.* **2004**, *27*, 605–618, doi:10.1002/ceat.200406134.
139. Walker, E.E. The properties of powders. Part VI. The compressibility of powders. *Trans. Faraday Soc.* **1923**, *19*, 73–82, doi:10.1039/tf9231900073.
140. Poquillon, D.; Lemaitre, J.; Baco-Carles, V.; Tailhades, P.; Lacaze, J. Cold compaction of iron powders-relations between powder morphology and mechanical properties-Part I: Powder preparation and compaction. *Powder Technol.* **2002**, *126*, 65–74, doi:10.1016/S0032-5910(02)00034-7.
141. Tomas, J. Energy Absorption at Particle Contact, Compression, and Shear Flow of Dry Ultrafine Powder. *Part. Sci. Technol.* **2009**, *27*, 337–351, doi:10.1080/02726350902991049.
142. Schulze, D. *Powders and Bulk Solids*; English Ed.; Springer Berlin Heidelberg: Berlin, Heidelberg, 2007; ISBN 978-3-540-73767-4.
143. Castellanos, A.; Valverde, J.M.; Quintanilla, M.A.S. Physics of compaction of fine cohesive particles. *Phys. Rev. Lett.* **2005**, *94*, 075501, doi:10.1103/PhysRevLett.94.075501.
144. Valverde, J.M.; Quintanilla, M.A.S.; Castellanos, A. Jamming Threshold of Dry Fine Powders. *Phys. Rev. Lett.* **2004**, *92*, 258303, doi:10.1103/PhysRevLett.92.258303.
145. Hostler, S.R. Wave propagation in granular materials, Ph.D. Thesis, California Institute of Technology, Pasadena, CA, USA, 2005.
146. Liu, C. Spatial patterns of sound propagation in sand. *Phys. Rev. B* **1994**, *50*, 782–794, doi:10.1103/PhysRevB.50.782.
147. Majmudar, T.S.; Sperl, M.; Luding, S.; Behringer, R.P. Jamming Transition in Granular Systems. *Phys. Rev. Lett.* **2007**, *98*, 058001, doi:10.1103/PhysRevLett.98.058001.
148. Sederman, A.J.; Alexander, P.; Gladden, L.F. Structure of packed beds probed by

Magnetic Resonance Imaging. *Powder Technol.* **2001**, *117*, 255–269, doi:10.1016/S0032-5910(00)00374-0.

149. Boutreux, T.; de Gennes, P.G. Compaction of granular mixtures: A free volume model. *Phys. A Stat. Mech. Appl.* **1997**, *244*, 59–67, doi:10.1016/S0378-4371(97)00236-7.
150. Richard, P.; Philippe, P.; Barbe, F.; Bourlès, S.; Thibault, X.; Bideau, D. Analysis by X-ray microtomography of a granular packing undergoing compaction. *Phys. Rev. E* **2003**, *68*, 02030, doi:10.1103/PhysRevE.68.020301.
151. Atkinson, J. *The Mechanics of Soils and Foundations*; 2nd Editio.; Taylor & Francis Group: New York, NY, USA, 2007; ISBN 9780415362566.
152. Dwivedi, S.K. Analysis of Particle Deformation Mechanisms and Compact Expansion During Compaction on a high speed Rotary Tablet Press, Ph.D. Thesis, The University of British Columbia, Vancouver, BC, Canada, 1992.
153. Khomane, K.S.; Bansal, A.K. Effect of particle size on in-die and out-of-die compaction behavior of ranitidine hydrochloride polymorphs. *AAPS PharmSciTech* **2013**, *14*, 1169–77, doi:10.1208/s12249-013-0008-4.
154. McCabe, W.L.; Smith, J.; Harriot, P. *Unit operations of chemical engineering.*; 5th editio.; McGraw-Hill, Inc.: Singapore, 1993; Vol. 7; ISBN 0070448442.
155. Quintanilla, M.A.S.; Valverde, J.M.; Castellanos, A. The transitional behaviour of avalanches in cohesive granular materials. *J. Stat. Mech. Theory Exp.* **2006**, *P07015*, doi:10.1088/1742-5468/2006/07/P07015.
156. Kantzas, Apostolos; Bryan Jonathan; Taheri, S. *Fundamentals of Fluid Flow in Porous Media*; PERM Inc (TIPM Laboratory): Calgary, 2015;
157. Krumbein W. C.; Sloss, L.L. *Stratigraphy and Sedimentation*; 1st Ed.; W.H. Freeman and Company: San Francisco, CA, USA, 1951;
158. Carman, P.C. Fluid flow through granular beds. *Chem. Eng. Res. Des.* **1997**, *75*, S32–S48, doi:10.1016/S0263-8762(97)80003-2.
159. Walker, W.H. *Principles of chemical engineering*; Second Edi.; McGraw Hill Book Company, Inc: New York, 1927;
160. Darcy, H. *Les fontaines publiques de la ville de Dijon : exposition et application des principes à suivre et des formules à employer dans les questions de distribution d'eau.*; Dalmont, V., Ed.; Paris, 1856;
161. Dupuit, J. *Études théoriques et pratiques sur le mouvement des eaux dans les canaux découverts et à travers les terrains perméables*; Paris, 1863;
162. Slichter, C.S. Theoretical Investigation of the Motion of Ground Waters. In *Nineteenth Annual Report of the United States Geological Survey Part II*; Washington, 1897; pp. 295–385.
163. Stanton, T.E.; Pannell, J.R. *Collected Researches, National Physical Laboratory, Vol. 11 (Quoted by Othmer, D. F. 1956)*; London, 1914;
164. Schiller, L. Über den Strömungswiderstand von Rohren verschiedenen Querschnitts und Rauhigkeitsgrades. *ZAMM - Zeitschrift Für Angew. Math. Und Mech.* **1923**, *3*, 2–13, doi:10.1002/zamm.19230030102.
165. Blake, F.C. The Resistance of Packing to Fluid Flow. In *Transactions of the American Institute of Chemical Engineers*; D. Van Nostrand Company: New York, 1922; Vol. XIV, pp. 415–421.
166. Kozeny, J. Über kapillare Leitung des Wassers im Boden (Aufstieg, Versickerung

und Anwendung auf die Bewässerung). *Ber. Wien Akad.* **1927**, *136A*, 271–306.
167. Piercy, N.A. V.; Hooper, M.S.; Winny, H.F. LIII. Viscous flow through pipes with cores. *London, Edinburgh, Dublin Philos. Mag. J. Sci.* **1933**, *15*, 647–676, doi:10.1080/14786443309462212.
168. Fair, G.M.; Hatch, L.P. Fundamental Factors Governing the Streamline Flow of Water Through Sand. *Trans. Am. Water Work. Assoc.* **1933**, *25*, 1551.
169. McCabe, W.L.; Smith, J.; Harriot, P.; McCabe, Warren L, Smith, J., Harriot, P. *Unit operations of chemical engineering*.; 5th edi.; McGraw-Hill Inc.: Singapore, 1993; Vol. 7; ISBN 0070448442.
170. Leva, M. Pressure Drop Through Packed Tubes. Part I: A General Coorelation. *Chem. Eng. Prog.* **1947**, *43*, 551.
171. Leva, M. Pressure Drop Through Packed Tubes. Part II: Effect of Surface Roughness. *Chem. Eng. Prog.* **1947**, *43*, 633.
172. Chilton, T.H.; Colburn, A.P. Pressure drop in packed tubes. *Trans. AIChE* **1931**, *26*, 178–196.
173. Chilton, T.H.; Colburn, A.P. Heat Transfer and Pressure Drop in Empty Baffled and Packed Tubes, Part II, Pressure Drop in Packed Tubes. *Ind. Eng. Chem.* **1931**, *23*, 913–919, doi:10.1021/ie50260a016.
174. Rose, H.E. An Investigation into the Laws of Flow of Fluids through Beds of Granular Materials. *Proc. Inst. Mech. Eng.* **1945**, *153*, 141–148, doi:10.1243/pime_proc_1945_153_018_02.
175. Rose, H.E.; Rizk, A.M.A. Further Researches in Fluid Flow through Beds of Granular Material. *Proc. Inst. Mech. Eng.* **1949**, *160*, 493–511, doi:10.1243/PIME_PROC_1949_160_047_02.
176. Brownell, L.E.; Katz, D.L. Flow of fluids through porous media. I: single homogeneous fluids. *Chem. Eng. Prog.* **1949**, *45*, 537–548.
177. Foust, A.S.; Wenzel, L.A.; Clump, C.W.; Maus, L.; Anderson, L.B. *Principles of Unit Operations*; 2nd editio.; John Wiley & Sons: New York, NY, USA, 1980; ISBN 978-0471268970.
178. Ergun, S.; Orning, A.A. Fluid Flow through Randomly Packed Columns and Fluidized Beds. *Ind. Eng. Chem.* **1949**, *41*, 1179–1184, doi:10.1021/ie50474a011.
179. Martin, J.J.; McCabe, W.L.; Monrad, C.C. : Pressure drop through stacked spheres - effect of orientation. Chem. Eng. Prog. 47, 91 (1951). *Chem. Eng. Prog.* **1951**, *47*, 91–98.
180. Berend, J.E. An analytical approach to the clogging effect of suspended matter. *Bull. Int. Assoc. Hydrol.* **1967**, *12*, 42–55.
181. Cheng, W.K. Consolidation of Sand Formation Using Freon -11 Hydrate, M.Sc. Thesis, The University of British Columbia: Vancouver, BC, Canada, 1975.
182. Read, A.; Piccioli, R. Introduction to multiphase flows. In *STAR South East Asian Conference*; Singapore, 8-9 June, 2015.
183. EDEM 2019 User Guide. In; DEM Solutions Ltd., Edinburgh, Scotland, UK. Copyright ©, 2019.
184. ANSYS FLUENT User's Guide. In *Release 17.2*; ANSYS, Inc., Canonsburg, PA, USA, 2016; pp. 1–2763.
185. *Compiling the EDEM-Fluent Coupling UDF*; ANSYS, Inc.: Canonsburg, PA, USA, 2016; pp. 1–26;.

186. Alder, B.J.; Wainwright, T.E. Molecular Dynamics by Electronic Computers. In *Proceedings of the International Symposium on Transport Processes in Statistical Mechanics (Brussels, August 27–31, 1956)*; Interscience Pub., London, 1958; pp. 97–131.
187. Battimelli, G.; Ciccotti, G. Berni Alder and the pioneering times of molecular simulation. *Eur. Phys. J. H* **2018**, *43*, 303–335, doi:10.1140/epjh/e2018-90027-5.
188. Cundall, P.A.; Strack, O.D.L. A discrete numerical model for granular assemblies. *Géotechnique* **1979**, *29*, 47–65, doi:10.1680/geot.1979.29.1.47.
189. Hoomans, B.P.B.; Kuipers, J.A.M.; Briels, W.J.; van Swaaij, W.P.M. Discrete particle simulation of bubble and slug formation in a two-dimensional gas-fluidised bed: A hard-sphere approach. *Chem. Eng. Sci.* **1996**, *51*, 99–118, doi:https://doi.org/10.1016/0009-2509(95)00271-5.
190. Schwartz, S.R.; Richardson, D.C.; Michel, P. An implementation of the soft-sphere discrete element method in a high-performance parallel gravity tree-code. *Granul. Matter* **2012**, *14*, 363–380, doi:10.1007/s10035-012-0346-z.
191. Luding, S. Molecular Dynamics Simulations of Granular Materials. In *The Physics of Granular Media*; 2005; pp. 297–324 ISBN 9783527603626.
192. Zhu, H.P.; Zhou, Z.Y.; Yang, R.Y.; Yu, A.B. Discrete particle simulation of particulate systems : Theoretical developments. *Chem. Eng. Sci.* **2007**, *62*, 3378–3396, doi:10.1016/j.ces.2006.12.089.
193. Tsuji, Y.; Tanaka, T.; Ishida, T. Lagrangian numerical simulation of plug flow of cohesionless particles in a horizontal pipe. *Powder Technol.* **1992**, *71*, 239–250, doi:https://doi.org/10.1016/0032-5910(92)88030-L.
194. Di Renzo, A.; Di Maio, F.P. Comparison of contact-force models for the simulation of collisions in DEM-based granular flow codes. *Chem. Eng. Sci.* **2004**, *59*, 525–541.
195. Zhou, Y.C.; Wright, B.D.; Yang, R.Y.; Xu, B.H.; Yu, A.B. Rolling friction in the dynamic simulation of sandpile formation. *Phys. A Stat. Mech. its Appl.* **1999**, *269*, 536–553, doi:10.1016/s0378-4371(99)00183-1.
196. Ai, J.; Chen, J.; Rotter, J.M.; Ooi, J.Y. Assessment of rolling resistance models in discrete element simulations. *Powder Technol.* **2011**, *206*, 269–282, doi:10.1016/j.powtec.2010.09.030.
197. Johnson, K.L.; Kendall, K.; Roberts, A.D. Surface Energy and the Contact of Elastic Solids. In *Proceedings of the Royal Society of London. Series A: Mathematical, Physical and Engineering Sciences, 324*; London, UK, 1971; pp. 301–313.
198. Mitarai, N.; Nori, F. Wet granular materials. *Adv. Phys.* **2006**, *55*, 1–45, doi:10.1080/00018730600626065.
199. Potyondy, D.O.; Cundall, P.A. A bonded-particle model for rock. *Int. J. Rock Mech. Min. Sci.* **2004**, *41*, 1329–1364, doi:10.1016/j.ijrmms.2004.09.011.
200. Contacts, S.; Encounters, M. Contact and Rubbing of Flat Surfaces. *J. Appl. Phys.* **2004**, *24*, 981–988, doi:10.1063/1.1721448.
201. Chaudhuri, B.; Muzzio, F.J.; Tomassone, M.S. Modeling of heat transfer in granular flow in rotating vessels. *Chem. Eng. Sci.* **2006**, *61*, 6348–6360, doi:10.1016/j.ces.2006.05.034.
202. Walton, O.R.; Braun, R.L. Stress Calculations for Assemblies of Inelastic Spheres in Uniform Shear. *Acta Mech.* **1986**, *63*, 73–86.
203. EDEM 2.7 Theory Reference Guide. In; DEM Solutions, Edinburg, UK, 2015; pp. 1–

19.
204. Hertz, H. Über die Berührung fester elastischer Körper. *J. für die reine und Angew. Math.* **1881**, *92*, 156–171.
205. Mindlin, R.D.; Deresiewicz, H. Elastic Spheres in Contact under Varying Oblique Force. *Trans. ASME, J. Appl. Mech.* **1953**, *20*, 327–344.
206. Qin, R.; Fang, H.; Liu, F.; Xing, D.; Yang, J.; Lv, N.; Chen, J.; Li, J. Study on Physical and Contact Parameters of Limestone by DEM. In *IOP Conference Series: Earth and Environmental Science 252*; 2019; pp. 052110 (1–12).
207. What is DEM? Available online: https://www.edemsimulation.com/what-is-dem-ebook-download.
208. O'Sullivan, C. *Particulate Discrete Element Modelling-a Geomechanics Perspective*; 1st Ed.; Spon Press/Taylor & Francis: London, UK, 2011; ISBN 0415490367.
209. Cook, R.D.; Malkus, D.S.; Plesha, M.E.; Witt, R.J. *Concepts and Applications of Finite Element Analysis*; John Wiley and Sons. Inc., 2001; ISBN 978-0-471-35605-9.
210. Boyle, M. The integration of angular velocity. *Adv. Appl. Clifford Algebr.* **2017**, *27*, 2345–2374, doi:10.1007/s00006-017-0793-z.
211. *ANSYS Fluent Tutorial Guide, Release 18.0*; ANSYS, Inc. Canonsburg, PA, USA, 2017;
212. *Workbench User's Guide, Release 18.0*; ANSYS, Inc. Canonsburg, PA, USA, 2017;
213. Kawaguchi, T.; Tanaka, T.; Tsuji, Y. Numerical simulation of two-dimensional fiuidized beds using the discrete element method (comparison between the two- and three-dimensional models). *Powder Technol.* **1998**, *96*, 129–138, doi:10.1016/S0032-5910(97)03366-4.
214. Yu, A.B.; Xu, B.H. Particle-scale modelling of gas-solid flow in fluidisation. *J. Chem. Technol. Biotechnol.* **2003**, *78*, 111–121, doi:10.1002/jctb.788.
215. Li, J.; Kwauk, M. Exploring complex systems in chemical engineering — the multi-scale methodology. *Chem. Eng. Sci.* **2003**, *58*, 521–535, doi:10.1016/S0009-2509(02)00577-8.
216. van der Hoef, M.A.; van Sint Annaland, M.; Deen, N.G.; Kuipers, J.A.M. Numerical Simulation of Dense Gas-Solid Fluidized Beds : A Multiscale Modeling Strategy. *Annu. Rev. Fluid Mech.* **2008**, *40*, 47–70, doi:10.1146/annurev.fluid.40.111406.102130.
217. *EDEM Coupling Interface : Interface Programming Guide*; DEM Solutions Ltd., Edinburgh, Scotland, UK, 2015;
218. Xu, B.H.; Yu, A.B. Numerical simulation of the gas-solid flow in a fluidized bed by combining discrete particle method with computational fluid dynamics. *Chem. Eng. Sci.* **1997**, *52*, 2785–2809.
219. Tsuji, Y.; Kawaguchi, T.; Tanaka, T. Discrete particle simulation of two-dimensional fluidized bed. *Powder Technol.* **1993**, *77*, 79–87, doi:10.1016/0032-5910(93)85010-7.
220. Di Renzo, A.; Di Maio, F.P. Homogeneous and bubbling fluidization regimes in DEM – CFD simulations: Hydrodynamic stability of gas and liquid fluidized beds. *Chem. Eng. Sci.* **2007**, *62*, 116–130, doi:10.1016/j.ces.2006.08.009.
221. Anderson, T.B.; Jackson, R. Fluid mechanical description of fluidized beds: Equations of Motion. *Ind. Eng. Chem. Fundam.* **1967**, *6*, 527–539, doi:10.1021/i160024a007.
222. Gidaspow, D. *Multiphase Flow and Fluidization*; Elsevier Inc., 1994; ISBN 9780080512266.

223. Arastoopour, H.; Gidaspow, D. Vertical Pneumatic Conveying Using Four Hydrodynamic Models. *Ind. Eng. Chem. Fundam.* **1979**, *18*, 123–130, doi:10.1021/i160070a006.
224. Feng, Y.Q.; Yu, A.B. Assessment of model formulations in the discrete particle simulation of gas-solid flow. *Ind. Eng. Chem. Res.* **2004**, *43*, 8378–8390, doi:10.1021/ie049387v.
225. Li, Y.; Zhang, J.; Fan, L.-S. Numerical simulation of gas–liquid–solid fluidization systems using a combined CFD-VOF-DPM method: bubble wake behavior. *Chem. Eng. Sci.* **1999**, *54*, 5101–5107, doi:10.1016/S0009-2509(99)00263-8.
226. Xiong, Y.; Zhang, M.; Yuan, Z. Three-dimensional numerical simulation method for gas–solid injector. *Powder Technol.* **2005**, *160*, 180–189, doi:10.1016/J.POWTEC.2005.08.029.
227. Potic, B.; Kersten, S.R.A.; Ye, M.; Van Der Hoef, M.A.; Kuipers, J.A.M.; Van Swaaij, W.P.M. Fluidization with hot compressed water in micro-reactors. *Chem. Eng. Sci.* **2005**, *60*, 5982–5990, doi:10.1016/j.ces.2005.04.047.
228. Wen, C.Y.; Yu, Y.H. Mechanics of Fluidization. *Chem. Eng. Prog. Symp. Ser.* **1966**, *162*, 100–111.
229. Di Felice, R. The voidage function for fluid-particle interaction systems. *Int. J. Multiph. Flow* **1994**, *20*, 153–159, doi:10.1016/0301-9322(94)90011-6.
230. Koch, D.L.; Sangani, A.S. Particle pressure and marginal stability limits for a homogeneous monodisperse gas-fluidized bed: kinetic theory and numerical simulations. *J. Fluid Mech.* **1999**, *400*, 229–263, doi:10.1017/S0022112099006485.
231. Koch, D.L.; Hill, R.J. Inertial effects in suspension and porous-media flows. *Annu. Rev. Fluid Mech.* **2001**, *33*, 619–647, doi:10.1146/annurev.fluid.33.1.619.
232. Mogan, J.P.; Taylor, R.W.; Booth, F.L. The value of the exponent n in the Richardson and Zaki equation, for fine solids fluidized with gases under pressure. *Powder Technol.* **1971**, *4*, 286–289, doi:10.1016/0032-5910(71)80051-7.
233. Choi, H.G.; Joseph, D.D. Fluidization by lift of 300 circular particles in plane Poiseuille flow by direct numerical simulation. *J. Fluid Mech.* **2001**, *438*, 101–128, doi:10.1017/S0022112001004177.
234. Zhang, J.; Fan, L.; Zhu, C.; Pfeffer, R.; Qi, D. Dynamic behavior of collision of elastic spheres in viscous fluids. *Powder Technol.* **1999**, *106*, 98–109, doi:10.1016/S0032-5910(99)00053-4.
235. Bruno, M.; Massaro, F.R.; Prencipe, M. Surface science theoretical structure and surface energy of the reconstructed {01.2} form of calcite (CaCO3) crystal. *Surf. Sci.* **2008**, *602*, 2774–2782, doi:10.1016/j.susc.2008.07.002.
236. Materials Science and Engineering Department- Michigan Technological University-USA , Mechanical Properties Data Available online: http://www.mse.mtu.edu/~drjohn/my4150/props.html.
237. Vallero, D.A. *Fundamentals of Air Pollution*; 5th Editio.; Academic Press: New York, NY, USA, 2014; ISBN 978-0124017337.
238. Cordero, M.E.; Uribe, S.; Zárate, L.G.; Rangel, R.N.; Regalado-Méndez, A.; Reyes, E.P. CFD Modelling of Coupled Multiphysics-Multiscale Engineering Cases. In *Computational Fluid Dynamics - Basic Instruments and Applications in Science*; InTech, 2018; pp. 237–263 ISBN 978-953-51-3791-7.

Publications and presentations

The publications and presentations related to this dissertation in national and international journals and conferences are listed as follow:

Publications in National and International Journals, and in Conference Proceedings

1- Abbas Kamranian Marnani, Andreas Bück, Sergiy Antonyuk, Berend van Wachem, Dominique Thévenin, and Jürgen Tomas "*The Effect of Very Cohesive Ultra-Fine Particles in Mixtures on Compression, Consolidation, and Fluidization*", Processes 2019, 7(7), 439; DOI:10.3390/pr7070439.

2- Abbas Kamranian Marnani, Andreas Bück, Sergiy Antonyuk, Berend van Wachem, Dominique Thévenin, and Jürgen Tomas "*The Effect of the Presence of Very Cohesive Geldart C Ultra-Fine Particles on the Fluidization of Geldart A Fine Particle Beds*", Processes 2019, 7(1), 35; DOI:10.3390/pr7010035.

3- Abbas Kamranian Marnani, Rahmon Idowu, Andreas Bück, Sergiy Antonyuk, Dominique Thévenin, and Jürgen Tomas "*Classification of Ultra-Fine Adhesive Particles at Fine Cohesive Powders*", 12th International Conference of Bulk Materials Storage, Handling and Transportation (ICBMH 2016), 11-14 July 2016, Darwin, Australia; ISBN: 978192107886.

4- Abbas Kamranian Marnani, Andreas Bück, Sergiy Antonyuk, Dominique Thévenin, and Jürgen Tomas "*Study on the Compression, Flow, and Permeation of Fine and Ultra-Fine, Cohesive and Compressible Powders*", 9th International Conference on Multiphase Flow (ICMF 2016), 22-27 May 2016, Firenze, Italy.

Oral and Poster Presentation in National and International Conferences and Workshops

1- Abbas Kamranian Marnani, Andreas Bück, Sergiy Antonyuk, Berend van Wachem, and Dominique Thevenin, "*The Effect of Very Cohesive Ultrafine Particles in Mixtures on Compression, Consolidation, and Fluidization*", presented (poster) in GRK Final workshop, 20-22 June 2019, Magdeburg, Germany.

2- Abbas Kamranian Marnani, Andreas Bück, Sergiy Antonyuk, Berend van Wachem, and Dominique Thevenin, "*Effect of compression process on re-fluidization of the fine particle bed*", presented (poster) in GRK workshop, 24-25 May 2018, Tangermünde, Germany.

3- Abbas Kamranian Marnani, Andreas Bück, Sergiy Antonyuk, Berend van Wachem, and Dominique Thevenin, "*Influence of adding cohesive ultra-fine powders (Geldart group C) on particulate fluidization of fine (Geldart group A) particle beds*", presented (oral) in GRK workshop, 27-28 Oct. 2017, Wolfenbüttel, Germany.

4- Abbas Kamranian Marnani, Andreas Bück, Sergiy Antonyuk, and Dominique Thevenin, "*Study on the fluidization, compression, and Permeation of fine and ultra-fine, cohesive and compressible powders*", presented (oral) in GRK workshop, 19-20 May 2017, Leipzig, Germany.

5- Abbas Kamranian Marnani, Andreas Bück, Sergiy Antonyuk, and Dominique Thevenin, "*Fluidization and compression of fine particles*", presented (oral) in IVT Colloquium workshop, 17 Jan. 2017, Magdeburg, Germany.

6- Abbas Kamranian Marnani, Andreas Bück, Sergiy Antonyuk, and Dominique Thevenin, "*CFD-DEM Simulation of Fine Particles Fluidized Bed*", presented (poster) in GRK workshop, 20-21 October 2016, Potsdam, Germany.

7- Abbas Kamranian Marnani, Andreas Bück, Sergiy Antonyuk, and Dominique Thevenin, "*Classification of ultra-fine adhesive powders in a fine particle bed*", presented (oral) in GRK workshop, 9-10 Jun. 2016, Erfurt, Germany.

8- Abbas Kamranian Marnani, "*An effective method for classification of ultra-fine adhesive particles at fine cohesive powders*", presented (oral) in Annual meeting of the ProcessNet crushing and classifying group, 5-6 Apr. 2016, Hamm, Germany.

9- Abbas Kamranian Marnani, "*CFD-DEM Simulation of Fluidized Bed using Representative Particle Model*", presented (oral) in Workshop of DEM-particle contact models and simulation of multiphase systems using CFD-DEM, under the SPP 1486 "PiKo" and the SPP 1679 "Dyn-Sim-FP" 16-18 Mar. 2016, Magdeburg, Germany.

10- Abbas Kamranian Marnani, Peter Müller, Jürgen Tomas, "*Study on the compression, flow and permeation of fine and ultra-fine, cohesive and compressible powders*", presented (oral) in GRK workshop, 13-14 Nov. 2015, Brandenburg, Germany.

11- Abbas Kamranian Marnani, "*Fluidization, Compression and Permeation behavior of different fine to ultra-fine cohesive powders*", presented (oral) in GRK Summer School, 8-12 Jun. 2015, Berlin, Germany.

12- Abbas Kamranian Marnani, Peter Müller, Jürgen Tomas, "*Fluidization, Consolidation & Re-Fluidization of Cohesive Powder Beds*", presented (oral) in GRK workshop, 7-8 Nov. 2014, Quedlinburg, Germany.

13- Abbas Kamranian Marnani, Peter Müller, Jürgen Tomas, "*Study on the Fluidization of Cohesive Powder Beds*", presented (oral) in GRK workshop, 23-24 May 2014, Dessau, Germany.

14- Abbas Kamranian Marnani, Katja Mader-Arndt, and Jürgen Tomas, "*Compression, Consolidation, Permeation & Flow of Ultrafine Cohesive Powders*", presented (poster) in GRK workshop, 14-15 Jan. 2014, Magdeburg; Germany